

https://dspace.org/

3D printed, artificial extracellular matrix for potential neuroregeneration

Da Silva, Kate

2021
https://hdl.handle.net/10539/32537

Downloaded from a DSpace repository. https://dspace.org/

3D PRINTED, ARTIFICIAL EXTRACELLULAR MATRIX FOR POTENTIAL NEUROREGENERATION

KATE DA SILVA



A dissertation submitted to the Faculty of Health Sciences,
University of the Witwatersrand,
in fulfillment of the requirements for the degree of Master of Science in Medicine

Supervisor:
Professor Viness Pillay
Department of Pharmacy and Pharmacology, University of the Witwatersrand,
South Africa

Co-Supervisors:
Professor Yahya.E Choonara
Department of Pharmacy and Pharmacology, University of the Witwatersrand,
South Africa

Associate Professor Pradeep Kumar
Department of Pharmacy and Pharmacology, University of the Witwatersrand,
South Africa

Johannesburg, 2020

DECLARATION

I, Kate Da Silva, declare that this dissertation is my own work. It is being submitted for the degree of Master of Science in Medicine in the Faculty of Health Sciences in the University of the Witwatersrand, Johannesburg. It has not been submitted before for any degree or examination at this or any other University.



……

Signed this 6th day of November 2020

ANIMAL ETHICS WAIVER

Considering that the cell line (PC12) used in this study is commercially available, no ethics waiver/clearance certificate is required for their usage.

PUBLICATIONS ARISING FROM THIS WORK

1. Kate Da Silva, Pradeep Kumar, Yahya E. Choonara, Lisa C. du Toit and Viness Pillay (2020). 3D Printing of Extracellular Matrix (ECM) Mimicking Scaffolds: A Critical Review of the Current ECM Materials, *Journal of Biomedical Materials Research Part A.* **108** (12), 2324-2350 (Appendix A1).
   Note: This review paper forms part of Chapter 2
   Author contribution by candidate: The candidate assisted with devising and outlining the main ideas of the manuscript. She is the first author of the manuscript, took the lead in writing and modifying the manuscript as well as providing the necessary feedback and approving the final manuscript.

2. Kate Da Silva, Pradeep Kumar, Yahya E. Choonara, Lisa C. du Toit and Viness Pillay (2019). Pre-processing of Medical Image Data for 3D Printed Customized-Neural-Scaffolds, *Tissue Engineering: Part C Methods*, **25** (7), 401-410 (Appendix A2).
   Note: This research paper forms part of Chapter 5
   Author contribution by candidate: The candidate assisted with conceptualising the presented idea. She identified the concept and then developed the hypothesis for the paper by translating the idea from other medical applications. She is the first author of the manuscript, took the lead in writing and modifying the manuscript as well as providing the necessary feedback and approving the final manuscript.

3. Kate Da Silva, Pradeep Kumar, Yahya E. Choonara and Viness Pillay. 3D Printability of an ECM-based Gelatin Methacryloyl (GelMA) Biomaterial for Potential Tissue Engineering Applications (To be submitted to *Biomaterials*).

4. Kate Da Silva, Sandy van Vuuren, Pradeep Kumar, Yahya E. Choonara and Viness Pillay. The antimicrobial effects of Genipin against neurological pathogens to potentially reduce post-surgical infection (To be submitted to *Pharmaceutical Research*).

RESEARCH PRESENTATIONS ARISING FROM THIS WORK

1. Kate Da Silva, Pradeep Kumar, Yahya E. Choonara and Viness Pillay. 3D Printed, Artificial Extracellular Matrix for Potential Neuroregeneration, School of Therapeutic Sciences (STS) Biennial Research Day 2019, University of the Witwatersrand, Johannesburg, 10 September 2019 (Appendix B1).
   Note: Winner of Emerging Researcher Category

2. Kate Da Silva, Pradeep Kumar, Yahya E. Choonara and Viness Pillay. 3D Printed, Artificial Extracellular Matrix for Potential Neuroregeneration, Annual Conference on Pharmaceutical Sciences of the Academy of Pharmaceutical Sciences (Young Scientist of the Year) 2019, Kleinkaap Boutique Hotel, Centurion, 9-11 October 2019 (Appendix B2).

3. Kate Da Silva, Pradeep Kumar, Yahya E. Choonara and Viness Pillay. 3D Printed, Artificial Extracellular Matrix for Potential Neuroregeneration, Annual Molecular Biosciences Research Trust (MBRT) Postgraduate Research Day 2019, University of the Witwatersrand, Johannesburg, 28 November 2019 (Appendix B3).
   Note: 2nd Place Junior category – Honours/Masters

4. Kate Da Silva, Pradeep Kumar, Yahya E. Choonara and Viness Pillay. A Peptide-based 3D-Printed Artificial Extracellular Matrix for Potential Neuroregeneration in Traumatic Brain Injury, 11th Wits Cross Faculty Postgraduate Symposium, University of the Witwatersrand, Johannesburg, 14 October 2020 (Appendix B4).
   Note: Oral Presentation Runner-up

5. Kate Da Silva, Pradeep Kumar, Yahya E. Choonara and Viness Pillay. Regeneration and Repair: Designing a 3D-Printed Artificial Extracellular Matrix for Potential Neuroregeneration in Traumatic Brain Injury, Faculty of Health Sciences Biennial Research Day 2020, University of the Witwatersrand, Johannesburg, 15 October 2020 (Appendix B5).
   Note: Student Winner – Clinical Sciences and Therapeutics for Health, Category B

RESEARCH AWARDS AND FUNDING

1. School of Therapeutic Sciences (STS) Biennial Research Day 2019
   Winner of Emerging Researcher Category (Cash Prize)

2. Annual Molecular Biosciences Research Trust (MBRT) Postgraduate Research Day 2019
   2nd Place Junior category – Honours/Masters (Non-cash Prize)

3. 11th Wits Cross Faculty Postgraduate Symposium
   Oral Presentation Runner-up (Cash Prize)

4. Faculty of Health Sciences Biennial Research Day 2020 (Cash Prize)
   Student Winner – Clinical Sciences and Therapeutics for Health, Category B (Cash Prize)

5. Student Winner – Clinical Sciences and Therapeutics for Health, Category B (Cash Prize)

6. University Postgraduate Merit Award (2018-2019)

7. National Research Foundation DST-NRF Innovation Master's Scholarship (2019-2020)

ABSTRACT

Traumatic Brain Injury (TBI) is a complex, heterogeneous injury ranging in severity and clinical outcomes. TBI is characterised by various stages of brain damage. The primary injury causes mechanical injury to the brain whereas the secondary injury results in further damage from molecular cascade responses. Despite great strides in knowledge and research, no significant improvement in TBI treatments has occurred to date. As this injury affects a significant portion of the population, it is prudent for research to be dedicated towards the development of an effective treatment. Artificial Extracellular Matrix (aECM) hydrogel scaffolds are gaining in popularity due to their inherent ability to provide a microenvironment similar to the in vivo microenvironment. Since the Extracellular Matrix (ECM) is directly implicated in scar formation, the fabrication of an aECM scaffold to prevent early glial scar formation in TBI may provide the much-needed therapeutic strategy in potentially regenerating affected neurons. It is postulated that if intervention can occur soon after injury, ECM manipulation of the injury site can occur, which may promote native functioning and lead to functional recovery. With the drive towards patient customisable treatments, 3D printing is becoming an indispensable fabrication tool. Despite the advancements in 3D bioprinting, 3D biomaterial development for neural tissue engineering is hindered due to the numerous material requirements which need to be satisfied. This study aimed to investigate and design the proposed concept of a 3D printable hydrogel peptide aECM as a novel strategy for the treatment of TBI. An initial study into material selection for hydrogel 3D printing identified Gelatin Methacryloyl (GelMA) and a combination of collagen and elastin, as the material candidate for biomaterial development. Further optimizations saw the inclusion of Genipin into the biomaterial and resulted in the realization of the potential formation of a semi and full Interpenetrating Polymer Network (IPN). Thermodynamic results confirmed the formation of the two IPN biomaterials since the endothermic peak of the semi IPN and full IPN occurred at 140.59 °C and 168.18 °C, respectively indicating the increased thermal stability of the full IPN system. Thermogravimetric Analysis (TGA) indicated that the main loss of weight occurred between approximately 175 ˚C - 475 ˚C and approximately 200 ˚C - 500 ˚C for the semi IPN (64% weight loss) and full IPN (67% weight loss), respectively. Molecular vibrations analysis indicated that two minutes of Ultra Violet (UV) crosslinking did not affect the Amide peaks of the biomaterial IPN systems as the Amide bands are still intact with similar transmittance intensities. Therefore, no alteration to the peptide secondary structure was noted. Both IPN biomaterials were further shown to be amorphous in nature with a high Full Width at Half Maximum (FWHM) value of 7.82 and 7.67 for the full IPN and semi IPN, respectively. The IPN biomaterials have a stiffness of around 600 Pa and are suitable for softer tissue engineering applications – i.e. the brain. Furthermore, viscoelastic studies for all samples indicate that G'>G'' and demonstrates that the hydrogels are more "solid" in nature. Furthermore, the semi IPN displayed the highest elasticity followed by the GelMA polymer and then the full IPN. In addition, both IPN biomaterial scaffolds displayed a "shape-memory" feature in artificial cerebral spinal fluid (aCSF). Scanning Electron Micrographs indicated that the IPN biomaterials had a morphological structure with a significant resemblance to the native rat cortex. Both IPN scaffolds exhibited an increased biodegradation rate of 8 and 6 days, for the semi IPN and full IPN, respectively. The full IPN exhibits 1.5 times greater fluid uptake ability than the semi IPN and after 8 hours, the semi IPN and full IPN had a fluid uptake of 483.0 % and 725.6 %, respectively, in comparison to their initial dry masses. Both biomaterial scaffolds were shown to support the growth of PC12 cells over a 72-hour period. Furthermore, the increased nuclear eccentricity and nuclear area was shown to support the postulation that the IPN biomaterials maintain the cells in a healthy state encouraging cellular mitosis and proliferation. In addition, through fluorescent cell tracking, cellular migration was observed throughout the IPN biomaterial scaffolds. The Genipin component of the full IPN was further shown to exhibit antimicrobial properties in microdilution assays followed by the determination of the minimum bactericidal concentration. This suggests that Genipin can prevent the growth of pathogens associated with post-surgical brain infections. This research therefore contributes to the collection of potential biomaterials for TBI applications. Lastly, 3D printing coupled with the two novel biomaterials can assist in the progression of neural treatments towards patient specific scaffolds through the development of Custom-Neural-Scaffolds (C-N-S) as no two brain injuries are the same. In conclusion, the two biomaterial scaffolds developed in this research demonstrate potential for neuroregeneration in new TBI cases.

ACKNOWLEDGEMENTS

At the completion of this dissertation, there are several individuals who I would like to offer my sincere appreciation for their role in enabling me to complete this research project.

To my Mom and Gran, thank you for supporting my decision to pursue this degree. Thank you for instilling in me the values of perseverance, dedication and passion – for they have helped me get to where I am today. Thank you for your love and guidance, for your unwavering support, constant sacrifices and for always being there when I needed a shoulder to cry on! Mom, thank you for never allowing me to see walking away as an option and for pushing me to strive for more – for you see the potential in me that I cannot see in myself.

To Erin, thank you for inspiring me to pursue this degree. Thank you for teaching me what true bravery really means. Thank you for always listening when times were tough and for never giving up on me.

To my research supervisor, Professor Viness Pillay, for seeing potential in me and for affording me the opportunity to join his postgraduate team. Thank you for all the assistance and guidance in dark times. Thank you for always expecting the best and striving for perfection as you have taught me core qualities that I will forever cherish. Your hunger for knowledge and innovation is unmatched and I will forever be grateful for this opportunity. The pharmaceutics discipline has lost a giant when you passed and I am extremely privileged to have known you.

To my co-supervisors, Professor Yahya Choonara and Associate Professor Pradeep Kumar. Thank you for providing direction and support when needed. I am immensely grateful for the time you both invested in this project. Thank you for providing me with the challenging conversations which ultimately assisted in me thinking ‘outside of the box’ to find the solution. Professor Kumar, thank you for being an excellent mentor. I cannot express how appreciative I am for the numerous passage/5-minute conversations we’ve had – without which this work would not have been possible. Your knowledge and love for science is unparalleled!

To Professor Sandy van Vuuren, thank you for your assistance with the microbiology component of this research. Thank you for your patience and guidance and for always ensuring I had what I needed to complete this section.

To my incredible colleagues at WADDP, thank you for your assistance and for allowing me to spring ideas off you. Your support means the world to me!

To my ‘Crazy 7’, Zakkiyya Cassim, Leschika Singh, Nazihah Hoosen, Rabia Ahmed Khan, Lara Freidus, Azraa Parak and Gillian Mahumane, what a dull world it would be without you! Thank you for the laughs, coffee dates and the crazy times, especially in the difficult stages of this work. Thank you for your constant support, assistance and encouragement. You all have fantastic minds and will accomplish so much! I am so fortunate to know amazing female scientists as yourselves!

To Ms Phumzile Moerane, thank you for always offering a helping hand in the microbiology lab and for assisting with my training. Thank you ensuring everything I required was always timeously prepared.

To Mr Sello Ramarumo, Mr Kleinbooi Mohlabi, Mr Bafana Temba and Ms Tshidi Mosete, thank you for your indispensable efforts in ensuring proficient procurement of chemicals and for always being available whenever I needed anything – something that never went unnoticed.

Financial support received from the National Research Foundation (NRF), the Wits Financial Aid and Scholarships Office (PG Merit Award) and the FRC for this project is acknowledged.

“Character consists of what you do on the third and fourth tries.”

James A. Michener

DEDICATION

This dissertation is dedicated to my Mom and Gran for always encouraging and supporting me, especially when times were tough. I am here today because you never doubt my capabilities.

I love you.

TABLE OF CONTENTS

CHAPTER 1
INTRODUCTION AND MOTIVATION FOR STUDY

1.1 Background for this research 1
1.2 Rationale and motivation for this research 4
1.3 Potential therapeutic applications of the 3D printed scaffolds 7
1.4 Novelty of this study 8
1.5 Aim and objectives of this study 8
1.6 Overview of this dissertation 9
1.7 References 10

CHAPTER 2

A LITERATURE REVIEW OF THE CURRENT EXTRACELLULAR MATRIX (ECM) MATERIALS CURRENTLY UITILIZED FOR 3D PRINTING OF ARTIFICIAL ECM SCAFFOLDS

2.1 Introduction 14
2.2 Current Requirements of ECM Mimics 15
2.3 ECM Components 17
2.3.1 Glycosaminoglycans (GAGs) 17
2.4 ECM Proteins 24
2.4.1 Collagen 24
2.4.2 Elastin 26
2.4.3 Fibrin 27
2.5 ECM Mimics 28
2.5.1 Chitosan 28
2.5.2 Silk Fibroin 30
2.5.3 Self-Assembling Peptides 32
2.6 Processed ECM 35
2.6.1 Gelatin 35
2.6.2 Decellularized ECM (dECM) 37
2.7 Conclusions and Future Perspective 45
2.8 References 47

CHAPTER 3
PRELIMINARY DESIGN AND PROOF OF CONCEPT OF 3D PRINTED ARTIFICIAL EXTRACELLULAR MATRIX SCAFFOLDS

3.1 Introduction 54
3.2 Potential Polymers for 3D Printing of an aECM 56
3.2.1 Poly(ethylene glycol) diacrylate (PEGDA) 56
3.2.2 Gelatin Methacryloyl (GelMA) 57
3.3 Materials and Methods 58
3.3.1 Materials 58
3.3.2 Evaluation of Polymer Blends as Potential 3D Printable Biomaterials 58
3.4 Results and Discussion 60
3.4.1 PEGDA-based Biomaterial 60
3.4.2 GelMA-based Biomaterial 64
3.5 GelMA Biomaterial Optimization 70
3.6 Conclusive Remarks 74
3.7 References 76

CHAPTER 4

DESIGN, FABRICATION, OPTIMIZATION and NEURAL COMPATIBILITY OF THE 3D PRINTED BIOMATERIAL ARTIFICIAL EXTRACELLULAR MATRIX SCAFFOLDS UITILISING THE INTEPENETRATING POLYMER NETWORK APPROACH

4.1 Introduction 79

4.2 Materials and Methods 82

4.2.1 Materials 82

4.2.2 Synthesis of the Neuro-Platform 82

4.2.3 3D printing of the IPN Biomaterial Hydrogel Scaffolds 83

4.2.4 Physiocochemical Characterisation of the 3D Printed IPN Biomaterial Hydrogel Scaffolds 84

4.2.5 Physicomechanical Characterisation of the 3D Printed IPN Biomaterial Hydrogel Scaffolds 85

4.2.6 Morphological Analysis of the 3D Printed IPN Biomaterials Hydrogel Scaffolds 85

4.2.7 Architectural Performance of the 3D Printed IPN Biomaterials Hydrogel Scaffolds 85

4.2.8 In vitro cell analysis of the 3D Printed IPN Biomaterials Hydrogel Scaffolds .. 86

4.2.9 Antimicrobial Activity of Genipin 88

4.3 Results and Discussion 89

4.3.1 Molecular Vibrational Transitions and Thermodynamic Analysis Confirming the Formation of Different 3D Printable IPN Biomaterial Hydrogel Scaffolds 90

4.3.2 Confirmation of the amorphous nature of the 3D Printed IPN Biomaterial Hydrogel Scaffolds 95

4.3.3 Real-Time Viscoelastic properties, Material Stiffness and Hydration of the 3D Printed IPN Biomaterial Hydrogel Scaffolds using a constant frequency 97

4.3.4 Validation of the formation of a morphological neuro-mimicking platform 102

4.3.5 Degradation, Fluid Uptake and Swelling profiles of the 3D Printed IPN Biomaterial Hydrogel Scaffolds 104

4.3.6 Hysteresis and "Shape-Memory" features 107

4.3.7 Determination of neuro-compatibility and neuronal cell proliferation 107

4.3.8 Analysis of the Nuclear Morphology and Migration in response to the 3D printed IPN Scaffolds 108

4.3.9 Antimicrobial Activity of Genipin 112

4.4 Final Formulation 113

4.5 Concluding Remarks..... 114
4.6 References 114

CHAPTER 5
THE PROGRESSION TOWARDS PERSONALISED AND CUSTOM PATIENT TREATMENTS FOR NEURAL INJURIES THROUGH THE DEVELOPMENT OF CUSTOM-NEURAL-SCAFFOLDS (C-N-S)

5.1 Impact Statement 121
5.2 Introduction 121
5.3 Problem Statement 126
5.4 Our solution 127
5.5 Proposed Approach for GPU Implementation in Producing C-N-S 128
5.5.1 GPU Implementation in Medical Imaging 128
5.5.2 Use of Medical Imaging and the Incorporation of GPUs in Nerve Regenerative Attempts 128
5.6 Overview of the proposed method 129
5.6.1 Data Pre-Processing 130
5.6.2 Centerline Extraction and Segmentation 131
5.6.3 3D Bioprinting 132
5.7 Patient Implications, Considerations and Limitations of C-N-S 133
5.8 Conclusion 135
5.9 References 136

CHAPTER 6
CONCLUSIONS AND RECOMMENDATIONS

6.1 Conclusion 142
6.2 Recommendations 143
APPENDICES 144

LIST OF ABBREVIATIONS

^{1}H NMR – Proton Nuclear Magnetic Resonance

2D – Two Dimensional

3D – Three Dimensional

4D – Four Dimensional

aCSF – Artificial Cerebrospinal Fluid

adECM – Adipose Decellularized Extracellular Matrix

aECM – Artificial Extracellular Matrix

$A_{positive\ control}$ – Absorbance of the positive control (absence of treatment)

APS – Ammonium Persulphate

A_{sample} – Absorbance of the treated cells

ATDC5 – Chondrogenic cell line

ATR-FTIR - Attenuated Total Reflectance–Fourier Transform InfraRed

AuPd – Gold palladium

BMSCs– Human bone-marrow derived mesenchymal stem cells

C2C12 – Immortalised mouse myoblast cell line

CAD – Computer-Aided Design

CB – Cucurbit uril

cdECM – Cartilage Decellularized Extracellular Matrix

CNS – Central Nervous System

C-N-S – Custom-Neural-Scaffold

CPU - Central Processing Unit

CPUs - Central Processing Units

CS – Chondroitin Sulphate

CT scan – Computed Tomography scan

DAH – 1,6-diaminohexane

DAPI - 4′,6-diamidino-2-phenylindole

dECM – Decellularized Extracellular Matrix

d-H2O – Deuterated water

DMEM – Dulbecco's Modified Eagle Medium

DoS – Degree of Substitution

DSC – Differential Scanning Calorimetry

ECM – Extracellular Matrix

ECS – Extracellular Space

EDS - Energy Dispersive Spectroscopy

ER – Emergency Room
FBR – Foreign Body Reaction
FBS – Fetal bovine serum
f-gelatin – Furfuryl-gelatin
FTIR – Fourier Transform Infrared
FWHM - Full Width at Half Maximum
GAGs – Glycosaminoglycans
GCE – GelMA Collagen Elastin (no crosslinkers)
GCS – Glasgow Coma Scale
GelMA – Gelatin Methacryloyl
GPU – Graphical Processing Unit
GPUs – Graphical Processing Units
HA – Hyaluronic acid
HACs – Human articular chondrocytes
hASCs/hADSCs – Human adipose-derived stem cells
hCMPCs – Human fetal cardiac-derived progenitor cells
hCPCs – Human cardiac progenitor cells
hdECM – Cardiac Decellularized Extracellular Matrix
hiPSCs – Human-derived induced pluripotent stem cells
hMSCs – Human mesenchymal stem cells
hTMSCs – Human nasal inferior turbinate tissue-derived mesenchymal progenitor cells
hTMSCs - Human turbinate-derived mesenchymal stromal cells
HUASMCs – Human umbilical artery smooth muscle cells
IPN – Interpenetrating Polymer Network
Irgacure 2959 – 2-hydroxy-4-(2-hydroxyethoxy)-2-methylpropiophenone
MBA - N, N'-MethylenebisacrylAmide
MBC – Minimum Bactericidal Concentration
MIC – Minimum Inhibitory Concentration
MMP – Matrix Metalloproteinase
MRI – Magnetic Resonance Imaging
MTT – Methyl-thiazolyl-tetrazolium
MW – Molecular Weight
Ninhydrin - 2,2-dihydroxy-1,3-indanedione
P/S/AB – Penicillin/Streptomycin/Amphotericin B
PBS – Phosphate Buffered Saline
PEG – Poly(ethylene) Glycol

PEGDA – Poly(ethylene glycol) Diacrylate

PNS – Peripheral Nervous System

ppm – Parts per million

PVA – Polyvinyl Alcohol

RGD – Arg-Gyl-Asp (Arginine, Glycine, and Aspartate)

Ru (II) bpy32+ – Ruthenium (II) tris-bipyridyl dication

SAPs – Self-Assembling Peptides

SEM – Scanning Electron Microscopy

SEM-EDS – Scanning Electron Microscopy- Energy Dispersive Spectroscopy

SF – Silk Fibroin

SLA – Stereolithography

SMCs – Smooth Muscle Cells

SOP – Standard Operating Procedure

STL – StereoLithography File Format (3D printing)

STO – Mouse fibroblast cells

TBI - Traumatic Brain Injury

TEMED – Tetramethylethylenediamine

TGA – Thermogravimetric

UCs – Urothelial Cells

UV – Ultra Violet

Wd – Post dry mass

WHO – World Health Organization

Wi – Initial dry mass

Ws – Swollen blotted mass

XRD – X-Ray Diffraction

LIST OF FIGURES

Figure 1.1: Considerations for the development of a biomaterial scaffold for TBI.

Figure 1.2: Schematic displaying the rationale behind the study. The solid lines depict the native occurrences in the tissue whereas the dashed lines represent the potential success of the proposed TBI intervention.

Figure 2.1: Schematic diagram highlighting the homeostasis established between the resident cells and the external ECM. The cells secrete the ECM components and in turn cause remodelling of the ECM. The ECM then facilitates the placement of the cells to form functional tissues through various signalling pathways. This figure is reused from Current Opinion in Rheumatology, **25**, Hubmacher and Apte. The biology of the extracellular matrix: novel insights, pp. 65-70, 2013, with permission from Wolters Kluwer Health, Inc.

Figure 2.2: Evaluation of hCMPC survival *in vivo* after implantation of the 3D bioprinted patch. The implanted scaffolds remained visible on the ventricular wall (infarcted area) in the treated mice over the testing period (A) 1 week and (C) 4 weeks. To analyze cell survival immunofluorescence and bioluminescence imaging was employed. Immunofluorescence was used to confirm the presence CMPCs by measuring (B) human-specific b-integrin and (D) human Laminin A/C whereas bioluminescence imagining was used to establish CMPC survival by detecting luciferase (E and F). Results indicated that CMPCs were present in the transplanted patch and survived over the experimental period. This figure is reused from Biomaterials, **61**, Gaetani *et al*. Epicardial application of cardiac progenitor cells in a 3D-printed gelatin/hyaluronic acid patch preserves cardiac function after myocardial infarction, pp. 339-348, 2015, with permission from Elsevier.

Figure 2.3: Evaluation of cellular movement (A) Chondrocytes and (B) Osteoblasts towards the preferential ECM component. Individual cellular movements were tracked and captured by MetaMorph. Chondrocytes (A) exhibited preferential movement towards HA based hydrogels whereas osteoblasts (B) exhibit preferential movement towards collagen-based hydrogels. This figure is reused

from Biofabrication, **6**, Park *et al*. A comparative study on collagen type I and hyaluronic acid dependent cell behaviour for osteochondral tissue bioprinting, pp. 035004, 2014, with permission from IOP Publishing.

Figure 2.4: Schematic illustrating the first peptide-amphiphile (PA) fabricated in 2001. Section **A** represents the key features of the PA. Area (1) represents the hydrophobic alkyl tail whereas areas (2-5) represent the amino acid residues used during fabrication. Section **B** is a molecular representation of the PA. The hydrophobic region remains slender whereas the peptide region is bulkier. Section **C** represents the spontaneous assembly of the PA molecules into a cylindrical arrangement to create the micelle. Furthermore, the re-assembly process of the PA molecules is illustrated. This figure is reused from Science, **294**, Hartgerink *et al*. Self-Assembly and Mineralization of Peptide-Amphiphile Nanofibers, pp. 1684-1688, 2001, with permission from The American Association for the Advancement of Science.

Figure 2.5: Biochemical analysis of the dECM materials prepared. Images (a), (b) and (c) represent the native and decellularized tissues of cartilage (scale: 50 mm), heart (scale: 100 mm) and adipose (scale: 100 mm), respectively. If cartilage is considered (d), a significant loss in the GAG and collagen content is observed. If the heart tissue is considered (e), no significant loss of GAG and collagen content is observed. If adipose tissue is considered (f), a slight decrease in GAG content and a moderate increase in collagen content is observed. Standard deviation is indicated with the use of error bars (*P<0.05; NS: no significance). This image is reproduced from Pati *et al.,* 2014 under the Creative Legal Code Attribution-NonCommercial-NoDerivs 3.0 Unported Licence.

Figure 2.6: Schematic highlighting the features of an “ideal” bioink.

Figure 3.1: Summary of the biomaterial requirements for successful 3D printing and TBI aECM fabrication.

Figure 3.2: Standard curve of H-Lysine(Boc)-OH used to determine the percentage lysine conjugation of the lysine amino acid moieties in the GelMA polymer relative to the gelatin starting material.

Figure 3.3: Spectral analysis of the synthesized GelMA polymer. ^{1}H analysis of the GelMA polymer is shown in (a) and the gelatin starting material is shown in (b). The red arrows indicate the increase in the methacrylate vinyl signals (δ=5.9 ppm and δ=6.3 ppm) and the green arrow indicates the decrease in the lysine methylene group signal (δ=2.8 ppm).

Figure 3.4: Proposed formation of the semi IPN.

Figure 3.5: Proposed formation of the full IPN.

Figure 3.6: Tilt tests indicating (a) non-crosslinked IPN systems and (b) photo-crosslinked IPN systems.

Figure 3.7: Images of the different layers imaged on the printer during a print. (a) An unsuccessful print of the semi IPN where gaps and over extrusion causes a compounding error and leads to the failure of the scaffold. (b) A successful print of the full IPN indicating the importance of proper parameter optimization. Scale: 1 mm = 2.49 mm for all images.

Figure 3.8: A phase diagram indicating the effect of cartridge and platform temperature on the 3D printability of the optimized biomaterials.

Figure 4.1: Visual representation and relative size of (a) the semi IPN and (b) the full IPN.

Figure 4.2: FTIR spectra of the comparison between the starting material and the two IPN biomaterials. From the spectra, it is evident that, despite the small wavenumber band shifts, the addition of the crosslinking agents had no effect on the appearance of the spectra.

Figure 4.3: Differential Scanning Calorimetric analysis of the IPN Biomaterials. (a) DSC thermograms for all materials during the first run from 0-125 °C. (b) Indication of the thermal transitions of the starting materials and (c) indicates the thermal transitions of the semi and full IPN biomaterials as well as the biomaterial without any crosslinker (GCE).

Figure 4.4: TGA thermograms depicting the weight changes as a function of temperature for GelMA, the semi IPN and full IPN hydrogels.

Figure 4.5: (a) XRD diffractograms of the starting materials and the IPN biomaterials. 'A' indicates the peak considered for analysis. (b) The crystalline nature of Irgacure. (c) The crystalline nature of Genipin.

Figure 4.6: (a) Kinetic gelation, shown as the Shear storage modulus (G'), of the semi and full IPN (without Irgacure 2959) relative to the GelMA polymer alone. (b) Shear Loss modulus of the semi and full IPN relative to the GelMA polymer alone. (c) Kinetic gelation mimicking the manufacturing process, shown as the Shear storage modulus (G'), of the semi and full IPN (without Irgacure 2959) relative to the GelMA polymer alone. In all spectra, the semi IPN is shown in green, the full IPN is shown in red and the GelMA polymer is shown in black.

Figure 4.7: Indication of the elastic ability of the disks after 4 hours of hydration in aCSF. The semi IPN is shown at the top and the full IPN is shown at the bottom.

Figure 4.8: The real-time material stiffness, depicted as the average shear storage modulus (G'), of the IPN hydrogels as non-hydrated and hydrated samples (# indicates the SD = ± 0.44663, ## indicates the SD = ± 0.04732 and ### indicates the SD = ± 0.02858).

Figure 4.9: Scanning Electron Microscopy (SEM) analysis of (a) the semi IPN and (b) the full IPN.

Figure 4.10: An electron micrograph displaying a section of the rat cortex indicating the Extracellular Space (ECS), the space where the ECM is found, outlined in red (Scale bar, 1 μm). This figure is reused from Trends in Neuroscience, **21** (5), Nicholson and Syková. Extracellular space structure revealed by diffusion analysis, 207-215, 1998, with permission from Elsevier.

Figure 4.11: (a) Degradation, (b) Fluid Uptake and (c) Swelling Ratio of the two-3D printed IPN hydrogel biomaterials.

Figure 4.12: Images indicating the "memory" property of the semi IPN hydrogel. (a) Indicates the hydrated gel in artificial cerebral spinal fluid (aCSF) where the fabricated

internal 3D pattern is clearly visible. (b) Indicates the hydrated gel when removed from the aCSF where no fabricated internal 3D pattern is visible.

Figure 4.13: (a) MTT PC12 viability studies in response to the semi (Green) and full (Red) IPN scaffolds (SD≤0.3, n=3) and (b) the normalised cell viability data relative to the positive control set to 0, which represents 100%.

Figure 4.14: Nuclei area in response to the different leachable time points (n=3).

Figure 4.15: Nuclei eccentricity (n=3) in response to the different leachable time points (*indicates p<0.01 compared to the full IPN 24 hours).

Figure 4.16: (a) DAPI stained nuclei of PC12 cells indicating that the nuclei are not rounded but are more elliptical in shape. (b) An overlay of the nucleus stained in DAPI with a brightfield image of the cell body allowing for improved visualisation of the nuclear and cellular morphology.

Figure 4.17: (a) Evidence of cellular migration in both 3D printed IPN scaffolds after 24 hours (cell cluster populations indicated by the yellow arrows). (b) CY5 channel indicating cell clusters with reduced background staining.

Figure 5.1: Schematic displaying the current workflow used in the health care setting to diagnose potential nerve damage as well as the available treatment and management options.

Figure 5.2: Schematic providing an overview of the proposed procedure. The steps are as follows: The area of interest is captured, the image is processed and refined, a CAD model is developed and lastly, the patient Customized-Neural-Scaffold is bioprinted. This image is adapted from Bücking *et al.,* 2017 under the Creative Commons Legal Code Attribution 4.0 International Licence.

Figure 5.3: Schematic displaying the proposed workflow that should be implemented in health care settings to diagnose potential nerve damage. This proposal provides a time efficient solution to prepare patients for surgery, which can

potentially aid in the patient regaining the functioning of the nerve using the fabricated C-N-S.

LIST OF TABLES

Table 2.1: Summary of the natural bioinks and bioink blends presented in the review.

Table 3.1: Evaluation of PEGDA MW 575 as a potential biomaterial for 3D printing and aECM fabrication.

Table 3.2: Evaluation of PEGDA MW 700 as a potential biomaterial for 3D printing and aECM fabrication.

Table 3.3: Evaluation of PEGDA MW 575 and 700 and as a potential biomaterial for 3D printing and aECM fabrication.

Table 3.4: Evaluation of GelMA as a potential biomaterial for 3D printing and aECM fabrication. The green shading represents the formation of a successful biomaterial.

Table 3.5: Optimization of GelMA as a potential biomaterial for 3D printing and aECM fabrication. The green shading represents the formation of a successful biomaterial.

Table 4.1: Cidal activity (MBC values in mg/ml) of Genipin against six bacterial test pathogens

Table 4.2: Processing parameters for the optimized IPN biomaterials.

Table 5.1: A brief comparison of the four most common bioprinting methods.

LIST OF EQUATIONS

Equation 4.1: Mass Swelling Ratio

Equation 4.2: % Fluid Uptake

Equation 4.3: % Degradation

Equation 4.4: % Cell Viability

CHAPTER 1
INTRODUCTION AND MOTIVATION FOR STUDY

1.1 Background for this research

Traumatic Brain Injury (TBI), is a heterogeneous injury resulting in a spectrum of severities determined largely by the Glasgow Coma Scale (GCS), and is one of the leading causes of morbidity, disability and mortality worldwide (Saatman *et al.,* 2008). Due to the nature of the injuries, TBI carries a high socio-economic burden (Fernández-Gajardo *et al*., 2014; Wittchen *et al.,* 2011) and is an extremely complex injury resulting in several forms of brain damage. The primary injury, comprising of the original mechanical force to the head, results in mechanical damage (stretching, tearing and shearing) to the axons, glia, neurons and blood vessels (Adams *et al.,* 1983; Saatman *et al.,* 2008) and results in immediate clinical presentations such as contusions, haemorrhages and lacerations (Mendelow and Crawford, 1997). The secondary injury, initiated at the onset of the primary injury, is a molecular cascade response resulting in further brain damage through amongst others: neuronal death, apoptosis, mitochondrial dysfunction, inflammation, autophagy, and glial scar formation (MacIntosh *et al.,* 1996; Zhou *et al.*, 2020). Despite oxidative damage being strongly believed to be associated with the propagation of the secondary damage after TBI (Clausen *et al.,* 2004; Clausen *et al.,* 2012), the formation of the glial scar is considered to be the main hinderance in axonal regeneration and repair of axonal connectivity (Cregg *et al.,* 2014; Voskuhl *et al.,* 2009). “Compounding this issue is the high risk of patients developing nosocomial infections after a sustained TBI (Boque et al., 2000; Dziedzic et al., 2004), especially penetrating wounds which may allow pathogens to enter the brain (Mayo Clinic, undated). Due to this, the search for an effective TBI solution that can promote healthy tissue proliferation and regeneration as well as reduce the risk of infection, has been intensified.

Despite the knowledge gained over the years, the poor clinical translation of potential treatments has resulted in no significant improvement in TBI treatments (Saatman *et al.,* 2008). Current therapies are more focused on preventing further damage from the secondary injury than repairing the tissue from the primary injury (Sun, 2014). To compound this problem, treatments have been largely directed towards addressing single injury mechanics, when TBI is a multi-factorial injury (Kabadi and Faden, 2014). For effective brain tissue regeneration after TBI, the brain must undergo neurogenesis (production of neurons) as well as the production of other cell types associated with the area of damage. In addition, the correct neural architecture, support structures and connectivity of the new cells has to occur for complete recovery (Arzate and Covarrubias, 2020; Modo, 2019). In this way, TBI treatments

must assist in bridging the injury gap, promote effective axonal communication throughout the injury gap and prevent further neurological deficits (Andriessen *et al.*, 2010; Guo *et al*., 2007) Biomaterial nerve conduits can be used to bridge the injury site to provide directional axonal growth via contact guidance (Priestley *et al.,* 2002) or through a delivery vehicle mechanism where cells and bioactive factors are delivered to the injury site (Nomura *et al.,* 2006). However, despite providing the required porous structure and contact guidance (Priestley *et al.,* 2002), many of these treatments have been largely unsuccessful (Le Blanc and Ringdén, 2007; Lee *et al.,* 2000; Tam *et al*., 2014). More recently, polymer-mediated scaffolds have seen the design and formation of neural scaffolds composed of polymers and biomaterials. Such scaffolds are capable of mimicking the native brain cues (both physical and chemical) in an attempt to promote neuronal regeneration in the fabricated artificial environments (Shoichet, 2010).

In the current absence of a successful polymer-mediated biomaterial scaffold for TBI treatment, the following criteria has to be taken into consideration during the fabrication process. As summarised in **Figure 1.1**, the intended material has to provide the necessary support, through conforming to the dimensions of the lesion site, to prevent further tissue collapse and inflammation. The scaffold should be easy to implant, preferably during the scheduled neurosurgery, to prevent further damage to the lesion site and to the surrounding healthy brain tissue. The scaffold should mimic the biochemical aspects of the native tissue to lower the risk of rejection and the development of a foreign body reaction (FBR). Furthermore, promotion of the native signals (topographical, electrical and mechanical etc.) of the ECM will allow for cellular infiltration, nutrient exchange and adequate mimicking of the surrounding brain tissue. The chosen biomaterials themselves, should not promote an inflammatory response, should be biocompatible and biodegradable to prevent further damage at the lesion site as well as minimizing inflammation and neuronal death (Kumar *et al.,* 2017; Maclean *et al.,* 2018; Subramanian *et al.,* 2009; Willerth and Sakiyama–Elbert, 2007). The emergence of peptide-based biomaterials for neural tissue engineering are showing potential success as they are able to provide innate cell binding sites to promote the native signals of the ECM (Gough *et al.,* 2012) and therefore, are good biomaterial considerations for ECM-mimicking and targeted tissue regeneration.

With the requirement of producing TBI treatments that are able to conform to the exact dimensions of the injury lesions, 3D biologically printed scaffolds are a major consideration as the exact dimensions of the lesion site can be reproduced to bridge the injury gap (Ventola, 2014). ECM hydrogel mimics have been suggested to provide a more "*in vivo*-like" 3D microenvironment for cells in terms of the biological, biomechanical and topographical cues

as well as providing the required water content (Gough *et al.,* 2012). Hence, the significant shift towards fabricating 3D printed scaffolds, which have the ability to closely mimic the architecture of the tissues found *in vivo*. As our understanding of the 3D microenvironment of cells continues to expand, the emergence of ECM-based bioinks incorporating native peptides and ECM components holds great potential for the development of 3D printed ECM-mimicking scaffolds in regenerative medicine and for TBI.

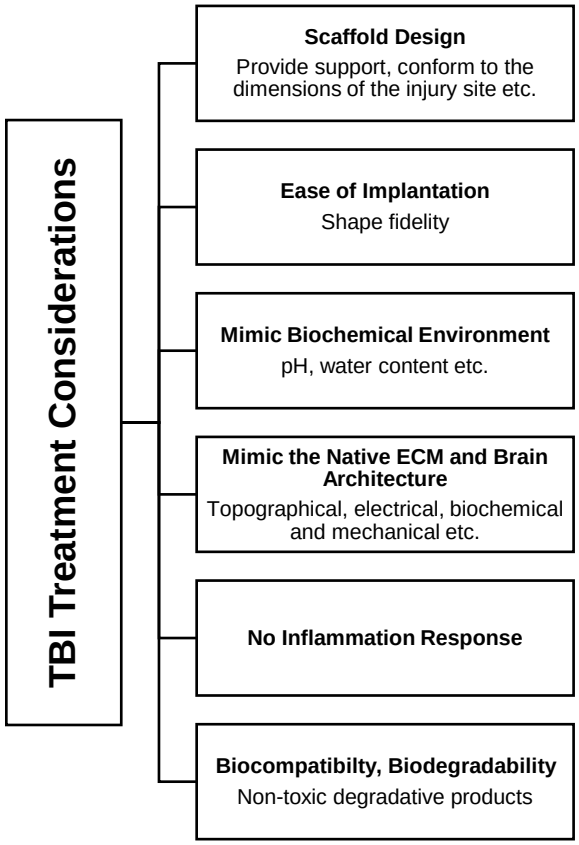


Figure 1.1: Considerations for the development of a biomaterial scaffold for TBI.

The approach focuses on designing a biodegradable, 3D printed peptide/polymer-based scaffold with properties found within the native brain ECM. Therefore, this study focuses on the development of a 3D printed artificial extracellular matrix (aECM) scaffold to provide a potential solution to TBI by controlling the scaffold size and fabricated porosity as well as ensuring biodegradability and physicomechanical/physicochemical mimicking. It is hypothesized that the human body is constructed as an interpenetrating polymer network (IPN) system and to ensure the formation of the 'ideal' scaffold, the formation of an IPN is a major consideration in the development of this aECM scaffold.

1.2 Rationale and motivation for this research

It is estimated that 64-74 million people globally will suffer a new TBI annually (Dewan *et al.,* 2018), with the annual incidence of TBI in South Africa estimated at approximately 361 per one hundred thousand people (GBD 2016 Traumatic Brain Injury and Spinal Cord Injury Collaborators, 2019). TBI can result from a multitude of events including but not limited to road accidents, violence, sports related events and other accidental injuries (e.g. falls, machinery/electrical equipment) (Wang *et al.,* 2016). Although TBI can affect anyone at any age, USA statistics indicate that certain populations are more vulnerable to experiencing a TBI event. For example, between the years of 2002-2006, children between the ages of 0-4 years old had the highest rate of TBI-related Emergency Room (ER) visits (1256 per 100 000 people) followed by adolescents aged between 15-19 years old (757 per 100 000 people). Adults aged 75 years and older had the highest rates of TBI-related hospitalizations and deaths over this period at 339 per 100 000 people and 57 per 100 000 people, respectively. Over this 4-year period, there were overall increases in both ER visits (14.4%) and hospitalisations (19.5%) (US Department of Health and Human Services, 2010). TBI can range from mild to severe and whilst in mild cases the patient can make a full recovery (providing no extenuating circumstances prevent a full recovery), severe TBI will include a period of unconsciousness and can result in prolonged coma and possible death. Since the nerve regeneration capabilities of the human nervous system is insufficient in providing complete repair and regain of function, especially with regards to the Central Nervous System (CNS), there is a growing need for successful TBI therapeutic treatments to regenerate nerves damaged from the injury.

Due to the complexity of TBI pathophysiology and the poor clinical translation of TBI therapeutics, the current shortfall in successful TBI therapeutics provides an interesting venture into the development of an aECM scaffold to overcome the current experienced issues and improve TBI outcomes. In this study, an optimized 3D printed biomaterial scaffold was designed to satisfy the criteria presented in **Figure 1.1** to provide a potential therapeutic solution for TBI by potentially translating preclinical success into a successful patient TBI treatment. This was achieved through the use of neuro-compatible biomaterials and 3D printing technology to potentially bridge the injury gap and provide localised support whilst mimicking the native brain ECM in terms of the 3D printed (designed) and intrinsic material porosity as well as the induction of native ECM signals, for example cellular attachment, migration and proliferation, to potentially assist with nerve regeneration after TBI. As shown in **Figure 1.2**, this study design was based on the following reasoning. In the healthy, uninjured tissue state (solid line) the ECM is kept in homeostasis through controlled ECM degradation and regeneration (formation of new networks through ECM deposition). However, upon a TBI, the ECM deposits materials that give rise to the formation of a glial scar and it is this scar

formation that is proposed to impede native brain tissue regeneration. With this in mind, if intervention can occur soon after injury (dashed line), ECM manipulation of the injury site can occur from the designed 3D printed scaffold, which may promote native functioning and lead to functional recovery.

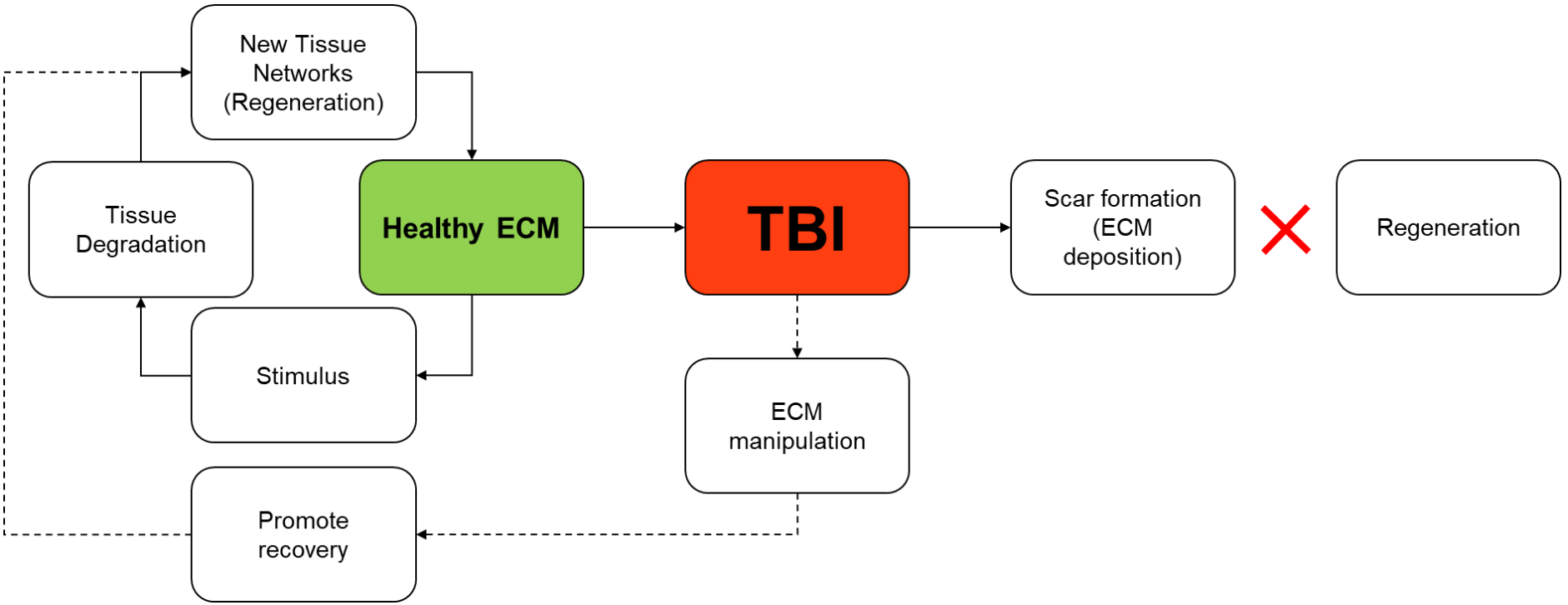


Figure 1.2: Schematic displaying the rationale behind the study. The solid lines depict the native occurrences in the tissue whereas the dashed lines represent the potential success of the proposed TBI intervention.

The use of 3D printing for TBI applications ensures the accuracy and reproducibility of the aECM scaffold during every print to ensure the native ECM is mimicked correctly. In addition, 3D printing is more time efficient than a lab based designed scaffold, it is a cheaper approach for smaller production runs, and most importantly allows for the designing of custom sized and shaped products based on the specific requirements of the nerve damage for a given patient. In addition, the development of this 3D printed aECM scaffold can act as a spring-board for further development as bioactives and therapeutically relevant drugs can be included in the biomaterial for local delivery and sustained release at the site of injury based on the requirements set by the neurosurgeon.

1.3 Potential therapeutic applications of the 3D printed scaffolds

- The biomechanical-co-biomorphological compatibility of the aECM scaffold will ensure no rejection of the scaffold will occur and therefore, no anti-rejection medication post-surgery will be required. This is important in circumventing reopening of the wound and reducing the risk of infection at the trauma site.
- No invasive surgery for the removal and retrieval of stem cells is required as is the case with traditional tissue engineering therapeutics as the scaffolds acellular. Thus, mitigating the need for additional medical procedures resulting in both a reduction in the opportunity for infection and healing time.
- No additional surgery is required to insert the polymeric scaffold if the patient is already undergoing a nerve damage related procedure. This will ensure that no further pain and discomfort is experienced by the patient.
- Since the 3D printer is more time efficient and consistent than lab-based methods, the aECM scaffold can be implanted sooner after the injury has occurred, which is vitally important in the manipulation of the ECM prior to native scar formation in TBI.
- Patient specific nerve conduits printed to the exact shape and size of neuronal injury to beneficially shorten the recovery process.
- Regain of full tissue and nerve functioning, helping patients to regain an independent life.
- A potential solution to neurodegenerative and motor neuron diseases serving as a steppingstone in strides towards providing a possible mechanism for inhibition of neurodegeneration and atrophy as well as a platform for brain regeneration.
- With the use of a Magnetic Resonance Imaging (MRI) scan, the exact shape and size of neuronal injury can be considered when 3D printing the aECM for clinical use (personalized medicine).

1.4 Novelty of this study

- This study networked native brain peptides with a semi-synthetic polymer to develop self-assembling, biofibrous artificial Extracellular Matrix (aECM) archetype scaffolds suitable for neural tissue engineering.
- The aECM archetype scaffold biomaterial was based on a 'fibre floating in gel matrix' framework design principle whereby this novel biomaterial blend, comprising an interpenetrating polymer network archetype, was assembled in a one-step process.
- This all-protein neural system was optimized for 3D printing to overcome the current limitations of neural biomaterials.
- The scaffolds were fabricated to provide a triad of biological cues to ensure the aECM scaffolds would mimic the complexity as well as the signals of the native brain ECM. Chemical cues were provided through the presence of cell adhesion sites on the proteins and gelatin-polymer, architectural cues were provided through the formation of 'pockets' and interconnected channels for increased surface area to promote cell attachment and matrix remodelling and lastly, hierarchical cues were provided through the presence of nano-, micro- and macroporous scale features to assist with possible tissue integration with the native brain tissue.

1.5 Aim and objectives of this study

To develop a 3D printed, self-assembled biomaterial artificial extracellular matrix (aECM) for potential nerve regeneration in TBI applications. To achieve the above-mentioned aim, the following objectives were completed:

1. Fabrication of an interpenetration polymer network-like aECM scaffold through the selection of the appropriate biodegradable polymers, either synthetic or natural, and peptides to resemble the native ECM.
2. To optimize the aECM biomaterial for 3D extrusion-based printing to ensure reproducibility.
3. To perform physicochemical and physicomechanical characterisation analyzes on the 3D printed aECM scaffolds utilizing Fourier Transform Infrared (FTIR) spectroscopy, Scanning Electron Microscopy (SEM), Differential Scanning Calorimetry (DSC), Thermogravimetric (TGA) and X-ray diffraction (XRD).
4. To assess *in vitro* swelling, degradation and fluid retention properties of the 3D printed aECM scaffolds.
5. To assess the neuro-compatibility, nuclear area and nuclear eccentricity of the 3D printed IPN aECM scaffold in *in vitro* cell cultures.

1.6 Overview of this dissertation

Chapter One of this dissertation provides a background to the current study by discussing the current shortfalls in TBI treatments. The important considerations for TBI treatments are presented. The importance, rationale and novelty of the aECM archetypes are discussed. Lastly, the aim and objectives as well as the potential therapeutic benefits of the study is highlighted.

Chapter Two of this dissertation provides a comprehensive review on the current ECM materials utilised for 3D printing of aECM scaffolds for several tissue engineering applications. It discusses the use of glycosaminoglycans, ECM proteins, ECM material mimics and processed ECM materials. Under each sub-section, the chapter considers biomaterial blends and/or individual materials as potential biomaterials. Furthermore, this chapter provides the advantages and disadvantages of each material presented. In addition, this chapter proposes the use of Self-Assembling Peptides (SAPs). SAPs are a biomaterial that have not been extensively utilised in 3D printing, and therefore a new avenue for biomaterial development is proposed. Since the 'ideal' bioink has not yet been developed, the chapter presents the features of an ideal bioink.

Chapter Three of this dissertation provides the design and the proof-concept for the study by evaluating the ability of two polymers – the synthetic polymer Poly(ethylene glycol) diacrylate (PEGDA) and the natural polymer Gelatin Methacryloyl (GelMA) – in their ability to form aECM scaffolds. Both polymers were blended with native peptides namely collagen and elastin to form the aECM archetype. Secondly, this chapter focuses on determining whether the designed biomaterials are able to be optimized for extrusion-based 3D printing on the 3D bioplotter 3D printer. The preliminary formulations with concentration ranges, crosslinking strategies and attempts at 3D printing of the novel peptide networked archetype are presented. The chapter provides the 3D printing optimization for the selected biomaterial – 10% GelMA, 1% Elastin and 0.5% collagen. The chapter further proposes the formation of a semi and full IPN.

Chapter Four of this dissertation firstly provides a section dedicated to IPN systems and the formation of the semi and full IPN 3D printed systems in this work. The chapter describes the physiochemical characterization of the 3D printed IPN scaffolds (Fourier Transform Infra-red (FTIR), thermal, and X-ray diffraction analyzes) as well as the physicomechanical characterizations (material stiffness) to confirm the premise that both a semi and full IPN 3D printed system had been fabricated. Furthermore, a morphology (scanning electron microscopy) comparison between the 3D printed IPN scaffolds and native rat brain tissue is

provided. The chapter then further provides the neuro-compatibility and biological *in vitro* performance (MTT assay) of both 3D printed IPN scaffolds is presented. Furthermore, the effects of different chemical leaching time points on PC12 cells was established (nuclear eccentricity and nuclear area).

Chapter Five of this dissertation provides a futuristic approach to the design of personalised and customized patient treatments using medical imaging, Graphical Processing Units (GPUs) and 3D printing. This chapter provides a proposal of using current algorithms for tubular structures (for example blood vessels and the bronchus) and modifying such algorithms to rod structures (like nerves). Firstly, an algorithm is utilized to crop the medical image to the area of interest (lesion) to reduce the amount of data required for computation. Following this a smoothing algorithm is then applied to reduce the dataset's susceptibility to noise. Centreline extraction is then performed to describe 3D shapes exhibiting a circular symmetry and to determine the accurate length of the structure. Image segmentation is then performed to identify features found within the structure of interest as well as allowing for patient- and injury-specific considerations to be made. The resulting file is then converted into G-code for 3D printing. This will then ensure that the 3D printed scaffold is unique to the patient, thereby offering a customisable treatment plan on a per patient basis. Furthermore, this chapter provides an approach on improving the current limitations of how TBI is handled in a hospital setting.

Chapter Six of this dissertation presents the research conclusions and presents recommendations for future neural advancement and use of the 3D printed aECM scaffold archetype.

1.7 References

Adams, J. H., Graham, D. I. and Gennarelli, T. A. (1983). Head injury in man and experimental animals: Neuropathology. Acta Neurochirurgica's Supplement. **32**, 15–30.

Andriessen, T. M. J. C., Jacobs, B. and Vos, P. E. (2010). Clinical characteristics and pathophysiological mechanisms of focal and diffuse traumatic brain injury. Journal of Cellular and Molecular Medicine. **14**, 2381–2392.

Arzate, D. M. and Covarrubias, L. (2020). Adult Neurogenesis in the Context of Brain Repair and Functional Relevance. Stem Cells and Development. **29** (9), 544.

Boque, M. C., Bodi, M. and Rello, J. (2000). Trauma, head injury, and neurosurgery infections. Seminars in Respiratory Infections. 15 (4), 280-286.

Clausen, F., Lundqvist, H., Ekmark, S., Lewén, A., Ebendal, T. and Hillered, L. (2004). Oxygen free radical-dependent activation of extracellular signal-regulated kinase mediates apoptosis-like cell death after traumatic brain injury. Journal of Neurotrauma. **21**, 1168–1182.

Clausen, F., Marklund, N., Lewén, A., Enblad, P., Basu, S. and Hillered, L. (2012). Interstitial F(2)-isoprostane 8-iso-PGF(2α) as a biomarker of oxidative stress after severe human traumatic brain injury. Journal of Neurotrauma. **29**, 766–775.

Cregg, J. M., DePaul, M. A., Filous, A. R., Lang, B. T., Tran, A. and Silver, J. (2014). Functional regeneration beyond the glial scar. Experimental Neurology. **253**, 197–207.

Dewan, M. C., Rattani, A., Gupta, S., Baticulon, R. E., Hung, Y. C., Punchak, M., Agrawal, A., Adeleye, A. O., Shrime, M. G., Rubiano, A. M., Rosenfeld, J. V., and Park, K. B. (2018). Estimating the global incidence of traumatic brain injury. Journal of Neurosurgery. **130** (4), 1039-1408.

Dziedzic, T., Slowik, A. and Szczudlik. A. (2004). Nosocomial infections and immunity: lesson from brain-injured patients. Critical Care. 8, 266.

Fernández-Gajardo, R., Matamala, J.M., Carrasco, R., Gutiérrez, R., Melo, R. and Rodrigo, R. (2014). Novel Therapeutic Strategies for Traumatic Brain Injury: Acute Antioxidant Reinforcement. CNS Drugs. **28**, 229–248.

GBD 2016 Traumatic Brain Injury and Spinal Cord Injury Collaborators. (2019). Global, regional, and national burden of traumatic brain injury and spinal cord injury, 1990-2016: a systematic analysis for the Global Burden of Disease Study 2016. The Lancet Neurology, **18** (1), 56–87.

Gough, J. E., Saiani, A. and Miller A. F. (2012). Peptide Hydrogels: Mimicking the Extracellular Matrix. Bioinspired, Biomimetic and Nanobiomaterials. **1** (1), 4–12.

Guo, J., Su, H., Zeng, Y., Liang, Y., Wong, W.M., Ellis–Behnke, R.G. So, K. and Wu, W. (2007). Reknitting the injured spinal cord by self–assembling peptide nanofiber scaffold. Nanomedicine: Nanotechnology, Biology and Medicine. **3**, 311–321.

Kabadi, S. V. and Faden, A. I. (2014). Neuroprotective strategies for traumatic brain injury: improving clinical translation. International Journal of Molecular Sciences, **15** (1), 1216–1236.

Kumar, P., Choonara, Y. E., Khan, R. A. and Pillay, V. (2017). The Chemo-Biological Outreach of Nano-Biomaterials: Implications for Tissue Engineering and Regenerative Medicine. Current Pharmaceutical Design. **23** (24), 3538-3549.

Le Blanc, K. and Ringdén, O. (2007). Immunomodulation by mesenchymal stem cells and clinical experience. Journal of Internal Medicine. **262**, 509–525.

Lee, R. J., Springer, M. L., Blanco-Bose, W. E., Shaw, R., Ursell, P. C. and Blau, H. M. (2000). VEGF Gene Delivery to Myocardium Deleterious Effects of Unregulated Expression. Circulation. **102**, 898-901.

Maclean, F. L., Horne, M. K., Williams, R. J. and Nisbet, D. R. (2018). Review: Biomaterial systems to resolve brain inflammation after traumatic injury. APL Bioengineering. **2**, 021502.

Mayo Clinic. (undated). Traumatic brain injury. Mayo Clinic. https://www.mayoclinic.org/diseases-conditions/traumatic-brain-injury/symptoms-causes/syc-20378557 (Accessed Feb 6, 2021).

McIntosh, T. K., Smith, D. H., Meaney, D. F., Kotapka, M. J., Gennarelli, T. A. and Graham, D. I. (1996). Neuropathological sequelae of traumatic brain injury: relationship to

neurochemical and biomechanical mechanisms. Laboratory Investigation - Nature. **74**, 315–342.

Mendelow, A. D. and Crawford, P. J. Primary and secondary brain injury. In: Reilly, P. L. and Bullock, R., editors. Head injury: pathophysiology and management of severe closed injury. 1st ed. London: Chapman & Hall; 1997. p. 72–88.

Modo, M. (2019). Bioscaffold-Induced Brain Tissue Regeneration. Frontiers in Neuroscience. **13**, 1156.

Nomura, H., Tator, C. H. and Shoichet, M. S. (2006). Bioengineered strategies for spinal cord repair. Journal of Neurotrauma. **23**, 496–507.

Priestley, J. V., Ramer, M. S., King, V. R., McMahon, S. B. and Brown, R. A. (2002). Stimulating regeneration in the damaged spinal cord. The Journal of Physiology. **96**, 123–133.

Saatman, K. E., Duhaime, A. -C., Bullock, R., Maas, A. I. R., Valadka, A., Manley, G. T., Workshop Scientific Team and Advisory Panel Members. (2008). Classification of traumatic brain injury for targeted therapies. Journal of Neurotrauma. **25**, 719–738.

Shoichet, M. S. (2010). Polymer Scaffolds for Biomaterials Applications. Macromolecules. **43**, 581–591.

Subramanian, A., Krishnan, U.M. and Sethuraman, S. (2009). Development of biomaterial scaffold for nerve tissue engineering: Biomaterial mediated neural regeneration. Journal of Biomedical Science. **16**, 108–118.

Sun, D. (2014). The potential of endogenous neurogenesis for brain repair and regeneration following traumatic brain injury. Neural Regeneration Research. **9** (7), 688–692.

Tam, R. Y., Fuehrmann, T., Mitrousis, N. and Shoichet, M. S. (2014). Regenerative Therapies for Central Nervous System Diseases: A Biomaterials Approach. Neuropsychopharmacology Reviews. **39**, 169–188.

U.S. Department of Health and Human Services. (2010). Traumatic Brain Injury in the United States: Emergency Department Visits, Hospitalizations and Deaths 2002-2006 (Blue Book). Available: https://www.cdc.gov/traumaticbraininjury/pdf/blue_book.pdf. Last accessed 12 January 2020.

Ventola, C. L. (2014). Medical Applications for 3D Printing: Current and Projected Uses. Pharmacy and Therapeutics. **39** (10), 704-711.

Voskuhl, R. R., Peterson, R. S., Song, B., Ao, Y., Morales, L. B. J., Tiwari-Woodruff, S. and Sofroniew, M. V. (2009). Reactive Astrocytes Form Scar-Like Perivascular Barriers to Leukocytes during Adaptive Immune Inflammation of the CNS. The Journal of Neuroscience. **29** (37), 11511-11522.

Wang, K., Cui, D., and Gao, L. (2016). Traumatic brain injury: a review of characteristics, molecular basis and management. Frontiers in Bioscience (Landmark edition). **21**, 890–899.

Willerth, S. M. and Sakiyama–Elbert, S. E. (2007). Approaches to neural tissue engineering using scaffolds for drug delivery. Advanced Drug Delivery Reviews. **59**, 325–338.

Wittchen, H. U., Jacobi, F., Rehm, J., Gustavsson, A., Svensson. M., Jönsson, B., Olesen, J., Allgulander, C., Alonso, J., Faravelli, C., Fratiglioni, L., Jennum, P., Lieb, R., Maercker, A., van

Os, J., Preisig, M., Salvador-Carulla, L., Simon, R. and Steinhausen, H. -C. (2011). The size and burden of mental disorders and other disorders of the brain in Europe 2010. European Neuropsychopharmacology. **21**, 655–679.

Zhou, Y., Shao, A., Yao, Y., Tu, S. Deng, Y. and Zhang, J. (2020). Dual roles of astrocytes in plasticity and reconstruction after traumatic brain injury. Cell Communication and Signalling. **18** (1), DOI: 10.1186/s12964-020-00549-2.

CHAPTER 2
A LITERATURE REVIEW OF THE CURRENT EXTRACELLULAR MATRIX (ECM) MATERIALS CURRENTLY UITILIZED FOR 3D PRINTING OF ARTIFICIAL ECM SCAFFOLDS

Abstract

The loss of tissues and organs through injury and disease has stimulated the development of therapeutics that have the potential to regenerate and replace the affected tissue. Such therapeutics have the benefit of reducing the reliance and demand for life-saving organ transplants. Of the several regenerative strategies, 3D printing has emerged as the forerunner in regenerative attempts due to the fact that biologically and anatomically correct 3D structures can be fabricated according to the specified need. Despite the progress in this field, improvement is still limited by the difficulty in fabricating scaffolds that adequately mimic the native cellular microenvironment. In response, despite the complexities of the native extracellular matrix (ECM), the inclusion of ECM components into bioinks has emerged as a cutting-edge research area in terms of providing possible ECM mimicking abilities of the 3D printed constructs. Furthermore, the development of ECM-mimicking scaffolds can potentially assist in improving personalised patient treatments. This review provides a critical analysis of selected naturally occurring ECM components as well as synthetic self-assembling peptides in their ability to provide the required ECM microenvironment for tissue regeneration. The success and possible short comings of each material, as well as the specific characteristics of each bioink, is evaluated.

2.1 Introduction

Globally, a shortage of patient-compatible tissues and organs results in significant waiting times for patients to undergo organ transplant surgeries (Donderwinkel *et al*., 2017). As of October 2018, the United States of America Department of Health and Human Services have reported that 115 000 patients are requiring lifesaving organ transplants whilst only 14 500 donors are available (https://optn.transplant.hrsa.gov/). Whilst the number of donors has increased from 5200 since June 2017 and the number of patients requiring organ transplants has dropped slightly from 120 000 during the same time frame (Derakhshanfar *et al*., 2018), the supply-demand ratio remains severely disproportionate. In an attempt to provide patients with solutions, 3D printing has emerged as the forerunner in regenerative medical attempts and is potentially the future of organ transplants.

Three-dimensional (3D) bioprinting allows for the creation of complex and anatomically correct structures through the integration of cells and biomaterials (Gopinathan and Noh, 2018). Due to the fact that the goal of the fabricated structure is to ultimately replace the damaged organ, the bioink used during structure fabrication has to satisfy several criteria for its clinical implementation such as, but not limited to: biocompatibility, biodegradability, pore structure for vascularisation, non-toxic degradation by-products, minimisation of secondary damage and inflammation, controlled degradation rate, mechanically strong to withstand normal body movements as well as to facilitate cell attachment, proliferation and differentiation (Daley *et al.,* 2005; Gopinathan and Noh, 2018; Kumar *et al*., 2017; Smelyanskiy *et al.,* 2009; Subramanian *et al*., 2009; Velasco *et al*., 2015). Ultimately, apart from the geometry of the structure, the material of the bioink is responsible for the manipulation of the native biochemical and biological environment (Hospodiuk *et al*., 2017). Despite the number of bioink types and blends that have been developed, many lack 3D printing properties, cellular compatibility as well as tunability. For this reason, the development of a "perfect or ideal" bioink is yet to be developed and due to these complexities, progress in the tissue engineering field is limited (Malda *et al*., 2013; Parak *et al*., 2018; Rutz *et al*., 2015). In spite of this, 3D bioprinting allows for the incorporation of the patient's cells, which has accelerated the progression of regenerative medicine towards personalised and patient-specific treatments (Mok *et al*., 2016).

This critical review focuses on potential natural materials (GAGs, ECM proteins, ECM mimics and processed ECM) currently utilised in producing ECM-mimicking scaffolds. In addition, this review will evaluate the potential of synthetic self-assembling peptides for 3D printing ECM mimicking applications. Studies for the given material are critically reviewed and where possible contrasted and compared. This review does not focus on the basics and types of 3D bioprinting which can be found elsewhere (Derakhshanfar *et al.,* 2018; Mandrycky *et al*., 2016). Furthermore, polysaccharidic biomaterials such as alginate, cellulose, agarose, dextran and gellan gum are outside the scope of this review (Derakhshanfar *et al.,* 2018; Mandrycky *et al*., 2016).

2.2 Current Requirements of ECM Mimics

The Extracellular Matrix (ECM) is not only a space-filling structure providing physical scaffolding to support organs and tissues but is the dynamic structure responsible for generating signals to control and regulate cellular behaviour (Daley *et al*., 2008; Jarvelainen *et al*., 2009, Theocharis *et al*., 2016). The ECM plays a role in directly regulating, amongst others, cellular growth, shape, survival, differentiation, migration, morphogenesis, homeostasis and apoptosis (**Figure 2.1**) (Daley *et al*., 2008; González-Diaz and Varghese,

2016; Hubmacher and Apte, 2013; Jhala and Vasita, 2015; Theocharis *et al*., 2016). This three-dimensional structure is a complex, mesh-like structure consisting of several matrix macromolecules whose precise composition is unique to every native tissue (Frantz *et al*., 2010; Hinderer *et al*., 2016; Theocharis *et al*., 2016). The matrix is mainly composed of fibre-forming proteins (e.g. collagens, elastin, fibronectin) and non-fibre-forming proteins (glycosaminoglycans and proteoglycans) and other soluble factors secreted by the resident cells of the tissue (Badylak *et al.,* 2009; Frantz *et al*., 2010; Theocharis *et al*., 2016). The functions of the individual components as well as the protein networks that are formed within the ECM ultimately make the ECM well suited to its function (Yue, 2014).

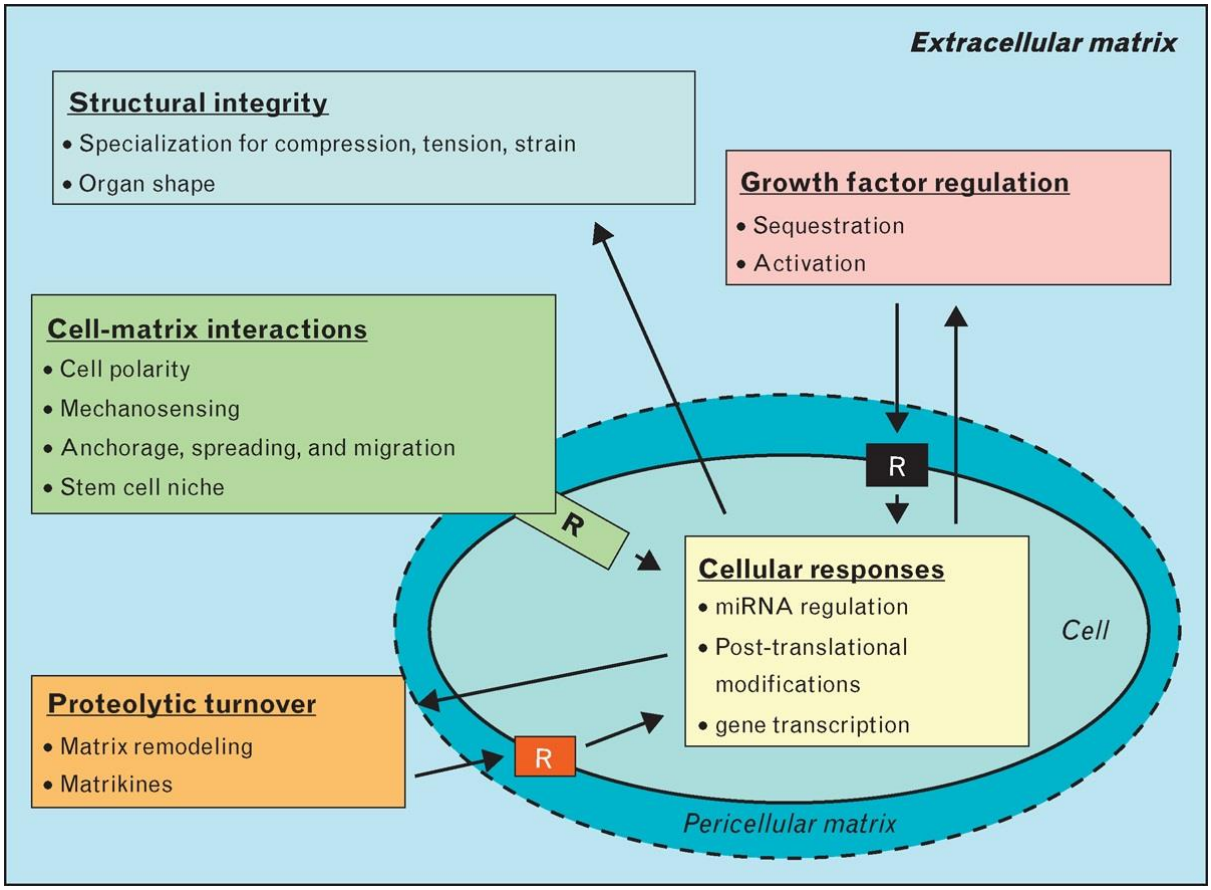


Figure 2.1: Schematic diagram highlighting the homeostasis established between the resident cells and the external ECM. The cells secrete the ECM components and in turn cause remodelling of the ECM. The ECM then facilitates the placement of the cells to form functional tissues through various signalling pathways. This figure is reused from Current Opinion in Rheumatology, **25**, Hubmacher and Apte. The biology of the extracellular matrix: novel insights, pp. 65-70, 2013, with permission from Wolters Kluwer Health, Inc.

Through the remodelling and reshaping of the ECM, the ECM plays a vital role in maintaining the “normal, healthy state” of the tissues (**Figure 2.1**) (Daley *et al.,* 2008). Any changes to a component or network in the ECM can alter the mechanical state and/or organisation of the

ECM, which can result in several disease states (Frantz *et al*., 2010; Jarvelainen *et al.,* 2009; Yue, 2014). The importance of the ECM, the biochemistry, biomechanics, structural organisation and the various biomaterials that constitute the ECM provide an interesting venture into the design and fabrication of 3D printed ECM-mimicking scaffolds (Daley *et al.,* 2008). With this in mind, producing ECM-mimicking scaffolds may provide a promising and new approach to mimicking the biomechanical-co-biomorphological and biophysical cues of the native ECM. Whilst mimicking an incredibly complex matrix poses several issues and difficulties (Hinderer *et al.,* 2016), the usage of native ECM components signals the beginning of generating functional mimicking scaffolds for regenerative medical attempts.

2.3 **ECM Components**

ECM mimics have been suggested to provide a more "*in vivo*-like" 3D microenvironment for cells in terms of the biological, biomechanical and topographical ques as well as providing the required water content (Gough *et al.,*2012). Hence, the significant shift towards fabricating 3D printed scaffolds, which have the ability to closely mimic the architecture of the tissues found *in vivo* is a growing research area. A comprehensive summary of all components analyzed is provided in **Table 1**.

2.3.1 Glycosaminoglycans (GAGs)

Glycosaminoglycans (GAGs) are a major component of the ECM of animal tissues. GAGs are considered to be complex polysaccharide molecules that contribute significantly to the functioning of the ECM (Yamada *et al.,* 2011). GAGs are long, unbranched polysaccharide chains composed of repeating disaccharide sugars, either *N*-acetyl-D-galactosamine or *N*-acetyl-D-glucosamine and a hexuronic acid, either iduronic acid or glucuronic acid (Schaefer and Schaefer, 2010; Yamada *et al.,* 2011). GAGs are hydrophilic in nature and carry a highly negative charge. This causes osmotically active cations and large volumes of water to be attracted towards the GAGs structure, which allows the GAGs to withstand the native compressive forces of the tissue (Prydz, 2015). Despite the benefits that GAGs can offer in 3D printed ECM-mimicking scaffolds, many have not been extensively used and therefore, available research is limited. In spite of this, incorporating GAGs into 3D printed ECM mimics is of utmost importance if researchers are to mimic the native microenvironment of the tissues needing replacement.

2.3.1.1 Hyaluronic Acid (Hyaluronan)

Hyaluronic acid (HA), a naturally occurring ECM component, is an abundant component of connective tissues and synovial fluid (Yoo *et al.,* 2005). Despite the fact that the usage of HA is wide spread in 3D printing structure fabrication, HA exhibits low mechanical strength, slow

gelation and poor printability (Gopinathan and Noh, 2018; Ouyang *et al.,* 2016). In response, blends incorporating HA have emerged as a common biomaterial in 3D printing for the development of 3D printed ECM-mimicking scaffolds to improve the mechanical properties, gelation and 3D printability of HA (Gopinathan and Noh, 2018; Ouyang *et al.,* 2016). In addition, chemical modifications to HA enables the bioinks to be crosslinked to augment HA's rheological properties (Gaetani *et al.,* 2015; Hospodiuk *et al.,* 2017; Shim *et al.,* 2016, Skardal *et al.,* 2017; Yoo *et al.,* 2005). HA is a good candidate for 3D printing as its negatively charged structure attracts water towards the fabricated structure, which plays a critical role in keeping the ECM mimic hydrated (Vigier and Fülöp, 2016). An analysis of the available research has indicated that the importance of HA in the native ECM is undeniable and for this reason has become a common biomaterial utilised in the regenerative attempts of several different tissues.

In studies involving the bioprinting of human-derived induced pluripotent stem cells (hiPSCs), Nguyen and co-workers established that a combination of HA and Nano-fibrillated cellulose (NFC) had not been used when bioprinting hiPSCs. This research group aimed to test this hydrogel combination (and compare it to an NFC-alginate blend) in the extrusion based bioprinting of hiPSCs for cartilage regeneration (Nguyen *et al*., 2017). In another study, Koch and co-workers highlighted that all the available data for hiPSCs bioprinting is extrusion based. This research group aimed to laser bioprint hiPSCs in a selection of sols and gels, including HA (Koch *et al.,* 2018). The difference between the research was that Koch and co-workers did not use the hiPSCs for any application and different blends of HA were used between the research groups. However, cellular proliferation, pluripotency and differentiation were evaluated in both cases. The results from Nguyen and co-workers showed that despite ensuring the 3D structure of the cartilage ECM mimic and its functionality, the hydrogel combination of a 2D construct exhibited low cellular proliferation of the cellular population after encapsulation in the construct. In addition, the cells exhibited phenotypic adjustments associated to be away from pluripotency, which was attributed to the crosslinking conditions (Nguyen *et al*., 2017). This is in direct contrast with the findings of Koch and co-workers who established that laser bioprinting a combination of HA and Matrigel supported the generation of pre-patterned hiPSCs, where cells maintained their differentiation potential and pluripotency. Furthermore, this bioink supported cellular survival, viability, attachment, aggregation and proliferation (Koch *et al.,* 2018). Despite the poor results generated by Nguyen and co-workers, there were slight positives associated with this bioink in the bioprinted structures. RNA expression analysis displayed phenotypic increases in chondrogenic markers after growth factor mediated differentiation. Furthermore, GAG synthesis was slightly increased. Therefore, this bioink can still be promising if an increase in cell numbers could be

achieved through delivery and/or proliferation (Nguyen *et al*., 2017). Analysis of the research suggests that HA could in fact be beneficial in supporting the native cues of pluripotent stem cells, however the blend of materials may affect the intrinsic functioning of native HA.

In 2015, Gaetani and co-workers highlighted that during myocardial infarction, the ECM is altered and scar tissue replaces healthy tissue. In addition, they drew attention to the fact that cardiac stem cell therapies are still suffering from poor engraftment, differentiation and delivery in the myocardium. In response to this, this research group aimed to assess the therapeutic potential of a 3D printed scaffolding patch composed of a HA and gelatin matrix, which was bioprinted with human fetal cardiac-derived progenitor cells (hCMPCs). The patches (with CMPCs) were implanted into a murine model of myocardial infarction to test the patch *in vivo*. Importantly, the patch did not produce any significant inflammatory response after implantation. The patch exhibited optimal integration into the ventricular tissue wall as well as decreasing adverse remodelling and fibrosis and enhanced cellular viability, survival, attachment and engraftment of the hCMPCs (**Figure 2.2**). Furthermore, the infarct wall was thickened and therefore, improved cardiac function in mice with the transplanted patch was noted (Gaetani *et al.,* 2015).

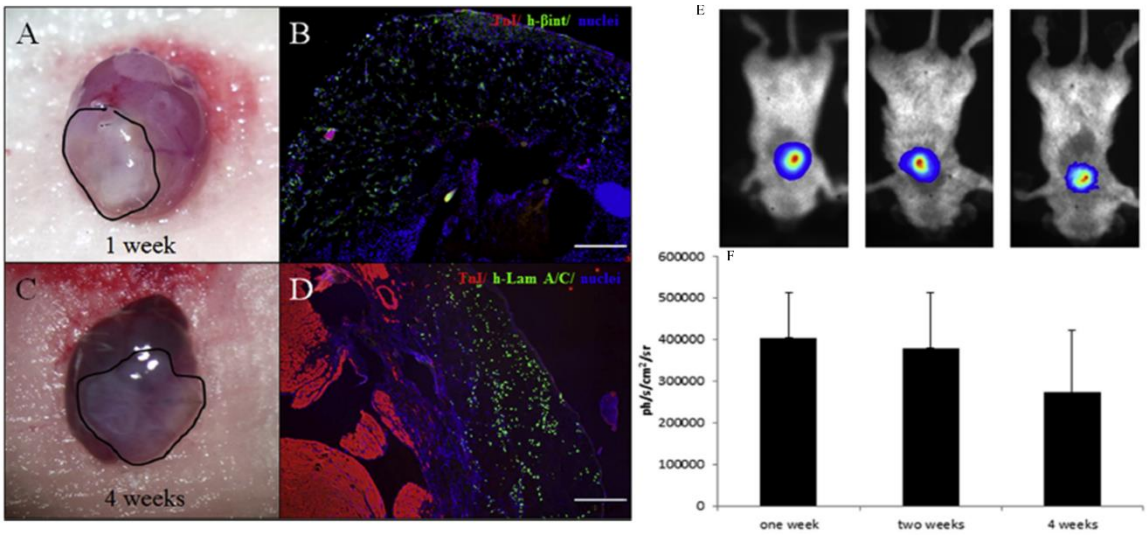


Figure 2.2: Evaluation of hCMPC survival *in vivo* after implantation of the 3D bioprinted patch. The implanted scaffolds remained visible on the ventricular wall (infarcted area) in the treated mice over the testing period (A) 1 week and (C) 4 weeks. To analyze cell survival immunofluorescence and bioluminescence imaging was employed. Immunofluorescence was used to confirm the presence CMPCs by measuring (B) human-specific b-integrin and (D) human Laminin A/C whereas bioluminescence imagining was used to establish CMPC survival by detecting luciferase (E and F). Results indicated that CMPCs were present in the transplanted patch and survived over the experimental period. This figure is reused from Biomaterials, **61**, Gaetani *et al*. Epicardial application of cardiac progenitor cells in a 3D-printed

gelatin/hyaluronic acid patch preserves cardiac function after myocardial infarction, pp. 339-348, 2015, with permission from Elsevier.

Due to the fact that HA is abundant in cartilage (Park *et al.,* 2014), it is not surprising that many research groups are directing their attention towards the usage of HA in regenerating osteochondral tissue. In an osteochondral study performed by Park and co-workers, it became clear that despite HA and collagen type I being widely used for both bone and cartilage tissue engineering, the ECM material best suited for each tissue had not been established. To examine this, the research group conducted a study on the roles of both biomaterials on the migration, proliferation and functioning of osteoblasts and chondrocytes. Following this, osteochondral mimicking 3D bioprinted tissue structures were fabricated. The results indicated that HA based hydrogels, support better functioning and proliferation of chondrocytes than collagen type I (the same was established for osteoblasts in collagen type I hydrogels). These results proved that the native ECM component surrounding the encapsulated cells of a given tissue enhance proliferation, maintain tissue specific phenotypes as well as aid in directing the migration of cells within the tissue (**Figure 2.3**). Following this, the cells and their specific ECM were encapsulated and a 3D bioprinted tissue mimic was produced. Results showed that cells within the mimic were viable and functional in a 14-day *in vitro* experiment. To analyze the biophysical microenvironment of the fabricated hydrogel, the Young's Modulus of the hydrogel was shown to be 21.4 ± 5.7 kPa with a pore diameter of 114.9 ± 95.3 μm. Importantly, no significant degradation of the hydrogel was noticed over a 21-day period. The resistance to degradation was thought to be as a consequence of ECM deposition by the encapsulated cells (Park *et al.,* 2014).

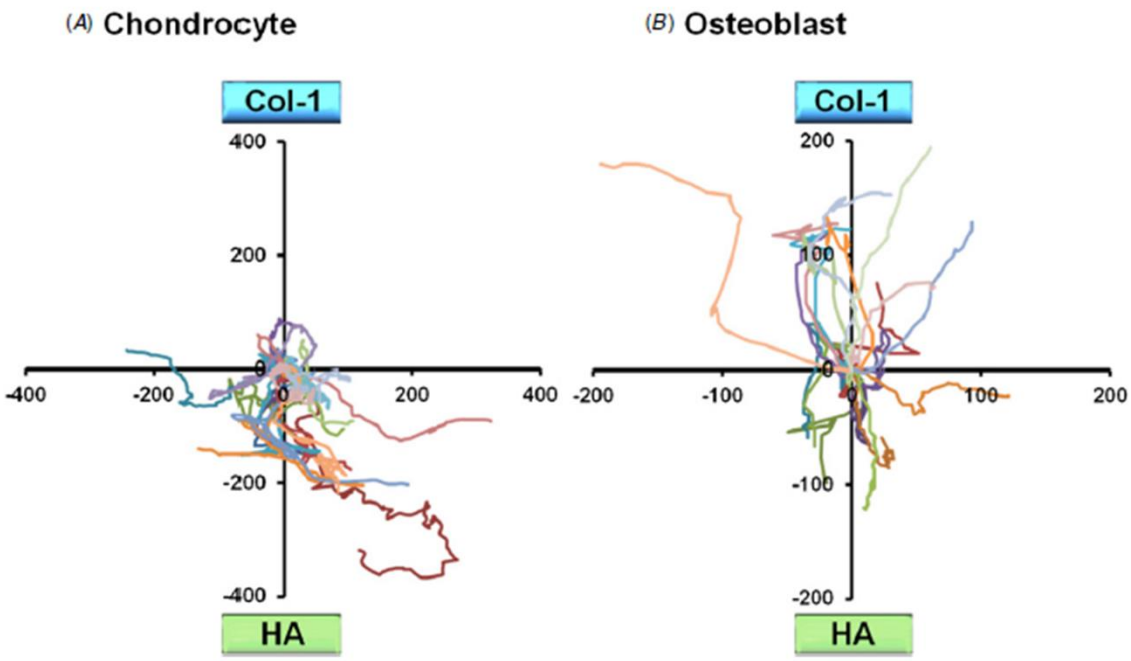


Figure 2.3: Evaluation of cellular movement (A) Chondrocytes and (B) Osteoblasts towards the preferential ECM component. Individual cellular movements were tracked and captured by MetaMorph. Chondrocytes (A) exhibited preferential movement towards HA based hydrogels whereas osteoblasts (B) exhibit preferential movement towards collagen-based hydrogels. This figure is reused from Biofabrication, **6**, Park *et al*. A comparative study on collagen type I and hyaluronic acid dependent cell behaviour for osteochondral tissue bioprinting, pp. 035004, 2014, with permission from IOP Publishing.

In a different study performed by Shim and co-workers, the team discovered that no research had been employed into the development of a printable multi-layered ECM to produce a cell-entrapped, cytocompatible and heterogeneous construct for osteochondral tissue regeneration. In response, the team developed a method to create a multi-layered, 3D bioprinted ECM-cell construct consisting of cucurbit uril (CB), 1,6-diaminohexane (DAH), polycaprolactone, HA, atelocollagen and human turbinate-derived mesenchymal stromal cells (hTMSCs). The results showed that the encapsulated hTMSCs cells remained viable and divided to increase the cell number on a daily basis within the differing layers. Furthermore, the cells in the differing layers exhibited differing phenotypic morphologies (chondrogenic and osteogenic phenotype was identified in the HA and atelocollagen layers, respectively) and expressed specific factors. These results support that the materials used during the fabrication of the differing layers are capable of inducing cellular differentiation specific to the ECM environment. This result corresponds to the findings by Park and co-workers. The *in vivo* efficacy of the ECM and cell rich multi-layered construct was assessed using osteochondral defects in the knee joints of rabbits. Results showed that significant reconstruction and regeneration of the osteochondral tissue had occurred in the knee joints. The only concern associated with the *in vivo* studies was the presence of collagen type X in the superficial layer

of the newly formed neocartilage. This finding requires long-term observation to establish the effects (Shim *et al.,* 2016). The results from both research groups corelate in terms of HA supporting the ECM cues in cartilage where collagen supports the cues for bone. In addition, the results confirm that the biomaterial surrounding a given cell type will induce the native differentiation patterns of the tissue.

In a 2016 investigation by Skardal and co-workers, the team aimed to optimize hydrogels so to improve on the half-lives of growth factors, which will improve their effectiveness even after the cells are no longer present. They hypothesized that a heparin-hyaluronic acid (HA) hydrogel would promote paracrine activity and facilitate the healing of chronic/large wounds. To assess this hydrogel combination, human amniotic fluid multipotent stem cells were delivered during the printing process. The heparin-HA hydrogel was shown to keep cells viable as well as supporting cellular proliferation and migration. In addition, the hydrogel was shown to support long term growth factor and cytokine release in comparison to HA hydrogels. Despite a noted decline in growth factor release, the presence was significant to contribute to increased angiogenesis and wound healing. To understand the hydrogel created, the effect of crosslinking on pore size was then assessed. Linear crosslinking was shown to produce the largest pores (on average around 100 μm). Furthermore, an increase in the number of arms on the crosslinking molecule results in decreased pore sizes (4-arm molecule – average around 50 μm and 8-arm molecule – average around 25 μm). Rheological data indicated that the type of crosslinker used did not significantly affect the elastic modulus of the hydrogel, however their previous studies saw an increase in the elastic modulus when crosslinker density was increased. In a murine model, wounds treated with the heparin-HA hydrogel were shown to heal quicker and wound healing displayed more uniformity in comparison to HA only hydrogels. In addition, increased vascularisation was noted for the heparin-HA hydrogel with a higher deposition of ECM materials, namely, elastin, GAGs and proteoglycans. Furthermore, lower collagen type I (associated with scarring) deposition was noted in the heparin-HA hydrogels, which promotes a healthier ECM to be deposited post injury (Skardal *et al.,* 2017). With this data, inclusion of heparin was shown to be beneficial and therefore, offers a new direction for regenerative medical attempts.

In recent work published in 2018, Mazzocchi and co-workers produced a physiologically relevant, native ECM containing bioink composing thiolated HA and methacrylated collagen type I. This team hypothesised that this bioink would be better suited to native liver tissue organisation than that of a HA/gelatin based bioink. To assess this hypothesis, a liver model using primary hepatocytes and liver stellate cells were used to assess the capabilities of the bioink in terms of liver functioning and its response to acetaminophen. The results showed

that the bioink maintained high cellular viability and promoted the deposition of ECM relevant materials, like collagen. The functionality of the printed system was established by exposing the cell rich bioink to acetaminophen. Results indicated that the functionality of the system was maintained for two weeks, which was likely due to the physiologically relevant, native ECM containing bioink. To characterise the hydrogel, shear storage (G') and loss (G'') moduli were investigated before and after Ultra Violet (UV) crosslinking. The results indicated that prior to crosslinking, formulations have greater G' than G'' with loss tangents between 0.29-0.33. After crosslinking, G' is significantly increased whereas G'' remains largely unchanged. Furthermore, loss tangents fell below 0.1, which indicates that the material becomes more elastic during crosslinking (Mazzocchi *et al.,* 2018). To conclude, despite the intrinsic issues' researchers face when working with HA, HA is a common and important biomolecule utilised in mimicking the native ECM of different tissues.

2.3.1.2 Chondroitin Sulphate

Chondroitin Sulphate (CS), is the most common GAG found bonded to aggrecan (Rodriguez *et al.,* 2006). Aggrecan is the predominant proteoglycan in the ECM of cartilage and intervertebral disks (Kiani *et al.,* 2002; Urban *et al*., 2000). Aggrecan, through the charged nature of the CS, allows the tissues to resist native compressive forces during movement due to its turgid nature (Rodriguez *et al.,* 2006). In terms of the printability of CS, it is yet another native ECM molecule plagued with poor mechanical and shear thinning properties essential for such applications (Abbadessa *et al*., 2016; Costantini *et al.,* 2016). To overcome the issues, blends incorporating CS have emerged as biomaterials in 3D printing for the development of 3D printed ECM-mimicking scaffolds. Despite this, CS like HA, is an important candidate for 3D printing as the negatively charged GAG structure attracts water towards the fabricated structure, which plays a role in keeping the ECM mimic hydrated (Vigier and Fülöp, 2016).

A 2016 study by Abbadessa and co-workers, aimed to develop a hydrogel system suitable for additive 3D printing based on UV-responsive methacrylated chondroitin sulphate and a thermo-sensitive synthetic polymer for cartilage tissue engineering. To assess the suitability of the hydrogel in cartilage regeneration, the ATDC5 chondrogenic cell line was used. The results showed that the hydrogel promoted adequate cellular survival, cellular viability and the cells displayed the expected rounded morphology. In addition, cellular proliferation was detected over a 6-day culture period. An analysis of the rheological properties of the polymer solutions, over a temperature sweep of 4-40 °C, found that G' increases with an increase in temperature. At 40 °C, the G' was 380.8 ± 2.5 Pa with the temperature of gelation (G' intersects G'') found to be 21.4 °C. This result indicated that the hydrogel exhibits thermo-responsive behaviours. A shear rate test indicated that the hydrogel displays sheer-thinning behaviour

(decrease of viscosity from 514 Pa ·s to 0.1 Pa ·s), which indicates the suitability of this hydrogel for 3D printing applications. Furthermore, the hydrogel was shown to possess a yield strength of 19.2 ± 7.0 Pa with a statistically valid R^2 value, which further indicates the suitability for 3D printing. During recovery tests, low strain deformation was reported under constant G' (283 ± 7 Pa) pressures. A significant decrease in G' (10.8 Pa) is recorded under high (100 %) strain with a full recovery to the original G' value under low strain. Such results indicate that the hydrogel exhibits good properties for 3D printing as the values ensure good shape fidelity after extrusion (Abbadessa *et al*., 2016). Despite the fact that this study was more concerned with the printing characteristics and tuneability of the hydrogel, the hydrogel was shown to support cellular activity and therefore, offers a new platform for regenerative medical attempts.

2.4 **ECM Proteins**

In the ECM of each tissue, a unique combination and concentration of proteins is found. The function of each protein in the ECM is critical in providing the distinctive features of that tissue (Hinderer *et al*., 2016). With this in mind, the sheer combination and concentration of native ECM proteins is endless and provides a very interesting platform for regenerative medicine. The combination of proteins within the native ECM of a given tissue, will guide scaffold fabrication in regenerative attempts. In addition, known individual and co-existent protein functioning will allow for non-native protein combinations to be assessed for the development of functional ECM-mimicking scaffolds.

2.4.1 Collagen

Collagen is the most common protein found in the ECM of animals. Collagen is considered to have a triple helical structure made up of three poly-peptide chains wound around each other. In addition, collagen is rich in RGD (Arg-Gyl-Asp) domains, which aids in providing binding support to the cells in the body (Shanwong *et al.,* 2012). Despite the benefits of incorporating collagen into scaffolds, pure collagen has low viscosity which makes bioprinting extremely difficult. For this reason, collagen blends have emerged to improve the viscosity issues (Panwar and Tan, 2016). Collagen is a good candidate for 3D printing as its insoluble, fibrous structure provides extra strength and stability to the ECM mimic whilst promoting the native biological cues. Thus, shape fidelity of the ECM mimic can be maintained (Alberts *et al.,* 2002; Nocera *et al.,* 2018).

Due to the fact that collagen is a major component of the ECM of cartilage (Yang *et al.,* 2018), it is no surprise that collagen blends have emerged as a promising bioink for cartilage and osteogenic tissue engineering. In a previous study, Lee and co-workers indicated that due to the fact that alginate does not contain cell activating sites (RGD domains), cellular attachment

and migration are not promoted. The work performed by this research team aimed to develop a novel bioink with increased bioactivity, consisting of collagen/native ECM and alginate without the need for toxic chemical crosslinkers. In this study, the efficacy of the bioink was tested using encapsulated preosteoblasts and compared to an alginate control. The results indicated that the cells remained viable whilst an increase in cellular density was noted as well as observing an increase in cell proliferation and osteogenic gene expression. In addition, the bioink supported an osteogenic 3D microenvironment, which promoted osteoblastic differentiation of the cells. This was confirmed through the detection of increased mineralisation levels as compared to the alginate control. To prove the suitability of the bioink for other cell types, the research group fabricated the bioink in the presence of human adipose stem cells to identify if hepatogenic differentiation could be achieved. The results proved that there was a meaningful level of liver-specific gene expression, which promoted hepatogenic differentiation and indicated the versatility of the bioink. The rheology of the cell-collagen bioink indicated that increasing the culture time of the hydrogel with cells, G' increases from 67.5 ± 9.8 Pa (0.1 Hz) to 397.2 ± 37.7 Pa (0.1 Hz) over 5 days. Despite the increase in G', processing ability was low resulting in the usage of alginate for reinforcement (Lee *et al*., 2015).

In a similar study performed by Yang and co-workers, the research team identified that a bioink comprising collagen and alginate had not been developed for cartilage 3D bioprinting. Therefore, in response, they 3D bioprinted chondrocytes in a bioink comprising the stated biomaterials. The results indicated that in comparison to the alginate control, the blend promotes increased cellular attachment and adhesion, improves viability of cells, accelerates cellular proliferation, increases GAG synthesis and an upregulation of cartilage specific genes was observed. In addition, the research group indicated that the blend was effective in maintaining the phenotype of the cells by suppressing cellular dedifferentiation. With regards to the mechanics of the hydrogel, the mass swelling ratio and water content in cell-free constructs was shown to have decreased by 43.02 % and 34.78 %, respectively in comparison to alginate only gels. Furthermore, both compressive stiffness (without seeded cells) and tensile behaviour (in comparison to alginate only gels) was increased by 1.87-fold and 124.48 %, respectively (Yang *et al*., 2018). Results from both research groups indicated that a blend of alginate and collagen was beneficial in promoting the native functions of the ECM in comparison to alginate-only bioinks.

In an interesting study only focussing on the usage of collagen hydrogels as bioinks in cartilage tissue engineering, Rhee and co-workers acknowledged that although alginate forms biocompatible hydrogels, high density collagen-based hydrogels could potentially be more desirable for applications requiring load bearing. Furthermore, they identified that although

collagen gels exhibit poor mechanical properties, using higher concentrations of collagen, in ranges between 10 to 20 mg/ml, had not been attempted in bioprinting. With this in mind, they set out to develop and bioprint high density hydrogels consisting only of collagen at different concentrations containing fibrochondrocytes. The results indicated that cell viability was maintained irrespective of the collagen concentration. In addition, the hydrogels supported increased cellular dispersion and infiltration into the printed fibre structures (Rhee *et al*., 2016). This work revealed that the mechanical issues facing pure collagen hydrogels could be overcome by simply increasing the concentration and therefore, highlights the fact that hydrogel blends may not always be the best approach.

In an unrelated study of hydrogel blends, Köpf and co-workers presented work based on the hypothesis that longer lasting cellular encapsulation of human umbilical artery smooth muscle cells (HUASMCs) could be possible using a blend of collagen type I and agarose. The results of the study showed that cellular morphology varied from a mixture of round and spread to only round cells with increases in agarose concentration. Furthermore, cell viability was maintained for seven days with evidence of cell spreading within the hybrid hydrogel. Lastly, encapsulation of the HUASMCs was evident after 21 days in TPLSM images. In terms of the bioink, an average of 20 % degradation was observed over 21 days. Furthermore, the scaffolds exhibited swelling behaviour below 10 % with an average mechanical strength and breaking strain percentages of 1597.76 ± 191.23 Pa (12.0 %) and 38.12 ± 2.07 (5.4 %), respectively (Köpf *et al.,* 2016). Although this hybrid hydrogel represents a promising strategy of hydrogel blending, the research group acknowledges the need for future work.

From the work presented, it is evident that due to the native properties of collagen, it has become an important biomolecule in several tissue engineering approaches. More importantly, the study performed by Rhee and co-workers highlights the need to optimize the issues facing an ECM mimicking material before blends are decided upon.

2.4.2 Elastin

Elastin is a common protein found in the mammalian ECM. Elastin has a conserved arrangement of crosslinking and alternating hydrophobic domains, which makes it insoluble and allows the tissues, such as the lungs, ligaments, skin and arteries, to exhibit elastic properties (Chung *et al.,* 2006; Saxena and Nanjan, 2015). Despite the potential benefits of incorporating elastin into bioprinted ECM mimics, limited research has been found indicating its use in 3D printed regenerative attempts. Despite this, elastin is still a worthy candidate for 3D printing as the crosslinking of the elastin fibres forms insoluble elastic networks, which

gives the ECM mimic elasticity, an important feature for countering the tensile strength of collagen (Alberts *et al.,* 2002; Vigier and Fülöp, 2016).

In a 2018 study by Costa and co-workers, the research team highlighted that the currently available treatments for intervertebral disk degeneration do not consider individual patient requirements and also exhibit poor clinical outcomes. In response, the research team designed a silk fibroin (SF) and elastin-based hydrogel to 3D print patient-specific intervertebral disk structures. The suitability of this bioink was determined using human adipose-derived stem cells (hASCs). The seeded cells were shown to be viable, dispersed and active with a spread morphology. In addition, the hydrogel was shown to promote cellular proliferation. For proof-of-concept, the team successfully 3D printed a patient specific annulus fibrosus structure. In terms of the biophysics of the bioink, a weight loss percentage of 30.3 ± 2.2 % was evident after 28 days in a protease (XIV) solution. This result indicates that the bioink may have a favourable degradation profile for its intended *in vivo* application. In terms of the swelling profile, increased water uptake was observed in the first 24 hours (375 ± 22 %), without significant changes over a 28-day period. The viscoelastic property of storage modulus (E') was observed to increase from 0.56 ± 0.06 MPa to 0.86 ± 0.07 MPa with increasing frequencies from 0.1-10 Hz. Furthermore, loss factor (tan δ) was also observed to increase from 0.33 ± 0.01 to 0.38 ± 0.01 over the same frequency increase. Lastly, lyophilisation was shown to induce a micro-porosity structure ranging between 70-100 μm whilst 3D printing was able to tune macro-pore structures between 400-500 μm in size (Costa *et al.,* 2018). The printing success of this structure opens many doors in personalised medicine and tissue engineering attempts.

2.4.3 Fibrin

Fibrin is a blood protein formed from the mixture of thrombin and fibrinogen. Fibrin can be crosslinked through incubation of calcium ions, fibrinogen and thrombin. Fibrin has been incorporated into regenerative medical attempts due to its promotion of cell adherence. In addition, fibrin is a suitable bioink as its properties can be easily manipulated by altering the mixture components. Fibrin has also been shown to have good biocompatible, bioactive and biodegradable properties. In terms of its printability, fibrin has a low viscosity and poor mechanical properties. In response, fibrin blends have emerged as a means to improve its limitations (Gopinathan and Noh, 2018; Panwar and Tan, 2016). Fibrin is emerging as an essential candidate for 3D printing as its fibrous structure is able to provide not only elasticity but stability to the ECM mimic. Furthermore, fibrin exhibits fast gelation properties that is able to be exploited for the required application (Litvinov and Weisel, 2017; Wang *et al.,* 2019).

In a study performed by Zhang and co-workers, the team noticed that a scarcity of materials and the inadequacy of current therapies are limiting the treatment of urethral stricture. In response, the research team bioprinted an *in vitro*, cell-laden urethra using different polymeric materials and hence, different structural properties. In addition, fibrin based, cell-laden hydrogels were hypothesised to provide a better microenvironment for cellular growth for incorporated smooth muscle cells (SMCs) and urothelial cells (UCs). The results indicated that the fibrin-based hydrogel supported better differentiation, expansion, proliferation, viability, attachment, cellular activity and distribution of the encapsulated UCs and SMCs. Lastly, specific biomarker expression was detected for 14 days post printing. These results have provided that bioprinting of native urethral tissue has been possible and provides a platform for future development (Zhang *et al.,* 2017).

In a different study, England and co-workers highlighted that despite the fact that fibrin-based scaffolds provide advantages in tissue repair fabrication, printing has been challenging due to the poor mechanical properties of the protein. In their research, they developed a novel approach to 3D printing fibrin scaffolds with Schwann cells. The technique involved extruding fibrinogen into a thrombin-based solution with HA and PVA to increase the viscosity of the fibrinogen and thrombin, respectively. Lastly, the XIII clotting factor was incorporated to enhance crosslinking of the fibrin for nerve regeneration applications. The final scaffold was a fibrin-factor XIII-HA 3D printed hydrogel. The results showed that cellular viability remained high after 7 days post printing. In addition, the Schwann cells aligned in a parallel orientation to the bioprinted strands with an elongated, bipolar morphology. Furthermore, nuclear elongation in the direction of the cellular alignment accompanied cellular elongation. In an important finding, directional neurite outgrowth along the strands of the fibrin-based hydrogels was noted whereas in comparison to laminin coated surfaces no directional preference was observed. Lastly, the fibrin-factor XIII-HA scaffolding mimics fabricated in this study were shown to mimic the native fibrin clot that forms after an injury to a nerve fibre and this finding could aid in inducing a powerful response in native nerve regeneration (England *et al*., 2017).

From these two studies it is evident that a fibrin-based hydrogel supports cellular attachment and growth and enables sufficient ECM cues. In addition, it is no wonder that fibrin hydrogels are increasing in popularity for a number of regenerative applications.

2.5 **ECM Mimics**

2.5.1 Chitosan

Chitosan is a naturally derived polysaccharide growing in popularity in the tissue engineering sphere due to its inherent beneficial properties. Properties aiding in the popularity of

incorporating chitosan in bioinks include, but are not limited to, biodegradability, antifungal and antibacterial activity and non-toxicity are sort after characteristics of biomaterials (Panwar and Tan, 2016). In addition to this, Chitosan contains the GAG structural moiety *N*-acetyl-D-glucosamine and in this review is considered to be a GAG-like molecule. Due to the fact that the structure is analogous to that of the GAGs, this GAG-like molecule has been proposed to have related and similar bioactivity to the GAGs (Francis Suh and Matthew, 2000). Chitosan is a good candidate for 3D printing as its GAG-like, fibrous structure allows for the modification of its amine and hydroxyl functional groups to manipulate the mechanical and solubility (insoluble in water) properties to further broaden its biocompatibility. Furthermore, Chitosan has antimicrobial properties, which makes this polysaccharide extremely attractive for regenerative medical attempts (Goy *et al.,* 2009).

In a 2016 publication by Ng and co-workers, they identified that skin bioprinting is delayed by a limited number of printable materials. In particular, many studies have used collagen-based constructs, which have been plagued by long crosslinking times and poor printability. In response, the team designed a polyelectrolyte hydrogel composed of gelatin modified with chitosan. Human foreskin fibroblast cells were used to assess the biocompatibility of the bioink. Results indicated that in addition to improving the printability of the bioink, the bioink facilitated cellular proliferation, attachment, viability and maintained the fibroblast morphology. In terms of the hydrogel biophysics, hydrogels with higher gelatin concentrations were observed to exhibit a higher viscosity and yield strength. Lastly, gels comprising 5 and 7.5 % gelatin were observed to exhibit gel behaviour between 20-40 °C as well as having a high G'/G'' ratio. Such results indicated that good shape fidelity of the printed structures would be achieved (Ng *et al.,* 2016).

In another study performed in 2016, Morris and co-workers highlighted that both PEGDA and chitosan exhibit unfavourable limiting properties and that a hybrid hydrogel of these two biomaterials had not been attempted for stereolithographic 3D printing. The team successfully created the hybrid hydrogel as well as printing the hydrogel in the shape of a complex geometric ear shape. The hybrid scaffold was shown to facilitate cellular proliferation, migration and cell survival of the seeded human mesenchymal stem cells (hMSCs). The porosity of the bioink was shown to have pore sizes ranging between 25-100 μm with an average pore size of 67.3 ± 15.6 μm (n = 15). In addition, increases in PEGDA concentrations caused a 7-fold increase in the elastic modulus for both low and high molecular weight chitosan. Lastly, the hydrogel was shown to fully recover after 50 % strain deformation. Furthermore, the hydrogel was shown to possess the mechanical strength required in cartilage regeneration (Morris *et al.,* 2017).

Although most studies incorporating chitosan are proof of printing concept, the chitosan based bioinks have proven to facilitate in providing the native ECM microenvironment cells require to remain viable in an *in vitro* culture setting. Furthermore, this is one biomaterial requiring further optimizations before further regenerative applications can progress.

2.5.2 Silk Fibroin

Silk Fibroin (SF) is a naturally occurring, high molecular weight protein obtained from the silk produced by the Bombyx mori silkworm. Although not a native ECM material in animals, silk has emerged as an important biomaterial in regenerative medicine due to its biocompatibility, low inflammatory response, controllable degradation rate and exceptional mechanical properties. In addition, SF possesses a high viscosity and decent sheer thinning properties making it an attractive bioink for 3D printing applications (Floren *et al.,* 2016; Panwar and Tan, 2016). Furthermore, the presence of β-Sheets provides strength and hydration to the ECM mimic whilst allowing for structural modification of the SF backbone (Wang *et al.,* 2019).

In a 2017 study performed by Chawla and co-workers, the research group identified that the existing strategies for cartilage repair had several limitations. The group designed the study to investigate whether a SF and gelatin based 3D bioprinted construct, cultured without TGF-β1, would support the differentiation of articular cartilage similar to that of an *in vivo* model. To assess the efficacy of the construct, human bone-marrow derived mesenchymal stem cells (BMSCs) were encapsulated in the bioink. The results indicated that the construct supported cell viability, cellular attachment, cellular proliferation as well as articular cartilage differentiation through gene expression of chondrogenic markers. In addition, the BMSCs where shown to resist hypertrophic differentiation (Chawla *et al.,* 2017).

In another study performed by Compaan and co-workers, the team recognised that the bioprinting of truly freeform silk-based 3D constructs had not been achieved due to slow gelation mechanisms. The study aimed to fabricate SF freeform 3D constructs using calcium alginate crosslinking for quicker gelation during the printing process. In addition, calcium chelation would then be employed to remove the sacrificial alginate after the printing process. The results of the freeform constructs showed that the encapsulated NIH 3T3 mouse fibroblast cells were able to proliferate, migrate and form cellular networks within the hydrogel. In terms of the hydrogel biophysics, SF-alginate hydrogels with and without citrate treatment had a Young's modulus of 6.6 ± 0.4 kPa and 7.5 ± 1.8 kPa, respectively. Furthermore, the results indicate that the SF-alginate samples are less stiff than alginate only samples, however become more elastic, with good elastic recovery, upon the removal of alginate. Therefore, the results indicated that the removal of the alginate did not affect cell morphology or metabolic

activity and that the constructs are appropriate for long term culturing of cells (Compaan *et al.,* 2017).

In a similar study performed by Das and co-workers, the research team also noted that progress in cell delivery and encapsulation is limited by bioink choices and slow gelation mechanisms. The team aimed to develop a 3D bioprinted strategy to deliver human nasal inferior turbinate tissue-derived mesenchymal progenitor cells (hTMSCs) encapsulated in a SF-gelatin bioink optimized via different crosslinking mechanisms. The results were compared to an alginate construct. The results showed that the bioink displayed a thermo-responsive behaviour which was exploited during the printing process. In comparison to the alginate control, the results showed that the hTMSCs cells remained viable for over a month *in vitro* whilst maintaining a 3D structure. The bioink supported a higher rate of cellular proliferation, however, the rate decreased after 2 weeks indicating the important balance between differentiation and proliferation of cells. In addition, the bioink supported native ECM and mineral deposition, cell-cell interaction and GAG synthesis whilst initiating multilineage differentiation through the upregulation of gene expression. In terms of the bioink biophysics, the viscosity was shown to be 6-fold lower at 37 °C than 28 °C. Using this, it was identified that the bioinks are in a sol state at 37 °C and therefore, structures were printed at 28 °C as samples are in semi-gel state. In addition to this, the storage modulus was higher at 18 °C (printer platform temperature) than 28 °C, which ensures shape retention of the printed structure. Lastly, no significant degradation was observed until day 21 (Das *et al.,* 2015). In both studies, SF was shown to improve the native cues of the ECM over alginate and hence, highlight the importance of including SF in regenerative medical attempts.

After reviewing a newly injectable hydrogel composed of SF and PEG, a 2018 study saw Zheng and co-workers utilise a PEG-SF based bioink for 3D bioprinting applications using human bone marrow mesenchymal stem cells (hMSCs). After testing a non-cellular and cellular variant with and without the removal of PEG, respectively, the results showed that lower concentrations of PEG supported cellular viability as well as preserving cellular activity. In addition, hMSCs cultured onto PEG free hydrogels supported cellular attachment and growth, preserved cellular activity and proved that PEG residue (if any remained) did not adversely affect cell function. PEG-SF 3D constructs printed in the presence of hMSCs indicated that the cells remained viable and did not sediment during printing. In addition, cellular morphology and proliferation was seen to be SF concentration dependent. Additionally, encapsulated NIH 3T3 cells in an *in vivo* experiment indicated that the cells had survived the pre-processing of the scaffold and remained viable in the bioink when implanted in a mouse model. In terms of the rheological properties of the hydrogel, G’ was observed to

be greater than G'' over the full angular frequency range tested. Furthermore, both moduli (G' and G'') indicated a slight dependence on the frequency, which indicates that the hydrogel has a typical gel structure under the experienced conditions. In addition, it was suggested that G' was dependant on silk concentrations and, therefore, higher silk/PEG concentrations would be optimal for 3D printing applications. Lastly, a higher viscosity was observed at lower shear stresses (Zheng *et al.,* 2018).

From analysing the available research, it is evident that the addition of SF to hydrogel preparations enhances the native cues of the ECM. Furthermore, silk concentration seems to play a pivotal role in the rheological properties of the hydrogels. Despite SF not being a native mammalian ECM component, research into the usage of SF has proven to be beneficial and may continue to enhance regenerative attempts.

2.5.3 Self-Assembling Peptides

As previously mentioned in the introduction, bioink complexities are still hindering 3D printing regenerative attempts. To further complicate the issue, the complexities of the ECM architecture are extremely difficult to replicate to achieve the desired biological function (Murphy and Atala, 2014). Furthermore, from reviewing the current materials, it appears unlikely that any single material – both natural and synthetic – currently used in bioink design will possess all the required properties to perfectly replicate the ECM microenvironment.

By following natures lead, Professor Samuel I. Stupp strategically designed a new class of molecules termed Self-Assembling Peptides (SAPs) (Hartgerink *et al.*, 2001). As research into this field continues to occur, SAPs are also known as peptide-amphiphiles and Lego peptides (Cui *et al.,* 2010; Hartgerink *et al.,* 2001; Hartgerink *et al.*, 2002; Niece *et al.,* 2003; Paramonov *et al.,* 2006; Zhao and Zhang, 2007). To design SAPs, the approach involves the fabrication of an amphiphilic, synthetic biomolecule composed of a hydrophobic region, generally a short alkyl chain, attached to a defined hydrophilic/ionic peptide sequence (**Figure 2.4a and 2.4b**). (Cui *et al.,* 2010; Hartgerink *et al.,* 2001; Sieminski *et al.,* 2007). According to the laws of free-energy physics, self-assembly involves the spontaneous assembly of the synthetic biomolecule in aqueous environments into diverse 3D structures (micelles, vesicles, cylinders, ribbons, tubes, bilayers, monolayers, tapes and fibres) due to the amphiphilic nature of the peptide (Cokkoli *et al.,* 2006; Cui *et al.,* 2010; Hartgerink *et al.,* 2001; Lakshmanan *et al.,* 2012). The resulting structure will contain the hydrophobic tails in the centre of the micelle with the hydrophilic peptide functional groups exposed to the aqueous environments on the surface of the micelle (**Figure 2.4c**) (Hartgerink *et al.,* 2001). This structure is established and facilitated by weak intermolecular interactions namely: hydrophobic, electrostatic, hydrogen

bonding, van der Waals, ionic bonds and aromatic π-stacking (Zhang, 2003; Zhao and Zhang, 2007). Furthermore, dynamic biomolecular re-assembly has been demonstrated after disruptive sonication, which highlights the versatility of these molecules (Zhao and Zhang, 2007). A further advantage of these biomolecules is that assemblies can be manipulated and tuned to obtain desired functions and characteristics. Simple manipulations in, amongst others: the pH, ionic strength, solvents, temperature, assembly kinetics, light and co-assembling molecules can assist in achieving the desired characteristics (Cui *et al.,* 2010; Lakshmanan *et al.,* 2012). Last, but certainly not least, the usage of amino acids as the building blocks in fabrication ensures biocompatibility, bioactivity, stability and can facilitate biodegradation with the fabrication of enzymatic cleavage sites (Chau *et al.,* 2008; Cui *et al.,* 2010; Loo and Hauser, 2015; Loo *et al.,* 2015).

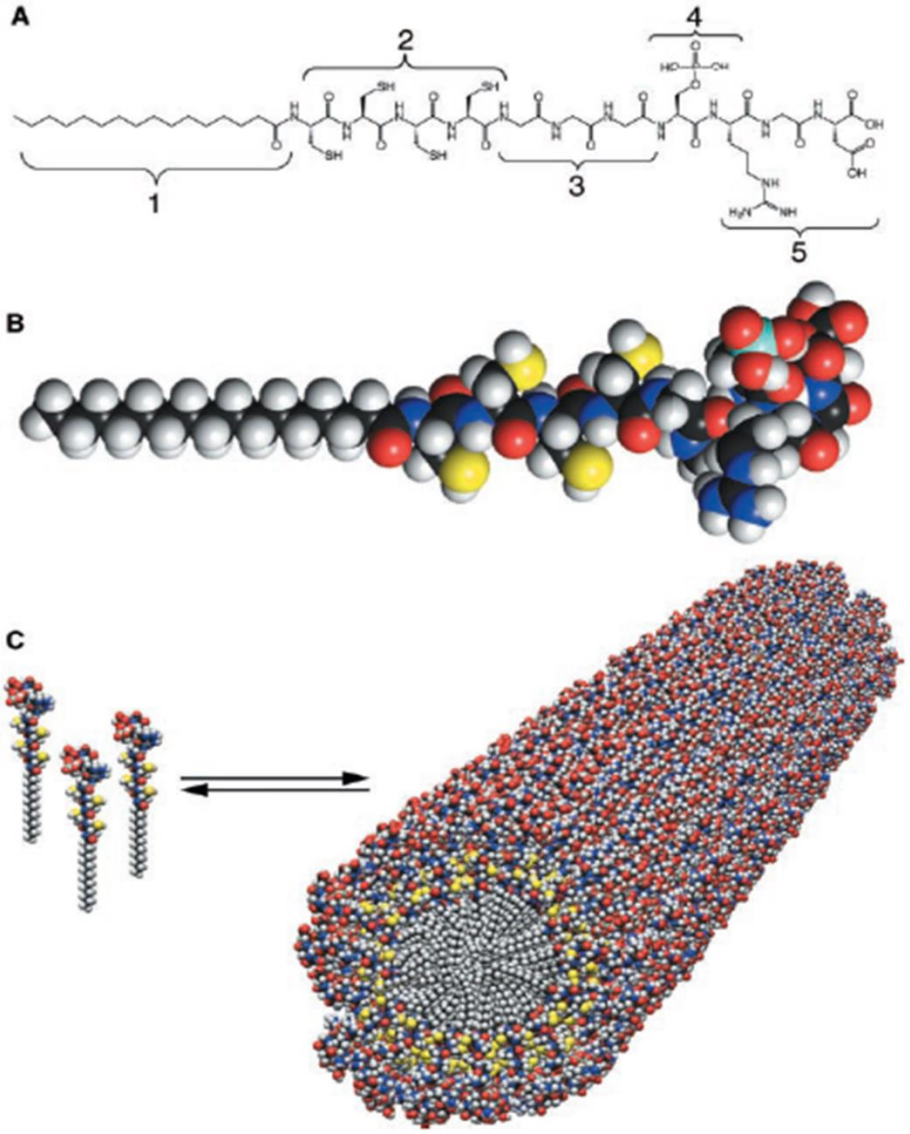


Figure 2.4: Schematic illustrating the first peptide-amphiphile (PA) fabricated in 2001. Section **A** represents the key features of the PA. Area (1) represents the hydrophobic alkyl tail whereas areas (2-5) represent the amino acid residues used during fabrication. Section **B** is a molecular representation of the PA. The hydrophobic region remains slender whereas the peptide region is bulkier. Section **C** represents the spontaneous assembly of the PA molecules into a cylindrical arrangement to create the micelle. Furthermore, the re-assembly process of the PA molecules is illustrated. This figure is reused from Science, **294**, Hartgerink *et al*. Self-Assembly and Mineralization of Peptide-Amphiphile Nanofibers, pp. 1684-1688, 2001, with permission from The American Association for the Advancement of Science.

As the importance of amino acids in controlling structure, function and molecular interactions continues to increase, it is no wonder that well researched SAPs have been commercialised. The two most common SAPs include PuraMatrix (RADA16-1) and Matrigel®, which have both been used extensively in the successful culturing of several cell lines and types due to the ability of these SAPs to adequately mimic the native ECM (Corning Incorporated, undated;

Zhao and Zhang, 2007; Zhao *et al.,* 2005). Noteworthy is that Matrigel® is prepared around a neutral pH whereas PuraMatrix is prepared at an acidic pH and then slowly brought up to physiological pH, which is a limitation of this SAPs (Corning Incorporated, undated; Zhao *et al.,* 2005).

Extensive research into SAPs has seen these biomolecules become important biosensing molecules able to detect, amongst others, a variety of metals, viruses and pathogens (Lakshmanan *et al.,* 2012). Even more crucial, SAPs of different lengths and amino acid compositions, have been extensively shown to exceptionally mimic the native ECM by promoting cellular motility, growth, adhesion, spreading and differentiation (Beniash *et al.,* 2005; Jun *et al.,* 2005; Paramonov *et al.,* 2006; Sieminski *et al.,* 2007; Silva, 2004). Despite the vast benefits of SAPs, SAPs are only beginning to be considered and incorporated into versatile bioinks for 3D printing applications. A major advantage of utilising SAPs for bioprinting applications is the tuneable characteristics and gelation kinetics. Furthermore, despite improving the printing process from their synthetic nature, SAP-based bioinks allow for the expansion of tuneable characteristics to customise physical, chemical and biological properties of the 3D fabricated structures to design and create structurally and functionally more complex structures than materials presented thus far (Rutz *et al.,* 2015; Sieminski *et al.,* 2007). In addition, due to their amphiphilic nature, SAPs entrap a very high percentage of water which can prevent cellular dehydration during printing (Loo *et al.,* 2015). With this in mind, bioprinting SAPs can revolutionize regenerative medicine as SAPs facilitate in better replicating the native ECM environment and may in fact hold the key to developing the “ideal” bioink everyone is desperate to create.

2.6 **Processed ECM**

2.6.1 Gelatin

Gelatin is another nature derived biomaterial not naturally found in the ECM of animals. Gelatin is formed through the hydrolysis of collagen derived from specific body tissues of animals. Gelatin has been widely utilised in a number of 3D printing regenerative tissue applications due to its beneficial properties, for example biodegradation, biocompatibility and most importantly, support of cellular growth and attachment through RGD binding domains (Panwar and Tan, 2016). In addition, the RGD structural domains assist in making the gelatin backbone re-absorbable with non-toxic degradation products, making gelatin extremely attractive candidate in 3D printing and regenerative medicine (Contessi Negrini *et al.,* 2020). Furthermore, gelatin is soluble in water and exhibits thermo-responsive behaviours due to the non-specific nature of the bonding between the gelatin chains (Wang *et al.,* 2017) – a feature that can be easily manipulated for the desired application.

In a recent study, Sakai and co-workers identified that no reports were available on using a vis-initiated ruthenium (II) tris-bipyridyl dication (Ru (II) bpy_3^{2+}) and sodium ammonium persulfate crosslinking system to crosslink a gelatin and hyaluronic acid 3D bioprinted hydrogel. The suitability of the bioinks were then tested through the encapsulation of human adipose stem cells (hADSCs). The results indicated that the encapsulated hADSCs exhibited cellular elongation and proliferation whilst preservation of their differentiation potential was observed. In addition, cells maintained their morphology and remained viable. Despite attempting to observe the migration potential of the cells, meaningful data was not obtained. Furthermore, it was noted that there was an upregulation of pluripotency gene expression markers, which was found to be corroborated by another study performed using chitosan films (Cheng *et al*., 2012). Despite the promising results, further studies are required to assess the practical application of the bioprinted constructs in regenerative attempts. In terms of the biophysics of the bioink, hydrogelation time was decreased with increasing concentrations of Ru (II) bpy_3^{2+} and SPS. In addition, Young's modulus was affected by changes in SPS concentration but remained unaffected by changes in Ru (II) bpy_3^{2+} and lastly, a 50 % increase in Young's modulus was observed when the exposure to UV light is increased from 10 to 20 minutes (Sakai *et al.,* 2018). In addition, potential cellular defects caused by the crosslinking system was not assessed in this study and hence, the safety of this system needs to be established for tissue engineering applications.

In a 2018 study performed by AnilKumar and co-workers, the team identified that the use of furfuryl-gelatin (f-gelatin) as a bioink in regenerative medicine has not been explored. The team hypothesized that a bioink composed of f-gelatin would possess optimized bioprinting parameters as well as cytocompatibility and mechanical accuracy. To assess the suitability of the bioink, three cell lines namely, mouse mesenchymal stem cells, immortalised mouse myoblast cell line (C2C12) and mouse fibroblast cells (STO) were incorporated into different layers of the structure. The results indicated that the f-gelatin needed to be blended with a viscosity enhancer (in this case HA) for printability reasons. In terms of the bioink, the bioink was shown to be biocompatible and promoted cellular survival and viability. In addition, cellular migration and spreading, cellular differentiation, migration and expected morphology was evident within the fabricated structures. Furthermore, the bioink was believed to have provided cytoprotective properties to the cultured cells. In terms of the rheological properties of the bioink, the elastic modulus of the crosslinked bioinks had a G' of 1.3 ± 0.3 kPa whereas non-crosslinked variants had a G' of 1.4 ± 0.05 kPa. In addition, the complex viscosity of the bioinks was increased from 206.25 ± 11.79 to 319.7 ± 43.01 Pa s when crosslinked. In terms of the swelling behaviour, maximum swelling was detected after 24 hours with no significant changes noted over the following 5 days. In addition, it was noted that no significant degradation was

observed until day 21. Lastly, crosslinked bioinks had an average pore size of 142.20 ± 1.08 μm and an average porosity of 21 ± 0.45 %, visible from SEM images (AnilKumar *et al.,* 2018).

In a study performed by Bertlein and co-workers, thiol-ene click chemistry was reported as an alternative crosslinking mechanism through diol dimerization. In this approach, click chemistry was used to fabricate allylated gelatin bioinks and a comparison between radical based polymerisation and visible light polymerisation was made on both allylated and methacrylate based gelatin bioinks. To assess this crosslinking mechanism on cellular activity, human articular chondrocytes (HACs) were incorporated into the bioinks. The results showed that cellular viability was lower for both bioink types cured under photo-polymerisation in comparison to the visible light curing system, where an increase in metabolically active cells was noted. In addition, cellular viability and survival was maintained in allylated bioinks over three weeks in extrusion printed constructs. Furthermore, the allylated bioink was shown to be a versatile system, potentially providing a platform for differing regenerative medical approaches. For both crosslinkers (I2959 and Ru/SPS), the weakest hydrogels were observed with the lowest allyl:SH ratio. When the crosslinker concentration is increased, maximum compressive Young's moduli ratios are observed for a 1:3 ratio for I2959 (53.2 ± 5.8 kPa) and 1:6 ratio for Ru/SPS (103.6 ± 13 kPa). The visible-light system was shown to allow tuneable hydrogel stiffness (2-110 kPa) with variations in Ru/SPS concentration at a 1:6 allyl:SH ratio and fixed polymer weight percentage whereas in UV systems, increasing the polymer weight percentage was the only way to improve the hydrogel properties (Bertlein *et al.,* 2017).

From these studies, the importance of incorporating gelatin into regenerative attempts has seen to be beneficial in facilitating the microenvironment cells need to survive. Therefore, with the versatility of the biomaterial, further optimizations in this biomaterial are expected to occur in the not too distant future.

2.6.2 Decellularized ECM (dECM)

Bioinks derived from the ECM of native tissues offers a new avenue for regenerative medicine. dECM materials are extracted from native animal tissues where the cells are removed, the resulting intact ECM is then dried and crushed into a powder (Gopinathan and Noh, 2018; Panwar and Tan, 2016). In this way, the mechanical integrity and scaffolding architecture of the ECM remains (Jung *et al.,* 20165). The resulting bioink is a rich medium with native growth and differentiation factors, which supports the specific functioning of the chosen cell type. In terms of dECM printability, generally dECM bioinks have a low viscosity and are supplemented with additional polymeric hydrogels to enhance the printability of the solution (Panwar and Tan, 2016).

In a 2014 study, Pati and co-workers highlighted that many of the biomaterials utilised for bioprinting applications cannot fully represent the complexity of the native ECM and therefore, are unable to sustain intrinsic cell functions and morphologies. In response, they developed novel dECM based bioinks for different tissues including cardiac (hdECM), cartilage (cdECM) and adipose (adECM). The bioinks where then printed in the presence of human adipose-derived stem cells (hASCs) or human inferior turbine-derived mesenchymal stromal cells (hTMSCs). The results indicated that once the cells had been printed, the cells assumed the desired morphology as well as establishing cell-cell connections, which enhanced cellular viability, migration, growth and differentiation. In addition, cell specific gene expression and native ECM formation was observed, which indicated the biocompatibility of the dECM bioinks. In an interesting investigation, the biochemical composition of the native tissue was compared to that of the decellularized tissue (**Figure 2.5**). Heart tissue was observed to not experience any significant decrease in both collagen and GAG content after the decellularization process. As for adipose tissue, a slight increase in collagen and a moderate decrease in GAG content was observed. Lastly, cartilage tissue was the most effected tissue of all three as a significant decrease in both components was observed. This was attributed to the different decellularization procedures required for each tissue. In the case of cartilage, due to the denser native ECM, more trypsinization and enzymatic treatment is required to eliminate cellular debris (**Figure 2.5**). In terms of the rheology of the samples, all dECM pre-gels at 15 °C had storage and loss moduli exhibiting more liquid-like behaviour whereas at 37 °C a greater storage and loss moduli were observed. This indicated that the pre-gels behave more like crosslinked gels and retain their shape, a critical requirement for 3D printing. In terms of the pre-gel viscosities, adECM, cdECM and hdECM had viscosities of 6.13 Pa/s, 2.8 Pa/s and 23.6 Pa/s, respectively (Pati *et al.,* 2014). This study highlighted the importance of dECM bioinks in providing a “more native” ECM for tissues fabricated for regenerative medicine.

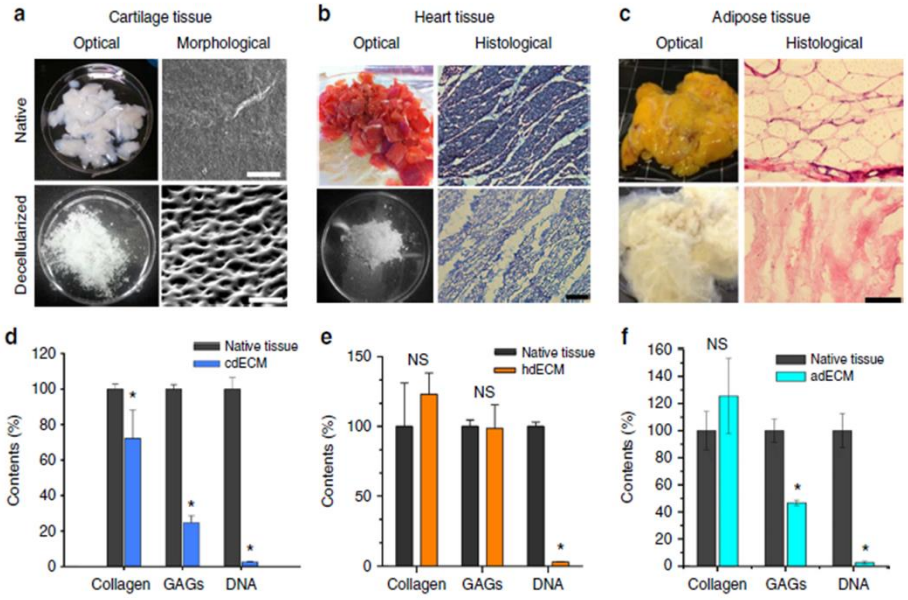


Figure 2.5: Biochemical analysis of the dECM materials prepared. Images (a), (b) and (c) represent the native and decellularized tissues of cartilage (scale: 50 mm), heart (scale: 100 mm) and adipose (scale: 100 mm), respectively. If cartilage is considered (d), a significant loss in the GAG and collagen content is observed. If the heart tissue is considered (e), no significant loss of GAG and collagen content is observed. If adipose tissue is considered (f), a slight decrease in GAG content and a moderate increase in collagen content is observed. Standard deviation is indicated with the use of error bars (*P<0.05; NS: no significance). This image is reproduced from Pati *et al.,* 2014 under the Creative Legal Code Attribution-NonCommercial-NoDerivs 3.0 Unported Licence.

In a more recent study, Jang and co-workers acknowledged that although stem cell therapies have shown promising results in ischemic heart disease treatments, such therapies have low efficacy after the incorporation of cells due to the altered state of the injured myocardium microenvironment. They aimed to 3D bioprint a stem cell dECM pre-vascularised cardiac patch to improve the efficacy of the therapy. The bioinks were printed in the presence of human cardiac progenitor cells (hCPCs) and/or human turbinate derived mesenchymal stromal cells (hTMSCs). Results indicated that cells contained within each bioink remained viable, hCPCs underwent structural maturation and vascular formation by hTMSCs was promoted. The vascular structures formed where shown to be similar in morphology to vascular structures formed by human dermal tissue derived microvascular endothelial cells. To assess the functional benefits of the dECM patch on tissue repair, the patch was transplanted into the myocardium of a murine MI model. Results revealed that in comparison to the control, a larger quantity of VEGF was secreted and less adverse tissue remodelling, and myocardial fibrosis occurred. In addition, the monitored cardiac repair genes were upregulated in the dECM patch group as compared to the MI group. Lastly, cardiac function was improved, and the patch acted as a delivery system for the stem cells (Jang *et al.,* 2017).

In a recent 2018 study performed by Toprakhisar and co-workers, it was identified that tuneable tendon dtECM hydrogels had not been developed for 3D bioprinting. This research team prepared a bovine Achilles tendon based dtECM hydrogel, which was tested using encapsulated NIH 3T3 cells. The results showed that in addition to the printability of the bioink, the bioink was shown to have no cytotoxic or immunogenic effects on the encapsulated fibroblasts. Therefore, the cells remained viable and exhibited homogenous distribution throughout the bioink. In addition, lineage specific cellular morphology and cellular extensions were observed at the third day of culture. The rheology of the bioink indicated, irrespective of the digestion time, increases in dtECM concentration increases G' before and after hydrogel network formation. Furthermore, increases in digestion time, under the same dtECM concentrations, decreases G' in pre-gel and hydrogel states and destabilises the hydrogel network. Lastly, increasing the dtECM concentration was shown to increase the rate of gel formation and increases both the maximum stress and compressive moduli (Toprakhisar *et al.,* 2018). These results highlight the potential of this bioink to act as an ECM mimic.

Despite the cellular benefits of dECM incorporation into bioinks, extraction and processing of the ECM before formulation of the bioink is a costly exercise (Gopinathan and Noh, 2018). Never the less, dECM bioinks are providing better microenvironments to support cellular processes and ECM cues.

Table 2.1: Summary of the natural bioinks and bioink blends presented in the review.

Bioink material of interest	3D Printing technique, printing parameters	Crosslinked, if so, crosslinking agent used	Architectural features of scaffold	Cell type and incorporation into bioink prior to printing	*In vivo* study performed and results	Tissue engineering application	Scaffold ECM mimicking ability	Ref
Glycosaminoglycan Bioinks								
HA with Nano-fibrillated cellulose	Extrusion	✓ 0.001 % (v/v) H_2O_2 in water	× Studies not performed	✓ Human iPSCs and/or irradiated chondrocytes (iChons)	×	Cartilage	• Low proliferation • Phenotypic changes away from pluripotency	Ngugen *et al.*, 2017
HA only HA with fibrinogen	Laser	× ×	× Studies not performed	✓ Human iPSCs	×	No application	• High cellular survival and viability • Cell attachment, aggregation, proliferation and directed differentiation • Pluripotency maintained with expression of pluripotency markers	Koch *et al.*, 2018
HA with gelatin	Extrusion	✓ Thiol reactive crosslinker	× Studies not performed	✓ Human foetal CMPCs	✓ (Mice) • No significant inflammatory response • Improved cardiac remodelling, decreases infarct fibrosis, thickens infarct wall and improves cardiac function	Cardiac	• Cellular attachment, proliferation, growth, survival, viability, engraftment, gene/protein expression and ECM deposition • Temporal phenotypic changes • hCMPCs retain cardiogenic properties	Gaetani *et al.*, 2015
HA only	In-house bioprinting system: Solid freeform fabrication technology	✓ 1-ethyl- 3-(3-dimethylaminopropyl)-carbodiimide hydrochloride (EDC), 1-hydroxybenzotriazole and cystamine	• Youngs Modulus: 21.4 ± 5.7 kPa • Pore diameter: 114.9 ± 95.3 μm • No significant degradation over 21 days	✓ Human chondrocytes and osteoblasts	×	Osteochondral tissue	• Chondrogenic proliferation, expression of chondrogenic marker genes, cellular migration, viability and survival	Park *et al.*, 2014
Cucurbit uril (CB), 1,6-diaminohexane (DAH), polycaprolactone (PCL), HA, atelocollagen	In-house bioprinting system: Dispensing into PCL framework	× (Non-covalent crosslinking)	× Studies not performed	✓ Human TMSCs	✓ Rabbit (Knee) • No significant inflammatory response • Osteochondral tissue regeneration at 8 weeks, neocartilage tissue present with no morphological difference to native cartilage • Concern: COL-X observed in superficial layer of neocartilage	Osteochondral tissue	• Cellular viability, division, differentiation and environmental specific gene expression • Characteristic cellular morphologies	Shim *et al.*, 2016
Heparin with HA	In-house bioprinting system: Extrusion layer deposition	✓ Photoinitiator: 2-hydroxy-40-(2-hydroxyethoxy) 22-methylpropiophenone and PEGDA	No quantitative data presented • Pore size decreases with increase in cross-linking molecule • Pore size decreases with increased cross-linking density • Elastic modulus increases with increasing cross-linking density	✓ Human AFS cells	✓ (Nude mice) • Wounds closed quicker with uniformity. • Elastin and GAGs secretion. • Lower collagen I production indication of reduced scarring	Wound healing	• Cellular viability, proliferation and migration • Long term growth factor and cytokine release	Skardal *et al.*, 2017
Thiolated HA with methacrylated collagen I	Extrusion	✓ Photoinitiator: 2-hydroxy-40-(2-hydroxyethoxy) 22-methylpropiophenone and UV light	• Prior to crosslinking: Formulations exhibit G'>G'' • After UV crosslinking: ***G'*** is significantly increased and G'' is not significantly changed. Loss tangents, below 0.1, indicate the material is more elastic	✓ Human hepatic stellate cell line, primary fetal activated hepatic stellate cells and primary human hepatocytes	×	Hepatic tissue	• Cellular viability and cell-cell interactions • Deposition of ECM relevant materials	Mazzocchi *et al.*, 2018
Methacrylated chondroitin sulphate and a PEG-based polymer	Additive	✓ Photoinitiator: 2-hydroxy-40-(2-hydroxyethoxy) 22-	• With increase in temperature G' increases. At 40 °C, G' was 380.8 ± 2.5 Pa. • Gelation temperature: 21.4 °C (thermo-responsive behaviour)	× Chondrogenic *ATDC5 cells*	×	Promising for cartilage	• Cellular survival, viability and proliferation	Abbadessa *et al.*, 2016

		methylpropiophenone and UV light	• Viscosity: Decreased from 514 Pa·s to 0.1 Pa·s (shear-thinning behaviour) • Yield stress: 19.2 ± 7.0 Pa with R^2 of 0.99 • Recovery tests: Initial G' value restored under low strain • The swelling ratio was found to be SR (V_{3h}/V_{0h}) = 1.34 ± 0.03				
ECM protein-based Bioinks							
Collagen with alginate	Additive	✓ Calcium chloride	• Increases in cell culture time, increases G' • Stable porous structure of 3D cell blocks due to crosslinker and aerosol system • Substantial increase in G' with aerosol system • Stress-strain moduli of bioinks was low, therefore bioinks enhanced using PCL. • Tensile modulus with PCL was significantly increased.	✓ Pre-osteoblast cells (MC3T3-E1) and Human ASCs	×	No application	• Cellular viability, survival, proliferation, migration, growth and differentiation • Tissue specific gene expression for both cell types	Lee *et al.*, 2015
Collagen with alginate	Extrusion	✓ Calcium chloride and fetal bovine serum	• Mass swelling ratio and water content decreased by 43.02 % and 34.78 %, respectively in cell-free constructs • Compressive stiffness increased by 1.87-fold • Tensile behaviour increased by 124.48 %	✓ Rat primary chondrocytes	×	Cartilage	• Cellular viability, survival, proliferation, attachment, GAG secretion • Cartilage specific gene expression	Yang *et al.*, 2018
Collagen only	Additive – several modifications made to printer	×	• Heated printing setup, increases shape fidelity • Equilibrium modulus increases with increasing collagen concentration	✓ Bovine meniscal fibrochondrocytes	×	No application	• Cellular viability, migration and attachment	Rhee *et al.*, 2016
Collagen and agarose	Drop-on-demand	×	• Average of 20 % degradation over 21 days • Scaffolds exhibited a swelling below 10 % • Bioink has an average mechanical strength of 1597.76 ± 191.23 Pa (12.0 %) and an average breaking strain percentage of 38.12 ± 2.07 (5.4 %)	× HUASMCs	×	No application	• Cellular viability, survival, spreading, attachment and encapsulation • Blend is not considered biomimetic approach	Köpf *et al.*, 2016
Elastin and SF	Extrusion	✓ Horseradish peroxidase and hydrogen peroxide solution	• After 28 days, the weight loss percentage was 30.3 ± 2.2 % after 28 days • Increased water uptake in first 24 hr (375 ± 22 %). Percentages remained the same after 28 days. • Increase of storage modulus (E') (0.56 ± 0.06 MPa to 0.86 ± 0.07 MPa) with increase in frequency • Increase in loss factor (tan δ) (0.33 ± 0.01 to 0.38 ± 0.01) with an increase in frequency • Micro-porosity (70–100 μm) induced by lyophilisation with 3D printing tuned macro-porosity (400–500 μm)	× Human ACSs	×	Intervertebral disc degeneration	• Cellular viability, attachment, migration and proliferation	Costa *et al.*, 2018
Fibrin-based hydrogel with PCL/PLCL	In-house IOP bioprinting system: Additive	✓ Thrombin	• The spiral design has a similar tensile stress, Young's modulus and strain at break values to native urethra tissue	✓ Rabbit bladder SMCs and UCs	×	Urethral stricture	• Cellular viability, attachment, proliferation, differentiation, expansion and distribution • Biomarker expression	Zhang *et al.*, 2017
Fibrin-factor XIII-HA	Extrusion	✓ NaCl, PVA and thrombin	× Studies not performed	✓ Rat Schwann cells	×	Nerve	• Cellular viability and proliferation • Tissue specific cell alignment	England *et al.*, 2017
SF with Gelatin	Additive	✓ Tyrosinase	× Studies not performed	✓ Human BMSCs	×	Cartilage	• Cellular viability, distribution, differentiation, attachment and proliferation • Tissue specific gene expression	Chawla *et al.*, 2017
Freeform SF (sacrificial alginate)	Inkjet	✓ H_2O_2 in 2 % $CaCl_2$•$2H_2O$ with HRP	• SF-alginate hydrogels with and without citrate treatment had a Young's modulus of 6.6 ± 0.4 kPa and 7.5 ± 1.8 kPa • SF-alginate however become more elastic, with good elastic recovery, upon the removal of alginate	✓ Mouse NIH 3T3 fibroblasts	×	No application	• Cellular viability, proliferation, growth and migration • Typical cell morphology,	Compaan *et al.*, 2017
SF with Gelatin	In-house bioprinting deposition system	✓ Tyrosinase	• Viscosity was shown to be 6-fold lower at 37 °C than 28 °C • Bioinks are in sol state at 37 °C, • Storage modulus is higher at 18 °C than 28 °C (shape retention) • No significant degradation until day 21	✓ Human TMSCs	×	No application	• Cellular viability and proliferation (up to day 14) • Tissue specific differentiation • Mineral/ECM deposition and GAG synthesis	Das *et al.*, 2015
SF with PEG	In-house bioprinting deposition system	× (Physical crosslinking)	• G'>G'' over all frequency ranges tested, with both moduli showing slight dependence on frequency. • Storage modulus: silk concentration dependant	✓ Human MSCs	✓ (Mice)	No application	• Cellular proliferation and growth at PEG concentrations < 1 %.	Zheng *et al.*, 2018

			• Bioinks display high viscosity at low shear stress		• Constructs with and without cells maintain shape after 6-week subcutaneous implantation. • Noteworthy, cell number in cell-laden constructs did not significantly change throughout the 6 weeks.		• Proliferation (silk concentration dependent, cell attachment and spreading	
ECM Mimic Bioinks								
Chitosan (Low MW) with PEGDA (1:7.5)	Stereolithographic	✓ Irgacure 819	• Low MW chitosan remains in shape, high MW chitosan deforms • Pores ranging from 25 to 100 µm with an average pore size of 67.3 ± 15.6 µm (n = 15) • Swelling ratio decreases with increasing photoinitiator concentrations • High MW chitosan gels exhibit higher swelling but lower mechanical strength • Low MW chitosan exhibits better printability • Increases in PEGDA, elastic modulus increases ~ 7-fold for both weights of chitosan • Recovery to original length after 50 % strain deformation	× Human MSCs	×	Shows mechanical strength for cartilage	• Cellular viability, survival, proliferation, spreading and penetration.	Ng *et al.*, 2016 Morris *et al.*, 2017
Processed ECM bioinks								
Gelatin with HA	Extrusion	✓ Vis-initiated ruthenium (II) tris-bipyridyl di-cation (Ru (II) bpy_3^{2+}) and sodium ammonium persulfate	• Increasing concentrations of Ru (II)$bpy^{2+}{}_3$ and SPS decreases hydrogelation time • Young's modulus (after UV exposure) is not affected by changes in Ru (II)$bpy^{2+}{}_3$ concentration, however is affected by changes in SPS concentration • UV exposure of from 10 to 20 min increases the Young's modulus by 50 %	✓ Human ADSCs	×	No application	• Cellular viability, proliferation and elongation • Gene specific expression • Maintenance of pluripotency	Sakai *et al.*, 2018
F-Gelatin with HA	Extrusion	✓ Visible light crosslinking (RB or RF)	• HA added as a viscosity enhancer • Crosslinked bioinks have elastic modulus of 1.3 ± 0.3 kPa, non-crosslinked variants had an elastic modulus of 1.4 ± 0.05 kPa • Crosslinking increased the complex viscosity from 206.25 ± 11.79 to 319.7 ± 43.01 Pa s • Maximum swelling observed after 24 hours, swelling unaffected over 5 days • No significantly degradation until day 21 • Average pore size of 142.20 ± 1.08 µm and an average porosity of 21 ± 0.45 %	✓ Mouse MSCs, Mouse STO fibroblasts and Mouse C2C12 myoblasts (bilayer printing)	×	No application (Authors hope to use bioink for myocardial tissue engineering)	• Cellular viability, proliferation, encapsulation and migration • Maintenance of cellular morphology • Noteworthy: Area occupied by cells is low	AnilKumar *et al.*, 2019
Allylated gelatin	Lithography-Based DLP printing Extrusion	✓ <u>UV-initiated (320–390 nm)</u> 2-hydroxy-1-[4-(hydroxyethoxy)-phenyl]-2-methyl-1-propanone (I2959) <u>Visible-light-initiated (390–500 nm)</u> tris(2,2′-bipyridyl) dichloro-ruthenium (II) hexahydrate with sodium persulfate (Ru/SPS).	• Both crosslinkers - weakest hydrogels were seen with the lowest allyl: SH ratio. Increasing the crosslinker, maximum compressive Young's moduli ratios are observed –1:3 for I2959 (53.2 ± 5.8 kPa) and 1:6 for Ru/SPS (103.6 ± 13 kPa) • Visible-light system allows for tuneable hydrogel stiffness • In UV systems, increasing polymer weight percentage, improves hydrogel properties	✓ <u>Porcine articular chondrocytes</u> × <u>Human articular chondrocytes</u>	×	No application	<u>Human articular chondrocytes</u> • Cytocompatibility over a range of allyl:SH ratios (Visible-light). • Increase of DTT above a ratio of 1:12 allyl:SH, effects both metabolic activity and viability • Cellular viability and metabolic activity: Lower in UV crosslinked hydrogels in comparison to visible-light hydrogels. <u>Porcine articular chondrocytes</u> • Cells viable for 23 days	Bertlein *et al.*, 2017
hdECM (heart) cdECM (cartilage) adECM (adipose)	In-house multi-head tissue/organ building *system with a* plunger-based low-Dosage dispensing system*: Extrusion*	×	• Viscosities of the dECM pre-gels at a shear rate of 2 Pa/s and 15 °C were as follows: 6.13 Pa/s (adECM), 2.8 Pa/s (cdECM) and 23.6 Pa/s (hdECM) • For all dECM pre-gels at 15 °C, storage and loss moduli have liquid-like behaviour. At 37 °C a greater storage and loss moduli were observed • Complex moduli increase after 15 °C (gelation) and increase significantly after 37 °C (crosslinked gel)	✓ hASCs and hTMSCs (adECM and cdECM) Rat myoblast cells (hdECM)	×	No application	• Cellular viability, cell-cell interactions, proliferation and migration • Lineage specific differentiation, ECM deposition, cell specific morphology maintenance and expression of tissue specific genes	Pati *et al.*, 2014

			• Although viscosities of the pre-gels are similar, their storage moduli differ					
hdECM (heart)	Extrusion	✓ UV light crosslinking (vitamin B2)	× Studies not performed	✓ Human CPCs and Human MSCs	✓ (Murine) <u>Functional enhancement (no cells) – Rat MI model</u> • Less adverse heart tissue remodelling and fibrosis • Large secretion of VEGF. • Expansion of the epicardium with upregulation of EMT gene marker <u>Vascularisation – subcutaneous nude mouse</u> • Patches with randomly mixed and patterned CPCs and MSCs: Blood vessel development in patch <u>Cardiac Function</u> • Patterned CPCs and MSCs: Significant left ventricle dilation with an increase in contractile area. • Improved left ventricle functioning with a thicker wall and less fibrosis	Ischemic heart disease	• Cellular viability, functionality, survival and migration.	Jang *et al.*, 2017
dtECM (tendon)	In-house novel piston driven microcapillary aspiration–extrusion method	×	• An increase in dtECM concentrations, increases G' over larger frequency ranges • Increasing digestion time, under the same dtECM concentrations, decreases G' in pre-gel and hydrogel states - hydrogel network destabilised • Increasing dtECM concentration increases the rate of gel formation and Newtonian flow. • Increasing dtECM increases both the maximum stress and compressive moduli • Increasing the digestion times decreases hydrogel network mechanical strength	× NIH 3T3 murine embryonic fibroblast cells	×	No application	• Cellular viability, distribution and elongation.	Toprakhisar *et al.*, 2018

HA: Hyaluronic Acid; SF: Silk Fibroin, RB: Rose Bengal, RF: Riboflavin, EMT: epithelial-mesenchymal transition

2.7 Conclusions and Future Perspective

As our understanding of the 3D microenvironment of cells continues to expand, the emergence of ECM-based bioinks has shown to hold great potential for the development of 3D printed ECM-mimicking scaffolds in regenerative medicine. As we begin to include native ECM components into current regenerative attempts, a fitting quote by Van Day Truex states that: “In design, Mother Nature is our best teacher.” The quote highlights the need to reconsider the benefit that the native environment can play in guiding our design efforts in attempting to re-engineer tissues and organs. A large number of studies, highlighted in this paper, have successfully exploited the functions of native ECM components in 3D printed systems. Such studies have shown the ability of the ECM mimicking structures to potentially provide the cells with the biological cues found in the native tissue. Despite the vast benefits of ECM-based bioinks, the printability and mechanical strength of these individual ECM components continues to be problematic. In response, bioink blends, with both natural and synthetic polymers, have become popular in overcoming the limitations (viscosity, sheer thinning etc) of ECM-based bioinks.

Since there is no ”ideal” bioink currently, **Figure 2.6** highlights the features that the “ideal” bioink needs to satisfy in order to meet the expetations of all the various tissue eggineering applications. Considering the bioink, the material developed has to be biocompatible with a controlled degradation profile (with non-toxic degradation byproducts) that is able to compliment the formation of the native tissue. In addition, the material must promote the biological cues of the native tissue in terms of encouraging, amongst others: cellular attachment, proliferation and growth (Gopinathan and Noh, 2018; Gungor-Ozkerim *et al.,* 2018; Hospodiuk *et al.,* 2017). Furthermore, cell-cell interactions have to be maximised whilst minimising cell loss and avoiding tissue necrosis. Depending on the tissue construct being designed, vascularization of larger constructs needs to be taken into account when tissue constructs are larger in diameter (Hospodiuk *et al.,* 2017). Lastly, adequate porosity has to be incorporated into tissue constructs to ensure that suffcient oxygen and nutrients reach the cells while any waste is adequately removed Gopinathan and Noh, 2018; Hospodiuk *et al.,* 2017). In terms of the 3D printability, the material needs to have the appropriate viscosity to allow for 3D printing and has to exhibit a favourable gelation profile to ensure structural integrity and mechanical stability is maintained post printing (Gopinathan and Noh, 2018; Gungor-Ozkerim *et al.,* 2018; Hospodiuk *et al.,* 2017). In addition, the material must exhibit shear thinning behaviour as shear thinning has a direct impact on the strand formation during a print (Gopinathan and Noh, 2018; Hospodiuk *et al.,* 2017, Joas *et al.,* 2018; Parak *et al.,* 2018). Importantly, if complex anatomical structures are fabricated, the various printing parameters need to be optimized for each specific tissue strand (Gopinathan and Noh, 2018;

Hospodiuk *et al.,* 2017). In addition, the constructs have to be resilient to withstand the native forces exerted upon it by the native tissue (Hospodiuk *et al.,* 2017; Parak *et al.,* 2018). Another consideration is material selection, which should be conducted in such a way that post printing (4D printing) modifications are possible should the desired application require further modifications (Gopinathan and Noh, 2018; Hospodiuk *et al.,* 2017). Lastly, throughout this process, researchers need to make the process as cost effective and time efficient as possible to achieve desirable patient outcomes in the clinic. Designing the "ideal" bioink is a complex task as each individual tissue has its own fundamental requirements. Despite this, inclusion of ECM mimicking biomaterials may in fact provide the solutions to overcome the current shortfalls and self-assembling peptides may begin to pave the way in offering a much-needed solution to this issue. In addition, through this review, it is evident that some ECM molecules, particularly the GAGs, require further consideration in regenerative medicine as data is limited. Although most of the studies presented here are for proof-of-concept, the potential benefits of ECM-mimicking scaffolds are undeniable.

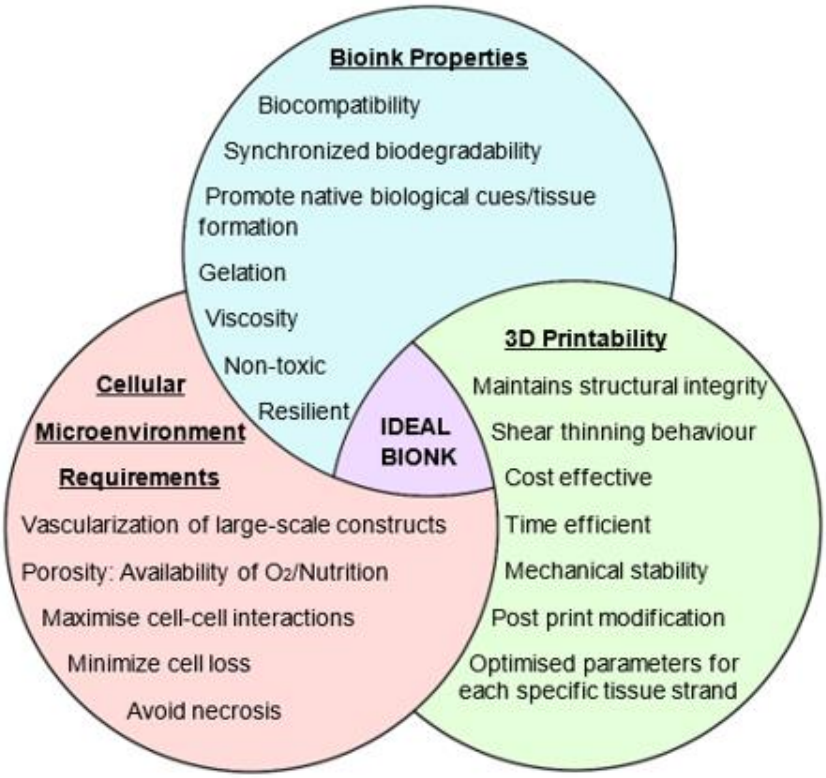


Figure 2.6: Schematic highlighting the features of an "ideal" bioink.

Due to the fact that the ECM mimics presented here have been shown to provide the necessary microenvironment to support cellular viability and promote the native ECM cues, inclusion of such biomaterials may provide the answer to successfully incorporating cells during the bioprinting process. Furthermore, emergence of 4D printing could assist in

overcoming experienced issues and achieving the desired characteristics for the tissue-specific ECM-mimicking scaffold. In addition, as mentioned in a recent report from our research group, post printing functionalisation has been shown to facilitate cellular attachment and biocompatibility as well as improving bioactivity and mechanical integrity of the 3D fabricated structure (Parak *et al.,* 2018). Lastly, due to the fact that 3D fabricated scaffolds still remain problematic in clinical trials, ECM-mimicking scaffolds could potentially offer solutions in translating pre-clinical success into successful, patient-specific organ transplants in the clinic.

2.8 References

Abbadessa, A., Blokzijl, M. M., Mouser, V. H. M., Marica, P., Malda, J., Hennink, W. E. and Vermonden, T. A. (2016). Thermo-Responsive and Photo-Polymerizable Chondroitin Sulfate-Based Hydrogel for 3D Printing Applications. Carbohydrate Polymers. **149**, 163–174.

Alberts, B., Johnson, A., Lewis, J., Raff, M., Roberts, K. and Walter, P. (2002). The Extracellular Matrix of Animals. In Molecular Biology of the Cell; New York: Garland Science. **91** (3), 401.

Anilkumar, S., Allen, S. C., Tasnim, N., Akter, T., Park, S., Kumar, A., Chattopadhyay, M., Ito, Y., Suggs, L. J. and Joddar, B. (2018). The Applicability of Furfuryl-Gelatin as a Novel Bioink for Tissue Engineering Applications. Journal of Biomedical Materials Research – Part B. **107** (2), 314-323.

Badylak, S., Freytes, D. and Gilbert, T (2009). Extracellular Matrix as a Biological Scaffold Material: Structure and Function. Acta Biomaterialia. **5** (1): 1–13.

Beniash, E., Hartgerink, J. D., Storrie, H., Stendahl, J. C. and Stupp, S. I. (2005). Self-Assembling Peptide Amphiphile Nanofiber Matrices for Cell Entrapment. Acta Biomaterialia. **1** (4), 387–397.

Bertlein, S., Brown, G., Lim, K. S., Jungst, T., Boeck, T., Blunk, T., Tessmar, J., Hooper, G. J., Woodfield, T. B. F. and Groll, J. (2017). Thiol–Ene Clickable Gelatin: A Platform Bioink for Multiple 3D Biofabrication Technologies. Advanced Materials. **29** (44), 1–6.

Chau, Y., Luo, Y., Cheung, A. C. Y., Nagai, Y., Zhang, S., Kobler, J. B., Zeitels, S. M. and Langer, R. (2008). Incorporation of a Matrix Metalloproteinase-Sensitive Substrate into Self-Assembling Peptides – A Model for Biofunctional Scaffolds. Biomaterials. **29** (11), 1713–1719.

Chawla, S., Kumar, A., Admane, P., Bandyopadhyay, A. and Ghosh, S. (2017). Elucidating Role of Silk-Gelatin Bioink to Recapitulate Articular Cartilage Differentiation in 3D Bioprinted Constructs. Bioprintin. **7**, 1–13.

Cheng, N. C., Wang, S. and Young, T. H. (2012). The Influence of Spheroid Formation of Human Adipose-Derived Stem Cells on Chitosan Films on Stemness and Differentiation Capabilities. Biomaterials. **33** (6), 1748–1758.

Chung, M. I. S., Miao, M., Stahl, R. J., Chan, E., Parkinson, J. and Keeley, F. W. (2006). Sequences and Domain Structures of Mammalian, Avian, Amphibian and Teleost Tropoelastins: Clues to the Evolutionary History of Elastins. Matrix Biology. **25** (8), 492–504.

Compaan, A. M., Christensen, K. and Huang, Y. (2017). Inkjet Bioprinting of 3D Silk Fibroin Cellular Constructs Using Sacrificial Alginate. ACS Biomaterials Science & Engineering. **3** (8), 1519–1526.

Contessi Negrini, N., Celikkin, N., Tarsini, P., Farè, S. and Święszkowski, W. (2020). Three-Dimensional Printing of Chemically Crosslinked Gelatin Hydrogels for Adipose Tissue Engineering. Biofabrication. **12** (2), 025001.

Corning Incorporated. Corning® Matrigel® Matrix Frequently Asked Questions. https://www.corning.com/media/worldwide/cls/documents/CLS-DL-CC-026 DL.pdf (accessed Nov 9, 2018).

Costa, J.B., Silva-Correia, J., Ribeiro, V. P., da Silva Morais, A., Oliveira, J. M. and Reis, R. L. (2018). Engineering Patient-Specific Bioprinted Constructs for Treatment of Degenerated Intervertebral Disc. Materierals Today Communication. **22** (5), 506-512.

Costantini, M., Idaszek, J., Szöke, K., Jaroszewicz, J., Dentini, M., Barbetta, A., Brinchmann, J. E. and Święszkowski, W. (2016). 3D Bioprinting of BM-MSCs-Loaded ECM Biomimetic Hydrogels for in Vitro Neocartilage Formation. Biofabrication. **8** (3), 035002.

Cui, H., Webber, M. J. and Stupp, S. I. (2010). Self-Assembly of Peptide Amphiphiles: From Molecules to Nanostructures to Biomaterials. Biopolymers. **94** (1), 1–18.

Daley, W. P., Peters, S. B. and Larsen, M. (2002). Extracellular Matrix Dynamics in Development and Regenerative Medicine. Journal of Cell Science. **121** (3), 255–264.

Das, S., Pati, F., Choi, Y., Rijal, G., Shim, J., Kim, S. W., Ray, A. R., Cho, D. W. and Ghosh, S. (2015). Bioprintable, Cell-Laden Silk Fibroin–Gelatin Hydrogel Supporting Multilineage Differentiation of Stem Cells for Fabrication of Three-Dimensional Tissue Constructs. Acta Biomaterialia. **11**, 233–246.

Derakhshanfar, S., Mbeleck, R., Xu, K., Zhang, X., Zhong, W. and Xing, M. (2018). 3D Bioprinting for Biomedical Devices and Tissue Engineering: A Review of Recent Trends and Advances. Bioactive Materials. **3** (2), 144–156.

Donderwinkel, I., van Hest, J. C. M. and Cameron, N. R. (2017). Bio-Inks for 3D Bioprinting: Recent Advances and Future Prospects. Polymer Chemistry. **8** (31), 4451–4471.

England, S., Rajaram, A., Schreyer, D. J. and Chen, X. (2017). Bioprinted Fibrin-Factor XIII-Hyaluronate Hydrogel Scaffolds with Encapsulated Schwann Cells and Their in Vitro Characterization for Use in Nerve Regeneration. Bioprinting. **5**, 1–9.

Floren, M., Bonani, W., Dharmarajan, A., Motta, A., Migliaresi, C. and Tan, W. (2016). Human Mesenchymal Stem Cells Cultured on Silk Hydrogels with Variable Stiffness and Growth Factor Differentiate into Mature Smooth Muscle Cell Phenotype. Acta Biomaterialia. **1**, 156–166.

Francis Suh, J. -K. and Matthew, H. W. (2000). Application of Chitosan-Based Polysaccharide Biomaterials in Cartilage Tissue Engineering: A Review. Biomaterials. **21** (24), 2589–2598.

Frantz, C., Stewart, K. M. and Weaver, V. M. (2010). The Extracellular Matrix at a Glance. Journal of Cell Science. **123** (24), 4195–4200.

Gaetani, R., Feyen, D. A. M., Verhage, V., Slaats, R., Messina, E., Christman, K. L., Giacomello, A., Doevendans, P. A. F. M. and Sluijter, J. P. G. (2015). Epicardial Application

of Cardiac Progenitor Cells in a 3D-Printed Gelatin/Hyaluronic Acid Patch Preserves Cardiac Function after Myocardial Infarction. Biomaterials. **61**, 339–348.

González-Díaz, E. and Varghese, S. (2016). Hydrogels as Extracellular Matrix Analogs. Gels. **2** (3), 20.

Gopinathan, J. and Noh, I. (2018). Recent Trends in Bioinks for 3D Printing. Biomaterials. Research. **22** (1), 11.

Gough, J. E., Saiani, A. and Miller, A. F. (2012). Peptide Hydrogels: Mimicking the Extracellular Matrix. Bioinspired, Biomimetic and Nanobiomaterials. **1** (1), 4–12.

Goy, R. C., de Britto, D. and Assis, O. B. G. (2009). A Review of the Antimicrobial Activity of Chitosan. Polímeros. **19** (3), 241–247.

Gungor-Ozkerim, P. S., Inci, I., Zhang, Y. S., Khademhosseini, A. and Dokmeci, M. R. (2018). Bioinks for 3D Bioprinting: An Overview. Biomaterial Science. **6** (5), 915–946.

Hartgerink, J. D., Beniash, E. and Stupp, S. I. (2002). Peptide-Amphiphile Nanofibers: A Versatile Scaffold for the Preparation of Self-Assembling Materials. Proceedings of the National Academy of Sciences of the United States of America. **99** (8), 5133–5138.

Hartgerink, J. D., Beniash, E. and Stupp, S. I. (2001). Self-Assembly and Mineralization of Peptide-Amphiphile Nanofibers. Science. **294** (5547), 1684–1688.

Hinderer, S., Layland, S. L. and Schenke-Layland, K. (2016). ECM and ECM-like Materials - Biomaterials for Applications in Regenerative Medicine and Cancer Therapy. Advanced Drug Delivery Reviews. **97**, 260–269.

Hospodiuk, M., Dey, M., Sosnoski, D. and Ozbolat, I. T. (2017). The Bioink: A Comprehensive Review on Bioprintable Materials. Biotechnology Advances. **35** (2), 217–239.

Hubmacher, D. and Apte, S. S. (2013). The Biology of the Extracellular Matrix. Current Opinion in Rheumatology. **25** (1), 65–70.

Jang, J., Park, H. J., Kim, S. W., Kim, H., Park, J. Y., Na, S. J., Kim, H. J., Park, M. N., Choi, S. H., Park, S. H., Kim, S. W., Kwon, S. M., Kim, P. J. and Cho, D. W. (2017). 3D Printed Complex Tissue Construct Using Stem Cell-Laden Decellularized Extracellular Matrix Bioinks for Cardiac Repair. Biomaterials. **112** (6), 264–274.

Jarvelainen, H., Sainio, A., Koulu, M., Wight, T. N. and Penttinen, R. (2009). Extracellular Matrix Molecules: Potential Targets in Pharmacotherapy. Pharmacological Reviews. **61**, 198–223.

Jhala, D. and Vasita, R. (2015). A Review on Extracellular Matrix Mimicking Strategies for an Artificial Stem Cell Niche. Polymer Reviews. **55** (4), 561–595.

Joas, S., Tovar, G., Celik, O., Bonten, C. and Southan, A. (2018). Extrusion-Based 3D Printing of Poly(Ethylene Glycol) Diacrylate Hydrogels Containing Positively and Negatively Charged Groups. Gels. **4** (3), 69.

Jun, H. W., Yuwono, V., Paramonov, S. E. and Hartgerink, J. D. (2005). Enzyme-Mediated Degradation of Peptide-Amphiphile Nanofiber Networks. Advanced Materials. **17** (21), 2612–2617.

Jung, J. P., Bhuiyan, D. B. and Ogle, B. M. (2016). Solid Organ Fabrication: Comparison of Decellularization to 3D Bioprinting. Biomaterial Research. **20** (1), 27.

Kiani, C., Chen, L., Wu, Y. J., Yee, A. J. and Yang, B. B. (2002). Structure and Function of Aggrecan. Cell Research. **12** (1), 19–32.

Koch, L., Deiwick, A., Franke, A., Schwanke, K., Haverich, A., Zweigerdt, R. and Chichkov, B. (2018). Laser Bioprinting of Human Induced Pluripotent Stem Cells—the Effect of Printing and Biomaterials on Cell Survival, Pluripotency, and Differentiation. Biofabrication. **10** (3), 035005.

Kokkoli, E., Mardilovich, A., Wedekind, A., Rexeisen, E. L., Garg, A. and Craig, J. A. (2006). Self-Assembly and Applications of Biomimetic and Bioactive Peptide-Amphiphiles. Soft Matter. **2** (12), 1015.

Köpf, M., Campos, D. F. D., Blaeser, A., Sen, K. S. and Fischer, H. (2016). A Tailored Three-Dimensionally Printable Agarose–Collagen Blend Allows Encapsulation, Spreading, and Attachment of Human Umbilical Artery Smooth Muscle Cells. Biofabrication. **8** (2), 025011.

Kumar, P., Choonara, Y. E., Khan, R. A. and Pillay, V. (2017). The Chemo-Biological Outreach of Nano-Biomaterials: Implications for Tissue Engineering and Regenerative Medicine. Current Pharmaceutical Design. **23** (24), 3538–3549.

Lakshmanan, A., Zhang, S. and Hauser, C. A. E. (2012). Short Self-Assembling Peptides as Building Blocks for Modern Nanodevices. Trends in Biotechnology. **30** (3), 155–165.

Lee, H. J., Kim, Y. B., Ahn, S. H., Lee, J. S., Jang, C. H., Yoon, H., Chun, W. and Kim, G. H. (2015). A New Approach for Fabricating Collagen/ECM-Based Bioinks Using Preosteoblasts and Human Adipose Stem Cells. Advanced Healthcare Materials. **4** (9), 1359–1368.

Litvinov, R. I. and Weisel, J. W. (2017). Fibrin Mechanical Properties and Their Structural Origins. Matrix Biology. **60–61** (1), 110–123.

Loo, Y. and Hauser, C. A. E. (2015). Bioprinting Synthetic Self-Assembling Peptide Hydrogels for Biomedical Applications. Biomedical Materials. **11** (1), 014103.

Loo, Y., Lakshmanan, A., Ni, M., Toh, L. L., Wang, S. and Hauser, C. A. E. (2015). Peptide Bioink: Self-Assembling Nanofibrous Scaffolds for Three-Dimensional Organotypic Cultures. Nano Letters. **15** (10), 6919–6925.

Malda, J., Visser, J., Melchels, F. P., Jüngst, T., Hennink, W. E., Dhert, W. J. A., Groll, J. and Hutmacher, D. W. (2013). 25th Anniversary Article: Engineering Hydrogels for Biofabrication. Advanced Materials. **25** (36), 5011–5028.

Mandrycky, C., Wang, Z., Kim, K. and Kim, D. H. (2016). 3D Bioprinting for Engineering Complex Tissues. Biotechnology Advances. **34** (4), 422–434.

Mazzocchi, A., Devarasetty, M., Huntwork, R. C., Soker, S. and Skardal, A. (2018). Optimization of Collagen Type I-Hyaluronan Hybrid Bioink for 3D Bioprinted Liver Microenvironments. Biofabrication. **11** (1), 015003.

Mok, S. W., Nizak, R., Fu, S. C., Ho, K. W. K., Qin, L., Saris, D. B. F., Chan, K. M. and Malda, J. (2016). From the Printer: Potential of Three-Dimensional Printing for Orthopaedic Applications. Journal of Orthopaedic Translation. **6**, 42–49.

Morris, V. B., Nimbalkar, S., Younesi, M., McClellan, P. and Akkus, O. (2017). Mechanical

Properties, Cytocompatibility and Manufacturability of Chitosan:PEGDA Hybrid-Gel Scaffolds by Stereolithography. Annals of Biomedical Engineering. **45** (1), 286–296.

Murphy, S. V. and Atala, A. (2014). 3D Bioprinting of Tissues and Organs. Nature Biotechnology. **32** (8), 773–785.

Ng, W. L., Yeong, W. Y. and Naing, M. W. (2016). Polyelectrolyte Gelatin-Chitosan Hydrogel Optimized for 3D Bioprinting in Skin Tissue Engineering. Polyelectrolyte Gelatin-Chitosan Hydrogel Optimized for 3D Bioprinting in Skin Tissue Engineering. International Journal of Bioprinting. **2** (1), 53–62.

Nguyen, D., Hägg, D. A., Forsman, A., Ekholm, J., Nimkingratana, P., Brantsing, C., Kalogeropoulos, T., Zaunz, S., Concaro, S., Brittberg, M., Lindahl, A., Gatenholm, P., Enejder, A. and Simonsson, S. (2017). Cartilage Tissue Engineering by the 3D Bioprinting of IPS Cells in a Nanocellulose/Alginate Bioink. Scientific Reports. **7** (1), 658.

Niece, K. L., Hartgerink, J. D., Donners, J. J. J. M. and Stupp, S. I. (2003). Self-Assembly Combining Two Bioactive Peptide-Amphiphile Molecules into Nanofibers by Electrostatic Attraction. Journal of the American Chemical Society. **125** (24), 7146–7147.

Nocera, A. D., Comín, R., Salvatierra, N. A. and Cid, M. P. (2018). Development of 3D Printed Fibrillar Collagen Scaffold for Tissue Engineering. Biomedical Microdevices. **20** (2), 26.

Ouyang, L., Highley, C. B., Rodell, C. B., Sun, W. and Burdick, J. A. (2016). 3D Printing of Shear-Thinning Hyaluronic Acid Hydrogels with Secondary Cross-Linking. ACS Biomaterials Science & Engineering. **2** (10), 1743–1751.

Panwar, A. and Tan, L. P. (2016). Current Status of Bioinks for Micro-Extrusion-Based. Molecules. **21** (6): E685.

Parak, A., Pradeep, P., du Toit, L. C., Kumar, P., Choonara, Y. E. and Pillay, V. (2018). Functionalizing Bioinks for 3D Bioprinting Applications. Drug Discovery Today. **18**, 1–8.

Paramonov, S. E., Jun, H. W. and Hartgerink, J. D. (2006). Self-Assembly of Peptide−Amphiphile Nanofibers: The Roles of Hydrogen Bonding and Amphiphilic Packing. Journal of the American Chemical Society. **128** (22), 7291–7298.

Park, J. Y., Choi, J. C., Shim, J. H., Lee, J. S., Park, H., Kim, S. W., Doh, J. and Cho, D. W. (2014). A Comparative Study on Collagen Type i and Hyaluronic Acid Dependent Cell Behavior for Osteochondral Tissue Bioprinting. Biofabrication. **6** (3), 035004.

Pati, F., Jang, J., Ha, D. H., Kim S. W., Rhie, J. W., Shim, J. H., Kim, D. H. and Cho, D. W. (2014). Printing Three-Dimensional Tissue Analogues with Decellularized Extracellular Matrix Bioink. Nature Communications. **5** (1): 3935.

Prydz, K. (2015). Determinants of Glycosaminoglycan (GAG) Structure. Biomolecules. **5** (3): 2003–2022.

Rhee, S., Puetzer, J. L., Mason, B. N., Reinhart-King, C. A. and Bonassar, L. J. (2016). 3D Bioprinting of Spatially Heterogeneous Collagen Constructs for Cartilage Tissue Engineering. ACS Biomaterials Science & Engineering. **2** (10), 1800–1805.

Rodriguez, E., Roland, S. K., Plaas, A. and Roughley, P. J. (2006). The Glycosaminoglycan Attachment Regions of Human Aggrecan. Journal of Biological Chemistry. **281** (27): 18444–18450.

Rutz, A. L., Hyland, K. E., Jakus, A. E., Burghardt, W. R. and Shah, R. N. (2015). A Multimaterial Bioink Method for 3D Printing Tunable, Cell-Compatible Hydrogels. Advanced Materials. **27** (9), 1607–1614.

Sakai, S., Ohi, H., Hotta, T., Kamei, H. and Taya, M. (2018). Differentiation Potential of Human Adipose Stem Cells Bioprinted with Hyaluronic Acid/Gelatin-Based Bioink through Microextrusion and Visible Light-Initiated Crosslinking. Biopolymers. **109** (2), e23080.

Saxena, R. and Nanjan, M. J. (2015). Elastin-like Polypeptides and Their Applications in Anticancer Drug Delivery Systems: A Review. Drug Delivery. **22** (2),156–167.

Schaefer, L. and Schaefer, R. M. (2010). Proteoglycans: From Structural Compounds to Signaling Molecules. Cell and Tissue Research. **339** (1), 237–246.

Wong, Y. S., Tay, C. Y., Wen, F. S., Venkatraman, S. and Tan, L. P. (2012). Engineered Polymeric Biomaterials for Tissue Engineering. Current Tissue Engineering. **1** (1), 41–53.

Shim, J. H., Jang, K. M., Hahn, S. K., Park, J. Y., Jung, H., Oh, K., Park, K. M., Yeom, J., Park, S. H., Kim, S. W., Wang, J. H., Kim, K. and Cho, D. W. (2016). Three-Dimensional Bioprinting of Multilayered Constructs Containing Human Mesenchymal Stromal Cells for Osteochondral Tissue Regeneration in the Rabbit Knee Joint. Biofabrication. **8** (1), 014102.

Sieminski, A. L., Was, A. S., Kim, G., Gong, H. and Kamm, R. D. (2007). The Stiffness of Three-Dimensional Ionic Self-Assembling Peptide Gels Affects the Extent of Capillary-like Network Formation. Cell Biochemistry and Biophysics. **49** (2), 73–83.

Silva, G. A. (2004). Selective Differentiation of Neural Progenitor Cells by High-Epitope Density Nanofibers. Science. **303** (5662), 1352–1355.

Skardal, A., Murphy, S. V., Crowell, K., Mack, D., Atala, A. and Soker, S. (2017). A Tunable Hydrogel System for Long-Term Release of Cell-Secreted Cytokines and Bioprinted in Situ Wound Cell Delivery. Journal of Biomedical Materials Research Part B. **105** (7), 1986–2000.

Smelyanskiy, M., Holmes, D., Chhugani, J., Larson, A., Carmean, D. M., Hanson, D., Dubey, P., Augustine, K., Kim, D., Kyker, A., Lee, V. W., Nguyen, A. D., Seiler, L. and Robb, R. (2009). Mapping High-Fidelity Volume Rendering for Medical Imaging to CPU, GPU and Many-Core Architectures. IEEE Transactions on Visualization and Computer Graphics. **15** (6), 1563–1570.

Subramanian, A., Krishnan, U. and Sethuraman, S. (2009). Development of Biomaterial Scaffold for Nerve Tissue Engineering: Biomaterial Mediated Neural Regeneration. Journal of Biomedical Science. **16** (1), 108.

Theocharis, A. D., Skandalis, S. S., Gialeli, C. and Karamanos, N. K. (2016). Extracellular Matrix Structure. Advanced Drug Delivery Reviews. **97**, 4–27.

Toprakhisar, B., Nadernezhad ,A., Bakirci, E., Khani, N., Skvortsov, G. A. and Koc, B. (2018). Development of Bioink from Decellularized Tendon Extracellular Matrix for 3D Bioprinting. Macromolecular Bioscience. **18** (10), 1800024.

Urban, J. P. G., Roberts, S. and Ralphs, J. R. (2000). The Nucleus of the Intervertebral Disc from Development to Degeneration. American Zoologist. **40** (1), 53–61.

Velasco, M. A., Narváez-Tovar, C. A. and Garzón-Alvarado, D. A. (2015). Design, Materials, and Mechanobiology of Biodegradable Scaffolds for Bone Tissue Engineering. BioMed

Research International. **2015**, 1–21.

Vigier, S. and Fülöp, T. (2016). Exploring the Extracellular Matrix to Create Biomaterials. In Composition and Function of the Extracellular Matrix in the Human Body; InTech, 2016: p 13.

Wang, Q., Han, G., Yan, S. and Zhang, Q. (2019). 3D Printing of Silk Fibroin for Biomedical Applications. Materials. **12** (3): 504.

Wang, X., Ao, Q., Tian, X., Fan, J., Tong, H., Hou, W. and Bai, S. (2017). Gelatin-Based Hydrogels for Organ 3D Bioprinting. Polymers. **9** (12), 401.

Yamada, S., Sugahara, K. and Özbek, S. (2011). Evolution of Glycosaminoglycans. Communicative & Integrative Biology. **4** (2), 150–158.

Yang, X., Lu, Z., Wu, H., Li, W., Zheng, L. and Zhao, J. (2018). Collagen-Alginate as Bioink for Three-Dimensional (3D) Cell Printing Based Cartilage Tissue Engineering. Materials Science and Engineering C. **83**, 195–201.

Yoo, H. S., Lee, E. A., Yoon, J. J. and Park, T. G. (2005). Hyaluronic Acid Modified Biodegradable Scaffolds for Cartilage Tissue Engineering. Biomaterials. **26** (14), 1925–1933.

Yue, B. (2014). Biology of the Extracellular Matrix. Journal of Glaucoma. **23**: S20–S23.

Zhang, K., Fu, Q., Yoo, J., Chen, X., Chandra, P., Mo, X., Song, L., Atala, A. and Zhao, W. (2017). 3D Bioprinting of Urethra with PCL/PLCL Blend and Dual Autologous Cells in Fibrin Hydrogel: An in Vitro Evaluation of Biomimetic Mechanical Property and Cell Growth Environment. Acta Biomaterialia. **50**, 154–164.

Zhang, S. (2003). Fabrication of Novel Biomaterials through Molecular Self-Assembly. Nature Biotechnology. **21** (10), 1171–1178.

Zhao, X., Zhang, S. and Spirio, L. (2005). PuraMatrix. In Scaffolding In Tissue Engineering; Ma, P. X., Elisseeff, J., Eds.; CRC Press: Boca Raton, FL, USA, 217–238.

Zhao, X. and Zhang, S. (2007). Designer Self-Assembling Peptide Materials. Macromolecular Bioscience. **7** (1), 13–22.

Zheng, Z., Wu, J., Liu, M., Wang, H., Li, C., Rodriguez, M. J., Li, G., Wang, X. and Kaplan, D. L. (2018). 3D Bioprinting of Self-Standing Silk-Based Bioink. Advanced Healthcare Materials. **7** (6), 1701026.

CHAPTER 3
PROOF OF CONCEPT: PRELIMINARY DESIGN OF 3D PRINTED ARTIFICIAL EXTRACELLULAR MATRIX SCAFFOLDS

3.1 Introduction

As discussed in Chapter 2, biomaterial selection for the design of the 3D printed artificial tissues through ECM mimicking is vitally important for all tissue engineering applications. Careful biomaterial selection on a per tissue basis, therefore, allows for the adequate mimicking of the native tissue properties to provide regeneration and host tissue integration at the injury site (Da Silva *et al.*, 2020). In the case of the brain, the brain is described as being an extremely complex, anisotropic soft tissue, ranging in the order of one kilopascal (Axpe *et al*., 2020; Budday *et al.,* 2020; Leipzig and Schoichet, 2009). In addition, the brain is further reported to be a fluid-saturated, porous tissue (Wagner and Ehlers, 2008). Since the World Health Organization (WHO) predicts that TBI will be the third leading cause of death and disability worldwide by 2020 (World Health Organisation, 2020), biomaterial selection for adequate native brain mimicry and the minimisation of secondary neural damage after TBI (Kumar *et al.,* 2017; Subramanian *et al.,* 2009), is vital.

To satisfy these criterias, aECM-based polymer hydrogel systems are gaining in popularity. As discussed in Chapter 2, native ECM materials and polymers for 3D printing tissue engineering applications are largely limited by their low mechanical strength, whereas synthetic materials and polymers are limited by poor biocompatibility and cell binding (Da Silva *et al.*, 2020). To overcome this, polymeric hydrogel blends of natural-natural, synthetic-natural or synthetic-synthetic polymers have been explored (Li *et al.,* 2020). Regardless of the materials selected, the biomaterials have to satisfy the criteria for TBI treatments as discussed in **Figure 1.1**. The rational design of polymer hydrogel scaffolds for soft tissue engineering is a promising strategy since hydrogels are crosslinked 3D networks with the ability to absorb large volumes of water/bodily fluid without dissolving as well as exhibiting tuneable mechanical properties (Kyung *et al*., 2002). Furthermore, in their swollen state, hydrogels are considered to be soft polymer systems (Kyung *et al*., 2002), making them ideal candidates for the engineering of softer tissues such as the brain. Lastly, once swelling equilibrium has been reached, the cohesive forces within the hydrogel systems resist further expansion (El-Sherbiny and Yacoub, 2013). This property in TBI applications is extremely important so that no further damage to the lesion site or surrounding tissue will occur.

Therefore, considering the above, the present study set out to design an aECM hydrogel biomaterial to satisfy the criteria explored in **Figure 1.1**. In this way, the inherent ECM mimicking properties of the biomaterials selected coupled with the discussed properties of the hydrogel is proposed to offer a suitable treatment for TBI by providing a more similar "*in vivo*-like" microenvironment to the lesion site and the surrounding healthy brain tissue (**Figure 3.1**). In addition to biomaterial selection, the physicochemical properties when using a respective 3D printing technique for the aECM scaffold fabrication provides another level of material selection complexity as not all 3D printing techniques are capable of printing hydrogels due to their harsh printing conditions and viscosity requirements (Li *et al.,* 2020). The 3D printing techniques capable of successfully 3D printing hydrogels include: Laser-based, extrusion-based and inkjet printing. Of these techniques, 3D plotting extrusion-based is the most suitable for hydrogel scaffold fabrication due to the variety of hydrogel biomaterials that are able to be printed (Da Silva *et al*., 2019). The biomaterials selected for extrusion-based printing are required to be viscous as well as undergo shear thinning and yield stress (Li *et al.,* 2020). Furthermore, the biomaterial must exhibit quick gelation or solidification of the layers post printing to ensure build-up structural fidelity of the scaffold (Kirchmajer, *et al*., 2015). Since extrusion-based printing is a pneumatic driven technique (Li *et al.,* 2020; Ozbolat and Hospodiuk, 2016), biomaterials are required to flow under modest pressure (Guvendiren *et al*., 2016). **Figure 3.1** summarises the most important 3D printing biomaterial requirements as well as the biological requirements for the fabrication of an aECM biomaterial scaffold using extrusion-based printing for TBI applications.

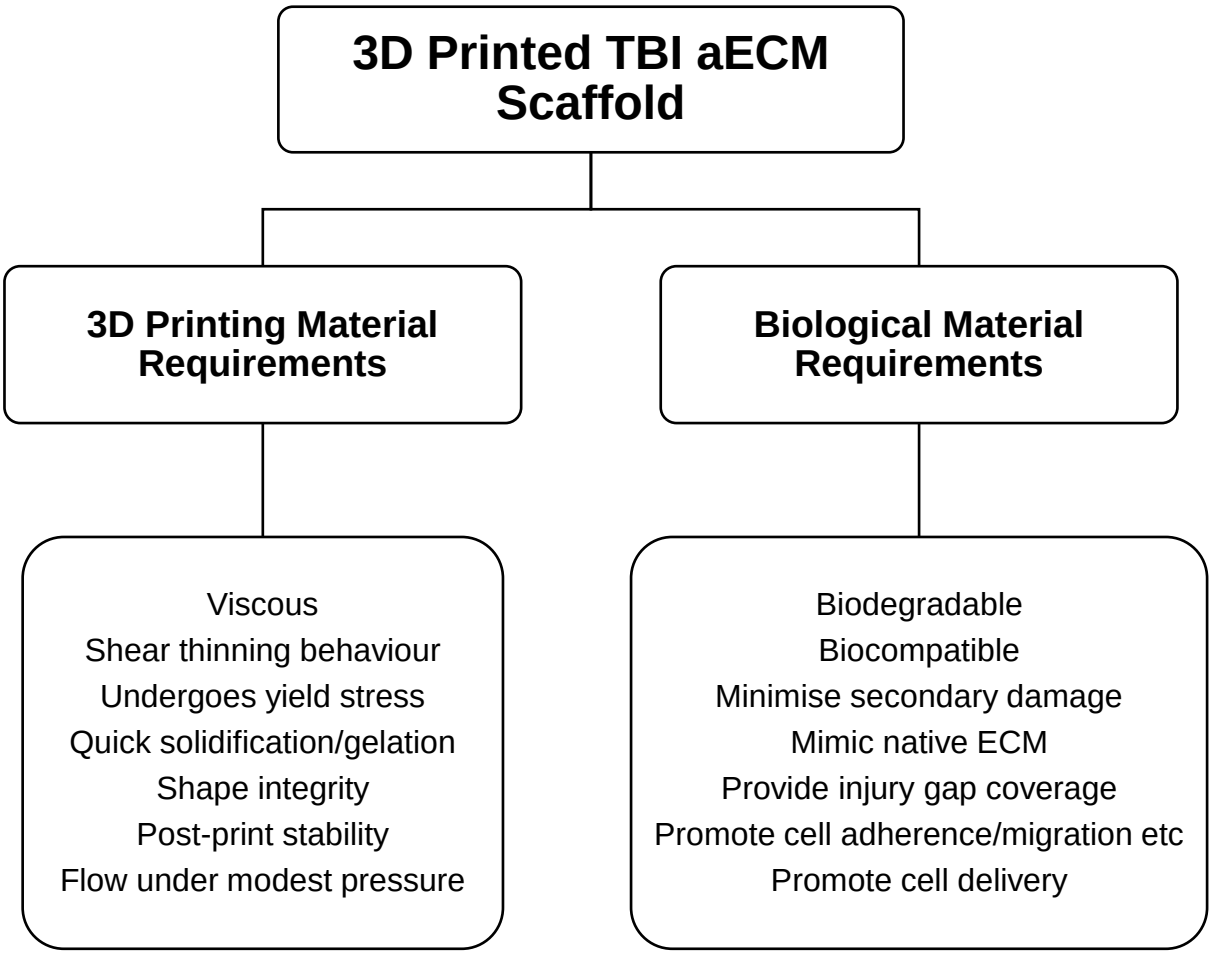


Figure 3.1: Summary of the biomaterial requirements for successful 3D printing and TBI aECM fabrication.

This work involved the preparation of aECM hydrogels through the blending of native brain peptides namely collagen and elastin with either the naturally derived polymer, Gelatin Methacryloyl (GelMA) or the synthetic polymer, Poly(ethylene glycol) diacrylate (PEGDA) in different concentration ratios. The success of the aECM hydrogel was determined by its ability to be 3D printed on a standard Envisiontec 3D Bioplotter (Envisiontec GmbH, Gladbeck, Germany).

3.2 **Potential Polymers for 3D Printing of an aECM**

3.2.1 Poly(ethylene glycol) diacrylate (PEGDA)

PEGDA is a common polymer utilised in the development of biomaterials for biological 3D printing. Despite being a synthetic polymer, PEGDA has been utilised in the fabrication of native ECM mimics (Zhang *et al.,* 2012). Despite PEGDA being a biocompatible, cheap, and photocurable polymer there are no native cell attachment sites on the PEGDA backbone (Shi

et al., 2015). Functionalization of PEGDA with cell binding motifs, like arginine-glycine-aspartic acid (RGD) sequences, can be performed to improve the cell binding capabilities of the polymer (Zhang *et al.,* 2012). PEGDA MW 575 was selected as studies have shown that it displays good thermo-responsive properties whilst PEGDA MW 700 exhibits better water solubility due to the presence of a higher hydrophilicity caused by longer PEG chains (Zhao *et al*., 2015). In this work, due to the inherent brittleness of PEGDA hydrogels (Frost *et al*., 2019; Priola *et al*., 1992), high MW PEGDA as well as high PEGDA concentrations were avoided.

3.2.2 Gelatin Methacryloyl (GelMA)

In recent years, GelMA has become a popular candidate in the fabrication of hydrogels for biological 3D printing. GelMA has a number of attractive features including but not limited to: biocompatibility and biodegradability as well as the promotion of cell adhesion and proliferation. Furthermore, GelMA is cost effective and has an uncomplicated synthesis making it a widely-used polymer in biomaterial development. Furthermore, photo-polymerisation of the methacrylate functional groups assists in the mechanical tunability of the hydrogel, which further strengthens the usage of GelMA as a 3D printable biomaterial (Yue *et al.,* 2015). Lastly, GelMA is a versatile polymer with the ability to be utilised in multiple 3D printing techniques for scaffold development (Bertassoni *et al*., 2014; Gauvin *et al*., 2012; Ouyang *et al*., 2016; Wang *et al*., 2016).

3.3 **Design Approach for the Biomaterial Development in this Chapter**

Using the polymer-mediated biomaterial design, as discussed in Chapter 1, a known polymer – PEGDA (synthetic) or GelMA (natural) – was individually blended with natural ECM components, namely collagen and elastin, to create a composite biomaterial (composed of both a polymer and biomaterial). The collagen-elastin peptide combination was selected for this design approach since research conducted on decellularized rat and porcine brain tissue identified both elastin and collagen as ECM components of the brain tissue (Baiguera *et al.,* 2014; Crapo *et al.,* 2012; DeQuach *et al.,* 2011; De Waele *et al.,* 2015). With this in mind, these peptides were proposed to be a suitable peptide-combination candidate for an aECM brain mimic for TBI applications. As highlighted in Chapter 2, collagen and elastin as biomaterials are plagued by low viscosity issues during 3D printing. To overcome this, these two peptides were blended with the above-mentioned polymers in an attempt to improve the viscosity of these biomaterials, especially for extrusion-based 3D printing. With the blending of the ECM peptides with the polymer, the composite biomaterial is therefore considered to be a biofibrous archetype since the peptides are considered to be a part of the fibrous protein classification of ECM components (Alberts *et al.,* 2002).

3.4 **Materials and Methods**

3.4.1 Materials

Gelatin (Bloom 160, Type B) derived from bovine skin was purchased from Fluka (Steinheim, Germany). Methacrylic anhydride (94%) containing 2000 ppm topanol A, collagen derived from bovine Achilles tendon, Phosphate Buffered Saline tablets (pH 7.4), high retention cellulose dialysis tubing (MW cut off 12 400 Da), ammonium persulphate, tetramethylethylenediamine, N, N'-Methylenebisacrylamide and glacial acetic acid were purchased from Sigma Aldrich (St Louis, MI, USA). Elastin derived from bovine neck ligament was purchased from Elastin Products Co., Inc (Owensville, MO, USA). All chemicals were used as received and were of an analytical grade.

3.4.2 Evaluation of Polymer Blends as Potential 3D Printable Biomaterials

3.4.2.1 PEDGA (MW 575 and 700), Collagen, and Elastin Potential Biomaterial

Various concentrations, namely 1%, 5%, 10% and 20% of the PEGDA polymers, utilized individually and in combination, was blended with 0.5% collagen solution and varying concentrations of elastin (1%, 6%, 10%, 12.5%) at 25 °C under constant stirring. The resulting potential biomaterial was then loaded into a clear barrel (30cc), Low Temperature Dispensing Head (30 ml) extrusion printing cartridge and a standard rectilinear 10x10x10 mm scaffold structure (0-90 ° cross hatch), designed using the Magics® V18 design software, was then attempted using a standard Envisiontec 3D Bioplotter (Envisiontec GmbH, Gladbeck, Germany) at 8 °C cartridge temperature and 4 °C platform temperature. The needle used was a 0.41 mm diameter SmoothFlow Tapered moulded polyethylene needle tip. The biomaterial was printed into a solution containing 0.5% Ammonium Persulphate (APS), 1% Tetramethylethylenediamine (TEMED) and 2.2% N, N'-MethylenebisacrylAmide (MBA).

3.4.2.2 GelMA, Collagen, and Elastin Potential Biomaterial

3.4.2.2.1 GelMA Synthesis

GelMA was synthesized as previously detailed (Van den Bulke *et al*., 2000). In brief, methacrylic anhydride was added in a dropwise manner (0.5 mL/min) to a 10% (w/v) solution of gelatin in PBS (pH 7.4) under constant stirring at 50 °C. To attain a high degree of functionalization in the polymer, 0.6 g of methacrylic anhydride was added per gram of gelatin. The reaction was left to react for 3 hours to increase the degree of functionalization. The resulting polymer was then dialyzed against distilled water at 40 °C for 5 days to remove methacrylic acid and unreacted anhydride. The GelMA was frozen at -80 °C for 24 hours and then lyophilized for 24 hours to obtain a porous, white sponge. The polymer was stored at -20 °C before use.

3.4.2.2.2 Evaluation of the Lysine Amino Acid Substitution in GelMA

The Kaiser assay is a colorimetric assay used extensively for the quantification of amino acids, peptides and proteins (Friedman, 2004). In the presence of primary amines, Ninhydrin reacts to form the quantifiable Ruhmann's purple complex (Friedman, 2004). The degree of substitution of the GelMA polymer was evaluated with the Ninhydrin (2,2-dihydroxy-1,3-indanedione) assay kit to quantitively determine the percentage of lysine amino acid conjugation during the synthesis reaction of gelatin and methacrylic anhydride. In test tubes, GelMA samples of 0.1% were suspended in 1 ml of the Ninhydrin solution. The samples were then capped and covered in aluminium foil and incubated at 80 °C for 20 minutes. Due to the low concentration of free amino acids in the GelMA backbone, an extended incubation period was required to release the Ruhmann's purple complex to the surrounding solution for quantification. The samples were then cooled to room temperature and then diluted with 4 mL of ethanol. The sample optical absorbance was then measured at 570 nm on a Varian Cary 50 UV/Vis Spectrometer (Agilent Technologies, Santa Clara, USA) against the gelatin starting material, which had been treated in the same way.

3.4.2.2.3 Confirmation of Lysine Amino Acid Functionalization in GelMA

Multinuclear ^{1}H Nuclear Magnetic Resonance (NMR) spectroscopy was performed to confirm the lysine conjugation of the synthesized GelMA polymer. The ^{1}H NMR spectroscopy was performed on the Bruker AVANCE II 500 MHz (Bruker Biospin, Ettlingen, Germany) using deuterated water (d-H_2O) as the solvent at room temperature. All chemical shift values are reported in parts per million (ppm).

3.4.2.2.4 GelMA, Collagen, and Elastin Potential Biomaterial

Various concentrations, namely 5%, 7.5%, 10% and 12.5% of the synthesized GelMA polymer, was blended with 0.5% collagen solution, varying concentrations of elastin (1%, 6%, 10%, 12.5%) and 0.5 % Irgacure 2959 at 37 °C under constant stirring. The resulting potential biomaterial was then loaded into an amber barrel (30cc), Low Temperature Dispensing Head (30 ml) extrusion printing cartridge and a standard rectilinear 10x10x10 mm scaffold structure (0-90 ° cross hatch), designed using the Magics® V18 design software, was then attempted using a standard Envisiontec 3D Bioplotter (Envisiontec GmbH, Gladbeck, Germany) at 20 °C. The needle used was a 0.41 mm diameter SmoothFlow Tapered moulded polyethylene needle tip. The scaffold was immediately placed into a UV chamber set to 365 nm and exposed to UV light for 2 minutes.

3.5 **Results and Discussion**

3.5.1 PEGDA-based Biomaterial

3.5.1.1 PEDGA MW 575, Collagen, and Elastin Potential Biomaterial

As depicted by **Table 3.1**, despite the elastin combinations tested with the different concentrations of PEGDA MW 575, the resulting biomaterials are not good candidates for the fabrication of aECM scaffolds as the biomaterial is not viscous enough to achieve extrusion. The rationale as to why this biomaterial failed include: PEGDA MW 575 is stored in the fridge according to supplier specifications where the polymer solidifies. Despite the cartridge of the printer being set to 8 °C, the biomaterial is not viscous enough resulting in the needle leakage. It is possible that in conjunction with the peptides, the thermo-responsive properties of the PEGDA MW 575 at the concentrations tested are not sufficient to achieve solidification at cooler temperatures. In an attempt to achieve solidification, the cartridge temperature was decreased to 4 °C but leakage still prevailed. Furthermore, no material adhesion (on the droplets) was present at the concentrations tested.

Table 3.1: Evaluation of PEGDA MW 575 as a potential biomaterial for 3D printing and aECM fabrication.

Conc. of elastin	Concentration of PEGDA MW 575 (0.1 bar print pressure) ⌘ °				Conc. of Collagen
	1%	**5%**	**10%**	**20%**	
1%	Formulation continually drips out of the needle - No extrusion possible. PEGDA MW 575 is not conducive in the formation of a viscous peptide hydrogel. Peptides do not increase the viscosity sufficiently to form a viscous hydrogel				**0.5 %**
6%					
12.5%					

⌘Crosslinker = Ammonium Persulphate (APS), Tetramethylethylenediamine (TEMED), N, N'-MethylenebisacrylAmide (MBA)
°No improvement in rate of material solidification/crosslinking at any concentration of crosslinkers tested
*No material adherence present at any concentrations tested

3.5.1.2 PEDGA MW 700, Collagen, and Elastin Potential Biomaterial

PEGDA MW 700 was chosen as a potential material candidate as in addition to displaying favourable water solubility, the longer PEG chain improves the viscosity of the PEGDA polymer over PEGDA MW 575. As depicted by **Table 3.2**, at low elastin and PEGDA MW 700 concentrations the resulting biomaterials are not good candidates for the fabrication of aECM scaffolds as the biomaterial is not viscous enough to achieve extrusion. As both the elastin and PEGDA MW 700 concentrations increase, despite marginal improvements in viscosity, the extrusion of the biomaterial is problematic, even at the lowest pressure of 0.1 bar. This results in poor strand dimensional accuracy and strand deformation. Furthermore, due to the

strand deformation, no pore formation is possible thereby defeating the objective of the aim to fabricate an aECM scaffold. This could also be as a result from delayed crosslinking in the crosslinker. To prevent cytotoxicity, higher concentrations of the crosslinking agents were not attempted. In addition, despite the higher concentrations of both elastin and PEGDA MW 700, the biomaterials exhibit poor layer adhesion resulting in poor resolution and structural fidelity. The rationale as to why PEGDA MW 700 showed marginal improvement over the PEGDA MW 500, yet still failed include: PEGDA MW 700 is solid at fridge temperatures (supplier storage specifications). Despite the cartridge of the printer being set to 8 °C, the viscosity of the biomaterial (despite minimal improvements) remains problematic resulting in the over-extrusion on the petri dish. As with PEGDA MW 575, conjunction with the peptides seems to affect the thermo-responsive properties of the PEGDA MW 700.

Table 3.2: Evaluation of PEGDA MW 700 as a potential biomaterial for 3D printing and aECM fabrication.

Conc. of elastin	Concentration of PEGDA MW 700 (0.1 bar print pressure) ⌘°				Conc. of Collagen
	1%	**5%**	**10%**	**20%**	
1%	Formulation continually drips out of the needle. No extrusion possible.	Formulation continually drips out of the needle. No extrusion possible.	Formulation not viscous enough for controlled extrusion (over extrusion). Strand deformation on petri dish after extrusion (poor dimensional strand accuracy).	Formulation not viscous enough for controlled extrusion (over extrusion). Strand deformation on petri dish after extrusion (poor dimensional strand accuracy).	**0.5 %**
6%	Formulation continually drips out of the needle. No extrusion possible.	Formulation continually drips out of the needle. No extrusion possible.	Formulation slightly more viscous, however, controlled extrusion is still poor (over extrusion). Narrower, wavy strands – poor dimensional strand accuracy, no pore or layer formation possible.	Formulation slightly more viscous, however, controlled extrusion is still poor (over extrusion). Narrower, wavy strands – poor dimensional strand accuracy, no pore or layer formation possible	
10%	Formulation continually drips out of the needle. No extrusion possible.	Formulation slightly more viscous, however, controlled extrusion is still poor (over extrusion). Wide strand, wavy strands – poor dimensional strand accuracy, no pore or layer formation possible.	Increase in formulation viscosity, however extrusion control is still problematic (over extrusion). Slightly less strand deformation. Slow crosslinking. No layer formation possible.	Further slight improvements in formulation viscosity. Strand width improving; however (strand deformation still present), extrusion control is still problematic (over extrusion) and crosslinking is too slow. No layer formation possible.	
12.5%	Formulation continually drips out of the needle. No extrusion possible.	Formulation slightly more viscous, however, controlled extrusion is still poor (over extrusion). Narrower, wavy strands – poor dimensional strand accuracy, no pore or layer formation possible	Further slight improvements in formulation viscosity. Strand width improving; however (strand deformation still present), extrusion control is still problematic (over extrusion) and crosslinking is too slow. No layer formation possible.	Formulation is more extrudable but over extrusion still present, slow solidification, compromised resolution and structural fidelity of strands. No pore or layer formation possible.	

⌘Crosslinker = Ammonium Persulphate (APS), Tetramethylethylenediamine (TEMED), N, N'-MethylenebisacrylAmide (MBA)
°No improvement in rate of material solidification/crosslinking at any concentration of crosslinkers tested
*No material adherence present at any concentrations tested

3.5.1.3 PEDGA MW 575 and 700, Collagen, and Elastin Potential Biomaterial

Since the PEGDA (MW 575 and 700) polymers alone did not produce biomaterials with the required properties for 3D printing, the polymers were mixed in an attempt to alter their individual chemistry to improve their 3D printability. The PEGDA MW 575 was kept constant at 20% while the PEGDA MW 700 and elastin was altered. As depicted by **Table 3.3**, the biomaterial characteristics seem to mirror the PEGDA MW 700 results (low elastin and PEGDA MW 700 concentrations results in biomaterial leakage and slight improvements in viscosity as the concentrations increase). Improvements in viscosity were achieved at lower PEGDA MW 700 concentrations in comparison to the PEGDA MW 700 polymer alone, however, the viscosity remains too low for controlled extrusion at 0.1 bar. Furthermore, the resulting printed strands lack resolution and structural fidelity and therefore, the aim to fabricate an aECM scaffold cannot be achieved. The crosslinker could also have contributed to this as above.

Table 3.3: Evaluation of PEGDA MW 575 and 700 as a potential biomaterial for 3D printing and aECM fabrication.

Conc. of elastin	Concentration of PEGDA MW 700 (0.1 bar print pressure) ⌘°				Conc. of Collagen
	1%	**5%**	**10%**	**20%**	
1%	Formulation continually drips out of the needle. No extrusion possible.	Formulation continually drips out of the needle. No extrusion possible.	Formulation not viscous enough for controlled extrusion (over extrusion). Strand deformation on petri dish after extrusion (poor dimensional strand accuracy).	Formulation not viscous enough for controlled extrusion (over extrusion). Strand deformation on petri dish after extrusion (poor dimensional strand accuracy).	**0.5 %**
6%	Formulation not viscous enough for controlled extrusion (over extrusion). Strand deformation on petri dish after extrusion (poor dimensional strand accuracy).	Slight improvement in viscosity. Formulation becoming more extrudable (over extrusion present), despite being of a low viscosity. Strand deformation still present. No layer/pore formation possible.	Further slight improvement in viscosity. Formulation slightly more extrudable (over extrusion), despite strand deformation still present. No layer/pore formation possible.	Formulation is somewhat extrudable. Formulation viscosity is problematic – over extrusion still present. Despite strand deformation resulting in no pore formation, first layer printed. No structural fidelity.	
12.5%	Formulation not viscous enough for controlled extrusion (over extrusion). Strand deformation on petri dish after extrusion (poor dimensional strand accuracy).	Formulation is somewhat extrudable. Formulation viscosity is problematic – over extrusion still present. Despite strand deformation resulting in no pore formation, first layer printed. No structural fidelity.	Slight improvement in formulation extrusion. Formulation viscosity is problematic – over extrusion still present. Despite strand deformation resulting in no pore formation, first layer printed. No structural fidelity.	Formulation is somewhat extrudable. Formulation viscosity is problematic – over extrusion still present. Despite strand deformation and no pore formation, second layer is compromised. No layer adherence. No structural fidelity.	
	20%				
	Concentration of PEGDA MW 575				

⌘Crosslinker = Ammonium Persulphate (APS), Tetramethylethylenediamine (TEMED), N, N'-MethylenebisacrylAmide (MBA)
°No improvement in rate of material solidification/crosslinking at any concentration of crosslinkers tested
*No material adherence present at any concentrations tested

3.5.2 GelMA-based Biomaterial

3.5.2.1 Evaluation of GelMA Lysine Conjugation

Prior to the design of the GelMA biomaterials, the percentage of lysine amino acid conjugation was determined using the Kaiser assay. The standard curve of H-Lysine(Boc)-OH in **Figure 3.2** was used to assess the lysine conjugation in both the GelMA polymer and gelatin starting material. Originally, the reaction time for the GelMA synthesis was one hour and the percentage lysine conjugation was determined to be ~70%. In spite of this, due to the fabrication method (extrusion-based 3D printing) and the fact that GelMA at lower degrees of substitution (DoS) are known to significantly deform due to the low crosslinking ability of the hydrogel (Shirahama *et al.,* 2016), the reaction time was increased to three hours to allow for almost complete substitution. After the three hours, the DoS of the lysine was determined to be ~95%. For the biomaterial development, the three-hour reaction time was kept.

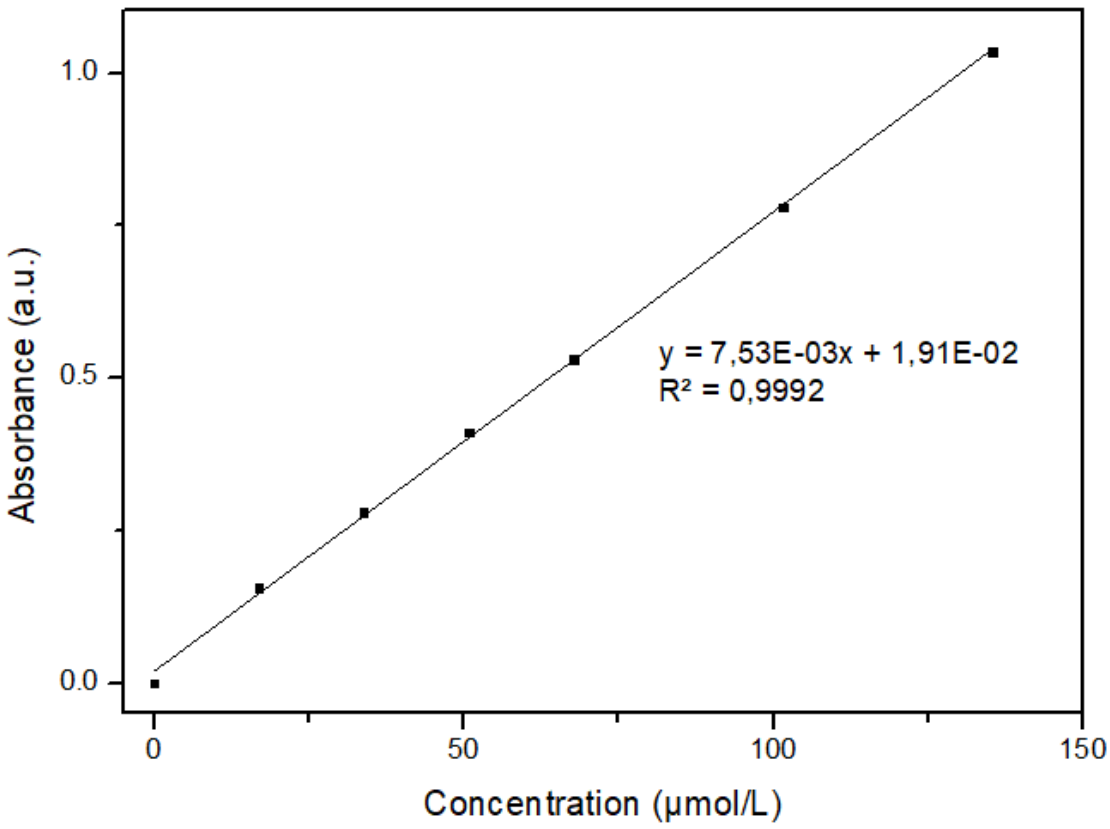


Figure 3.2: Standard curve of H-Lysine(Boc)-OH used to determine the percentage lysine conjugation of the lysine amino acid moieties in the GelMA polymer relative to the gelatin starting material.

3.5.2.2 Confirmation of Lysine Functionalization

GelMA prepared from the three-hour reaction was subjected to ^{1}H NMR analysis to confirm the conjugation of the methacryloyl groups to the lysine amino acids on the gelatin backbone. The increase of the methacrylate vinyl signal at δ=5.9 ppm and δ=6.3 (red arrows - **Figure**

3.3a) and the decrease of the signal at around δ=2.8 ppm (green arrows - **Figure 3.3a**) (protons associated with methylene group of the lysine signal) confirmed the functionalization of the lysine moieties on the GelMA backbone (**Figure 3.3**).

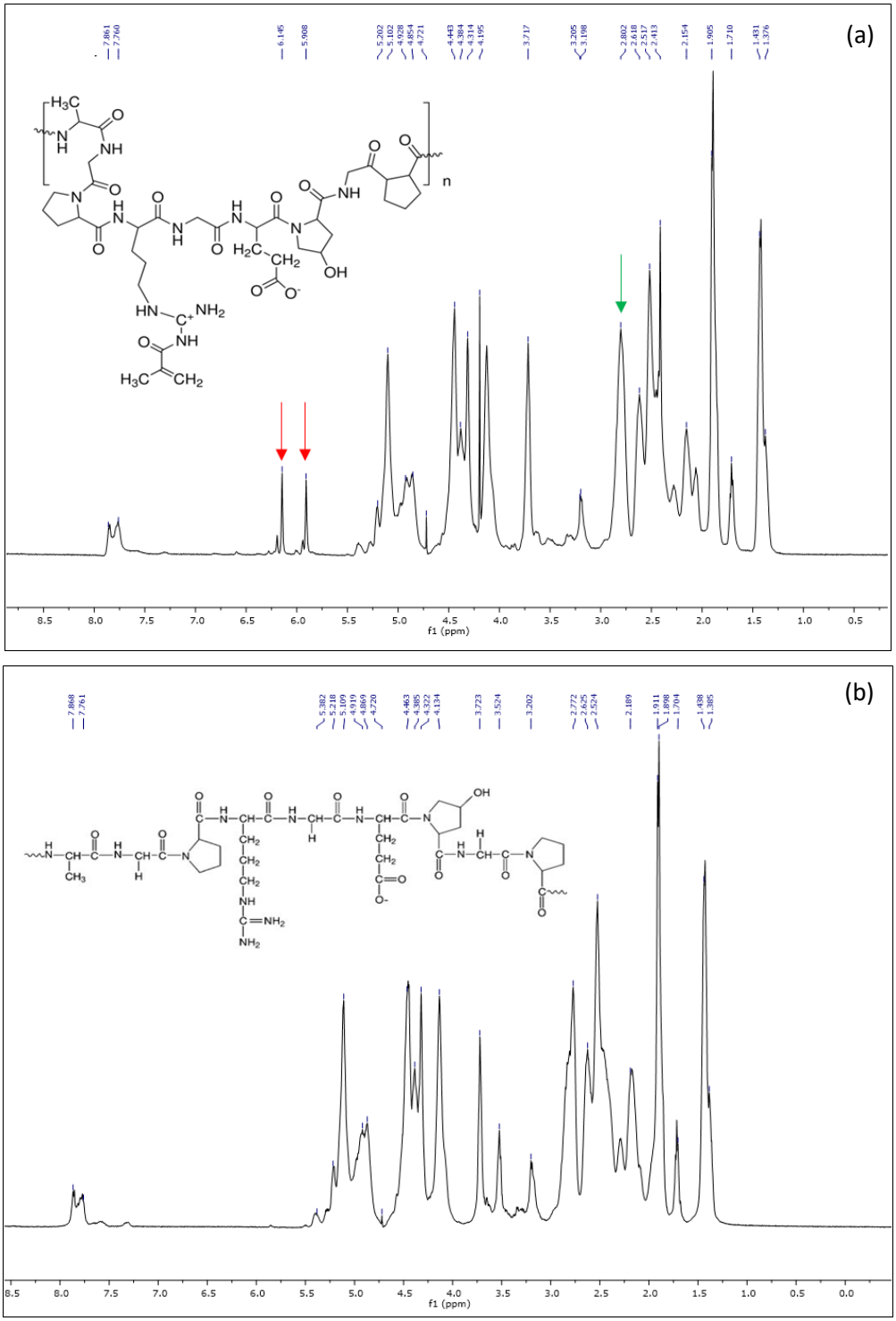


Figure 3.3: Spectral analysis of the synthesized GelMA polymer. ^{1}H analysis of the GelMA polymer is shown in (a) and the gelatin starting material is shown in (b). The red arrows indicate the increase in the methacrylate vinyl signals (δ=5.9 ppm and δ=6.3 ppm) and the green arrow indicates the decrease in the lysine methylene group signal (δ=2.8 ppm).

3.5.2.3 GelMA-Based Biomaterial

As depicted by **Table 3.4**, at the extreme concentrations of GelMA and elastin, the biomaterial viscosity is compromised and continuous strands cannot be extruded. At 12.5 % GelMA, the biomaterial solidifies too slowly resulting in 'sticky' layers which compromises the structure fidelity and resolution. At higher concentrations of elastin, the material is not continuously extrudable. Furthermore, the material contracts after extrusion when in contact with the petri dish. In addition, for successful printing, various temperature modifications occurred due to the thermo-responsive nature of GelMA whereby the hydrogel begins to liquify as the temperature begins to increase (Van den Bulke *et al*., 2000).

At 10% GelMA, 0.5% collagen, and 1% elastin, a successful candidate for biomaterial optimization was obtained (depicted as green in **Table 3.4**). This candidate exhibited good printability, fair solidification, surface adherence, resolution, and strand width.

Table 3.4: Evaluation of GelMA as a potential biomaterial for 3D printing and aECM fabrication. The green shading represents the formation of a successful biomaterial.

Conc. of elastin	Concentration of 10% GelMA (DoS ~ 95 %), 1 bar pressure				Conc. of Collagen
	5%	7.5%	10%	12.5%	
1%	Unable to extrude continuous strands. Biomaterial is not viscous enough. Formulation does not adhere to the petri dish.	Improvements in viscosity, continuous strands are extruded. However, resolution and structural fidelity are compromised.	Good printability, fair solidification and surface adherence, fair structural fidelity (layers), fair resolution and strand width.	Extrudable, but slow solidification present. Subsequent layers are compromised as layers stick to each other and are damaged upon printer head movement. Poor structural fidelity.	0.5 %
6%	Continuous strands are extruded; however, biomaterial is of a low viscosity. However, resolution and structural fidelity are compromised.	Continuous strands are extruded, however, spaces between the layers are evident from inconsistent material extrusion.	Good printability, however, reproducibility of strand geometry is poor resulting in irregular pore sizes.	Extrudable, but slow solidification present. Subsequent layers are compromised as layers implode inwards. Poor structural fidelity.	
12.5%	Unable to extrude continuous strands. Biomaterial is too elastic, resulting in the contraction of the strand.	Unable to extrude continuous strands. Biomaterial is too elastic, resulting in the contraction of the strand.	Needle continually clogs. Unable to extrude continuous strands.	Needle continually clogs. Unable to extrude continuous strands.	

At this stage of pre-formulation design, it was postulated that the optimized biomaterial formulation shown in **Table 3.4** was a semi IPN (**Figure 3.4**). This was proposed since the

biomaterial candidate contained two or more polymer networks crosslinked in the presence of each other, a requirement of an IPN system (Mathew, 2013). In the candidate biomaterial, the polymers are GelMA, collagen, and elastin. Furthermore, in a semi IPN only one polymer is crosslinked in the presence of the other (Mathew, 2013). In this case, only the GelMA polymer was proposed to be crosslinked through Ultra Violet (UV) radiation at 365 nm (**Figure 3.4**). The photoinitiator, Irgacure 2959 (2-hydroxy-4-(2-hydroxyethoxy)-2-methylpropiophenone), undergoes an α-cleavage reaction when exposed to UV light at 365 nm. This results in the formation of a benzoyl group and a free radical acetyl group. The new free radicals then propagate chain polymerisation through the functionalized groups on the GelMA polymer and results in the formation of a stable network (Pahoff *et al*., 2019). Since the GelMA polymer is crosslinked in the presence of the peptides, it was proposed that the semi IPN was designed as a 'fibre floating in gel matrix' network system owing to the fact that the peptides (fibre) would have the ability to intertwine in and around the crosslinked chains of the GelMA framework (gel matrix), as depicted in **Figure 3.4**.

Following this, the design of the candidate biomaterial was further modified with the addition of 1% Genipin – a natural protein crosslinker (Manickam *et al.,* 2014; Song *et al.,* 2017) – in the attempts of forming a full IPN. In a full IPN, both polymers are crosslinked in the presence of each other (Mathew, 2013). Since the Genipin would crosslink both the collagen and the elastin and the UV crosslinker would crosslink the GelMA, it was further proposed that a full IPN was also designed (**Figure 3.5**). In terms of the crosslinking mechanism of Genipin, one Genipin molecule crosslinks two free amino functional groups of the lysine molecules of the two peptide chains in the collagen and elastin (Elzoghby *et al.,*2015). Despite the fact that Genipin is able to crosslink gelatin through the lysine residues, during the functionalising of gelatin with the methacrylic anhydride to form the GelMA polymer the lysine functional group of the gelatin is modified by the methacrylate groups (Pepelanova *et al.,* 2018). In this way, the higher the degree of substitution (DoS) on the lysine residues, the less lysine residues are available to be crosslinked by Genipin. In this case, the DoS is >95%, and therefore the number of lysine residues available for Genipin crosslinking is assumed to be negligible. As with the semi IPN, the full IPN was also proposed to be designed as a 'fibre floating in gel matrix' network system. In this system, despite the double crosslinking, the peptide chains in their crosslinked form were proposed to still have the ability to intertwine in and around the crosslinked chains of GelMA (gel matrix) since the GelMA crosslinking occurred at a later stage of formulation were the GelMA crosslinks would form around the interwoven network of the peptides, as depicted in **Figure 3.5**.

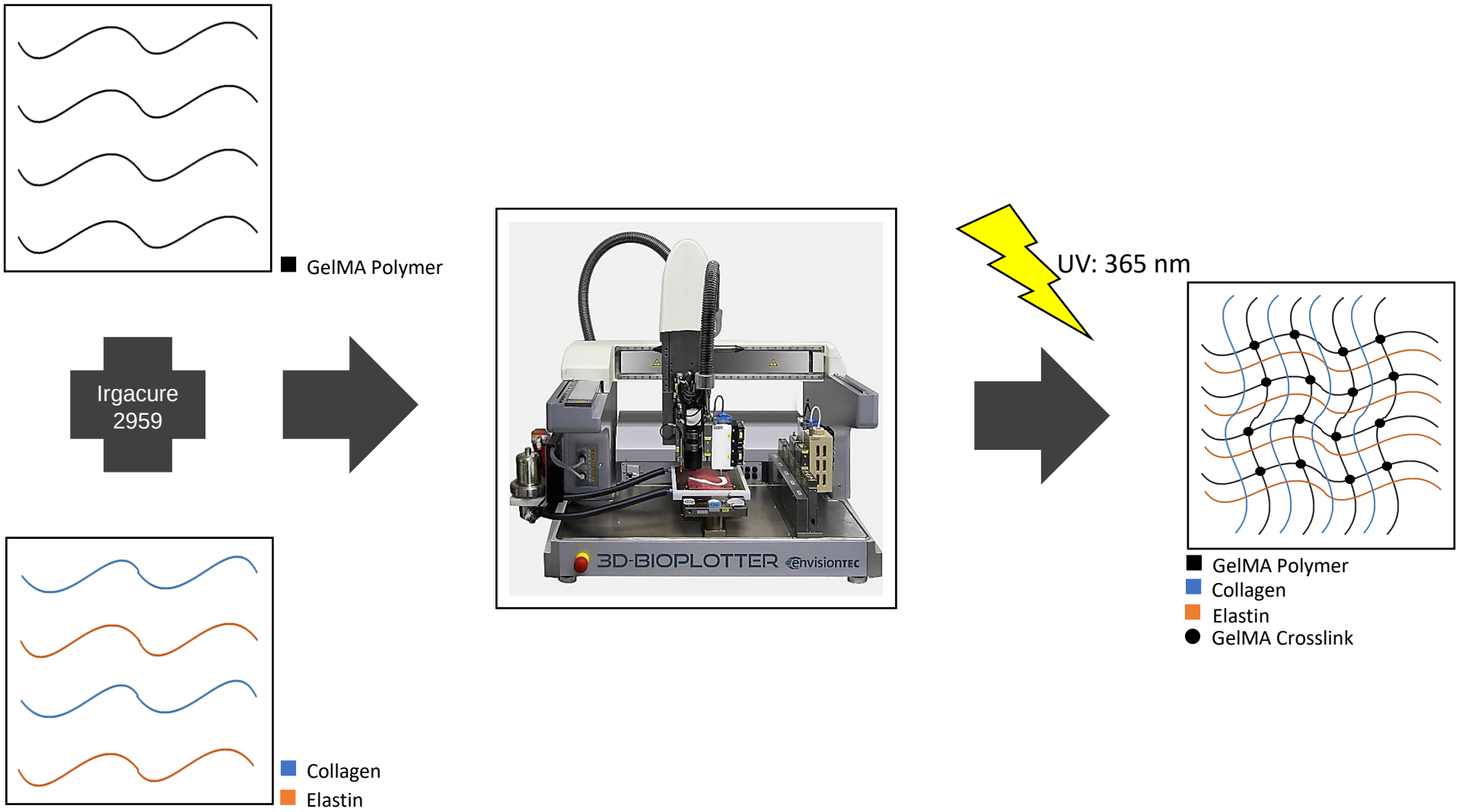


Figure 3.4: Proposed formation of the semi IPN.

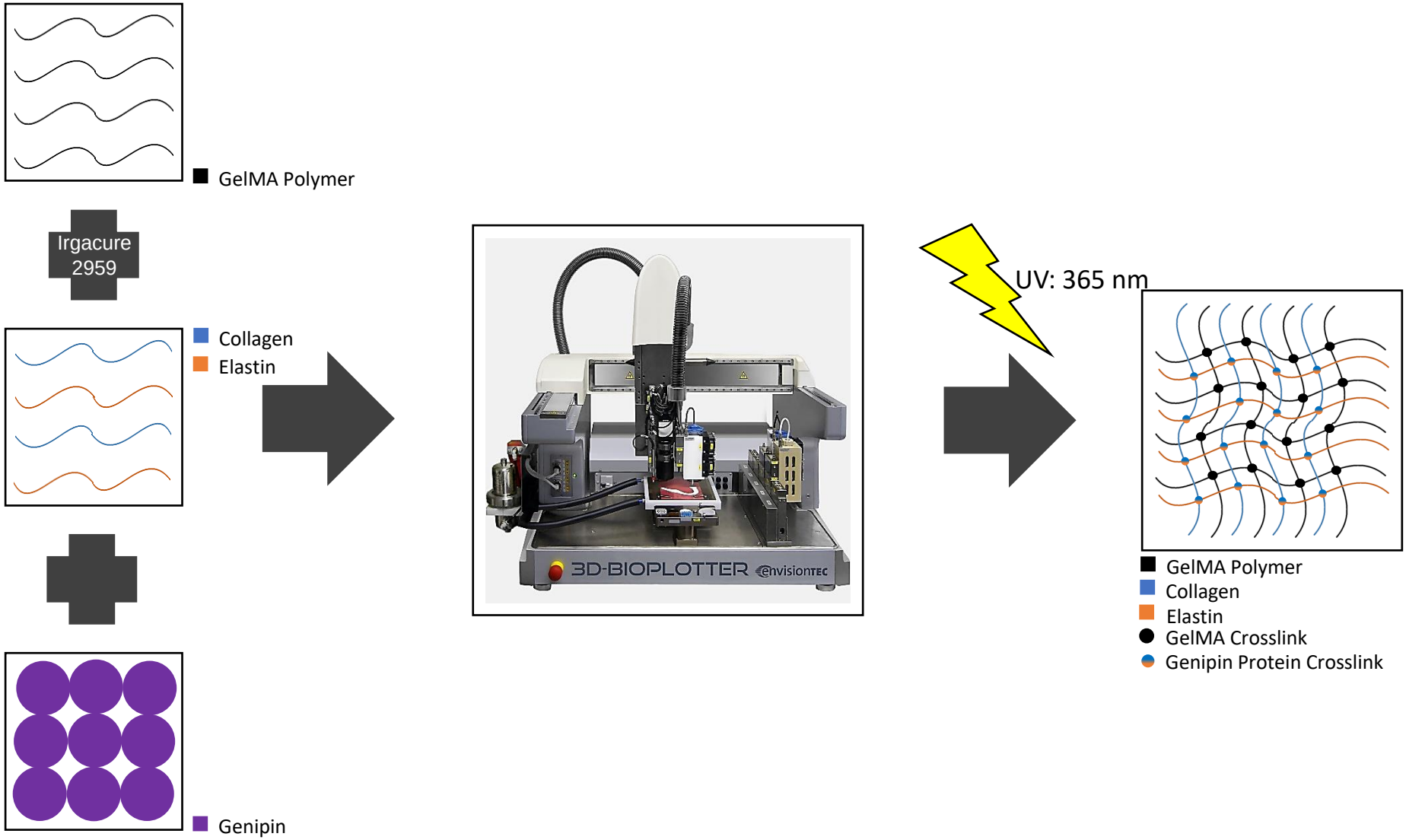


Figure 3.5: Proposed formation of the full IPN.

Due to the nature of the optimized formulation, both of the candidate biomaterials had to undergo UV crosslinking post-printing to prevent the scaffolds liquifying and losing their internal shape. This was performed since GelMA displays thermo-responsive properties liquifying at higher temperatures. **Figure 3.6** indicates the state of the candidate biomaterials before (a) and after (b) UV crosslinking at 37 °C (**Figure 3.6**)

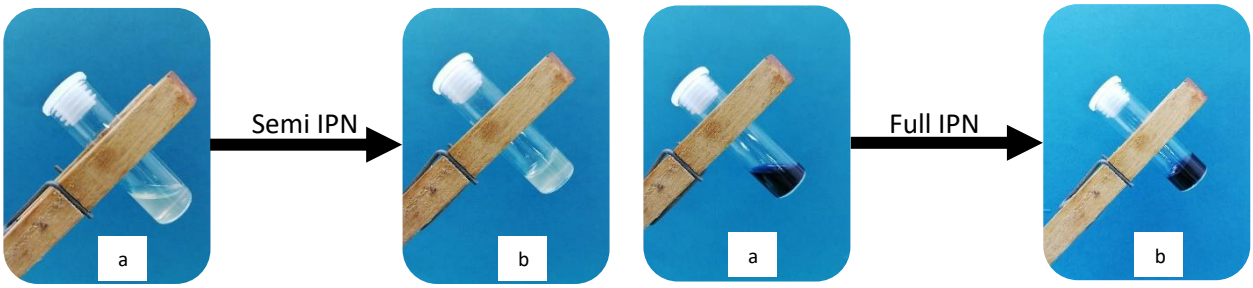


Figure 3.6: Tilt tests indicating (a) non-crosslinked IPN systems and (b) photo-crosslinked IPN systems.

3.6 GelMA Biomaterial Optimization

The successful biomaterial candidates obtained in the pre-formulation stage was optimized to improve on the solidification, structural fidelity, resolution, strand width and pore formation. To achieve this, several parameters namely; the needle transfer height, cartridge temperature, pressure, speed, post/pre-flow, wait time, platform temperature, needle internal diameter and scaffold height were optimized. During the optimization process, only one parameter was altered at a time so that the effect on the biomaterial could be noted.

Table 3.5 provides a brief summary of the optimizations performed to develop the optimized biomaterial for aECM scaffold fabrication and achieve a high printing resolution for the two IPN rectilinear scaffolds. Parameters producing, including but not limited to: non-extrudable stands (blocking needle), irregular strand widths, internal structure collapse and biomaterials that form droplets and not strands were excluded from the printing parameter programming. From **Table 3.5**, it is evident that the cartridge and platform temperature played the most important role in the successful printing of the scaffolds. Following these temperature adjustments, the pre- and post-flow delay optimizations were critical in ensuring that the strands extruded at the correct start and stop positions to prevent the formation of an irregular scaffold (**Figure 3.7a**). The optimized biomaterial is shown as the last entry in the table and is highlighted in green (**Figure 3.7b**).

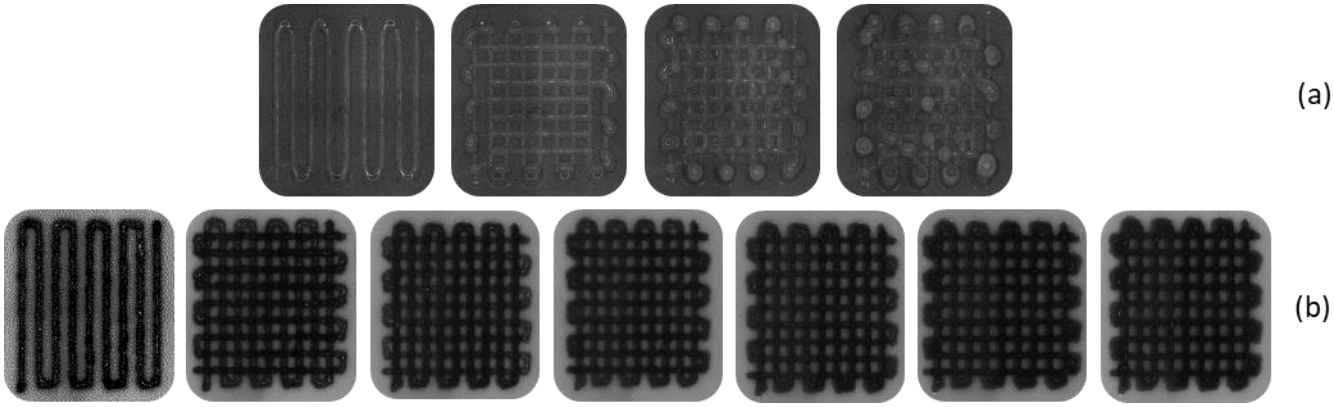


Figure 3.7: Images of the different layers imaged on the printer during a print. (a) An unsuccessful print of the semi IPN where gaps and over extrusion causes a compounding error and leads to the failure of the scaffold. (b) A successful print of the full IPN indicating the importance of proper parameter optimization. Scale: 1 mm = 2.49 mm for all images.

From the phase diagram in **Figure 3.8**, it is evident that when the cartridge temperature is below 13 °C, the needle blocks or forms crinkled strands (depicted in orange), which suggests that the physical crosslinking between the GelMA polymer strands is too rigid for extrusion. When the cartridge temperature exceeds 13 °C, the biomaterial is less viscous and drips from the needle but solidifies on the platform (depicted in red), which suggests that the physical crosslinks are not rigid enough for controlled extrusion. Therefore, 13 °C is the optimal temperature for sufficient physical crosslinking rigidity. On the other hand, when the platform temperature exceeds 18 °C, although the biomaterial is extrudable, the integrity of the scaffold is lost as the strands melt upon contact with the platform (depicted in blue). The optimal cartridge and platform temperature were 13 °C and 18 °C, respectively, which resulted in smooth biomaterial strands that retained the internal structure and solidified upon contact with the platform (depicted in green). Rectilinear scaffolds were then photo-crosslinked to fix the internal architecture.

Table 3.5: Optimization of GelMA as a potential biomaterial for 3D printing and aECM fabrication. The green shading represents the formation of a successful biomaterial.

Attempt	Transfer height (mm)	Cartridge Temperature (°C)	Pressure (bar)	Speed (mm/s)	Pre-Flow (s)	Post-Flow (s)	Wait time (s)	Platform Temperature (°C)	Needle Internal Diameter (mm)	Scaffold Height (mm)	UV Cured	Line Distance (mm)	Outcome
1	5	25	1	10	0	0	0	N/A	0.4	N/A	No	N/A	Hydrogel not viscous, does not solidify. Internal pattern does not hold form.
2	5	22	3	5	0	0	0	N/A	0.4	N/A	No	N/A	Hydrogel consistency improving. Pressure is too high/speed is too slow. Strands bulge to >1mm distance.
3	5	17	1.5	10	0	0	30	N/A	0.4	N/A	No	N/A	Hydrogel consistency is too stiff. Strands are not extruded as a continuous filament. Hydrogel does not get extruded at the start position and gets over extruded at the end position.
4	5	20	2	20	0	0	0	20	0.4	N/A	No	N/A	Hydrogel consistency is extrudable. Hydrogel melts on platform.
5	5	20	2	20	0	0	0	10	0.4	N/A	No	N/A	Hydrogel consistency is extrudable, however platform is too cold and needle continuously clogs.
6	5	20	2	20	0	0	0	15	0.4	N/A	No	N/A	Hydrogel consistency is extrudable, however, platform is slightly too warm and although hydrogel retains internal pattern, hydrogel takes too long to solidify.
7	5	20	2	20	0	0	0	13	0.4	N/A	No	N/A	Hydrogel consistency is extrudable and solidifies on platform. However, speed is too fast as too little material is extruded.
8	5	20	2	10	0	0	0	13	0.4	N/A	No	N/A	Hydrogel consistency is extrudable and solidifies on platform. Round rods are extruded; however, hydrogel is ''sticky'', poor structural fidelity.
9	5	20	2	10	0	0	30	13	0.4	~0.2	No	N/A	Hydrogel consistency is extrudable and solidifies on platform. Round rods are extruded, wait time allows layers to be printed. Excess material is extruded at the end of each layer so scaffold is uneven/warped.
10	5	20	2	10	0	-0.1	30	13	0.4	~0.2	No	N/A	Hydrogel consistency is extrudable and solidifies on platform. Round rods are extruded, wait time allows layers to be printed. Gap develops at the end of each layer due to increased post flow.

Table 3.5: Optimization of GelMA as a potential biomaterial for 3D bioprinting and aECM fabrication. The green shading represents the formation of a successful biomaterial (Continued).

Attempt	Transfer height (mm)	Cartridge Temperature (°C)	Pressure (bar)	Speed (mm/s)	Pre-Flow (s)	Post-Flow (s)	Wait time (s)	Platform Temperature (°C)	Needle Internal Diameter (mm)	Scaffold Height (mm)	UV Cured	Line Distance (mm)	Outcome
11	5	19	1.5	12	0	-0.03	60	13	0.4	~0.2	No	N/A	Hydrogel consistency is extrudable. Hydrogel solidifies on platform. Gap develops on start corner; therefore, scaffold fails on layer 3. Rectified post flow and slight over extrusion of material occurs at the end of each layer.
12	5	19	2	12	0.1	-0.03	30	13	0.4	~0.2	No	N/A	Hydrogel consistency is extrudable. Hydrogel solidifies on platform. Small gap still develops on start corner. Rectified post flow and slight over extrusion of material occurs at the end of each layer.
13	5	19	2.2	12	0.2	-0.03	30	13	0.4	~0.4	Yes	1	Hydrogel consistency is extrudable. Hydrogel solidifies on platform. Small gap still develops on start corner. Doubled the scaffold height of the previous print. Rectified post flow and slight over extrusion of material occurs at the end of each layer.
14	10	19	2.5	13	0.3	-0.04	30	13	0.2	~0.5	Yes	1	Hydrogel consistency is extrudable. Hydrogel solidifies on platform. Hydrogel is successfully printed through a 0,2 mm internal diameter needle. Post flow and pre flow optimized.
15	10	18	2.8	15	0.4	-0.05	30	13	0.2	10 and 20	Yes	1	Hydrogel solidifies on platform and maintains internal pattern. A successful 10 mm and 20 mm scaffold is printed. Scaffolds retain 3D printed shape and internal pattern after 2 minutes of UV exposure.

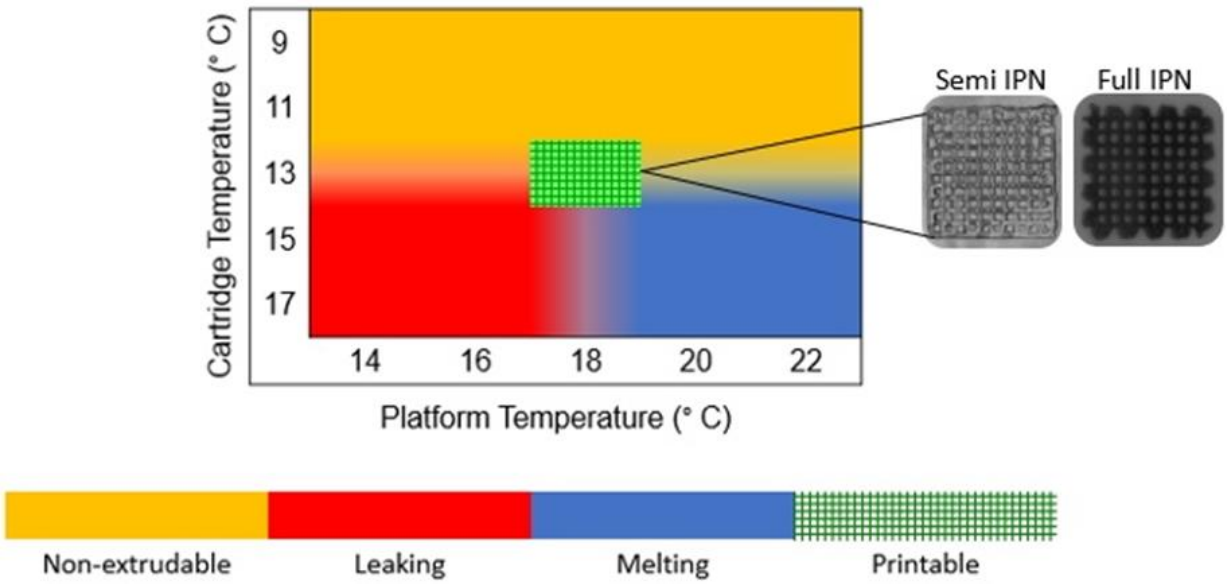


Figure 3.8: A phase diagram indicating the effect of cartridge and platform temperature on the 3D printability of the optimized biomaterials.

3.7 **Conclusive Remarks**

Despite the brain, both before and after injury, presenting multiple challenges in the selection of biomaterials to adequately mimic the native ECM, 3D printing technique biomaterial requirements has shown to provide further obstacles in the fabrication of artificial matrices for neural tissue engineering. In this chapter, two polymers namely PEGDA and GelMA were tested individually at various concentrations in blends with collagen and elastin in an attempt to fabricate a novel aECM that was optimized for extrusion-based printing.

In spite of the concentrations and various conditions tested, neither PEGDA MW biomaterials (MW 575 and MW 700) exhibited favourable 3D printing material requirements (**Table 3.6**). In terms of the PEGDA MW 575 biomaterial, no improvements in viscosity was achieved and the biomaterial continually dripped from the needle. With regard to the PEGDA MW 700 biomaterial, despite marginal improvements in the viscosity, the biomaterial still displayed an unfavourable viscosity for extrusion-based 3D printing. Furthermore, this biomaterial was plagued with over extrusion, poor strand fidelity and non-layer adherence, which supported the decision to abandon further optimizations to the PEGDA biomaterials in this work. Considering the above, it is likely that the PEGDA biomaterials formulated may be successfully 3D printed if the 3D printing technique is altered to accommodate a lower viscosity biomaterial. If this is not an option, potentially altering the crosslinking strategy and needle tip characteristics can be attempted to achieve successful 3D printing.

In terms of the GelMA bioink, a suitable novel candidate for further optimizations was discovered. Despite the extremes of the biomaterials proving to be unfavourable for biomaterial optimization, a biomaterial composed of 10% GelMA, 1% elastin and 0.5% collagen proved to exhibit good printability, fair solidification, surface adherence, resolution and strand width prior to optimization (**Table 3.6**). In this Chapter, the original biomaterial developed was proposed to be a semi IPN. To this candidate biomaterial, 1% Genipin was added and the formation of a full IPN was further proposed. Both proposed IPN biomaterials were then further optimized for extrusion-based 3D printing and were both found to possess a stable architecture, regular pore sizes, varying heights and a suitable solidification.

Table 3.6: Summary of the success between the polymers PEGDA and GelMA as a potential biomatrerial for 3D printing and aECM fabrication.

Parameter	PEGDA Mw 575	PEGDA Mw 700	PEGDA Mw 575+700	GelMA
3D printing technique	Extrusion based 3D printing			
3D printer	4th Generation Envisiontec 3D-Bioplotter			
Pressure (Bar)	0.1			1
Needle size (mm)	0.41			
Optimal collagen concentration (%)	N/A No successful formulation at any concentrations tested			1
Optimal elastin concentration (%)				0.5
Optimal polymer concentration (%)				10
Crosslinker	Ammonium Persulphate (APS) Tetramethylethylenediamine (TEMED) N, N'-MethylenebisacrylAmide (MBA)			Irgacure 2959
Optimal crosslinker concentration (%)	N/A No structural fidelity or strand solidification			1
Suitable viscosity at optimal polymer concentrations	N/A Even at the highest concentrations the formulation is only somewhat extrudable with viscosity remaining to be problematic (over extrusion still present). Furthermore, strand deformation, poor pore formation, poor strand solidification and poor layer adherence prevails. Subsequent layers are compromised. No structural fidelity			Yes
Solidification at optimal polymer concentrations				
Strand adherence at optimal polymer concentrations				
Shape/structure fidelity at optimal polymer concentrations				
Further optimization	No			Yes

Since the 3D printer technique plays a crucial role in the success of 3D printing the biomaterial, this proof-of-concept study was necessary to highlight the paramount importance that viscosity plays in extrusion-based 3D printing. Therefore, this study confirms the need for careful biomaterial selection that takes the 3D printing technique into account. Despite the successful 3D printing of the two biomaterials, further material characterisation is required to confirm the

formation of the two proposed IPN biomaterials. Such characterisations are discussed in Chapter 4.

3.8 References

Alberts, B., Johnson, A., Lewis, J., Raff, M., Roberts, K. and Walter, P. (2002). Molecular Biology of the Cell. 4th edition. New York: Garland Science; 2002. The Extracellular Matrix of Animals. Available from: https://www.ncbi.nlm.nih.gov/books/NBK26810/. (Accessed Nov 3, 2020).

Axpe, E., Orive, G., Franze, K. and Appel, E. A. (2020). Towards brain-tissue-like biomaterials. Nature Communications. **11**, 3423.

Baiguera, S., Del Gaudio, C., Lucatelli, E., Kuevda, E., Boieri, M., Mazzanti, B., Bianco, A. and Macchiarini, P. (2014). Electrospun gelatin scaffolds incorporating rat decellularized brain extracellular matrix for neural tissue engineering. Biomaterials. **35** (4), 1205–1214.

Bertassoni, L. E., Cecconi, M., Manoharan, V., Nikkhah, M., Hjortnaes, J., Cristino, A. L., Barabaschi, G., Demarchi, D., Dokmeci, M. R., Yang, Y. and Khademhosseini, A. (2014). Hydrogel bioprinted microchannel networks for vascularization of tissue engineering constructs. Lab on a Chip. **14** (13), 2202-2011.

Budday, S., Ovaert, T. C., Holzapfel, G. A., Steinmann, P. and Kuhl, E. (2020). Fifty Shades of Brain: A Review on the Mechanical Testing and Modeling of Brain Tissue. Archives of Computational Methods in Engineering. **27**, 1187–1230.

Crapo, P. M., Medberry, C. J., Reing, J. E., Tottey, S., van der Merwe, Y., Jones, K. E., and Badylak, S. F. (2012). Biologic scaffolds composed of central nervous system extracellular matrix. Biomaterials. **33** (13), 3539–3547.

Da Silva, K., Kumar, P., Choonara, Y. E., du Toit, L. C. and Pillay, V. (2019). Preprocessing of Medical Image Data for Three-Dimensional Bioprinted Customized-Neural-Scaffolds. Tissue Engineering Part C: Methods. 25, 401–10.

Da Silva, K., Kumar, P., Choonara, Y. E., du Toit, L. C. and Pillay, V. (2020). Three-dimensional printing of extracellular matrix (ECM)-mimicking scaffolds: A critical review of the current ECM materials. Journal of Biomedical Materials Research Part A. **108** (12), 2324-2350.

DeQuach, J. A., Yuan, S. H., Goldstein, L. S. and Christman, K. L. (2011). Decellularized porcine brain matrix for cell culture and tissue engineering scaffolds. Tissue Engineering Part A. **17** (21-22), 2583–2592.

De Waele, J., Reekmans, K., Daans, J., Goossens, H., Berneman, Z. and Ponsaerts, P. (2015). 3D culture of murine neural stem cells on decellularized mouse brain sections. Biomaterials. **41**, 122–131.

El-Sherbiny, I. M. and Yacoub, M. H. (2013). Hydrogel scaffolds for tissue engineering: Progress and challenges. Global Cardiology Science and Practice. **3**, 316–342.

Elzoghby, E. O., Elgohary, M. M. and Kamel, N. M. (2015). Implications of Protein- and Peptide-Based Nanoparticles as Potential Vehicles for Anticancer Drugs. Advances in Protein Chemistry and Structural Biology. **98**, 169-221.

Friedman, M. (2004). Applications of the ninhydrin reaction for analysis of amino acids, peptides, and proteins to agricultural and biomedical sciences. Journal of Agricultural and Food Chemistry. **52** (3), 385-406.

Frost, B. A., Sutliff, B. P., Thayer, P., Bortner, M. J. and Foster, E. J. (2019). Gradient Poly(ethylene glycol) Diacrylate and Cellulose Nanocrystals Tissue Engineering Composite Scaffolds via Extrusion Bioprinting. Frontiers in Bioengineering and Biotechnology. **7**, 280.

Gauvin, R., Chen, Y. -C., Lee, J. W., Soman, P., Zorlutuna, P., Nichol, J. W., Bae, H., Chen, S. and Khademhosseini, A. (2012). Microfabrication of complex porous tissue engineering scaffolds using 3D projection stereolithography. Biomaterials. **33**, 3824–3834.

Guvendiren, M., Molde, J., Soares, R. M. and Kohn, J. (2016). Designing Biomaterials for 3D Printing. ACS Biomaterials Science and Engineering. **2** (10), 1679–1693.

Kirchmajer, D., Gorkin, R. and in het Panhuis, M. (2015). An overview of the suitability of hydrogel forming polymers for extrusion-based 3D-printing. Journal of Materials Chemistry B. **3**, 4105-4117.

Kumar, P., Choonara, Y. E., Khan, R. A. and Pillay, V. (2017). The Chemo-Biological Outreach of Nano-Biomaterials: Implications for Tissue Engineering and Regenerative Medicine. Current Pharmaceutical Design. **23** (24), 3538-3549.

Kyung, J. H., Yeon, K. S., Jeong, K. S. and Moo, L. Y. (2002). pH / temperature-responsive semi-IPN hydrogels composed of alginate and poly(N-isopropylacrylAmide). Journal of Applied Polymer Science. **83**, 128–136.

Leipzig, N. D. and Shoichet, M. S. (2009). The effect of substrate stiffness on adult neural stem cell behavior. Biomaterials. **30** (36), 6867-6878.

Li, J., Wu, C., Chu, P. K. and Gelinsky, M. (2020). 3D printing of hydrogels: Rational design strategies and emerging biomedical applications. Material Science and Engineering: Reports: R. **140**, 100543.

Manickam, B., Sreedharan, R. and Elumalai, M. (2014). 'Genipin' - the natural water soluble cross-linking agent and its importance in the modified drug delivery systems: an overview. Current Drug Delivery. **11** (1), 139-45.

Mathew, A. P. (2013) Interpenetrating Polymer Networks: Processing, Properties and Applications. In: Visakh P., Thomas S., Chandra A., Mathew A. (eds) Advances in Elastomers I. Advanced Structured Materials, vol 11. Springer, Berlin, Heidelberg.

Ouyang, L., Highley, C. B., Sun, W. and Burdick, J. A. (2016) A generalizable strategy for the 3D bioprinting of hydrogels from nonviscous photo-crosslinkable inks. Advanced Materials. **29**, 1604983.

Ozbolat, I. T. and Hospodiuk, M. (2016). Current advances and future perspectives in extrusion-based bioprinting. Biomaterials. **76**, 321-343.

Pahoff, S., Meinert, C., Bas, O., Nguyen, L., Klein, T. J. and Hutmacher, D. W. (2019). Effect of gelatin source and photoinitiator type on chondrocyte redifferentiation in gelatin methacryloyl-based tissue-engineered cartilage constructs. Journal of Materials Chemistry B. **7**, 1761-1772.

Pepelanova, I., Kruppa, K., Scheper, T. and Lavrentieva, A. (2018). Gelatin-Methacryloyl (GelMA) Hydrogels with Defined Degree of Functionalization as a Versatile Toolkit for 3D Cell Culture and Extrusion Bioprinting. Bioengineering. **5** (3), 55.

Priola, A., Gozzelino, G., Ferrero, F. and Malucelli, G. (1992). Properties of polymeric films obtained from u.v. cured poly(ethylene glycol) diacrylates. Polymer. **34** (17), 3653-3657.

Shi, W., He, R. and Liu, Y. (2015). 3D printing scaffolds with hydrogel materials for biomedical applications. European Journal of BioMedical Research. **1** (3), 3.

Shirahama, H., Lee, B. H., Tan, L.P. and Cho, N. -J. (2016). Precise Tuning of Facile One-Pot Gelatin Methacryloyl (GelMA) Synthesis. Scientific Reports. **6**, 31036.

Song, W., Tang, Y., Qiao, J., Li, H., Rong, B., Yang, S., Wu, Y., and Yan, X. (2017). The comparative safety of genipin versus UVA-riboflavin crosslinking of rabbit corneas. Molecular vision. **23**, 504–513.

Subramanian, A., Krishnan, U.M. and Sethuraman, S. (2009). Development of biomaterial scaffold for nerve tissue engineering: Biomaterial mediated neural regeneration. Journal of Biomedical Science. **16**, 108–118.

Van Den Bulke, A. I., Bogdanov, B., De Rooze, N., Schacht, E. H., Cornelissen, M. and Berghmans, H. (2000). Structural and Rheological Properties of Methacrylamide Modified Gelatin Hydrogels. Biomacromolecules. **1**, 31-38.

Wagner, A. and Ehlers, W. (2008). A porous media model to describe the behaviour of brain tissue. Proceedings in Applied Mathematics and Mechanics. **8** (1), 10201–10202.

Wang, Z., Jin, X., Dai, R., Holzman, J. F. and Kim, K. (2016). An ultrafast hydrogel photocrosslinking method for direct laser bioprinting. RSC Advances. **6**, 21099–21104.

World Health Organization. (2002). Projection of Mortality and Burden of Disease to 2030: Deaths by Income Group. Geneva: World Health Organization.

Yue, K., Trujillo-De Santiago, G., Mois Es Alvarez, M., Tamayol, A., Annabi, N. and Khademhosseini, A. (2015) Synthesis, properties, and biomedical applications of gelatin methacryloyl (GelMA) hydrogels. Biomaterials. **73**, 254–271.

Zhang, A. P., Qu, X., Soman, P., Hribar, K. C., Lee, J. W., Chen, S. and He, S. (2012). Rapid Fabrication of Complex 3D Extracellular Microenvironments by Dynamic Optical Projection Stereolithography. Advanced Materials. **24** (31), 4266-4270.

Zhao, T., Zhang, H., Zhou, D., Gao, Y., Dong, Y., Greiser, U., Taic, H. and Wang, W. (2015). Water soluble hyperbranched polymers from controlled radical homopolymerization of PEG diacrylate. RSC Advances. **5**, 33823-33830.

CHAPTER 4
DESIGN, FABRICATION and NEURAL COMPATIBILITY OF THE 3D PRINTED BIOMATERIAL ARTIFICIAL EXTRACELLULAR MATRIX SCAFFOLDS UITILISING THE INTEPENETRATING POLYMER NETWORK APPROACH

4.1 Introduction

The homeostasis of the Extracellular Matrix (ECM) in the body is vital for the biological functioning of any living tissue. Furthermore, for optimal tissue functioning, the interplay of the various ECM components with the cells and surrounding capillaries to maintain the homeostatic balance, is therefore specific for the given tissue (Bonnans *et al.,* 2014; Schoen and Mitchell, 2004). To achieve this, an important feedback loop exists between the ECM and the resident cells of the tissue. The resident cells secrete and establish the versatile ECM network whereas the ECM then in turn influences the biology of the cells by controlling amongst others their migration, survival, differentiation and proliferation (Humphrey *et al.,* 2014). Through this loop, the ECM plays a crucial role in the regulation of repair and regeneration after physiological ECM degradation and most importantly, after injury (Lu *et al.,* 2011). With this in mind, it is no surprise that ECM dysregulation is implicated in several disease and injury states, as with TBI, since the ECM is remodelled in response to various stimuli (Schoen and Mitchell, 2004). Stimuli induced changes to the ECM include but are not limited to: changes to tissue stiffness, inflammation and fibrosis (Sonbol, 2018). Due to the uniqueness of the ECM in native biological tissues, developing the “ideal” bioink has proven to be difficult in the application of 3D printing for the tissue engineering field, as discussed in Chapter 3. Despite the many achievements in this field, a single bioink has yet to exhibit properties to be a potential universal bioink for any tissue requiring replacement.

As tissue engineering explores the usage of materials to produce 3D scaffolds to mimic the native microenvironment, it is no surprise that the formation of artificial Extracellular Matrix (aECM) hydrogel systems, formed by aqueous networked polymeric chains, incorporating native ECM material constituents has generated a lot of interest (Da Silva *et al.,* 2020; Kim *et al.,* 2016). Hydrogel systems have been shown to exhibit similar tuneable characteristics to the native *in vivo* extracellular matrix (ECM) microenvironments (Lei and Wu, 2018; Lu *et al.,* 2019). Furthermore, in the fabrication of these hydrogel systems, natural materials are generally a first-choice selection due to their favourable advantages over their synthetic counterparts. Most of the native ECM materials utilised in the fabrication of aECM hydrogel scaffolds are manufactured from connective tissue ECMs, making the materials deformable and fibre-reinforcing matrix composites, ideal for tissue engineering approaches (Yannas,

2004). Furthermore, natural materials are advantageous for biomaterial incorporation since they are able to be degraded by tissue specific enzymes, providing a foreseeable “guarantee” the fabricated implant will be metabolised/degraded through physiological mechanisms. In addition, this property ensures the implant is able to provide the necessary function for the required time before being naturally removed (Yannas, 2004). In spite of the benefits, natural materials exhibit drawbacks (poor printability, batch variation, immunogenicity etc.) (Caliari and Burdick, 2016) that has hindered the progression of material development for TBI (Malda *et al.,* 2013; Parak *et al.,* 2018; Rutz *et al.,* 2015). In response, biomaterial blends and material functionalization have assisted in the reversal of such shortcomings to produce materials with cell binding domains and ECM motifs as well as tissue specific mechanical strength, degradation, pore size and architecture amongst others (Shao *et al.* 2015).

Gelatin Methacryloyl (GelMA) is an example of a semi-synthetic, gelatin functionalized hydrogel polymer that has retained its “ECM-like” features. GelMA is a readily mechanically tuneable, UV/chemically crosslinkable and versatile polymer utilized in several tissue engineering applications (Zhang *et al.,* 2019; Zheng *et al.,* 2018). In addition, GelMA is attractive as despite the functionalization process, the polymer retains its arginine-glycine-aspartic acid (RGD) sequences as well as several Matrix Metalloproteinase (MMP) target sequences that are important for cell attachment and ECM remodelling, respectively (Yue *et al.,* 2015). Furthermore, GelMA can be considered a smart polymer, since it responds to changes in environmental temperatures (Hoffmann, 2004). This feature makes GelMA extremely attractive for 3D printing applications. From this, it is evident why GelMA and several GelMA blends are emerging as potential treatments for several diseases and injuries due to the inherent benefits the material possesses.

A further consideration for tissue engineering biomaterials is the formation of Interpenetrating Polymer Network (IPN) systems. IPN systems are described as an elastomer-type polymer where two or more polymers (natural or synthetic) with individual characteristics coexist and are crosslinked in the presence of each other (Bhardwaj *et al.,* 2012; Jenkins *et al.,* 1996; Lohani *et al.,* 2014; Roland, 2013). As such, IPN systems are generating much interest as IPNs can be used to control, including but not limited to: swelling, elasticity, porosity and stimuli-responsive behaviour by modulating the proportion of crosslinking agents and polymers utilized (Archana *et al.,* 2012). As a broad distinction, IPNs can be classified as semi IPNs or full IPNs depending whether one or both polymers are crosslinked in the presence of the other, respectively (Roland, 2013). Several crosslinking agents are available to tailor and control the property of the designed IPN. From the previous Chapter, two mechanisms of crosslinking were explored namely UV crosslinking and chemical crosslinking to establish the

two potential IPNs. The UV-based crosslinking system, was incorporated to ensure the formation of the GelMA network (Van den Bulke *et al*., 2000). In addition, for the potential full IPN – Genipin, a natural and safe protein crosslinker (Manickam *et al.,* 2014; Song *et al.,* 2017) – was utilized to promote the formation of the peptide network in addition to the GelMA network. In addition to its crosslinking abilities, Genipin is reported to possess antimicrobial properties (Hong and Kim, 2007; Ishiguro *et al*., 1983; Koo *et al.*, 2006; Yamamoto *et al.,* 2000; Yamazaki and Chiba, 2005) and as such is widely utilised in various biomedical fields (Chu *et al.,* 2020; Khan *et al.,* 2016; Kim *et al.,* 2012; Yu *et al.,* 2015). Since a severe TBI may result in the development of a nosocomial infection, the development of a TBI treatment with antimicrobial properties is vital since the infection-related mortality rates may be as high as 28% (Boque et al., 2000; Dando *et al.,* 2014; Dziedzic et al., 2004). Therefore, in the context of this work, the incorporation of Genipin into a neurological 3D printed scaffold implant may prevent the growth of pathogens associated with post-surgical infections. Considering the above, it is therefore no surprise that IPNs utilising various crosslinking strategies are considered to be one of the worthy candidates for novel biomaterial development (Bhardwaj *et al.,* 2012).

Since a tissue engineering scaffold for TBI is required to adequately mimic various tissue properties including brain region strength, cellular function, tissue integration and tissue morphology, several tissue engineering approaches combining different engineering applications, stem cells, and materials have the potential to assist in developing novel biomaterials for the replacement of damaged tissues and organs in several tissue engineering applications (Yang *et al.,* 2018). Of the several approaches, 3D printing has evolved into an indispensable tool to fabricate intricate 3D scaffolds shapes (Hyder *et al.,* 2007) to mimic the native tissue in terms of cell placement (Armstrong *et al.,* 2016), bioactive cues (Tamayol *et al.,* 2015) and biomaterial selection (Nakamura *et al.,* 2010) for the required application (Yang *et al.,* 2018). As brain injuries are very rarely similar in pathophysiology, 3D printing can offer several advantages, such as intricate and precise structures as well as having the ability to produce personalized and customizable structured scaffolds (Da Silva *et al.,* 2019; Yang *et al.,* 2018) through the incorporation of the patient's cells (Mok *et al.,* 2016), in comparison to conventional tissue engineering approaches. In addition, for adequate tissue mimicry, scaffold archetype resolution has to be exceptional and therefore, 3D printing resolution for organ replacement is also starting to improve (Ventola, 2014).

This study, therefore, formulated two fibrous novel IPN systems that were optimized for 3D printing. To the best of our knowledge, this study provides one of the first completely protein-based IPN aECM scaffolds for potential tissue engineering applications. The material

properties were assessed for its bio-functionality using Fourier-Transform Infrared Spectroscopy (FTIR), Differential Scanning Calorimetry (DSC), X-ray Diffraction (XRD) and Scanning Electron Microscopy (SEM) as well as Viscoelastic and Real-time mechanical analysis in an artificial biological fluid. This study may provide a new perspective for tissue engineering through the 3D printing of IPN systems.

4.2 **Materials and Methods**

4.2.1 Materials

Gelatin (Bloom 160, Type B) derived from bovine skin was purchased from Fluka (Steinheim, Germany). Methacrylic anhydride (94 %) containing 2000 ppm topanol A, collagen derived from bovine Achilles tendon, Phosphate Buffered Saline tablets (pH 7.4), high retention cellulose dialysis tubing (MW cut off 12 400 Da), glacial acetic acid, acetone, Ciprofloxacin, DAPI and the radical photo initiator 2-Hydroxy-4′-(2-hydroxyethoxy)-2-methylpropiophenone (Irgacure 2959, MW 224.25 g/mol, purity 98 %) were purchased from Sigma Aldrich (St Louis, MI, USA). Genipin was purchased from Challenge Bioproducts CO., LTD. (Yun-Lin Hsien, Taiwan). Elastin derived from bovine neck ligament was purchased from Elastin Products Co., Inc (Owensville, MO, USA). Glycine (MW: 75.07 g/mol) was purchased from Merck (Merck KGaA, Darmstadt, Germany). DAPI and MitoTracker™ Orange was purchased from Thermo Fisher Scientific (Johannesburg, South Africa). *Staphylococcus aureus* (ATCC 25923), *Listeria monocytogenes* (ATCC 19111), *Escherichia coli* (ATCC 8379), *Pseudomonas aeruginosa* (ATCC 27853), *Klebsiella pneumoniae* (ATCC 13887) and *Serratia marcescens* (ATCC 14756) were obtained from Davies Diagnostics (Randburg, South Africa). Tryptone Soya Broth and Agar were obtained from Oxoid (Hampshire, United Kingdom). Artificial cerebrospinal fluid (aCSF) (pH 7.4) was chosen as the hydration microenvironment and prepared using the method by Baumann *et al.* (2010): 1.4mM CaCl2, 148mM NaCl, 1.5mM Na2HPO4, 0.2 mM NaH2PO4, 0.8mM MgCl2 and 3mM KCl. All chemicals were used as received and were of an analytical grade.

4.2.2 Synthesis of the Neuro-Platform

4.2.2.1 Synthesis of Gelatin Methacryloyl (GelMA)

GelMA was synthesized as previously detailed in Chapter 3. The degree of substitution and functionalization of the lysine residues in the GelMA polymer was determined in the previous Chapter.

4.2.2.2 Preparation of the Semi IPN 3D printed Biomaterial Hydrogel

To prepare the semi IPN hydrogel, 0.5% collagen solution was heated to 37 °C under constant stirring. Under dark conditions, 10% GelMA, 1% elastin and 0.5 % Irgacure 2959 was added

to the peptide mixture and rapidly mixed until homogenous. The stirring speed was reduced for one hour to mitigate excess foam formation. Following this the biomaterial was placed into a UV chamber set to 365 nm and exposed to UV light for 2 minutes for GelMA crosslinking. The biomaterial was placed at -80 °C for 24 hours and then lyophilized for 24 hours. Samples were stored at -20 °C until used.

4.2.2.3 Preparation of the Full IPN 3D printed Biomaterial Hydrogel

Under constant stirring at 37 °C, the full IPN hydrogel was prepared by allowing 0.5% collagen solution, 1% elastin, 10% GelMA and 1% Genipin to chemically crosslink for 2 hours at 37 °C. This ensured that the collagen and elastin fibres would form a network in the presence of the GelMA polymer to meet the requirement for the formation of a full IPN. Under dark conditions, 0.5 % Irgacure 2959 was then added to the mixture and rapidly mixed until homogenous. The stirring speed was reduced for one hour to mitigate excess foam formation. Following this the biomaterial was placed into a UV chamber set to 365 nm and exposed to UV light for 2 minutes for GelMA crosslinking. The biomaterial was placed at -80 °C for 24 hours and then lyophilized for 24 hours. Samples were stored at -20 °C until used.

4.2.3 3D printing of the IPN Biomaterial Hydrogel Scaffolds

A standard rectilinear scaffold structure (0-90 ° cross hatch), 10x10 mm with varying heights, was designed using the Magics® V18 design software. The two different IPN biomaterial formulations were prepared as stated above and were then individually loaded into an amber barrel (30cc), Low Temperature Dispensing Head (30 ml) extrusion printing cartridge due to the photosensitive nature of the Irgacure 2959. Using a standard Envisiontec 3D Bioplotter (Envisiontec GmbH, Gladbeck, Germany), the temperature of the printing head was then reduced to 18 °C, the cartridges were then loaded and the cartridge was kept at 18 °C for 30 minutes to allow the material to reach 18 °C (material temperature equilibration). This allowed the biomaterial to approach gelation. The IPN biomaterial scaffolds were then printed onto a cold platform through a 0.2 mm bore precision tip needle at a predetermined pressure and speed. After completion of the printing, the scaffold was immediately placed into a UV chamber set to 365 nm and exposed to UV light for 2 minutes. The scaffolds were then placed at -80 °C for 24 hours and then lyophilized for 24 hours. Scaffolds were stored at -20 °C until used.

4.2.4 Physiocochemical Characterisation of the 3D Printed IPN Biomaterial Hydrogel Scaffolds

4.2.4.1 Analysis of the Molecular Vibrational Transitions of the 3D Printed IPN Biomaterial Hydrogel Scaffolds

The Fourier-Transform Infrared Spectroscopy (FTIR) spectra of the lyophilized biomaterials and pristine polymers were analyzed using a PerkinElmer Spectrum 2000 ATR-FTIR (PerkinElmer100, Wales, UK) to identify molecular transitions and interactions. The FTIR conditions were set as follows: wave range 4000-650 cm-1, 20 scans per spectrum with a resolution of 4 cm-1. The spectrometer was fitted with a diamond, single-reflection MIRTGS detector.

4.2.4.2 Thermophysical Characterisation of the 3D Printed IPN Biomaterial Hydrogel Scaffolds

The thermal properties of the lyophilized biomaterials, GelMA and pristine peptides were analyzed using a Differential Scanning Calorimeter (DSC) (Mettler Toledo DSC, STARe system, Swchwerzenback, Switzerland). The samples (between 3-10 mg) were sealed in aluminium crucibles and a small hole was pierced into the crucible lid to allow for pressure dissipation. Samples were subjected to two cycles of heating at a rate of 10 °C/minute under constant Nitrogen gas: (1) 0-125 °C to allow for the molecular water to be released and (2) 0-300 °C for analysis. The thermograms were then plotted as heat flow against temperature. Determining the percentage weight change as a function of temperature was performed using a Thermogravimetric analyzer (TGA) (PerkinElmer, TGA 4000, Llantrisant, Wales, UK). Samples were heated at a rate of 10˚C/min from 30-900˚C under continuous nitrogen purging. Thermograms were generated as percentage weight vs. temperature.

4.2.4.3 Crystallinity of the 3D Printed IPN Biomaterial Hydrogel Scaffolds

Due to the static nature of the GelMA polymer, the lyophilized sponges of the biomaterials as well as the GelMA polymer were first flattened and then cut into a circular shape using steel equipment (to reduce interfering fibres) to mimic the shape of the sample holder. The peptides were also analyzed in powder form. All material was fixed to the sample holder using double-sided tape. The phases and crystallinity of the samples were then determined using a benchtop Rigaku MiniFlex 600 X-ray diffractometer (Rigaku, Japan) with CuKα radiation at 15 mA and 40 kV. The parameters were as follows: 2θ range between 5-60 degrees at a scan rate of 5 degrees/minute.

4.2.5 Physicomechanical Characterisation of the 3D Printed IPN Biomaterial Hydrogel Scaffolds

4.2.5.1 Viscoelastic properties and Real-Time Material Stiffness Assessments of the 3D Printed IPN Biomaterial Hydrogel Scaffolds

The IPN hydrogels were prepared (without crosslinkers) as stated above and subsequently cooled to 20 °C on an ice bath. The viscoelastic properties of each IPN hydrogel was assessed using the Elastosens™ Bio (Rheolution, Montreal, Canada). In brief, following the instrument system calibration, 4 ml of the biomaterial (20 °C) was syringed into the sample holders and then placed into the thermal chamber for analysis. The analysis was performed for 4 hours at a constant temperature of 10 °C with a soak time and temporal step of 30.0 seconds. All samples were performed in triplicate (n=3).

To assess the soft mechanical properties, a novel real-time experiment was conducted in two ways, whereby lyophilized disks of the biomaterial (n=3) were (1) placed in the sample holders and 2 ml aCSF was placed over the disks and the material stiffness during hydration (G') was monitored for 8 hours at 25 °C and (2) lyophilized disks of the IPN systems were placed in the sample holders and 2 ml aCSF was placed over the disks and samples were allowed to swell to saturation for 8 hours prior to analysis and the material stiffness (G') was monitored for 8 hours at 25 °C. The soak time and temporal step was the same as for the viscoelastic studies.

4.2.6 Morphological Analysis of the 3D Printed IPN Biomaterials Hydrogel Scaffolds

4.2.6.1 Scanning Electron Microscopy for the Mapping of Surface Morphology of the 3D Printed IPN Biomaterial Hydrogel Scaffolds

Scanning Electron Microscopy (SEM) and Energy Dispersive Spectroscopy (EDS) analysis was performed on both IPN systems using the Zeiss Sigma 03-39 Field Emission Scanning Electron Microscope (Zeiss, Oberkochen, Germany) with an accelerating voltage of 0.02 to 30 kV. Prior to analysis, 3D printed scaffolds were mounted, using double sided tape, onto aluminium stubs and coated with two coats of gold palladium (AuPd) coating.

4.2.7 Architectural Performance of the 3D Printed IPN Biomaterials Hydrogel Scaffolds

4.2.7.1 Degradation, Fluid Uptake and Swelling Studies

Material hydration due to fluid uptake and degradation was performed on both IPN biomaterials under simulated in vitro conditions. The IPN biomaterials were prepared as above. Briefly, 1 ml of the material was placed into each well of a 48-well plate, crosslinked, frozen at -80 ° C and lyophilized for 24 hours. The disk was then removed and placed in a 24-well plate (n=5) with 2 ml of aCSF. The plate was then placed into an orbital shaking incubator (LM-530-2, MRC Laboratory Instruments Ltd., Holon, Israel) set at 37 ° C and 25 rpm for 8

hours. Swelling equilibrium was reached within the 8 hours where excess fluid was blotted before measurement. The mass swelling ratio, fluid uptake and degradation were calculated using Equation 1, 2 and 3, respectively.

$$Mass\ Swelling\ Ratio = \frac{Ws}{Wi} \quad \text{Equation 4.1}$$

$$\%\ Fluid\ Uptake = \frac{(Ws-Wi)}{Wi}\ x\ 100 \quad \text{Equation 4.2}$$

$$\%\ Degradation = \frac{(Wi-Wd)}{Wi}\ x\ 100 \quad \text{Equation 4.3}$$

Where Ws, Wi and Wd are the swollen blotted mass, dry initial mass and the post dry mass of the IPN biomaterials, respectively.

4.2.8 *In vitro* cell analysis of the 3D Printed IPN Biomaterials Hydrogel Scaffolds

4.2.8.1 PC12 Cell culture and MTT proliferation assay

Adherent rat adrenal gland pheochromocytoma PC12 cell line from Cellonex (Separations, South Africa) was cultured in tissue culture treated (TPP) T-75 flasks using DMEM supplemented 5%v/v FBS and 1%v/v P/S/AB solution in a humid 5% CO_2 atmosphere at 37˚C. The culture medium was replaced every 2 days.

For the detection of cell proliferation and cytocompatibility of the 3D printed scaffolds, the MTT-based Roche Cell Proliferation Kit I was utilised. IPN scaffold were prepared as above, however before UV crosslinking, the hydrogels were washed several times in 0.5% acetic acid and then capped in 2% glycine for 15 minutes to prevent ketone cytotoxicity from the exposed ketone groups on the radical crosslinker. Samples of size 1cm×1cm×1cm were sterilized under UV light (256 nm) for 12 hours before overnight incubation with cells in 100µL culture medium containing 5%v/v Fetal Bovine Serum (FBS) and 1%v/v P/S/AB (Penicillin/Streptomycin/Amphotericin B) in a 96-well plate maintained at 37˚C at 5% CO_2. PC12 cells were seeded into the 96-well plate at a density of 7.5×10^2 cells/well and incubated for 24, 48 and 72 hours. Thereafter, the culture medium was removed and each well was washed once with PBS before 100µL culture medium was returned to each well. Following this, 12 µL MTT solution was added to each well followed by a further 4-hour incubation period after which the culture medium was removed and 100µL solubilising agent was added to dissolve the formazan crystals. The 96-well plate was then measured for absorbance at 570nm, with a background subtraction at 690nm, using a multiplatereader (BioTek, USA).
Relative cell viability was calculated as follows:

$$Cell\ Viability\ (\%) = \frac{A_{Sample}}{A_{Positive\ Control}} \text{ x } 100 \qquad \text{Equation 4.4}$$

Where A_{sample} is the absorbance of the treated cells and $A_{positive\ control}$ is the absorbance of the positive control (absence of treatment).

4.2.8.2 Evaluation of Nuclear Morphology and Migration in response to 3D printed scaffolds

A leachable and extractables assay was performed to assess the nuclear morphological response of PC12 cells to the extracted components (chemical cues) of the IPN scaffolds over a period of 24 hours. This would give an indication if the cells are able to flourish in the absence of physical cues (the physical scaffold for anchorage etc). Briefly, the both IPN scaffolds were weighed out to a concentration of 0.02g/mL of media, sterilised overnight (265 nm) and then mixed with growth media and incubated at 37 ˚C for one hour. After the one-hour leach time point, any residual scaffolds were removed from the media and the resulting solution was filtered to remove any particulate matter. The PC12 cells were seeded at a density of 1×10^3 cells/well into a 96-well plate in 100µL culture medium containing 5%v/v FBS and 1%v/v P/S/AB and left to attached overnight at 37˚C at 5% CO_2 in a humid incubator. The culture medium was then aspirated off and the cells were treated with the filtered solution for 24 hours at 37˚C at 5% CO_2 in a humid incubator. Following this, the filtered solution was removed, the cells were washed twice with PBS and then 100µL culture medium containing 300 nM MitoTracker™ Orange was placed in each well and left to incubate for 45 minutes at 37˚C at 5% CO_2 in a humid incubator. The media was then removed and the all wells were washed with PBS to remove any unbound MitoTracker™ Orange. The cells were then fixed with 5% formaldehyde in PBS for 20 minutes. The cells were then incubated with 1 µg/mL solution of DAPI for 15 minutes. The cells were washed several times with PBS to remove unbound DAPI and reduce the fluorescence of the background. Plates were kept in the dark until analysis. Plates were analyzed on the Logos Biosystem CELENA® X High Content Imaging System and analyzes were performed using their proprietary software. Using the Logos Biosystem software, a pipeline was set up to determine the nuclei count, eccentricity and area. The following definitions were used:

- Eccentricity = ratio of the distance between the foci of the ellipse and its major axis length.
- Area = The number of pixels in the region.

For the migration assessment, the PC12 cells were prepared as follows. IPN scaffold samples of size 10x10x10 mm were sterilized under UV light (256 nm) for 12 hours before overnight

incubation in 100µL culture medium containing 5%v/v FBS and 1%v/v P/S/AB in a 96-well plate maintained at 37˚C at 5% CO_2. PC12 cells were seeded into the 96-well plate at a density of 1×10^3 cells/well and incubated for 24 hours. Thereafter, the culture medium was removed and each well was washed once with PBS and then were fixed with 5% formaldehyde in PBS for 20 minutes. The cells were then incubated with 1 µg/mL solution of DAPI for 15 minutes. The cells were then washed several times with PBS to remove unbound DAPI and reduce the fluorescence of the background. Plates were kept in the dark until analysis. Plates were analyzed on the Logos Biosystem CELENA® X High Content Imaging System and analyzes were performed using their proprietary software. Using the Logos Biosystem software, a different pipeline was established to perform a Z-stack of the 3D printed scaffolds. In this way, multiple planes along the Z-stack were captured in an attempt to monitor if cellular migration had occurred.

4.2.9 Antimicrobial Activity of Genipin

4.2.9.1 Culture Preparation

All cultures that were used are laboratory reference strains of the American Type Culture Collection (ATCC) that were available in the Department of Pharmacy and Pharmacology, University of the Witwatersrand, Johannesburg. The micro-organisms that were selected for this study due to their implication in brain infections are *Staphylococcus aureus* (ATCC 25923) and *Listeria monocytogenes* (ATCC 19111) which are Gram-positive strains, and *Escherichia coli* (ATCC 8379)*, Pseudomonas aeruginosa* (ATCC 27853)*, Klebsiella pneumoniae* (ATCC 13887) and *Serratia marcescens* (ATCC 14756) which are Gram-negative strains. Tryptone Soya Broth (TSB) was used to culture the bacteria, which was incubated at 37 °C for 24 hours.

4.2.9.2 Antimicrobial Studies

The first step of this study was to perform a Minimum Inhibitory Concentration (MIC) assay. Unfortunately, due to the deep blue colour produced by the Genipin, visualisation of the MIC value was not always possible and therefore, reliance of the next step, the Minimum Bactericidal Concentration (MBC) assay values had to be recorded to determine antimicrobial activity. The MIC is defined as the lowest concentration required to inhibit the growth of bacteria. Genipin at a stock concentration of 160 mg/ml, the semi IPN scaffold and full IPN scaffold were dissolved in a 50:50 acetone: water solvent as the preparation of the test samples. The 96-well micro-titre plate was aseptically prepared by adding 100 µL sterile TSB into each well after which, Genipin was added (100 µl) to the first row of the well plate and a serial doubling dilution was performed to achieve the following concentrations: 40, 20, 10, 5, 2.5, 1.25, 0.63 and 0.13 mg/ml. Ciprofloxacin (10 µg/ml stock concentration) was used as the positive control to confirm the susceptibility of the test micro-organism. The negative control

for the plates was the 50:50 acetone: water mix to confirm that the solvent was not responsible for any antimicrobial activity observed. A culture control was included to ensure the broth supports microbial growth. The inoculum was obtained by preparing a 1:100 dilution of the 0.50 McFarland's Standard into TSB to achieve an approximate concentration of 1 x 10^6 colony forming units per millilitre (CFU/ml) and 100 µl of the inoculum was added to each well. The plates were then sealed and incubated at 37 °C for 24 hours. After incubation, 40 µl of a 0.40 % p-Iodonitrotetrazolium (INT) indicator solution was added to all wells to screen for microbial growth (a colour change from clear to pink indicates presence of growth). The MIC value was interpreted as the lowest concentration demonstrating a visually clear well without colour (Johnston *et al.,* 2013). All tests were performed in triplicate. The Minimum Bactericidal Concentration (MBC) is defined as the lowest concentration of antimicrobial agent required to kill a micro-organism. After the MIC assay, an MBC assay was conducted due to the staining of the Genipin, which did not always allow for visual interpretation of the MIC value. A loop-full of the sample from each well of the Genipin and positive control columns at all concentrations were streaked onto subdivided Tryptone Soya Agar (TSA) plates. The plates were then incubated at 37 °C for 24 hours. Bactericidal activity was indicated by the complete absence of growth on the agar plate. MBC values ≤10 mg/ml was recorded as important activity as this was the concentration (10 mg/ml) incorporated into the 3D printed full IPN scaffold itself.

4.3 Results and Discussion

Two GelMA, collagen, and elastin IPN hydrogels were successfully 3D printed. Geometrically macroporus, equiangular equilateral quadrilateral scaffolds were obtained which maintained their shape after UV crosslinking and lyophilisation (**Figure 4.1**). After rehydration the scaffolds maintained their 3D fabricated internal structure, however care was taken during handling due to the soft nature of the biomaterial.

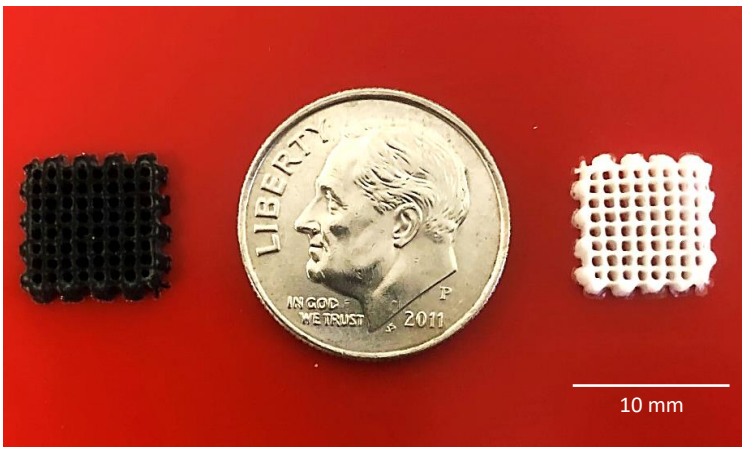


Figure 4.1: Visual representation and relative size of (a) the full IPN and (b) the semi IPN.

4.3.1 Molecular Vibrational Transitions and Thermodynamic Analysis Confirming the Formation of Different 3D Printable IPN Biomaterial Hydrogel Scaffolds

The FTIR spectrum of GelMA showed characteristic wavenumber bands at 3289 cm^{-1} (NH stretching), 2938 cm^{-1} (CH stretching), 1538 cm^{-1} (Amide II) and an Amide III bond present at 1238 cm^{-1}. These functional groups are from the gelatin moiety of the GelMA product. In addition, a wavenumber band at 3112 cm^{-1} (CH stretching at the CH_2 group) and at 1046 cm^{-1} (C-O-C stretching) are from the methacrylic anhydride moiety contribution during GelMA synthesis. Furthermore, no C=O groups are present in the GelMA spectrum from the methacrylic anhydride as this group is lost as an unsaturated methacrylic acid during synthesis. In addition, there is a characteristic wavenumber band at 1628 cm^{-1} indicative of the Amide I (C=O) bond which has formed between the gelatin and methacrylic anhydride during the synthesis reaction (**Figure 4.2**). The FTIR spectra further confirmed the successful synthesis of the GelMA polymer, which are in agreement with observations in literature (Resmi, 2012) and the ^1H NMR performed in Chapter 3.

For the following analysis, the following wavenumber bands will be monitored: Amide A, Amide B, Amide I, Amide II, and Amide III. The characteristic Amide wavenumber bands in the collagen peptide were detected at 3289 cm^{-1} (Amide A; N-H stretching vibration), which is indicative of hydrogen bonding between the N-H groups. In addition, a wavenumber band at 2926 cm^{-1} (Amide B; asymmetric stretching of CH_2), 1628 cm^{-1} (Amide I; C=O stretching vibrations), 1547 cm^{-1} (Amide II; N-H bending vibrations), and 1237 cm^{-1} (Amide III; C-H stretching) were also detected. The elastin FTIR spectrum showed the corresponding Amide bands at 3265 cm^{-1} (Amide A), 2962 cm^{-1} (Amide B), 1627 cm-1 (Amide I), 1517 cm^{-1} (Amide II), and 1239 cm^{-1} (Amide III). The presence of the Amide I wavenumber band is a marker used in the detection of the peptide secondary structure (Nagai, 2010).

In the absence of any crosslinking agents, the GelMA, collagen, and elastin formulation (denoted GCE, acting as the blank formulation for this analysis) produced the following wavenumber bands: 3300 cm^{-1} (Amide A), 2929 cm^{-1} (Amide B), 1630 cm^{-1} (Amide I), 1529 cm^{-1} (Amide II) and 1229 cm^{-1} (Amide III) (**Figure 4.2**). From these results it is evident that in the absence of crosslinking agents, small shifts in the wavenumber occur in the GelMA polymer and the two peptides indicating that homogenous mixing occurred during the formulation resulting in the overlapping of the relevant wavenumber bands. Furthermore, these small shifts could indicate that there could be molecular water associated with the peptides when networked in the GelMA (Kotanen *et al.,*2013) or from batch variation as all hydrogels are composed of proteins.

In terms of the IPN biomaterial hydrogels, the semi IPN (presence of Irgacure 2959 only) had characteristic wavenumber bands at 3289 cm^{-1} (Amide A), 2937 cm^{-1} (Amide B), 1634 cm^{-1} (Amide I), 1532 cm^{-1} (Amide II) and 1238 cm^{-1} (Amide III). The full IPN (presence of Irgacure 2959 and Genipin) had characteristic wavenumber bands at 3297 cm^{-1} (Amide A), 2936 cm^{-1} (Amide B), 1630 cm^{-1} (Amide I), 1535 cm^{-1} (Amide II) and 1235 cm^{-1} (Amide III) (**Figure 4.2**). For both IPN biomaterials in comparison to the blank formulation (GCE), particularly the Amide B, Amide II and Amide III bands had small shifts in their wavenumber possibly due to the addition of the crosslinkers (presence of -OH functional groups in both crosslinkers), a stronger molecular water association could be present. Furthermore, it is evident that the two minutes of UV exposure required for polymer photo-crosslinking does not affect the main Amide peaks of the biomaterial IPN systems as the Amide bands are still intact with similar transmittance intensities. Therefore, no alteration to the peptide primary structure was noted. Due to the similarities in the profiles, it was further established that the presence of the crosslinking agents did not impede the peptides from assuming a native conformation through native self-assembly. Since the peptide tertiary structure is dependent on the primary structure (Goldsack and Chalifoux, 1973), the proposal of the 'fibre floating in gel matrix' network design was confirmed. This was due to the fact that there was no hinderance in the peptides from assuming their native tertiary structure (no changes to primary structure) and interlocking mesh-like ECM network, as seen in native tissues (Bonnas *et al.,* 2014; Franz *et al.,* 2010).

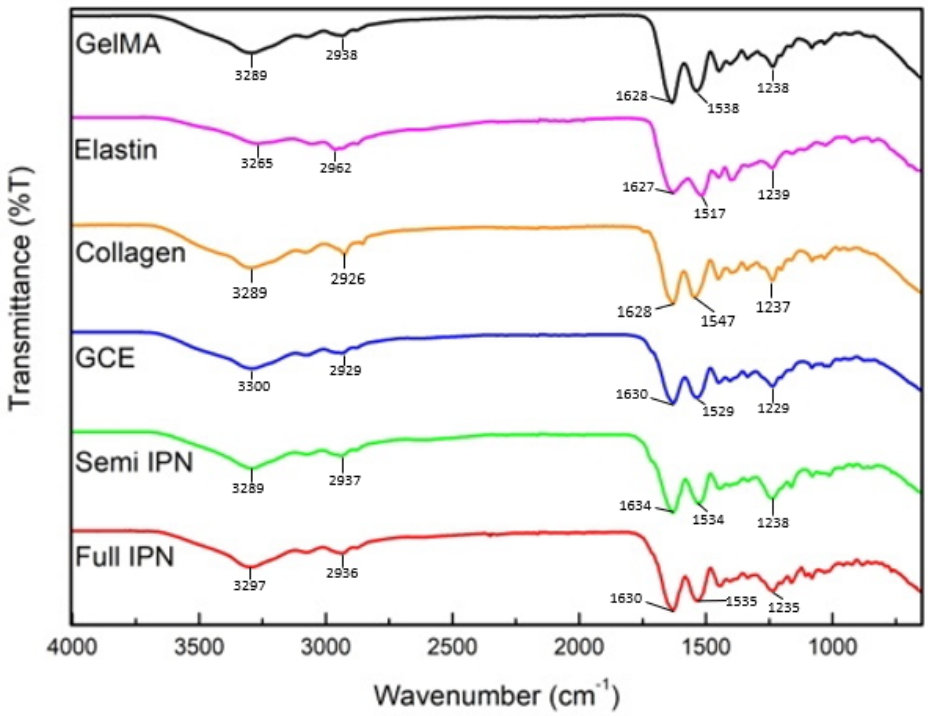
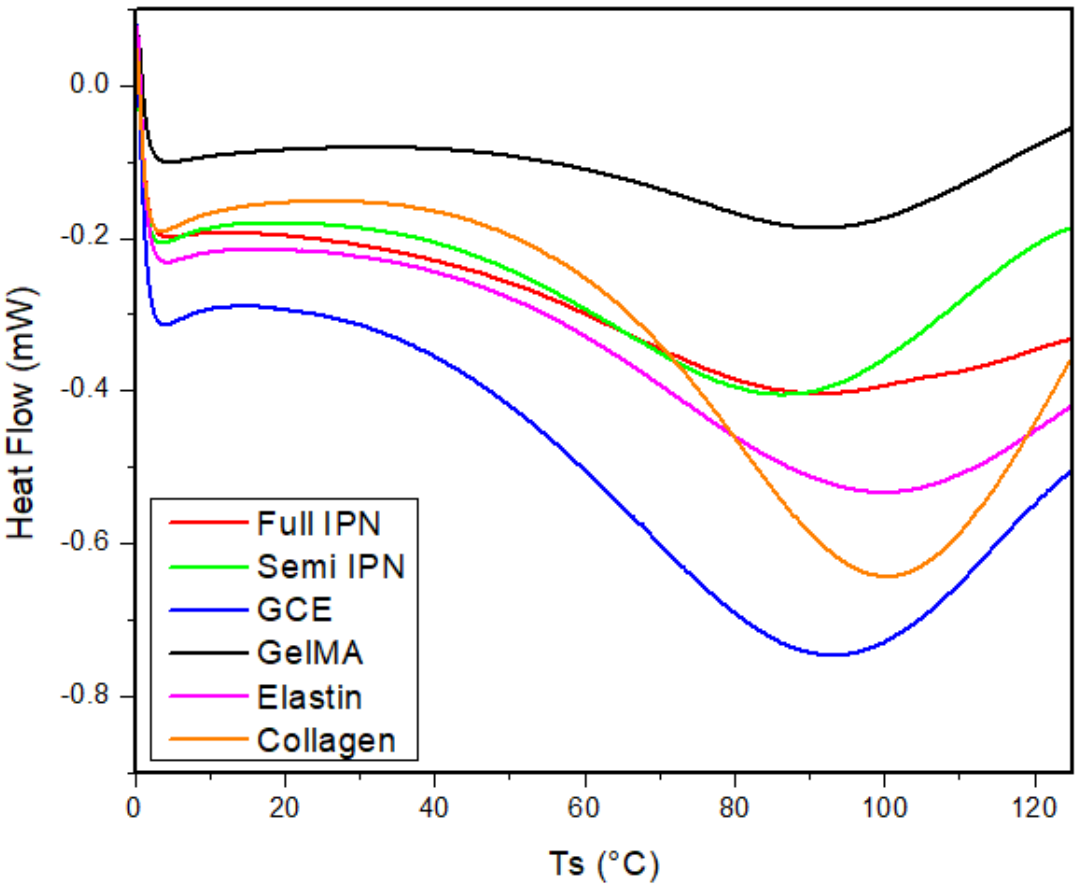


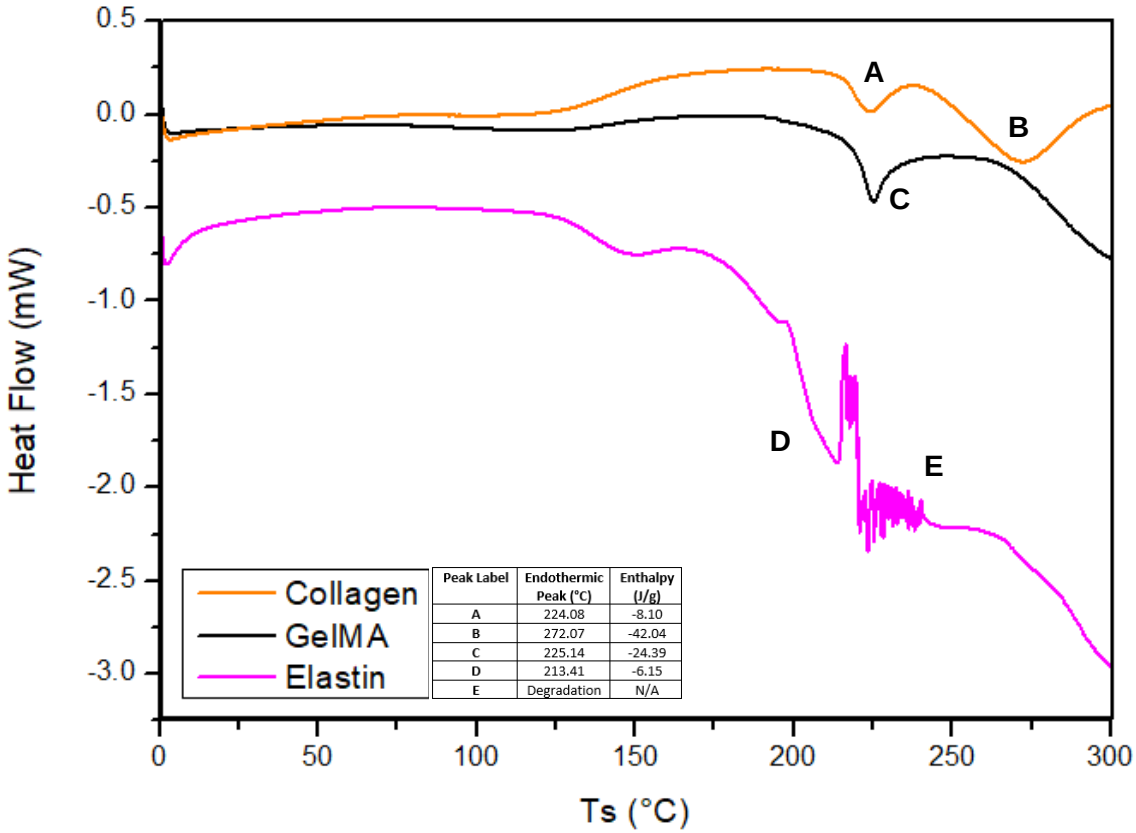
Figure 4.2: FTIR spectra of the comparison between the starting material and the two IPN biomaterials. From the spectra, it is evident that, despite the small wavenumber band shifts, the addition of the crosslinking agents had no effect on the appearance of the spectra.

All starting materials exhibited a broad peak during the first thermogram from 0-125 °C (**Figure 4.3a**) signifying the release of molecular water due to the rupturing of hydrogen bonds between the water molecules and the proteins around 100.5 °C, 100.2 °C and 90.6 °C for collagen, elastin and GelMA, respectively (Bozec and Odlyha, 2011; Samouillan *et al.,* 2004). Considering the second DSC thermograms in **Figure 4.3b**, collagen has two endothermic peaks at 224.08 °C (A) and 272.07 °C (B) signifying the conformational change and glass transition temperature from the triple helix structure to random coil and the bulk loss of mechanical integrity (degradation), respectively (Bozec and Odlyha, 2011; Lambri *et al.,* 2018; Samouillan *et al.,* 2011). GelMA has an endothermic peak at 225.14 °C (C) signifying the degradation of the gelatin matrix (Aldana *et al.,* 2017). Elastin has a thermal transition at 213.41 °C (D) signifying the transition from a glassy to a rubberier state (glass transition temperature: Tg) (Samouillan *et al.,* 2011) and the degradation of the elastin polymer is at (E). All starting materials have overlapping peaks around ~ 220 °C attributed to the peptide nature of all materials.

Considering the thermograms of the GCE (no crosslinkers present) and IPN systems, all systems had a broad peak around 94.0 °C, 93.8 °C and 95.1 °C for GCE, semi IPN and Full IPN, respectively, during the first DSC thermogram signifying the release of molecular water due to the rupturing of hydrogen bonds between the water molecules and the proteins (**Figure 4.3a**). This finding was expected as this feature is found in all thermograms of the starting materials. More crucial information was generated during the second thermogram where both IPN systems as well as the blend with no crosslinkers had a single endothermic peak at different temperatures. The endotherm was attributed to the denaturation of the peptide matrices. The endotherm peak of the GCE system, semi IPN and full IPN occurred at 183.60 °C (H), 140.59 °C (G) and 168.18 °C (F), respectively (**Figure 4.3c**). The GCE finding could potentially indicate that mixing the peptides with the polymer causes a decrease in the endothermic peak likely due to the penetration of the peptides into the GelMA network (Aldana *et al.,* 2017). Considering the IPN biomaterials, the full IPN system required more energy to break the bonds due to the presence of a double crosslinking mechanism. This melting point increase was attributed to increased thermal stability of the system (Bruylants *et al.,* 2005; Vera-Graziano *et al.,* 1995), which was used to confirm the formation of a full IPN for the double crosslinked system and a semi IPN for the single crosslinked system.

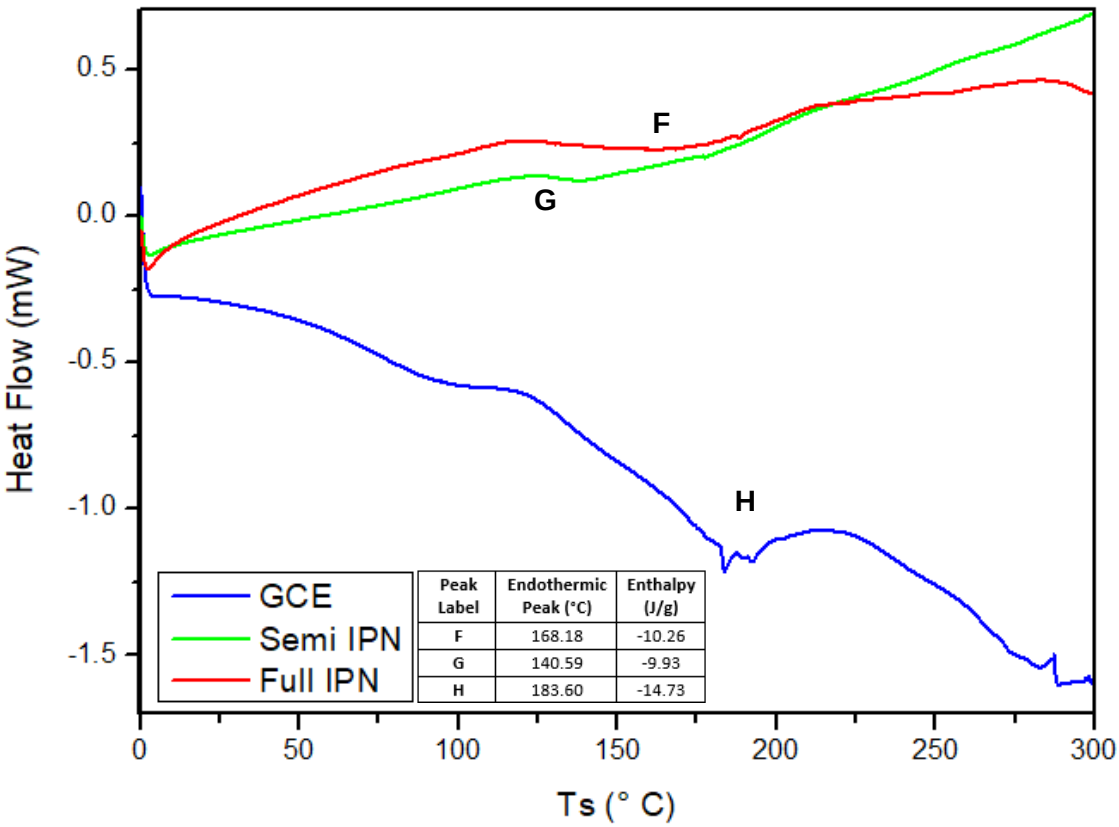


(a)



Peak Label	Endothermic Peak (°C)	Enthalpy (J/g)
A	224.08	-8.10
B	272.07	-42.04
C	225.14	-24.39
D	213.41	-6.15
E	Degradation	N/A

(b)



(c)

Figure 4.3: Differential Scanning Calorimetric analysis of the IPN Biomaterials. (a) DSC thermograms for all materials during the first run from 0-125 °C. (b) Indication of the thermal transitions of the starting materials and (c) indicates the thermal transitions of the semi and full IPN biomaterials as well as the biomaterial without any crosslinker (GCE).

The TGA thermograms (**Figure 4.4**) were then correlated with the thermal events obtained from the DSC thermograms. All TGA thermograms experience minimal loss of weight, occurring around 100 ˚C. This step correlates to the dehydration process and loss of the residual molecular water entrapped in the GelMA and peptide backbones in both the GelMA polymer and IPN scaffolds. Following this, the greatest loss of weight in the IPN scaffolds are observed, which was attributed to the degradation of the GelMA and peptide matrix in all samples. For the 3D printed IPN hydrogels, ~ 64% and ~ 67% loss of weight is observed for the semi IPN and full IPN, respectively. This loss of weight is observed between approximately 175 ˚C - 475 ˚C and approximately 200 ˚C - 500 ˚C for the semi IPN and full IPN, respectively. Since the DSC melting point endotherms of the IPN biomaterials were within 30 ˚C of each other, it is no surprise that the TGA thermograms present with a similar appearance between the two IPN hydrogels, with spectra that are close together (**Figure 4.4**). Despite this, there is a temperature shift between the two IPN systems. Furthermore, the DSC and TGA data correlate since there is a slight temperature shift towards a lower temperature for the semi IPN in comparison to the full IPN. This shift indicates that the protein stability in the semi IPN

is less than that of the full IPN and therefore, further confirms the formation of two IPN hydrogel systems.

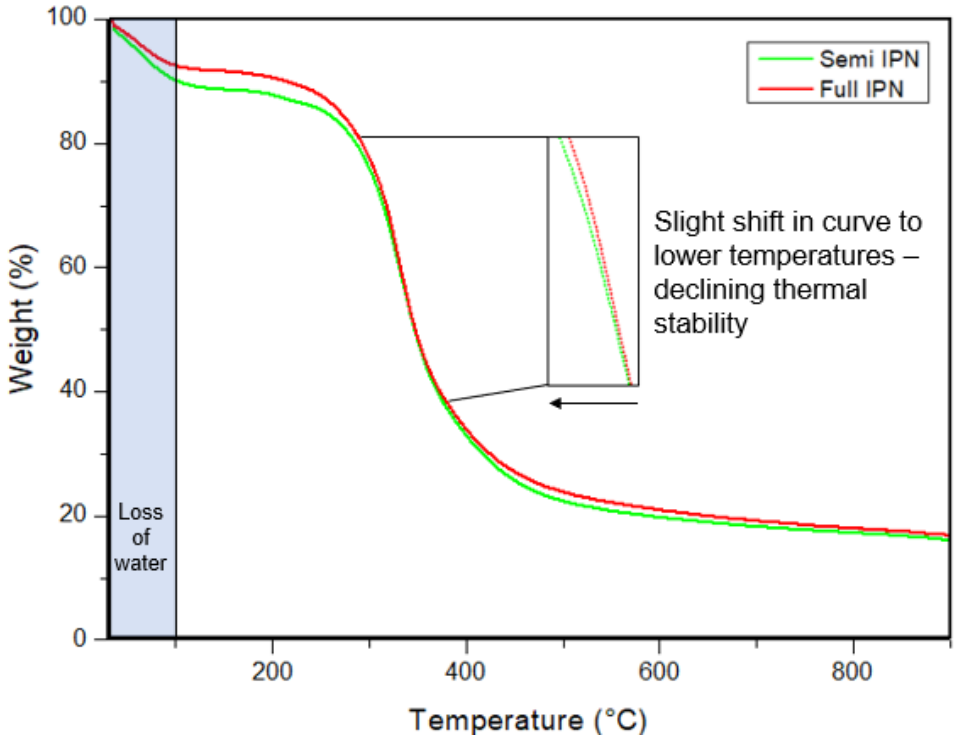


Figure 4.4: TGA thermograms depicting the weight changes as a function of temperature for GelMA, the semi IPN and full IPN hydrogels.

4.3.2 Confirmation of the amorphous nature of the 3D Printed IPN Biomaterial Hydrogel Scaffolds

The X-Ray diffractogram of the GelMA polymer exhibits a spectral profile very similar to that of gelatin, which was expected since the conjugated group (methacrylate group) is small in comparison to the gelatin backbone (Asma *et al.,* 2014; Ki *et al.,* 2005). Gelatin is reported to exhibit a crystalline structure originating from the presence of α-helices and triple-helical structures (Asma *et al.,* 2014; Ki *et al.,* 2005). Despite this crystallinity, during functionalization and formulation, the resulting GelMA polymer exhibits an amorphous structure (**Figure 4.5**). In terms of the X-ray diffractograms of collagen and elastin, both peptides are known to produce broad, amorphous peak pattens (Bailey, 1978; Liu *et al.,* 2015), which was confirmed in this study (**Figure 4.5**). Considering the blend without the presence of crosslinking agents (GCE), it is evident that the amorphous structure of the GelMA polymer is maintained over the 2Θ angle range (**Figure 4.5**). This trend was further noted for the semi and full IPN diffractogram patterns. This indicates that the addition of the peptides to the GelMA polymer does not affect the profile. Furthermore, despite the crystalline nature of the crosslinking agents (**Figure 4.5b and Figure 4.5c**), the crystallinity is lost in the IPN biomaterials. Lastly,

since all the spectra displayed a similar structure, no impurities were identified through the emergence of other peaks.

For the following analysis, only peaks around 20.00° was considered as this peak is largely indicative of the GelMA amorphous nature (Gu *et al.,* 2020). The amorphous nature of the samples was confirmed by the high Full Width at Half Maximum (FWHM) value of 12.3, 9.3, 7.82 and 7.67 obtained for the GelMA polymer, GCE, full IPN and semi IPN, respectively. A similar high FWHM was observed for both peptides. The FWHM is understood to indicate that the higher the value the broader the peak, the more amorphous/disordered the structure. Interestingly, over the 2Θ angle range all samples exhibited an amorphous halo, confirming the FWHM values as an indicator of a decrease in crystallinity. Despite all samples being amorphous, GCE, as well as both IPN biomaterials are considered to be more crystalline than the GelMA polymer due to the increase in the observed intensity. Furthermore, there was a notable difference in the intensities between the semi and full IPN biomaterial systems. This was attributed to the increase in crosslinking in the full IPN relative to the semi IPN, which induces an increase in the amorphous properties of the material (Nagaraj *et al.,* 2017). Also worthy of noting, the structure of the crosslinking agents is different and hence, could explain the intensity differences between the two IPN structures since the crystal structures between the crosslinkers differ (Hussein *et al.,* 2016). Furthermore, the crosslinking ratio is increased in the full IPN in comparison to the semi IPN and may further contribute to the decrease in the observed crystallinity (Hussein *et al.,* 2016). These results agree with the DSC and TGA findings and further confirm the formation of both a semi and full IPN system.

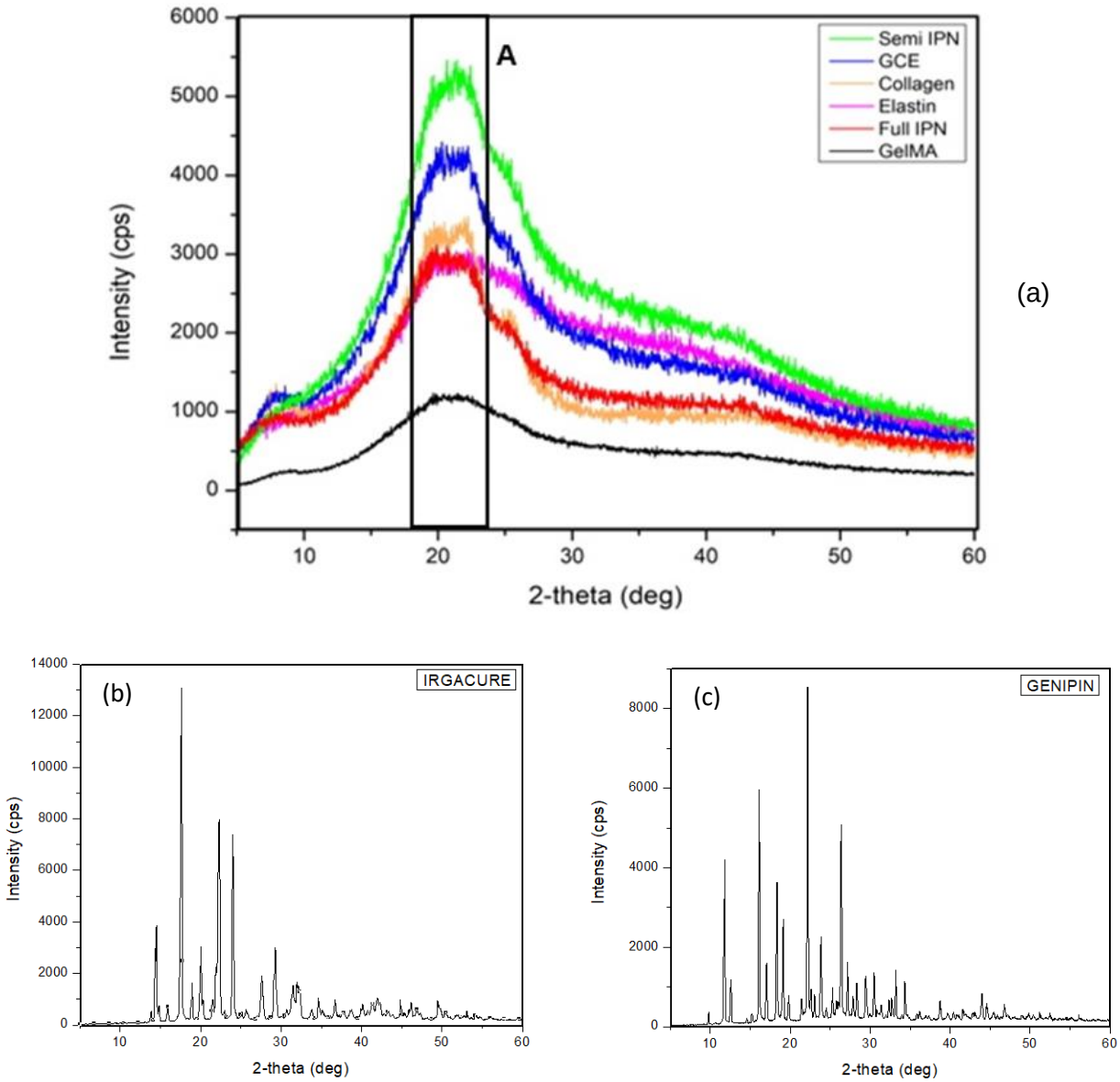


Figure 4.5: (a) XRD diffractograms of the starting materials and the IPN biomaterials. 'A' indicates the peak considered for analysis. (b) The crystalline nature of Irgacure. (c) The crystalline nature of Genipin.

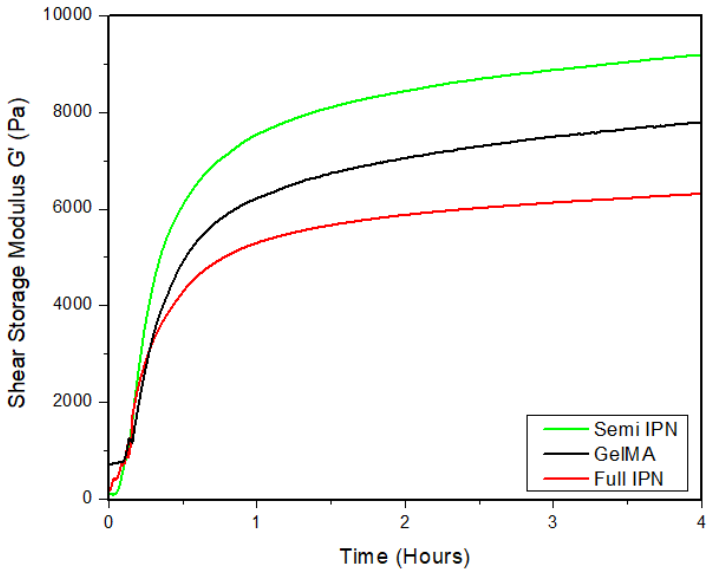
4.3.3 Real-Time Viscoelastic properties, Material Stiffness and Hydration of the 3D Printed IPN Biomaterial Hydrogel Scaffolds using a constant frequency

Viscoelastic elastic gelation studies were carried out on both the IPN systems without the radical polymer crosslinker to assess whether the physical crosslinking and the shear storage modulus G' of the GelMA would be affected with the addition of the peptides. As previously noted by Van den Bulke *et al*. (2000), when gelatin cools, the coils transition to helices and form a strong physical network. However, in the GelMA polymer, the methacrylamide content of modified gelatin chains obstruct the transition (fewer helices are present) and weaker

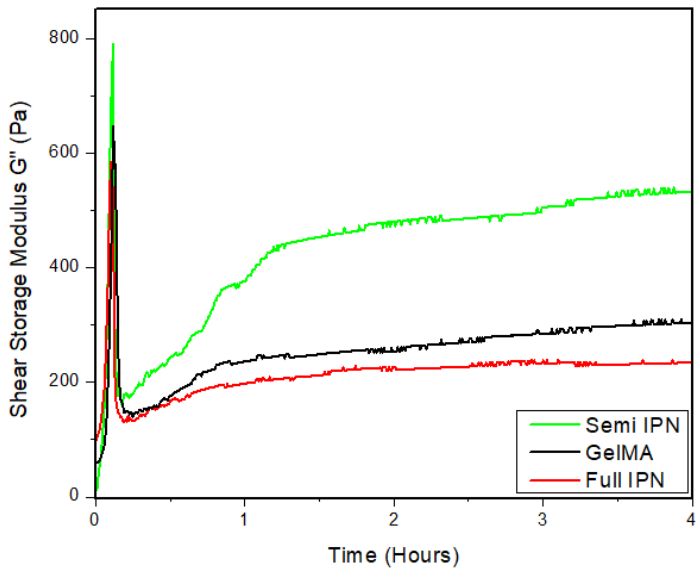
hydrogels are formed (Van den Bulke *et al*., 2000). With this in mind, it is shown that the addition of the peptides to the GelMA polymer did not affect the ability of the coil-helix transition to occur and therefore, the hydrogel IPN systems were able to physically crosslink at 10 °C (**Figure 4.6a**). The semi IPN was shown to have the highest shear storage modulus G' (~9195.5 Pa), followed by the GelMA polymer (~7797.6 Pa) and the full IPN (~6317.6 Pa) had the lowest shear storage modulus G' (**Figure 4.6a**). In the case of the semi IPN, it is proposed that the protein combinations could be forming native bodily protein networks and hence, could explain the increase in the G' values. Furthermore, supporting the development of an aECM hydrogel scaffold. The lower G' values in the full IPN could be explained by the fact that a higher degree of cross-linking can create brittle structures resulting in less elasticity (Lohani *et al.,* 2014). Viscoelastic studies for all samples indicate that G'>G'' and therefore, indicate that the gels are more "solid" in nature (**Figure 4.6b**). From **Figure 4.6b**, it is evident that the semi IPN had the highest shear loss modulus G" (~533.3 Pa), followed by the GelMA polymer (~304.1 Pa) and the full IPN (~234.9 Pa) had the lowest shear loss modulus G". This therefore confirms the platform printing temperature obtained during biomaterial optimization as this data confirms that the biomaterial solidifies upon contact with the platform. Furthermore, viscoelastic assessments were performed to simulate the viscoelastic behaviour of the hydrogels during the manufacturing and 3D printing processes (**Figure 4.6c**). Results indicated that the viscoelastic properties of the hydrogels are not affected as the results mimic the gelation results. The semi IPN was shown to have the highest shear storage modulus G' (~9103.6 Pa), followed by the GelMA polymer (~7719.6 Pa) and the full IPN (~6254.4 Pa) had the lowest shear storage modulus G'. After the 4 hours of gelation, the hydrogel disks were removed and photographed. From **Figure 4.7**, it is evident that, the semi IPN has a higher elasticity and it is able to retain its structure even after being deformed several times (n>5), thereby confirming the gelation results whereas the full IPN is less elastic and therefore does not hold its shape (**Figure 4.7**). No deformation of the full IPN system was possible validating the lower G' values observed during the viscoelastic studies.

For tissue engineering applications, the hydrogel material has to be stiff enough to promote and mimic the native microenvironment but not too strong that a secondary injury is caused. Material stiffness results indicated that the material stiffness of both the IPN systems were within a small margin of each other. Furthermore, swelling equilibrium was reached after 8 hours due to the formation of a steady plateau. The average material stiffness of the non-hydrated and hydrated semi IPN was 575 Pa and 597 Pa, respectively. The average material stiffness of the non-hydrated and hydrated full IPN was 577 Pa and 544 Pa, respectively. This indicates that prior hydration of the samples had no effect on the final material stiffness of the samples (**Figure 4.8**). Since brain tissue is known to be around the order of one kilopascal

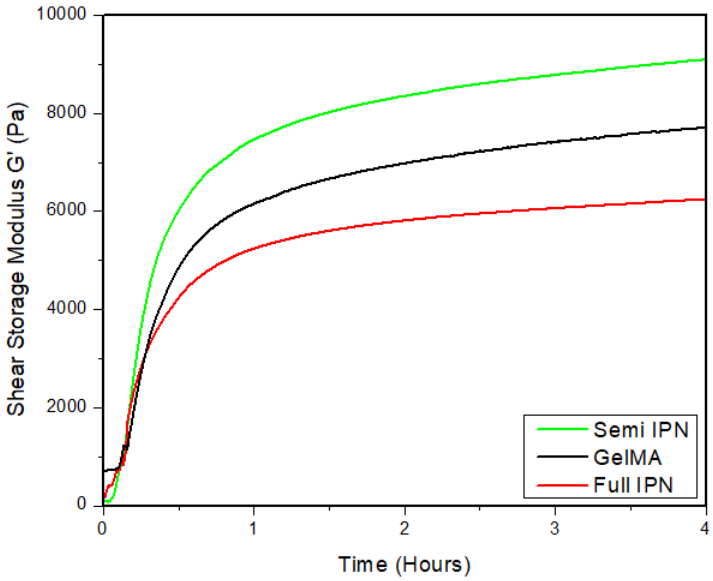
(Budday *et al.,* 2020; Leipzig and Schoichet, 2009) and is known to soften with age (Arani *et al.,* 2015), slight biomaterial stiffness enhancements may need to occur to accurately mimic the stiffness of the brain at the given patients age. The line graphs for both IPN systems in **Figure 4.8** provides a holistic overview during the material stiffness assessment. Both IPN systems produced spectra with an expected profile. Due to the fact that the semi IPN only undergoes single crosslinking, there are sections present within the material with different strengths. Therefore, the dips and peaks in the spectra are caused when the vibrations make contact with a softer/harder portion of the hydrogel. In comparison to the full IPN, the spectra are smoother as the system are dual crosslinked and therefore, the system has a more homogenous overall strength profile in comparison to the semi IPN.



(a)



(b)



(c)

Figure 4.6: (a) Kinetic gelation, shown as the Shear storage modulus (G'), of the semi and full IPN (without Irgacure 2959) relative to the GelMA polymer alone. (b) Shear Loss modulus of the semi and full IPN relative to the GelMA polymer alone. (c) Kinetic gelation mimicking the manufacturing process, shown as the Shear storage modulus (G'), of the semi and full IPN (without Irgacure 2959) relative to the GelMA polymer alone. In all spectra, the semi IPN is shown in green, the full IPN is shown in red and the GelMA polymer is shown in black.

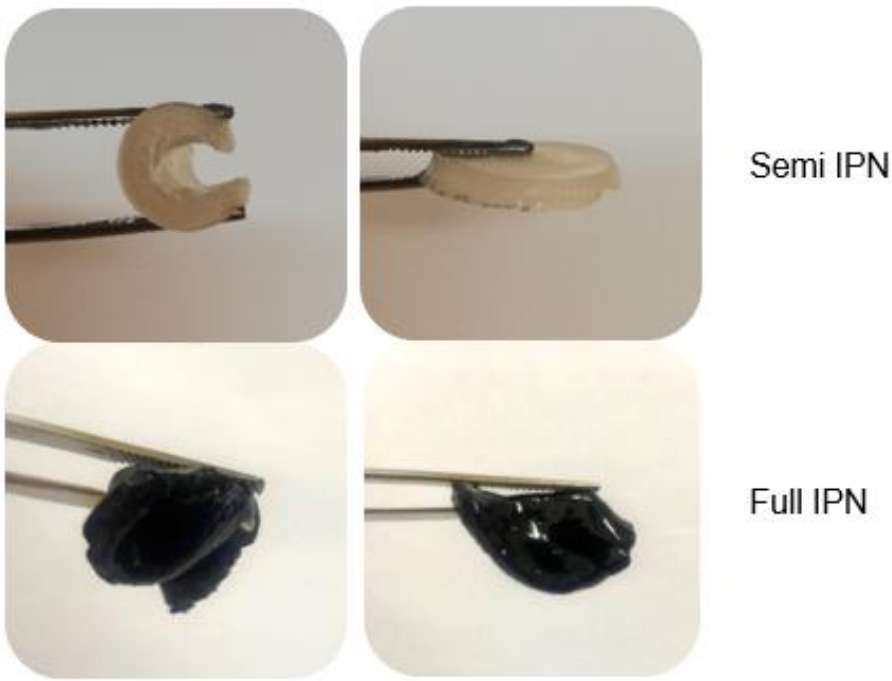


Figure 4.7: Indication of the elastic ability of the disks after 4 hours of hydration in aCSF. The semi IPN is shown at the top and the full IPN is shown at the bottom.

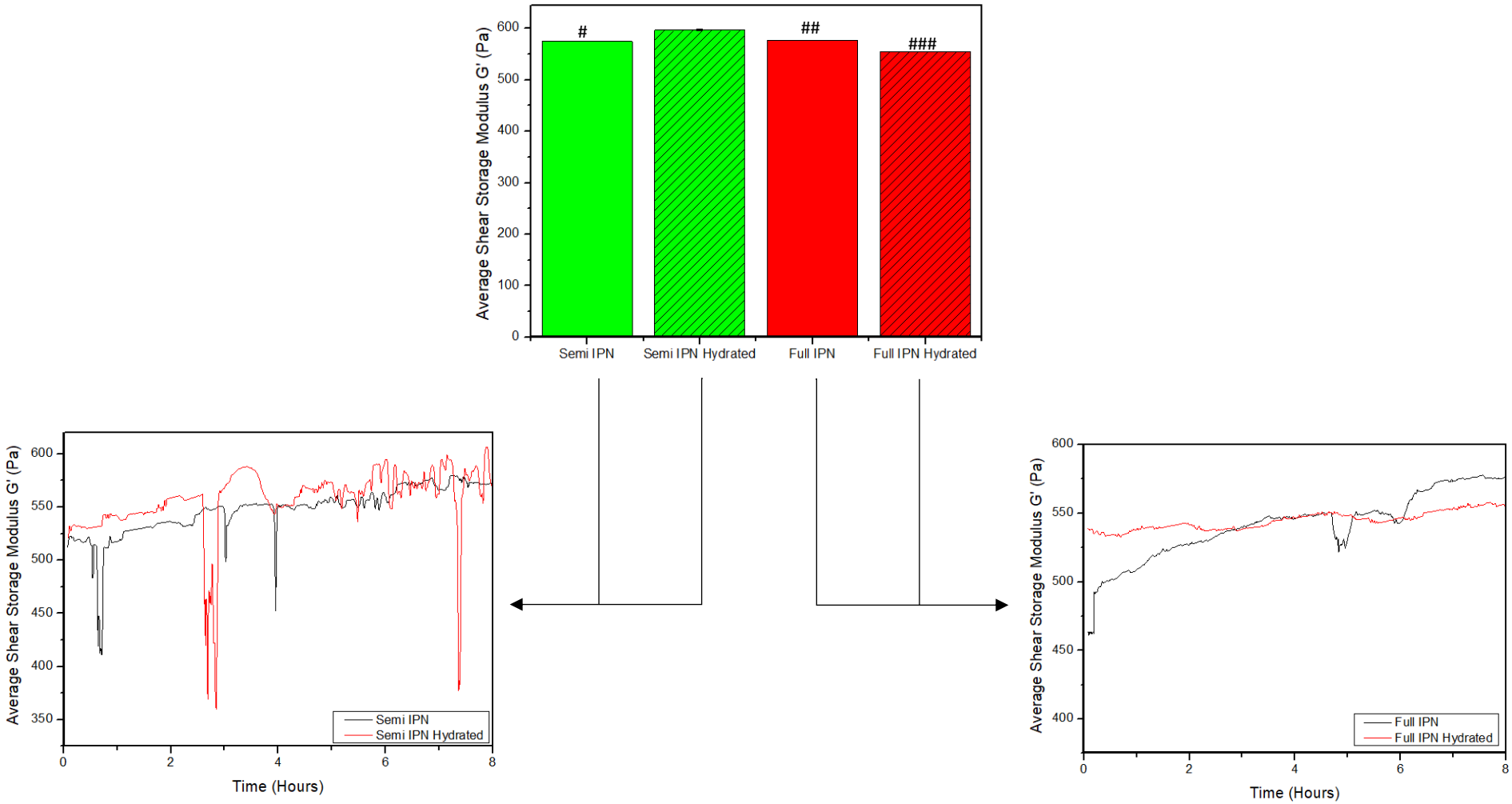
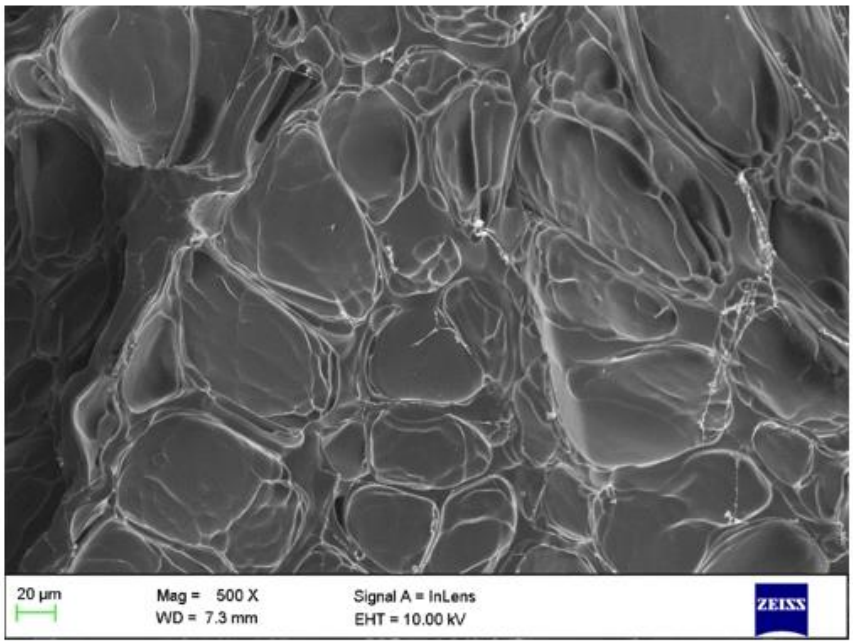


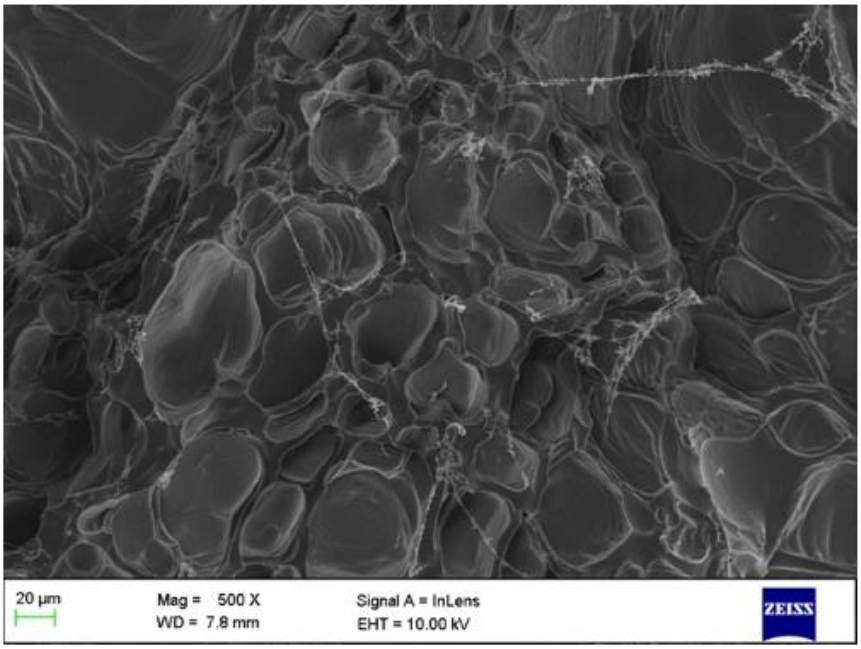
Figure 4.8: The real-time material stiffness, depicted as the average shear storage modulus (G'), of the IPN hydrogels as non-hydrated and hydrated samples (# indicates the SD = ± 0.44663, ## indicates the SD = ± 0.04732 and ### indicates the SD = ± 0.02858).

4.3.4 Validation of the formation of a morphological neuro-mimicking platform

Scanning Electron Microscope (SEM) image results indicated that both the semi and full IPN systems have an ordered, porous microstructure with both systems having pores with a similar shape. This finding is consistent with the structure of the GelMA polymer. This indicated that the crosslinking, lyophilization, and the 3D printing process did not alter the material porosity as there was no difference in the pore distribution between the samples. Although both IPN systems are crosslinked using the same photo-initiator, the full IPN system has a smaller pore structure than the semi IPN (Yoon *et al.,* 2016) as well as an increased pore density. This was proposed to be as a result of the increased stability of the proteins after Genipin crosslinking. In addition, the pores in both systems form “pockets” that do not penetrate through the system but show and interconnected pattern around the “pockets” that are separated by thin walls (Rahali *et al.,* 2017). Both systems have a fibrous-like network evident over the pores, which could be attributed to the elastin and collagen protein fibres (**Figure 4.9**). The SEM-EDS confirmed that the biomaterials were composed of Carbon, Nitrogen and Oxygen across several analysis positions of the 3D printed scaffold. This indicated that the samples were homogenous and confirms the formation of a purely biological system through the presence of three of the six elements required making up biological molecules.



(a)



(b)

Figure 4.9: Scanning Electron Microscopy (SEM) analysis of (a) the semi IPN and (b) the full IPN.

If an electron micrograph of the rat cortex is considered (**Figure 4.10**), it is evident that the cortex contains the neural cells surrounded by the Extracellular Space (ECS), the space where the ECM is found (red channels) (Nicholson and Syková, 1998). Upon close examination, it is evident that the morphological features of both of the biomaterial IPN scaffolds share a significant similarity to the rat cortex. Just as the cells are surrounded by the channels of the ECM, so too are the “pockets” of the IPN biomaterials surrounded by channels. This finding confirms the formation of a neuro-mimicking platform with respect to the scaffold morphology. Furthermore, the IPN scaffolds could provide a ‘blue-print’ to guide the cells where to migrate and settle to assist in the regeneration process. This could be achieved through the presence of topographical cues (“pockets” for increased surface area for cell migration and attachment), chemical cues (cell attachment sites on the proteins and polymer), architectural cues (physical structural cues provided by the scaffolds) as well as a multi scale predefined structure (hierarchical design incorporating nano-, micro- and macro-porous structures). Since the aim of a TBI treatment is to provide sufficient strength to prevent the tissue from collapsing, this ‘blue-print’ framework, coupled with the ECM architecture could provide the solution to the multiple failed attempts. Furthermore, due to the similarities, the framework can possibly be remodelled by the cells as the complexity of the native ECM has been fabricated.

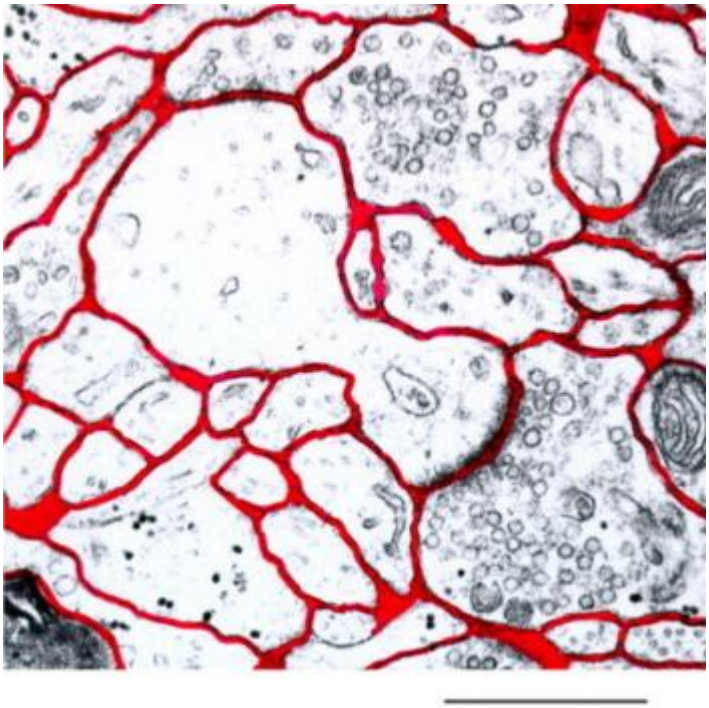


Figure 4.10: An electron micrograph displaying a section of the rat cortex indicating the Extracellular Space (ECS), the space where the ECM is found, outlined in red (Scale bar, 1 µm). This figure is reused from Trends in Neuroscience, **21** (5), Nicholson and Syková. Extracellular space structure revealed by diffusion analysis, 207-215, 1998, with permission from Elsevier.

4.3.5 Degradation, Fluid Uptake and Swelling profiles of the 3D Printed IPN Biomaterial Hydrogel Scaffolds

In any tissue engineering application, 3D printed scaffolds that are able to biodegrade without the need for further surgical intervention are crucial. Due to the fact that GelMA is a derivative of gelatin, GelMA is a hydrophilic polymer that forms a hydrogel of hydrophilic networks (Sun *et al.,* 2018). This feature allows for the biodegradation of the network by the uptake of the surrounding fluid. In terms of the peptides, folded collagen has been reported to have a largely hydrophobic side opposite a side with multiple hydrophilic lysine residues (Cole *et al.,* 2009). Similar to this, elastin contains alternating hydrophilic and hydrophobic domains (crosslinkable lysine sites) (Chow *et al.,* 2008). In this way, both peptides are important considerations in aECM biomaterials as they exhibit good aqueous chemical compatibility and controlled biodegradation (Chow *et al.,* 2008).

Biodegradation is important for any tissue engineering application as biodegradation will influence the repair and regeneration of the native tissue. In terms of the biodegradation of the two IPN systems, both systems exhibited a consistent degradation rate over 3 and 6 days for the full and semi IPN, respectively, after which the degradation increases. It has been reported in literature that the higher the DoS of the GelMA polymer, the slower the degradation rate

(Zhu *et al.,* 2019). Furthermore, 10% GelMA polymer alone has a degradation of 65 ± 3 % over 7 days (Zhao *et al.,* 2016). Despite the GelMA DoS being high in this work, the semi and full IPN exhibited an increased biodegradation rate of 8 and 6 days, respectively. Therefore, it is evident that the semi IPN degrades slightly slower than the full IPN. The increased rate of degradation of the two IPN systems in comparison to the GelMA polymer alone is attributed to the presence of the two peptides as they are easily degraded by the artificial cerebral spinal fluid (aCSF) (Zhao *et al.,* 2016; Vasile *et al.,* 2020). Furthermore, the increased degradation rate of the full IPN may be as a result of the increased crosslinking, which has been shown to embrittle materials (Roland, 2013). Therefore, when the network structure began to degrade the brittle structure collapses and an increased degradation rate was observed. This finding is in agreement with the viscoelastic findings. With this data, it is likely that these IPN hydrogels may be utilised for acute injuries across the tissue engineering discipline for soft tissues like the brain (**Figure 4.11a**).

In terms of the fluid uptake, the full IPN exhibits almost 1.5 times greater fluid uptake ability than the semi IPN. After 8 hours, the semi IPN and full IPN had a fluid uptake of 483.0% and 725.6%, respectively, in comparison to their initial dry masses (**Figure 4.11b**). In terms of the swelling properties as seen in **Figure 4.11c**, the full IPN swells to its maximum swelling ratio after 8 hours whereas the semi IPN swells to its maximum swelling ratio after one day. Furthermore, over the course of the experiment, both the IPN systems experience minor fluctuations around this maximum until fully degraded. This is a vital finding as the IPN biomaterials will not cause secondary damage if implanted in the swollen state as no further material swelling will occur. A similar trend to the fluid uptake was as the full IPN exhibited around 1.34 times more swelling than the semi IPN (**Figure 4.11c**). If the structure of Genipin is considered, it is noted that a couple -OH functional groups are present, therefore increasing the hydrophilicity of the system, and therefore, increased fluid uptake and swelling is possible (Mu *et al.,* 2013). Furthermore, the increased porosity as seen from the SEM micrographs, could further improve the fluid uptake and swelling properties of the full IPN.

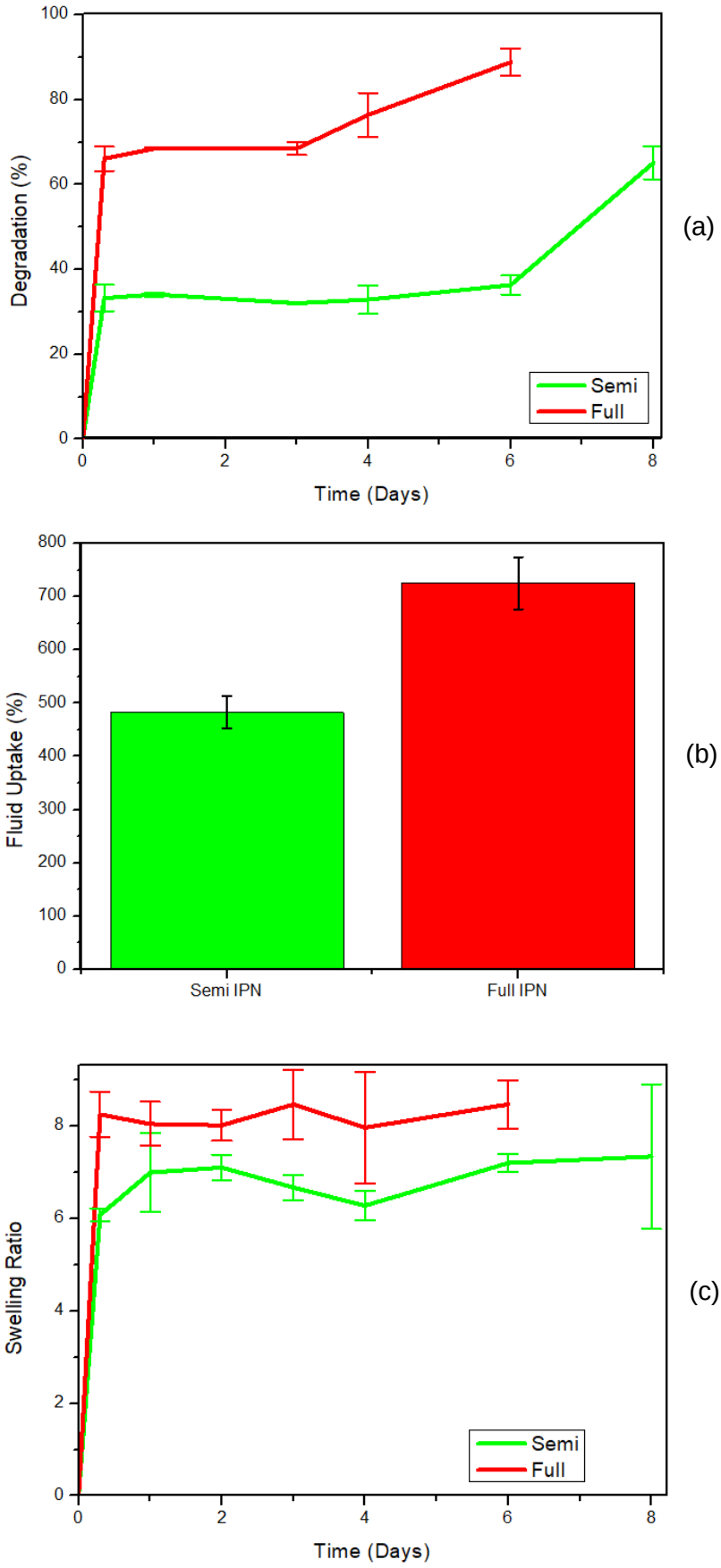


Figure 4.11: (a) Degradation, (b) Fluid Uptake and (c) Swelling Ratio of the two-3D printed IPN hydrogel biomaterials.

4.3.6 Hysteresis and “Shape-Memory” features

The lyophilized 3D printed IPN scaffolds were rehydrated for 8 hours in artificial cerebral spinal fluid (aCSF). When the IPN scaffolds were in the aCSF, the 3D printed/fabricated shape was maintained (**Figure 4.12a**). However, when the IPN scaffolds was removed from the aCSF, the 3D printed pattern collapsed (**Figure 4.12b**). Upon returning the scaffold back to the aCSF, the pattern prevailed to the original 3D printed pattern (**Figure 4.12a**) demonstrating a ‘shape-memory’ feature. This finding in significant as it is proposed to potentially facilitate in brain tissue mimicry. The proposal is as follows: once the scaffold is implanted, secondary injury will be minimised as the scaffold in its rehydrated form will allow for synchronous movement as the brain regenerates during the healing process. Furthermore, as the body deposits native ECM material (including but not limited to: hyaluronan, neurocan, brevican, versican, aggrecan, tenascin-R, collagen, fibronectin and vitronectin (Lam *et al.*, 2019)) during the regenerative process, the scaffold will allow for attraction and anchorage of the new ECM material onto the scaffold to serve as a framework for the neuro-regenerative process. Despite the hysteresis being observed in both IPN scaffolds, the royal blue colour of the full IPN prevented the capturing of decent images, therefore, only the images of the semi IPN are presented.

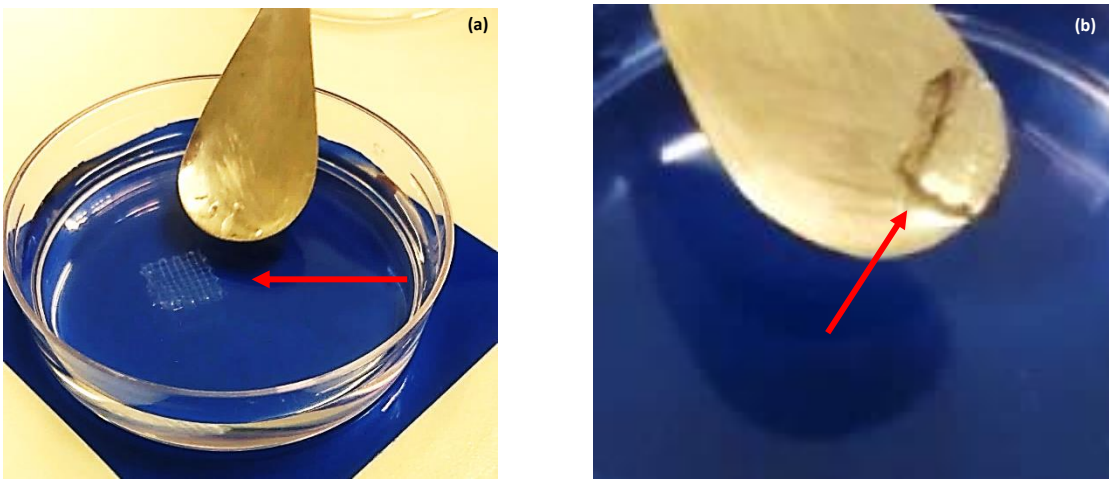


Figure 4.12: Images indicating the “memory” property of the semi IPN hydrogel. (a) Indicates the hydrated gel in artificial cerebral spinal fluid (aCSF) where the fabricated internal 3D pattern is clearly visible. (b) Indicates the hydrated gel when removed from the aCSF where no fabricated internal 3D pattern is visible.

4.3.7 Determination of neuro-compatibility and neuronal cell proliferation

The MTT proliferation studies indicated that the 3D printed IPN scaffolds were capable of supporting the growth of PC12 cells compared to the control over a 72-hour period. This confirmed the neuro-compatibility of the 3D printed IPN scaffolds as displayed in **Figure 4.13a**. The full IPN scaffold exhibited an increased cell viability, shown by the normalised cell viability

in **Figure 4.13b**, which is attributed to the neuro-protective effects of Genipin (Hughes *et al.,* 2014). Furthermore, both IPN systems indicated a higher proliferation to GelMA alone. This was accredited to the morphological similarities between the IPN scaffolds and the rat cortex and ECM. The MTT results indicate that both 3D printed IPN scaffolds would be safe for *in vivo* implantation.

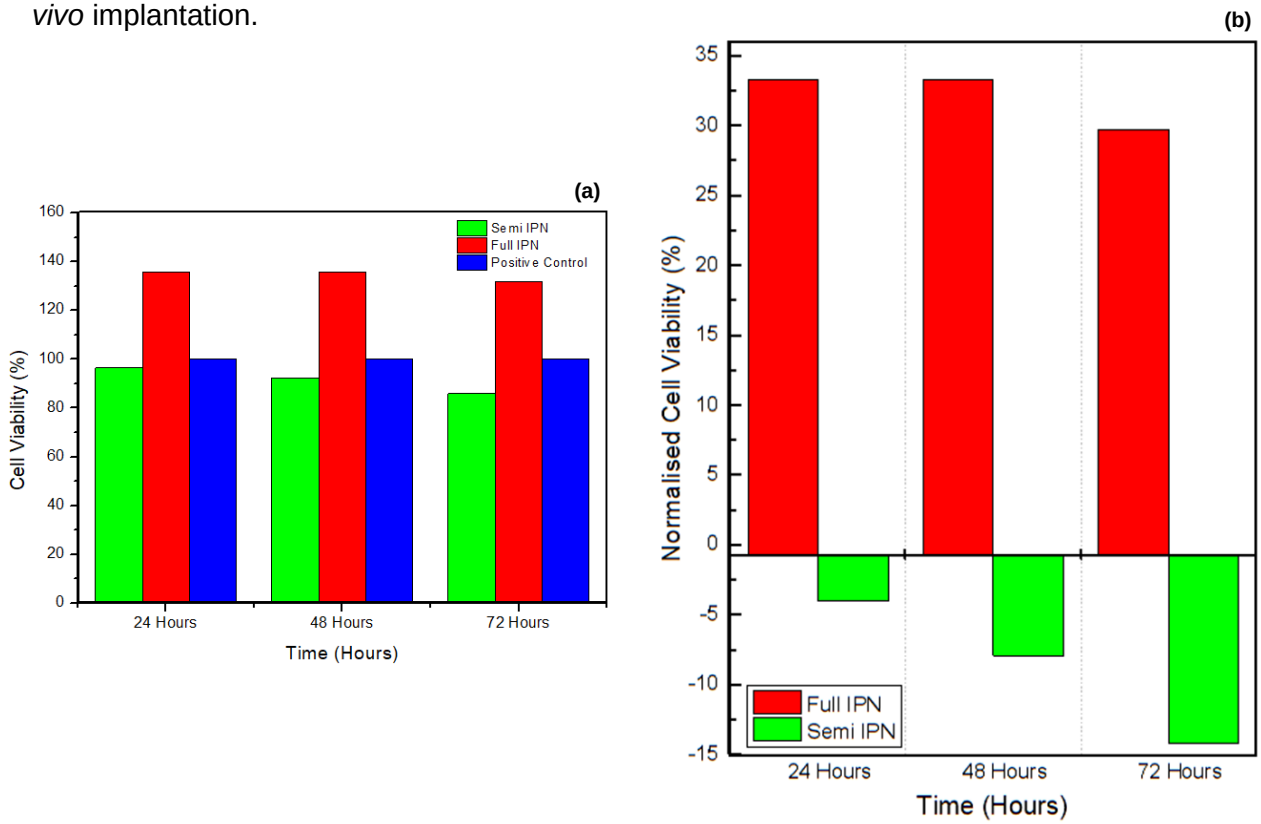


Figure 4.13: (a) MTT PC12 viability studies in response to the semi (Green) and full (Red) IPN scaffolds (SD≤0.3, n=3) and (b) the normalised cell viability data relative to the positive control set to 0, which represents 100% (SD≤0.2, n=3).

4.3.8 Analysis of the Nuclear Morphology and Migration in response to the 3D printed IPN Scaffolds

From the MTT results above, it is evident that the 3D printed IPN scaffolds promote an increased PC12 cell viability indicating that a higher number of healthy PC12 cells are present than in the GelMA polymer alone. Furthermore, a higher cell viability is indicative of an increased cellular activity (Khan, 2018) and from this, it is postulated that the cells are in a proliferative state. This is supported by the nuclear area. Since the data was captured as the number of pixels in a given region, in this case the nucleus, the greater the number of pixels the greater the area of the nucleus. Since nuclear volume is known to increase in cells undergoing mitosis (cell cycle) up until division (Huber and Gerace, 2007; Seaman *et al.,* 2015), a change in area will directly impact the nuclear volume. If **Figure 4.14** is considered, both IPN 3D printed scaffolds promote a greater nuclear area in the PC12 cells and therefore by default a greater nuclear volume with the increase in leachable time points. This indicates

that the components leaching out of the scaffolds are non-toxic as the PC12 cells are able to survive and flourish in the absence of any physical cues (attachment to the physical scaffold). This could further indicate that the tissue surrounding the scaffold once implanted will not be affected by any chemical leaching and in fact, taken with the viability data, could assist with tissue integration between the scaffolds and the surrounding brain tissue.

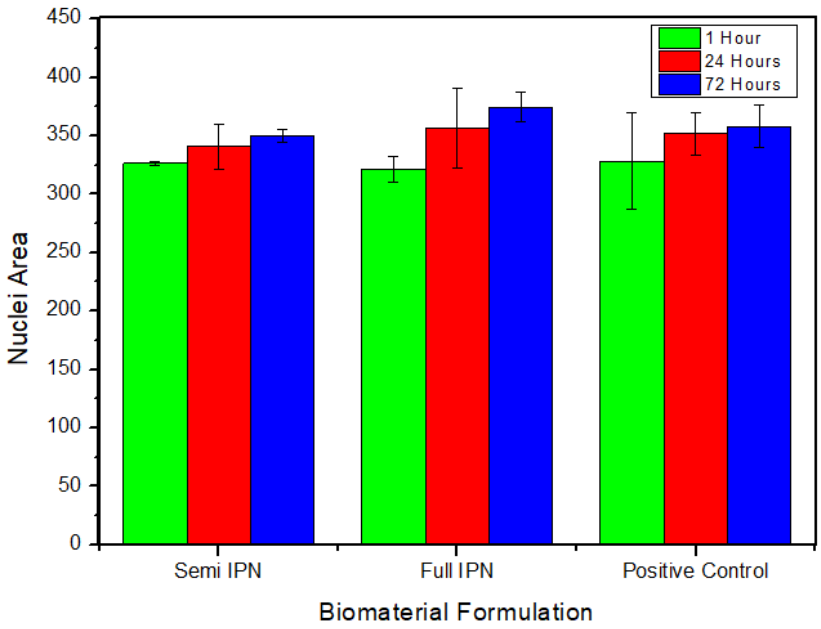


Figure 4.14: Nuclei area of PC12 cells in response to the different leachable time points (n=3) over 24 hours.

If the eccentricity of the nucleus is considered, eccentricity in simple terms is the measure of the circularity or flatness of an object, in this case the nucleus. A sphere has an eccentricity of zero whilst a pancake shape would have an eccentricity of one (Seaman *et al.,* 2015). In the cell cycle, eccentricity of the nucleus is known to increase after cell division has taken place (Seaman *et al.,* 2015). If **Figure 4.15** is considered, the eccentricity is closer to 1 in all leaching time points after the 24-hour incubation. This could indicate that the PC12 cells have completed the cell cycle and further supports the idea of the PC12 cells being in a proliferative state. Since there is an insufficient difference a 99 % confidence level between the eccentricity of the one hour and 24-hour leaching periods, the slight difference in eccentricity could be explained by the neuro-related effects, both neuroprotective and neurotrophic, of Genipin (Hughes *et al.,* 2014; Yamazaki and Chiba, 2005). After a one-hour leach, it is likely that the neuroprotective effects of Genipin are observable whereby proliferation is slightly arrested but a high cell viability is maintained (Giovanni *et al.,* 2005; Hughes *et al.,* 2014). Following this, it is possible that the 24- and 72-hour leach then results in the neurotrophic effects of Genipin wherein proliferation is stimulated (Hunsberger *et al.,* 2009; Yamazaki and Chiba, 2005). If these results taken with the high cell viability, the full IPN could be a beneficial treatment for

TBI since the Genipin constituent could assist in initially preventing further secondary brain damage (neuroprotective effects reducing apoptosis) whilst promoting proliferation to initiate the regenerative process. If **Figure 4.16a** is considered, it is evident that the nuclei, stained with DAPI, are not rounded but are more elliptical in shape (eccentricity closer to 1), thereby further supporting the idea of proliferating cells. **Figure 4.16b** indicates the morphology of the nucleus relative to the morphology of the cell body. The image displays an overlay of the nucleus stained in DAPI with a brightfield image of the cell body allowing for improved interpretation of the difference between the cellular and nuclear morphology.

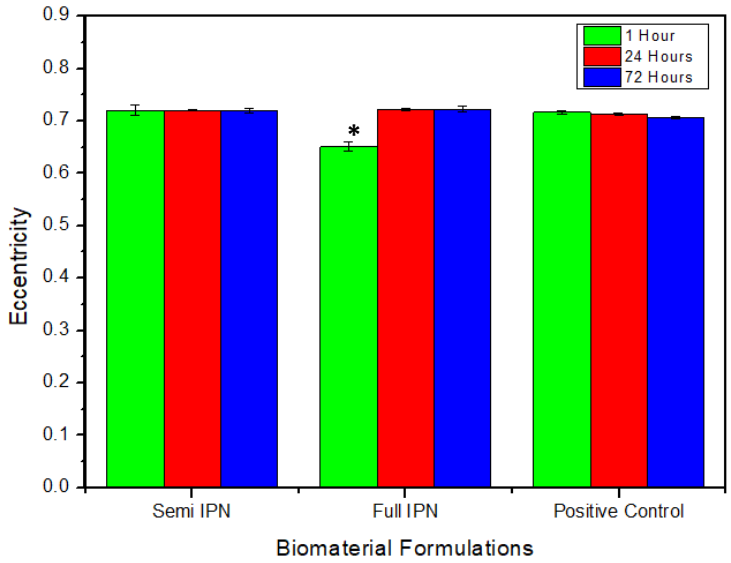
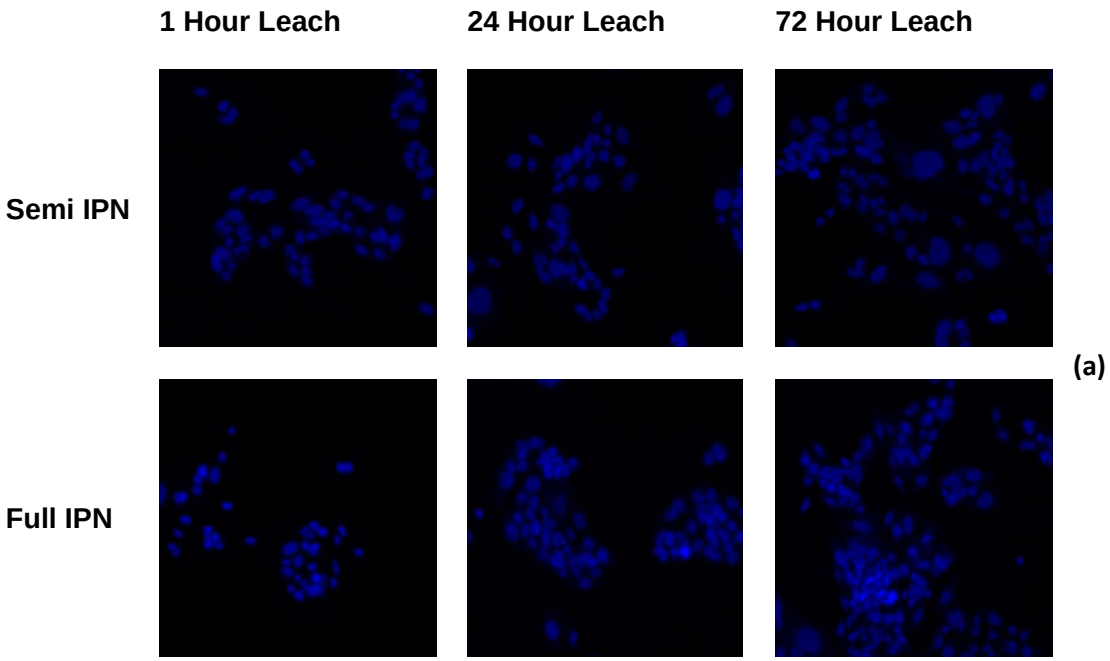


Figure 4.15: Nuclei eccentricity (n=3) of PC12 cells in response to the different leachable time points (*indicates p<0.01 compared to the full IPN 24 hours).



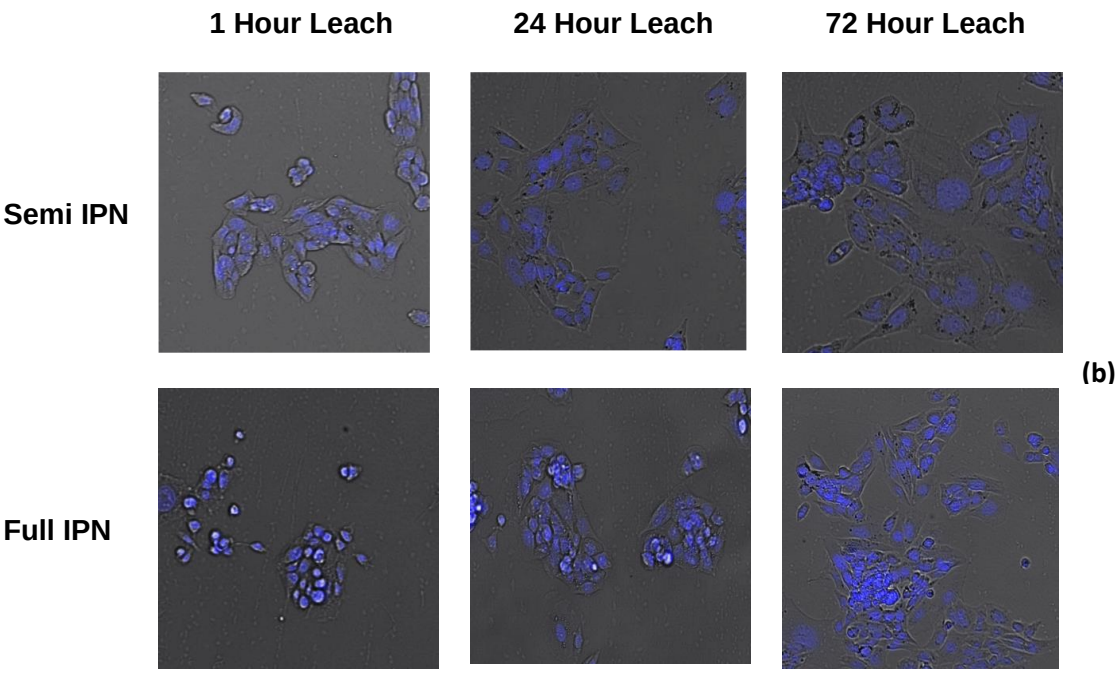


Figure 4.16: (a) DAPI stained nuclei of PC12 cells indicating that the nuclei are not rounded but are more elliptical in shape. (b) An overlay of the nucleus stained in DAPI with a brightfield image of the cell body allowing for improved visualisation of the nuclear and cellular morphology.

If **Figure 4.17a** is considered, it is evident that PC12 cellular migration was promoted in both 3D printed IPN scaffolds after 24 hours (cell cluster populations indicated by the yellow arrows). For this analysis, PC12 cells were stained with DAPI and MitoTracker™ Orange to monitor the nuclei and mitochondria, respectively. **Figure 4.17b** displays the cell clusters from the CY5 channel only (MitoTracker™ Orange monitoring) to assist in the visualisation of the cell clusters with a lower background noise. Cellular migration is promoted when cells interact with the ECM (Friedl *et al.,* 1998). Therefore, with evidence of migration, it is plausible that the fabrication of an aECM was successful. This is due to the fact that biophysical, topographical, and chemical cues were provided by the aECM to the PC12 cells. Furthermore, the morphological similarities between the IPN scaffolds and the rat cortex could further promote cellular migration by providing the 'blue-print' for the placement of cells, which could positively influence neural tissue regeneration.

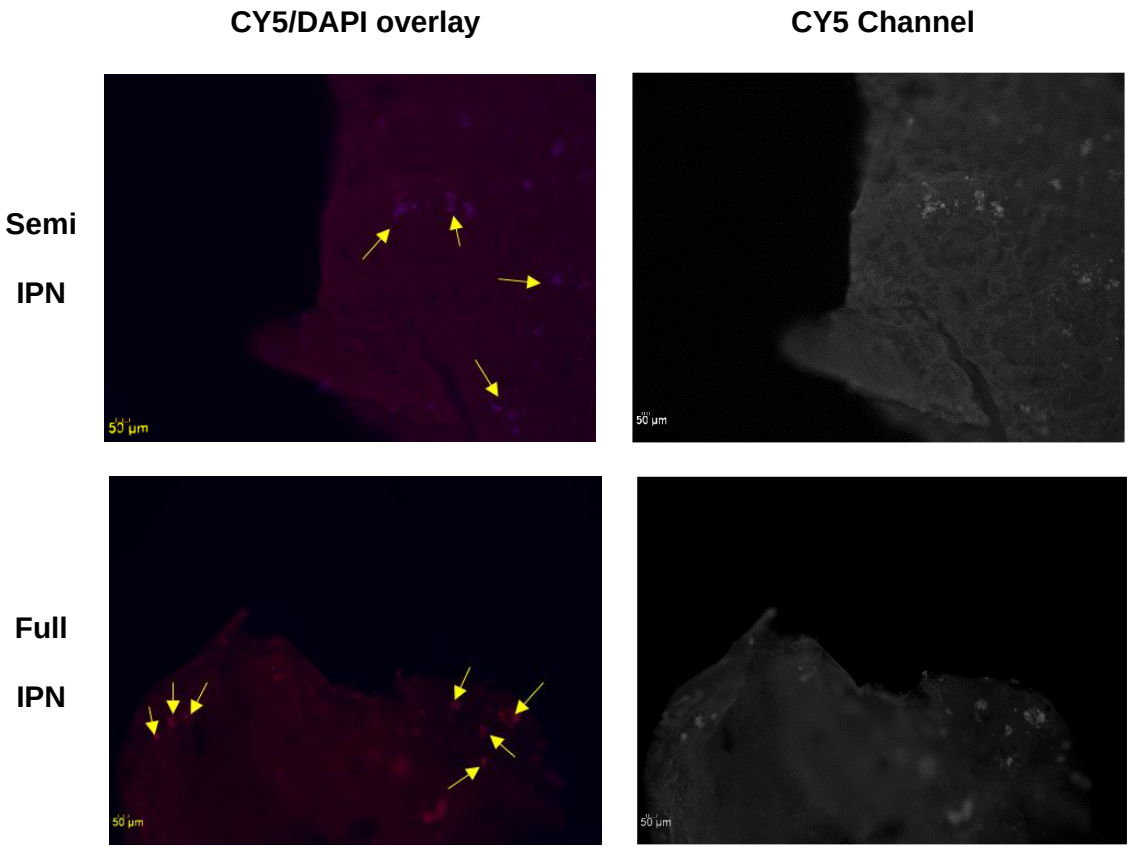


Figure 4.17: (a) Evidence of cellular migration in both 3D printed IPN scaffolds after 24 hours (cell cluster populations indicated by the yellow arrows). (b) CY5 channel indicating cell clusters with reduced background staining.

4.3.9 Antimicrobial Activity of Genipin

Table 4.1 summarises the MBC values obtained for the six pathogens in the study. All MBC values obtained were 10 mg/mL or below demonstrating notable activity. These results indicate that the concentration of Genipin (10 mg/mL) blended in the full IPN is sufficient to exhibit bactericidal activity. This suggests that Genipin has antimicrobial properties and can prevent the growth of pathogens associated with post-surgical brain infections. Further studies are required to confirm this finding in other brain pathogens associated with brain infections.

Table 4.1: Cidal activity (MBC values in mg/ml) of Genipin against six bacterial test pathogens		
Pathogen	**Average Genipin MBC Value and SD**	**Average Positive Control MBC (µg/ml) and SD**
S. aureus (ATCC 25923)	5±0.00	0.078±0.00
E. coli (ATCC 8379)	10±0.00	0.065±0.02
K. pneumoniae (ATCC 13887)	5±0.00	≤0.020±0.00
P. aeruginosa (ATCC 27853)	10±0.00	0.156±0.00
L. monocytogenes (ATCC 19111)	5±0.00	0.078±0.00
S. marcescens (ATCC 14756)	5±0.00	0.156±0.00

Initial screening of the IPNs against *S. aureus* indicated that the semi IPN and Irgacure 2959 displayed no antibacterial activity (MBC > 40 mg/ml, SD: ±0.00) as expected, however, the Genipin individually and full IPN both displayed antimicrobial activities (MBC of 5 mg/ml, SD: ±0.00). These results proved that Genipin was the compound responsible for the antimicrobial. The Genipin individually was then carried forward to be tested by the five other pathogens. The culture control displayed optimal growth for all the test pathogens. The negative control displayed clear wells indicating the solvent did not have any antimicrobial properties.

4.4 Final Formulation

Table 4.2 provides a summary of the optimized 3D printing parameters, scaffold design parameters, polymer and crosslinker concentrations and post-processing parameters presented in this Chapter for successful fabrication of the aECM biomaterial IPN scaffolds.

Table 4.2: Processing parameters for the optimized IPN biomaterials	
Parameter	**Value**
GelMA concentration (w/v)	10
Collagen concentration (w/v)	0.5
Elastin concentration (w/v)	1
Cartridge temperature (° C)	18
Platform Temperature (° C)	13
Plotting speed (mm/s)	10-20
Internal bore of needle (mm)	0.2
Dimensions of scaffold (mm)	10x10x10 10x10x20
Scaffold design	Rectilinear
Scaffold structure (°)	0-90 Cross-hatch
Material Temperature Equilibration (min)	30
Irgacure concentration (% w/v)	0.5
Genipin concentration – Full IPN only (% w/v)	1
UV crosslinking time (minutes)	2
Lyophilization time (hours)	24

4.5 Concluding Remarks

The study assessed the potential of two novel peptide-based 3D printable biomaterials composed of GelMA, collagen, and elastin as potential novel biomaterials for neural tissue engineering applications. This study developed two IPN systems which exhibited 3D printability at the optimized parameters reported above. In addition, shape fidelity was easily maintained in both IPN systems, making the two IPN hydrogels attractive for biological 3D printing. Through DSC, TGA and XRD analysis, the formation of both a semi and full IPN system was confirmed. Molecular vibrations indicated that the addition of the peptides to the GelMA retains the GelMA profile, whilst suggesting that the small shifts in the wave number indicate a molecular water interaction with the peptides in the biomaterials. Furthermore, it was shown that the crosslinkers do not change the native structure of the peptides nor does the two minutes of UV affect the integrity of the peptide backbone. Additionally, through viscoelastic analysis, it was inferred that the printing process did not have an adverse effect on either IPN system. The real-time mechanical stiffness analysis indicated that both IPN systems currently, could be utilized in developing scaffolds for several soft tissues such as the brain. However, since the brain stiffness can change with age, possible biomaterial modifications may need to occur to accurately mimic the stiffness of the patient's brain at the time of injury. SEM imagining indicated that the fabricated IPN scaffolds have a significant similarity to the native rat cortex in terms of structural morphology. Additionally, both IPN biomaterials exhibited a "shape-memory" feature proposed to assist with tissue mimicry. Both IPN scaffolds were shown to promote PC12 survival and promoted cellular migration. Furthermore, through nuclei eccentricity and area studies of the PC12 cells, it was postulated that the cells were in a proliferative state. Despite this, it is advisable that further studies are done to ensure the proliferation of cells is in order with healthy tissue ranges (no cancer promotion). Lastly, the full IPN was observed to have potential bactericidal effects against six bacterial pathogens associated with post-surgical brain infections. It is concluded that a biomaterial composed of GelMA, collagen, and elastin in different crosslinked states is a suitable candidate for potential tissue engineering applications. As the drive towards custom patient treatments continue to expand, the design of Custom-Neural-Scaffolds (C-N-S) is discussed in Chapter 5.

4.6 References

Aldana, A. A., Rial-Hermida, M. I., Abraham, G. A., Concheiro, A. and Alvarez-Lorenzo, C. (2017). Temperature-sensitive biocompatible IPN hydrogels based on poly (NIPA-PEGdma) and photocrosslinkable gelatin methacrylate. Soft Matter. **15**, 341–9.

Arani, A., Murphy, M. C., Glaser, K. J., Manduca, A., Lake, D. S., Kruse, S. A., Jack, C. R., Jr, Ehman, R. L. and Huston, J., 3rd (2015). Measuring the effects of aging and sex on regional brain stiffness with MR elastography in healthy older adults. NeuroImage. **111**, 59–64.

Archana, D., Manisha, G. and Divya, J. (2012). A review on interpenetrating polymer network. International Journal of Pharmacy and Pharmaceutical Sciences. **4**, 389-399.

Armstrong, J. P. K., Burke, M., Carter, B. M., Davis, S. A. and Perriman, A. W. (2016). 3D Bioprinting Using a Templated Porous Bioink. Advanced Healthcare Materials. **5**, 1724–30.

Asma, C., Meriem, E., Mahmoud, B. and Djaafer, B. (2014). Physicochemical Characterization of Gelatin-Cmc Composite Edibles Films from Polyion-Complex Hydrogels. Journal of the Chilean Chemical Society. **59**, 2279–83.

Bailey, A. J. (1978). Collagen and elastin fibres. Journal of Clinical Pathology. **31**, 49–58.

Baumann, M. D., Kang, C. E., Tator, C. H. and Shoichet, M. S. (2010). Intrathecal delivery of a polymeric nanocomposite hydrogel after spinal cord injury. Biomaterials. **31**, 7631–9.

Bhardwaj, V., Harit, G. and Kumar, S. (2012). Interpenetrating polymer network (IPN): Novel approach in drug delivery. International Journal of Drug Development and Research. **4**, 41–54.

Bonnans, C., Chou, J. and Werb, Z. (2014). Remodelling the extracellular matrix in development and disease. Nature Reviews Molecular Cell Biology. **15**, 786–801.

Boque, M. C., Bodi, M. and Rello, J. (2000). Trauma, head injury, and neurosurgery infections. Seminars in Respiratory Infections. 15 (4), 280-286.

Bozec, L. and Odlyha, M. (2011). Thermal Denaturation Studies of Collagen by Microthermal Analysis and Atomic Force Microscopy. Biophysical Journal. **101**, 228–36.

Bruylants, G., Wouters, J. and Michaux, C. (2005). Differential Scanning Calorimetry in Life Science: Thermodynamics, Stability, Molecular Recognition and Application in Drug Design. Current Medicinal Chemistry. **12**, 2011–20.

Budday, S., Ovaert, T. C., Holzapfel, G. A., Steinmann, P. and Kuhl, E. (2020). Fifty Shades of Brain: A Review on the Mechanical Testing and Modeling of Brain Tissue. Archives of Computational Methods in Engineering. **27**, 1187–1230.

Caliari, S. R. and Burdick, J. A. (2016). A practical guide to hydrogels for cell culture. Nature Methods. **13**, 405–14.

Chow, D., Nunalee, M. L., Lim, D. W., Simnick, A. J. and Chilkoti, A. (2008). Peptide-based biopolymers in biomedicine and biotechnology. Materials Science and Engineering R: Reports. **62**, 125–55.

Chu, X., Wu, F., Sun, B., Zhang, M., Song, S., Zhang, P., Wang, Y., Zhang, Q., Zhou, N. and Shen, J. (2020). Genipin cross-linked carbon dots for antimicrobial, bioimaging and bacterial discrimination. Colloids and Surfaces B: Biointerfaces. **190**, 110930.

Cole, D. J., Payne; M. C. and Ciacchi, L. C. (2009). Water structuring and collagen adsorption at hydrophilic and hydrophobic silicon surfaces. Physical Chemistry Chemical Physics. **11**, 11395.

Dando, S. J., Mackay-Sim, A., Norton, R., Currie, B. J., St. John, J. A., Ekberg, J. K. A., Batzloff, M., Ulett, G. C. and Beacham, I. R. (2014). Pathogens Penetrating the Central Nervous System: Infection Pathways and the Cellular and Molecular Mechanisms of Invasion. Clinical Microbiology. **27** (4), 691-726.

Da Silva, K., Kumar, P., Choonara, Y. E., du Toit, L. C. and Pillay, V. (2019). Preprocessing of Medical Image Data for Three-Dimensional Bioprinted Customized-Neural-Scaffolds. Tissue Engineering Part C: Methods. **25**, 401–10.

Da Silva, K., Kumar, P., Choonara, Y. E., du Toit, L. C. and Pillay, V. (2020). Three-dimensional printing of extracellular matrix (ECM)-mimicking scaffolds: A critical review of the current ECM materials. Journal of Biomedical Materials Research Part A. **108** (12), 2324-2350.

Dziedzic, T., Slowik, A. and Szczudlik. A. (2004). Nosocomial infections and immunity: lesson from brain-injured patients. Critical Care. 8, 266.

Frantz, C., Stewart, K. M. and Weaver, V. M. (2010). The extracellular matrix at a glance. Journal of cell science. **123** (24), 4195–4200.

Friedl, P., Bröcker, E. -B. and Zänker, K.S. (1998). Integrins, Cell Matrix Interactions and Cell Migration Strategies: Fundamental Differences in Leukocytes and Tumor Cells. Cell Adhesion and Communication. **6** (2-3), 225-236.

Giovanni, S. D., Movsesyan, V., Ahmed, F., Cernak, I., Schinelli, S., Stoica, B. and Faden, A. I. (2005). Cell cycle inhibition provides neuroprotection and reduces glial proliferation and scar formation after traumatic brain injury. Proceedings of the National Academy of Sciences. **102** (23), 8333-8338.

Goldsack, D.E. and Chalifoux, R.C. (1973). Contribution of the free energy of mixing of hydrophobic side chains to the stability of the tertiary structure of proteins. Journal of Theoretical Biology. **39** (3), 645-651.

Gu, L., Li, T., Song, X., Yang, X., Li, S., Chen, L. and Sun, L. (2020). Preparation and characterization of methacrylated gelatin/bacterial cellulose composite hydrogels for cartilage tissue engineering. Regenerative Biomaterials. **7**, 195–202.

Hoffmann, A. S. (2004). Natural Materials in: Biomaterial Sciences an Introduction to Materials in Medicine. Ratner, B. D., Hoffman, A. S., Schoen, F. J. and Lemons, J. E (eds). 2nd Edition. China: Elsevier, 107-115.

Hong, H. Y. and Kim, B. C. (2007). Mixed lineasge kinase 3 connects reactive oxygen species to c-Jun NH2-terminal kinase-induced mitochondrial apoptosis in genipin-treated PC3 human prostate cancer cells. Biochemical and Biophysical Research Communications. **362** (2), 307–312.

Huber, M. D. and Gerace, L. (2007). The size-wise nucleus: nuclear volume control in eukaryotes. The Journal of Cell Biology. **179** (4), 583–584.

Hughes, R. H., Silva, V. A., Ahmed, I., Shreiber, D. I. and Morrison, B. (2014). Neuroprotection by Genipin against reactive oxygen and reactive nitrogen species-mediated injury in organotypic hippocampal slice cultures. Brain Research. **1543**, 308-314.

Humphrey, J. D., Dufresne, E. R. and Schwartz, M. A. (2014). Mechanotransduction and extracellular matrix homeostasis. Nature Reviews Molecular Cell Biology. **15**, 802–12.

Hunsberger, J., Austin, D. R., Henter, I. D., and Chen, G. (2009). The neurotrophic and neuroprotective effects of psychotropic agents. Dialogues in Clinical Neuroscience. **11** (3), 333–348.

Hussein, M. A., El-Shishtawy, R. M., Abu-Zied, B. M. and Asiri, A. M. (2016). The impact of cross-linking degree on the thermal and texture behavior of poly(methyl methacrylate). Journal of Thermal Analysis and Calorimetry. **124**, 709–17.
Hyder, A. A., Wunderlich, C. A., Puvanachandra, P., Gururaj, G. and Kobusingye, O. C. (2007). The impact of traumatic brain injuries: a global perspective. NeuroRehabilitation. **22**, 341–53.

Ishiguro, K., Yamaki, M. and Takagi, S. (1983). Studies on iridoid-related compounds, II. The structure and antimicrobial activity of aglucones of galioside and gardenoside. Journal of Natural Products. **46** (4), 532–536.

Jenkins, A. D., Kratochvíl, P., Stepto, R. F. T. and Suter, U. W. (1996). Glossary of basic terms in polymer science (IUPAC Recommendations 1996). Pure and Applied Chemistry. **68**, 2287–311.

Johnston, D., Choonara, Y. E., Kumar, P., du Toit, L. C., van Vuuren, S. and Pillay, V. (2013). Prolonged Delivery of Ciprofloxacin and Diclofenac Sodium from a Polymeric Fibre Device for the Treatment of Peridontal Disease. BioMed Research International. **2013**, 460936.

Khan, A., Gallah, H., Riedl, B., Bouchard, J., Safrany, A. and Lacroix, M. (2016). Genipin cross-linked antimicrobial nanocomposite films and gamma irradiation to prevent the surface growth of bacteria in fresh meats. Innovative Food Science & Emerging Technologies. **35**, 96-102.

Khan, Y. (2018). Characterizing the Properties of Tissue Constructs for Regenerative Engineering, Editor(s): Narayan, R., Encyclopedia of Biomedical Engineering, Elsevier, 537-545.

Ki, C. S., Baek, D. H., Gang, K. D., Lee, K. H., Um, I. C. and Park, Y. H. (2005). Characterization of gelatin nanofiber prepared from gelatin–formic acid solution. Polymer. **46**, 5094–102.

Kim, T. H., Yoon, S. J. and Lee, S. M. (2012). Genipin attenuates sepsis by inhibiting Toll-like receptor signaling. Molecular medicine (Cambridge, Mass.). **18** (1), 455–465.

Kim, Y., Ko, H., Kwon, I. K. and Shin, K. (2016). Extracellular Matrix Revisited: Roles in Tissue Engineering. International Neurourology Journal. **20**, S23-29.

Koo, H. J., Lim, K. H., Jung, H. J. and Park, E. H. (2006). Anti-inflammatory evaluation of gardenia extract, geniposide and genipin. Journal of Ethnopharmacology. **103** (3), 496–500.
Kotanen, C. N., Moussy, F. G., Carrara, S. and Guiseppi-elie, A. (2013). Infrared Spectroscopy of Protein Structure. Roberts GCK, editor. Encyclopedia of Biophysics. Berlin, Heidelberg: Springer Berlin Heidelberg.

Lam, D., Enright, H. A., Cadena, J., Peters, S. K. G., Sales, A. P., Osburn, J. J., Soscia, D. A., Kulp, K. S., Wheeler, E. K. and Fischer, N. O. (2019). Tissue-specific extracellular matrix accelerates the formation of neural networks and communities in a neuron-glia co-culture on a multi-electrode array. Scientific Reports. **9**, 4159.

Lambri, M. L., Bozzano, P. B., Giordano, E. D. V., Bonifacich, F. G., Gargicevich, D., Zelada, G. I. and Lambri, O. A. (2018). Denaturation processes of collagen from cow bones as a function of temperature. Matéria. **23** (2), Doi: 10.1590/s1517-707620180002.0424.

Lei, Z. and Wu, P. (2018). A supramolecular biomimetic skin combining a wide spectrum of mechanical properties and multiple sensory capabilities. Nature Communications. **9**,1134.

Leipzig, N. D. and Shoichet, M. S. (2009). The effect of substrate stiffness on adult neural stem cell behavior. Biomaterials. **30** (36), 6867-6878.

Liu, C-Y., Matsusaki, M. and Akashi, M. (2015). Cell effects on the formation of collagen triple helix fibres inside collagen gels or on cell surfaces. Polymer Journal. **47**, 391–399.

Lohani, A., Singh, G., Bhattacharya, S. S. and Verma, A. (2014). Interpenetrating Polymer Networks as Innovative Drug Delivery Systems. Journal of Drug Delivery. **2014**, Doi: 10.1155/2014/583612.

Lu, B., Yuk, H., Lin, S., Jian, N., Qu, K., Xu, J. and Zhao, X. (2019). Pure PEDOT:PSS hydrogels. Nature Communications. **10**, 1043.

Lu, P., Takai. K., Weaver, V. M. and Werb, Z. (2011). Extracellular Matrix Degradation and Remodeling in Development and Disease. Cold Spring Harbor Perspectives in Biology. **3** (12), a005058.

Malda, J., Visser, J., Melchels, F. P., Jüngst, T., Hennink, W. E., Dhert, W. J. A., Groll, J. and Hutmacher, D. W. (2013). 25th Anniversary Article: Engineering Hydrogels for Biofabrication. Advanced Materials. **25**, 5011–5028.

Manickam, B., Sreedharan, R. and Elumalai, M. (2014). 'Genipin' - the natural water soluble cross-linking agent and its importance in the modified drug delivery systems: an overview. Current Drug Delivery. **11** (1), 139-45.

Mok, S-W., Nizak, R., Fu, S-C., Ho, K-W. K., Qin, L., Saris, D. B. F., Chan, K-M. and Malda, J. (2016). From the printer: Potential of three-dimensional printing for orthopaedic applications. Journal of Orthopaedic Translation. **6**, 42–49.

Mu, C., Zhang, K., Lin, W. and Li, D. (2013). Ring-opening polymerization of Genipin and its long-range crosslinking effect on collagen hydrogel. Journal of Biomedical Materials Research Part A. **101**, 385–393.

Nagai, T. (2010). Characterization of Acid-Soluble Collagen from Skins of Surf Smelt (Hypomesus pretiosus japonicus Brevoort). Food and Nutrition Sciences. **1**, 59–66.

Nagaraj, P., Sasidharan, A., David, V. and Sambandam, A. (2017). Effect of Cross-Linking on the Performances of Starch-Based Biopolymer as Gel Electrolyte for Dye-Sensitized Solar Cell Applications. Polymers. **9**, 667.
Nakamura, M., Iwanaga, S., Henmi, C., Arai, K. and Nishiyama, Y. (2010). Biomatrices and biomaterials for future developments of bioprinting and biofabrication. Biofabrication. **1**, 014110.

Nicholson, C. and Syková, E. (1998). Extracellular space structure revealed by diffusion analysis. Trends in Neurosciences. 21 (5), 207-215.

Parak, A., Pradeep, P., du Toit, L. C., Kumar, P., Choonara, Y. E. and Pillay, V. (2018). Functionalizing bioinks for 3D bioprinting applications. Drug Discovery Today. **24**,198–205.

Rahali, K., Messaoud, G. B., Kahn, C., Sanchez-Gonzalez, L., Kaci, M., Cleymand, F., Fleutot, S., Linder, M., Desobry, S. and Arab-Tehrany, E. (2017). Synthesis and Characterization of

Nanofunctionalized Gelatin Methacrylate Hydrogels. International Journal of Molecular Sciences. **18**, 2675.

Resmi, R. (2012). Gelatin-Hydroxypropyl Methacrylate Copolymers for Potential Antimicrobial Wound Dressing Applications, Masters of Philosophy, Sree Chitra Tirunal Institute for Medical Sciences & Technology, Trivandrum, India.

Roland, C. M. (2013). Interpenetrating Polymer Networks (IPN): Structure and Mechanical Behavior. In: Encyclopedia of Polymeric Nanomaterials. Berlin, Heidelberg: Springer Berlin Heidelberg; 1–9.

Rutz, A. L., Hyland, K. E., Jakus, A. E., Burghardt, W. R. and Shah, R. N. (2015). A Multimaterial Bioink Method for 3D Printing Tunable, Cell-Compatible Hydrogels. Advanced Materials. **27**, 1607–1614.

Seaman, L., Meixner, W., Snyder, J. and Rajapakse, I. (2015). Periodicity of nuclear morphology in human fibroblasts. Nucleus. **6** (5), 408–416.

Samouillan, V., André, C., Dandurand, J. and Lacabanne, C. (2004). Effect of Water on the Molecular Mobility of Elastin. Biomacromolecules. **5**, 958–964.

Samouillan, V., Delaunay, F., Dandurand, J., Merbahi, N., Gardou, J-P., Yousfi, M., Gandaglia, A., Spina, M. and Lacabanne, C. (2011). The Use of Thermal Techniques for the Characterization and Selection of Natural Biomaterials. Journal of Functional Biomaterials. **2**, 230–248.

Shao, Y., Sang, J. and Fu, J. (2015). On human pluripotent stem cell control: The rise of 3D bioengineering and mechanobiology. Biomaterials. **52**, 26–43.

Schoen, F. J. and Mitchell, R. N. (2004). Natural Materials in: Biomaterial Sciences an Introduction to Materials in Medicine. Ratner, B. D., Hoffman, A. S., Schoen, F. J. and Lemons, J. E (eds). 2nd Edition. China: Elsevier, 260-281.

Sonbol, H. (2018). Extracellular matrix remodeling in human disease. Journal of Microscopy and Ultrastructure. **6**, 123.

Song, W., Tang, Y., Qiao, J., Li, H., Rong, B., Yang, S., Wu, Y., and Yan, X. (2017). The comparative safety of genipin versus UVA-riboflavin crosslinking of rabbit corneas. Molecular vision. **23**, 504–513.

Sun, M., Sun, X., Wang, Z., Guo, S., Yu, G. and Yang, H. (2018). Synthesis and Properties of Gelatin Methacryloyl (GelMA) Hydrogels and Their Recent Applications in Load-Bearing Tissue. Polymers. **10**, 1290.

Tamayol, A., Najafabadi, A. H., Aliakbarian, B., Arab-Tehrany, E., Akbari, M., Annabi, N., Juncker, D. and Khademhosseini, A. (2015). Hydrogel Templates for Rapid Manufacturing of Bioactive Fibers and 3D Constructs. Advanced Healthcare Materials. **4**, 2146–2153.

Van Den Bulcke, A. I., Bogdanov, B., De Rooze, N., Schacht, E. H., Cornelissen, M. and Berghmans, H. (2000). Structural and rheological properties of methacrylAmide modified gelatin hydrogels. Biomacromolecules. **1**, 31–8.

Vasile, C., Pamfil, D., Stoleru, E. and Baican, M. (2020). New Developments in Medical Applications of Hybrid Hydrogels Containing Natural Polymers. Molecules. **25**, 1539.

Ventola, C. L. (2014). Medical Applications for 3D Printing: Current and Projected Uses. Pharmacy and Therapeutics. **39**, 704–711.

Vera-Graziano, R., Hernandez-Sanchez, F. and Cauich-Rodriguez, J. V. (1995). Study of crosslinking density in polydimethylsiloxane networks by DSC. Journal of Applied Polymer Science. **55**, 1317–1327.

Yamamoto, M., Miura, N., Ohtake, N., Amagaya, S., Ishige, A., Sasaki, H., Komatsu, Y., Fukudu, K., Ito, T. and Terasawa, K. (2000). Genipin, a metabolite derived from the herbal medicine, Inchin-ko-to, and suppression of Fas-induced lethal liver apoptosis in mice. Gastroenterology. **118** (2), 380–389.

Yamazaki, M. and Chiba, K. (2005). Neurotrophic Effects of Genipin on Neuro2a Cells. Journal of Health Science. **51** (6), 687-692.

Yang, X., Lu, Z., Wu, H., Li, W., Zheng, L and Zhao, J. (2018). Collagen-alginate as bioink for three-dimensional (3D) cell printing based cartilage tissue engineering. Materials Science and Engineering C. **83**, 195–201.

Yannas, I. V. (2004). Natural Materials in: Biomaterial Sciences an Introduction to Materials in Medicine. Ratner, B. D., Hoffman, A. S., Schoen, F. J. and Lemons, J. E (eds). 2nd Edition. China: Elsevier, 127-137.

Yoon, H. J., Shin, S. R., Cha, J. M., Lee, S-H., Kim, J-H., Do, J. T., Song, H. and Bae, H. (2016). Cold Water Fish Gelatin Methacryloyl Hydrogel for Tissue Engineering Application. PLoS One. **11**, e0163902.

Yu, S. H., Wu, S. J., Wu, J. Y., Wen, D. Y. and Mi, F. L. (2015). Preparation of fucoidan-shelled and genipin-crosslinked chitosan beads for antibacterial application. Carbohydrate Polymers. **126**, 97–107.

Yue, K., Trujillo-de Santiago, G., Alvarez, M. M., Tamayol, A., Annabi, N. and Khademhosseini, A. (2015). Synthesis, properties, and biomedical applications of gelatin methacryloyl (GelMA) hydrogels. Biomaterials. **73**, 254–71.

Zhang, Y., Zhou, D., Chen, J., Zhang, X., Li, X., Zhao, W. and Wu, T. (2019). Biomaterials Based on Marine Resources for 3D Bioprinting Applications. Marine Drugs. **17**, 555.

Zhao, X., Lang, Q., Yildirimer, L., Lin, Z. Y., Cui, W., Annabi, N., Ng, Kee, W., Dokmeci, M. R., Ghaemmaghami, A. M. and Khademhosseini, A. (2016). Photocrosslinkable Gelatin Hydrogel for Epidermal Tissue Engineering. Advanced Healthcare Materials. **5**, 108–118.

Zheng, J., Zhu, M., Ferracci, G., Cho, N-J. and Lee, B. H. (2018). Hydrolytic Stability of MethacrylAmide and Methacrylate in Gelatin Methacryloyl and Decoupling of Gelatin MethacrylAmide from Gelatin Methacryloyl through Hydrolysis. Macromolecular Chemistry and Physics. **219**, 1800266.

Zhu, M., Wang, Y., Ferracci, G., Zheng, J., Cho, N-J. and Lee, B. H. (2019). Gelatin methacryloyl and its hydrogels with an exceptional degree of controllability and batch-to-batch consistency. Scientific Reports. **9**, 6863.

CHAPTER 5
THE PROGRESSION TOWARDS PERSONALISED AND CUSTOM PATIENT TREATMENTS FOR NEURAL INJURIES THROUGH THE DEVELOPMENT OF CUSTOM-NEURAL-SCAFFOLDS (C-N-S)

Abstract

In spite of the promising nerve regeneration research, the lack of a clinical therapeutic to completely restore neurological function is still ongoing and the demand in providing patients with a successful therapeutic outcome is ever increasing. With the advancements in 3D bioprinting, custom scaffolds with a predetermined size and shape have been successfully fabricated, which can be utilised in nerve damage regenerative attempts to potentially aid in the regaining of nerve function. With the documented success of GPU implementation utilised for image-guided surgeries of tubular and organ structures, we propose the implementation of known processing methods as a means to drastically decrease the time required to process medical images related to nerve damage. In addition, we further propose that the merging of medical image cropping and 3D printing techniques provides a novel approach for providing patient specific Customized-Neural-Scaffolds (C-N-S) for patients suffering with newly acquired nerve damage. Lastly, we provide a proposed schematic which incorporates the implementation of GPUs and 3D printing, which we propose will beneficially decrease the waiting times for medical staff to provide patients with customized neural treatments.

5.1 Impact Statement

Nerve damage, which can be devastating, triggers several biological cascades, which results in the insufficiencies of the human nervous system to provide complete nerve repair and regain of function. Since no therapeutic strategy exists to provide immediate attention and intervention to patients with newly acquired nerve damage, we propose a strategy in which accelerated medical image processing through GPU implementation and 3D printing are combined to produce a time efficient, patient-specific (Custom-Neural-Scaffold) solution to nerve damage. This work aims to beneficially shorten the time required for medical decision-making so that improved patient outcomes are achieved.

5.2 Introduction

The nervous system plays an undeniable role in the functioning of several bodily systems, including but not limited to, the coordination of locomotion, sensory perception, various aspects of homeostasis and the propagation of information around the body.[1] Nerve system damage can be caused by physical trauma to the nerve fibre or through neurodegenerative

disease mechanisms and affects both the peripheral nervous system (PNS) and the central nervous system (CNS) (Steward *et al.,* 2013). In higher organisms with limited and variable nerve regeneration capabilities (largely attributed to the surrounding nerve environment), regeneration can be achieved (injury dependent) in the PNS whereas regeneration in the CNS is limited due to a slower clearance of injury matter, the formation of an astroglial scar and the impedance of neural impulses (Benfey and Aguayo, 1982; David and Aguayo, 1981; Houschyar *et al.,* 2016; Huebner and Strittmatter, 2009; Richardson *et al.,* 1980; Steward *et al.,* 2013). To restore neurological function, effective axonal communication must be established before, throughout and after the injury gap (Guo *et al.,* 2007). Despite a plethora of promising nerve regeneration studies, we are yet to achieve a successful clinical therapeutic to overcome the poor regenerative abilities of the human nervous system and provide complete regain of neural functioning (Fenrich and Gordon, 2004; Gordon, 2016; Huang and Huang, 2006; Moattari *et al.,* 2018; Pinho *et al.,* 2016, Williams, 2014).

Owing to the fact that injury matter can lead to further nerve trauma, medical imaging has become a fundamental tool in the evaluation of sustained nerve damage (Shah and Ross, 2016; Stoll *et al.,* 2013). Medical imaging modalities, namely Magnetic Resonance Imaging (MRI) and Computed Tomography (CT) Scans are the most common imaging techniques in assessing patient nerve damage (Shah and Ross, 2016, Tins, 2017). Medical imaging plays a vital role in, amongst others: evaluating preoperative and postoperative patient data, patient diagnosis and injury characterisation, confirmation of the precise location of the nerve damage, assessment of the stability of the damaged area, rapid medical decision making (including in-surgery decisions) and surgical planning as well as assisting in avoiding further neurological deterioration (Guarnieri *et al.,* 2016; Munera *et al.,* 2012; Shah and Ross, 2016; Thakkar *et al.,* 2012; Tins, 2017). Despite medical imaging providing invaluable assistance in the evaluation of patient nerve damage (Munera *et al.,* 2012; Ohana *et al.,* 2014; Shah and Ross, 2016; Stoll *et al.,* 2013), there are still pertinent challenges surgeons face during surgery. During surgery, injury and trauma to the nerve may cause abnormalities in the known nerve anatomy and hence, the anatomy may vary from individual to individual. In addition, injury matter may enter the nerve fibre and further influence the nerve anatomy. Additionally, the presence of water molecules along the nerve fibre, makes it increasingly more difficult to ascertain the exact outline and orientation of the nerve fibre (Saito *et al.,* 2018). Furthermore, in spite of the fact that medical imaging renders images in 3D, surgeries guided by images are limited as 3D images have to be viewed on flat screens and cannot provide a sufficient and complete understanding of the injury pathology (Rengier *et al.,* 2010. Therefore, standard imaging modalities alone cannot provide all the diagnostic evaluations required for all nerve injury cases.

As image guided surgeries become more popular, the introduction of algorithmic image analysis has begun to improve certain setbacks experienced by the standard imaging modalities. Regardless of the computational benefits, such requirements are time consuming and are not feasible for time-sensitive operations (Smistad *et al.,* 2015). In response, the introduction of powerful Graphical Processing Units (GPUs) has seen high-speed, more affordable and more energy efficient medical image processing in comparison to Central Processing Units (CPUs) (Smistad *et al.,* 2015). In addition, it is widely accepted that the entire medical dataset does not have to be computed and therefore, the pre-processing of medical image data (image simplification (Kaur and Kaur, 2014) and visualisation of the anatomical structures of interest (Smistad *et al.,* 2015) has become more popular in the clinical setting as a smaller dataset processing equates to faster processing times (Smistad *et al.,* 2014). Moreover, parallel GPU architecture allows for commands to be run in parallel to substantially decrease possessing time, however this is not an infinite feature as speedup is governed by the algorithm's sequential fraction (Smistad *et al.,* 2015).

The introduction of 3D bioprinting in various tissue engineering applications has greatly improved nerve regeneration attempts (Petcu *et al.,* 2018). This is due to the fact that complex nerve constructs can be designed to closely mimic the native shape of the nerve requiring replacement (Petcu *et al.,* 2018). Recent advancements in 3D printing technology has enabled researchers to fabricate scaffolds with defined dimensions, shapes and pore structures to control properties for various tissue regeneration applications (Giannitelli *et al.,* 2014; Seol *et al.,* 2012). Therefore, the current advancements in 3D bioprinting has opened many doors with regards to customized patient treatment (Hourd *et al.,* 2015; Ligon *et al.,* 2017; Rengier *et al.,* 2010). In addition, an article published by Rengier *et al*., 2010 reviewed the use of medical imaging to 3D print constructs to improve patient care, surgical planning and aid in the design of customized tissues and implants (Rengier *et al*., 2010). In terms of 3D bioprinting technologies, four main bioprinting techniques have emerged, namely: Stereolithography, laser-assisted 3D bioprinting, extrusion 3D bioprinting and inkjet 3D bioprinting (Derakhshanfar *et al.,* 2018; Donderwinkel *et al.,* 2017; Kačarević *et al.,* 2018). Each technology satisfies different criteria during the printing process and depending on the requirements of the fabricated structure, the appropriate bioprinting method will be selected (Donderwinkel *et al.,* 2017; Kačarević *et al.,* 2018). A brief comparison between these technologies is presented in **Table 5.1**. Of the various 3D printing methods, extrusion-based 3D bioprinting is the most common technique used in tissue regeneration and regenerative medicine (Zhang *et al.,* 2017). Extrusion based 3D bioprinting is preferred for many reasons, including its capacity to fabricate constructs using multiple bioink types (Ozbolat and

Hospodiuk, 2016; Zhang *et al.,* 2017), ease of operation and scalability (Ozbolat and Hospodiuk, 2016) whilst being a relatively low-cost production method (Zhang *et al.,* 2017). Moreover, extrusion-based 3D bioprinting utilises a computer software program, for example Computer-Aided Design (CAD), to design and/or load medical image files (CT and MRI scans) (Giannitelli *et al.,* 2014) to print the intended scaffold (Ozbolat and Hospodiuk, 2016).

Table 5.1: A brief comparison of the four most common bioprinting methods

Parameters	Stereolithography (SLA)	Laser-assisted 3D bioprinting (LAD)	Extrusion bioprinting	Inkjet 3D bioprinting
Technique summary	An additive manufacturing technique utilising light to photocrosslink a photocurable bioink in a layer-by-layer manner (Aljohani *et al.,* 2018; Derakhshanfar *et al.,* 2018; Guvendiren *et al.,* 2016; Jessop *et al.,* 2017, Kačarević *et al.,* 2018; Mandrycky *et al.,* 2016)	Technique involves the deposition and transfer of bioink/cells either using a pulsed laser or in a laser beam (Bishop *et al.,* 2017; Derakhshanfar *et al.,* 2018 Donderwinkel *et al.,* 2017; Jessop *et al.,* 2017; Kačarević *et al.,* 2018)	Technique involves the dispensing of a viscous bioink through a nozzle using pneumatic or mechanical forces (Bishop *et al.,* 2017; Donderwinkel *et al.,* 2017; Jessop *et al.,* 2017; Kačarević *et al.,* 2018; Murphy and Atala, 2014)	A technique involving a non-contact approach using either piezoelectric, thermal or electromagnetic forces to eject consecutive drops of a bioink onto a chosen substrate (Bishop *et al.,* 2017; Jessop *et al.,* 2017; Kačarević *et al.,* 2018; Murphy and Atala, 2014)
Viscosity	No limitation (Mandrycky *et al.,* 2016; Murphy and Atala, 2014; Yue *et al.,* 2016)	1-300 mPa/s (Derakhshanfar *et al.,* 2018; Murphy and Atala, 2014; Yue *et al.,* 2016)	30 mPa/s to > 6 x 10^7 mP/s (Aljohani *et al.,* 2018; Derakhshanfar *et al.,* 2018; Murphy and Atala, 2014; Yue *et al.,* 2016)	3.5 to 12 mPa/s (Aljohani *et al.,* 2018; Derakhshanfar *et al.,* 2018; Murphy and Atala, 2014; Yue *et al.,* 2016)
Cell density	Medium <10^8 cells/mL (Murphy and Atala, 2014)	Medium <10^8 cells/mL (Derakhshanfar *et al.,* 2018; Murphy and Atala, 2014; Yue *et al.,* 2016)	High (Aljohani *et al.,* 2018; Bishop *et al.,* 2017; Derakhshanfar *et al.,* 2018; Murphy and Atala, 2014; Yue *et al.,* 2016)	Low <10^6 cells/mL (Aljohani *et al.,* 2018; Derakhshanfar *et al.,* 2018; Murphy and Atala, 2014; Yue *et al.,* 2016)
Cell viability	> 85 % (Aljohani *et al.,* 2018; Derakhshanfar *et al.,* 2018; Murphy and Atala, 2014)	> 95 % (Kačarević *et al.,* 2018; Mandrycky *et al.,* 2016; Murphy and Atala, 2014)	40 – 80 % (Aljohani *et al.,* 2018; Bishop *et al.,* 2017)	> 85 % (Aljohani *et al.,* 2018; Bishop *et al.,* 2017; Derakhshanfar *et al.,* 2018)
Resolution	High (Aljohani *et al.,* 2018; Jessop *et al.,* 2017; Murphy and Atala, 2014; Wang *et al.,* 2016; Yue *et al.,* 2015)	High (Aljohani *et al.,* 2018; Jessop *et al.,* 2017; Murphy and Atala, 2014; Yue *et al.,* 2015)	Moderate (Aljohani *et al.,* 2018; Murphy and Atala, 2014; Yue *et al.,* 2015)	High (Aljohani *et al.,* 2018; Bishop *et al.,* 2017; Jessop *et al.,* 2017; Kačarević *et al.,* 2018; Murphy and Atala, 2014; Yue *et al.,* 2015)
Print speed	Fast (Derakhshanfar *et al.,* 2018; Murphy and Atala, 2014; Yue *et al.,* 2015)	Medium (Derakhshanfar *et al.,* 2018; Jessop *et al.,* 2017; Murphy and Atala, 2014; Yue *et al.,* 2015)	Slow (Aljohani *et al.,* 2018; Derakhshanfar *et al.,* 2018; Jessop *et al.,* 2017; Murphy and Atala, 2014; Yue *et al.,* 2015)	Fast (Aljohani *et al.,* 2018; Bishop *et al.,* 2017; Jessop *et al.,* 2017; Kačarević *et al.,* 2018; Murphy and Atala, 2014; Yue *et al.,* 2015)
Cost	Low (Aljohani *et al.,* 2018; Derakhshanfar *et al.,* 2018; Murphy and Atala, 2014; Yue *et al.,* 2015)	High (Aljohani *et al.,* 2018; Bishop *et al.,* 2017; Derakhshanfar *et al.,* 2018; Jessop *et al.,* 2017; Kačarević *et al.,* 2018; Murphy and Atala, 2014; Yue *et al.,* 2015)	Medium (Aljohani *et al.,* 2018; Bishop *et al.,* 2017; Derakhshanfar *et al.,* 2018; Jessop *et al.,* 2017; Murphy and Atala, 2014; Yue *et al.,* 2015)	Low (Aljohani *et al.,* 2018; Bishop *et al.,* 2017; Derakhshanfar *et al.,* 2018; Kačarević *et al.,* 2018; Murphy and Atala, 2014; Yue *et al.,* 2015)
Vertical printing capabilities	Good (Aljohani *et al.,* 2018; Derakhshanfar *et al.,* 2018)	Medium to low (Aljohani *et al.,* 2018; Derakhshanfar *et al.,* 2018; Jessop *et al.,* 2017)	Good (Aljohani *et al.,* 2018; Derakhshanfar *et al.,* 2018)	Poor (Aljohani *et al.,* 2018; Derakhshanfar *et al.,* 2018)
Advantages	Lower shear pressures due to nozzle-free approach (Kačarević *et al.,* 2018)	Clogging is avoided due to nozzle-free approach, deposition of bioink in solid or liquid phase (Donderwinkel *et al.,* 2017; Derakhshanfar *et al.,* 2018; Jessop *et al.,* 2017)	Can control scaffold porosity, ability to bioprint with high cell densities (Bishop *et al.,* 2017; Derakhshanfar *et al.,* 2018; Kačarević *et al.,* 2018)	Precise cellular positioning, can print low viscosity bioinks (Derakhshanfar *et al.,* 2018; Kačarević *et al.,* 2018)
Disadvantages	Requires intense UV curing (possible cell and DNA damage), possible cytotoxicity from photoinitiators, lengthy post-processing times, few compatible materials (Kačarević *et al.,* 2018; Guvendiren *et al.,* 2016)	Possible cell and DNA damage from laser exposure, low scalability and suitability (Donderwinkel *et al.,* 2017; Derakhshanfar *et al.,* 2018; Kačarević *et al.,* 2018)	Technique is sensitive to bioink viscosity – if incorrect leakage can occur, printing pressures could potentially alter cellular morphology, shape and function (Jessop *et al.,* 2017; Kačarević *et al.,* 2018)	Potential for higher cellular death due to higher nozzle temperatures, nozzles prone to clogging, continuous flow not sustained (Derakhshanfar *et al.,* 2018; Jessop *et al.,* 2017; Kačarević *et al.,* 2018)

Irrespective of the benefits introduced by 3D bioprinting, there are limitations with regards to neural 3D bioprinting across all 3D bioprinting method techniques. The biggest challenge with regards to neural 3D bioprinting is the lack of suitable bioinks with adequate biomimetic properties (Hsieh and Hsu, 2015; Lee *et al.,* 2018), for example the native electrical conductivity of the nerve fibre (Lee *et al.,* 2018). In addition, factors including but not limited to: bioink viscosity, bioink cytocompatibility, ability of the bioink to mimic the native ECM and the capability of the final scaffold to retain structural integrity are all aspects that have limited neural tissue 3D bioprinting (Hsieh and Hsu, 2015; Knowlton *et al.,* 2018; Lee *et al.,* 2018). Lastly, under current frameworks, customized 3D printed constructs face notable regulatory challenges with regards to software system chain control and the role customized constructs play in the variation in performance of constructs post-surgery (Hourd *et al.,* 2015).

In spite of the regulatory challenges regarding customized 3D printed constructs, the need for customized treatments is in high demand. Due to the nature of nerve damage, injuries are largely patient specific and current options are inadequate in repairing complex lesions. For this reason, personalised constructs can incorporate injury- and patient-specific considerations to customise designs on a per patient basis. Therefore, customized patient treatments may be able to provide ground breaking solutions to overcoming the current challenges in the repair of complex nerve injuries through the development of Custom-Neural-Scaffolds (C-N-S) (Mobini *et al.,* 2017).

5.3 **Problem Statement**

As previously mentioned, there is no known therapeutic that is able to completely restore neurological function. To compound the issue, nerve damage is particularly patient specific and nerve damage is complex as inflammatory events post injury lead to the progressive loss of nervous tissue and therefore, nerve functioning (Oudga *et al.,* 2005). The schematic shown in **Figure 5.1** provides a summary of the current approach in assisting and diagnosing newly acquired nerve damage in patients (Chin *et al.,* 2018; Cleveland Clinic, 2017; Mayo Clinic, 2018). From the schematic it is evident that the procedure is laborious (due to the wait period for diagnosis) whilst only providing palliative support to patients. Whilst this is the best current option for patients, it is evident that a successful therapeutic with reduced waiting times is in high demand for patient living with newly sustained nerve damage. Interestingly, no study to the best of our knowledge, has proposed the use of medical images coupled with GPU implementation and 3D bioprinting as a means to provide a solution to the current shortfalls in nerve regeneration.

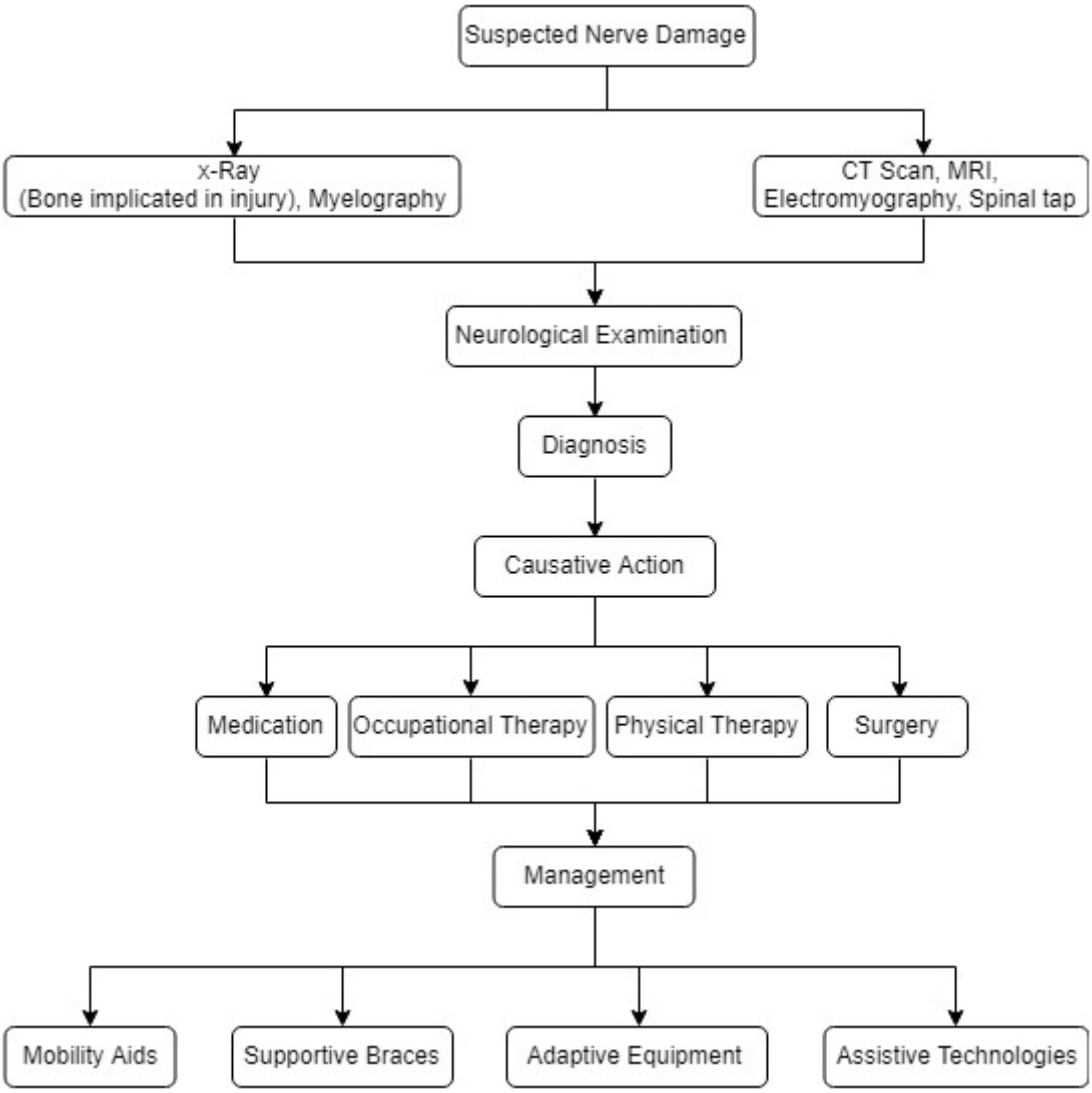


Figure 5.1: Schematic displaying the current workflow used in the health care setting to diagnose potential nerve damage as well as the available treatment and management options.

5.4 **Our solution**

Since no study has proposed the use of medical images and GPU implementation in an attempt to provide patient specific 3D bioprinted C-N-S, this technical note proposes the implementation of data image processing algorithms as a means to drastically decrease the time required to process medical images related to nerve damage events. In addition, we propose that with GPU utilisation and implementation from processing only the area of interest where nerve damage has occurred to the generation of the Gcode for 3D printing, we can achieve time efficient data processing to potentially produce patient C-N-S. Lastly, we envisage the development of an algorithm to provide a mechanism of examining the data (to ensure no computing errors have occurred) prior to the printing process.

5.5 **Proposed Approach for GPU Implementation in Producing C-N-S**

5.5.1 GPU Implementation in Medical Imaging

As medical imaging instruments increase in sophistication, the sheer volume of data processing in this field has exploded to a point where processing time has become the limiting factor in further advancements (Pratx and Xing, 2011). A modern-day solution to reducing processing time and increasing output speeds is with the implementation of parallel GPU systems (Castaño-Díez *et al.,* 2008; Eklund *et al.,* 2013; Pratx and Xing, 2011). The use of GPUs was incorporated originally into CT modalities as the reconstruction of CT data requires computationally intensive algorithms when compared to MRI data that requires a more simple, fast inverse Fourier Transform image reconstruction (Eklund *et al.,* 2013). Despite the benefits of GPU implementation, GPU memory is limited and may in fact limit the processing of large datasets (Smistad *et al.,* 2015; Smistad *et al.,* 2014).

The processing of pre-operative data from differing imaging modalities has gained popularity in image guided surgeries, such as in surgeries related to tubular structures (blood vessels and airways) and complete organ structures (Gibson *et al.,* 2018; Smistad *et al.,* 2015). With this in mind, the processing of such data has to be completed as fast as possible for patients requiring surgery. The results from a study performed by Smistad and co-workers indicated that to achieve the desirable speed of processing the area of interest within the image, various algorithms performed on parallel GPU systems was shown to significantly reduce the time required to process pre-operative medical image data (Smistad *et al.,* 2015). This study highlighted that real-time processing of data is possible and if utilised, could provide an interesting platform in providing the possible successful therapeutic outcomes required for nerve damage. To the best of our knowledge, processing of nerve bundles has been achieved using MRI images however, GPUs usage was not implemented in this study (Dalca *et al.,* 2011).

5.5.2 Use of Medical Imaging and the Incorporation of GPUs in Nerve Regenerative Attempts

Since MRI data has shown to have a higher resolution than that of CT scans in certain medical applications (Levin *et al.,* 1987; Levine *et al.,* 1987), the extraction of nerve damage from MRI data is advisable. In spite of this, it would be costly to implement the usage of MRI scanning throughout the health care sector. Therefore, this proposal is for the usage of images generated from both MRI and CT modalities. Due to the nature of nerve damage, we propose that successful segmentation and centreline extraction, utilising known algorithms in the literature, can be employed to crop, process, extract and reconstruct the images of the defined region where the damage has been sustained. This will help to reduce the time spent on the

extraction and reconstruction of the damaged area of the nerve requiring replacement. It is further proposed that following image extraction and reconstruction, further algorithm development and GPU implementation can be applied to ensure quick slicing, data checking and Gcode generation. Following this, the high-resolution data (from the medical images) will be sent to the 3D printer to print the patient specific scaffolds (C-N-S). This could ultimately speed up the entire pre-processing of data from the capturing of the image to the printing aspect, which will have a direct benefit for patients with sustained nerve damage.

5.6 Overview of the proposed method

A review of the available literature indicated that there are numerous algorithms that have been developed and/or modified for the medial application at hand. As such, no one set of algorithms has been proposed to be the 'gold standard' for all medical imagining processing requirements. Despite the number of algorithms proposed in the literature, this article will only consider investigations utilising extraction and image segmentation in the processing of medical images for different anatomical regions of the body. Additionally, this article will consider algorithms for both hollow tubular structures and solid organs as nervous tissue are rod-like structures with a dense bundling of axons and other associated structures (Sunderland, 1990).

Of the papers reviewed, despite the fact that different paths are selected to process the images, the outcome of the image processing is the same. That is the generation of a segmented image of the region of interest. This section aims to provide an overview of the main steps to produce a segmented image that can be utilised for, amongst others: surgical planning, intraoperative data analysis and diagnosis. **Figure 5.2** provides an overview of the procedural proposal from the capturing of the image to the fabrication of the 3D bioprinted patient Customized-Neural-Scaffold.

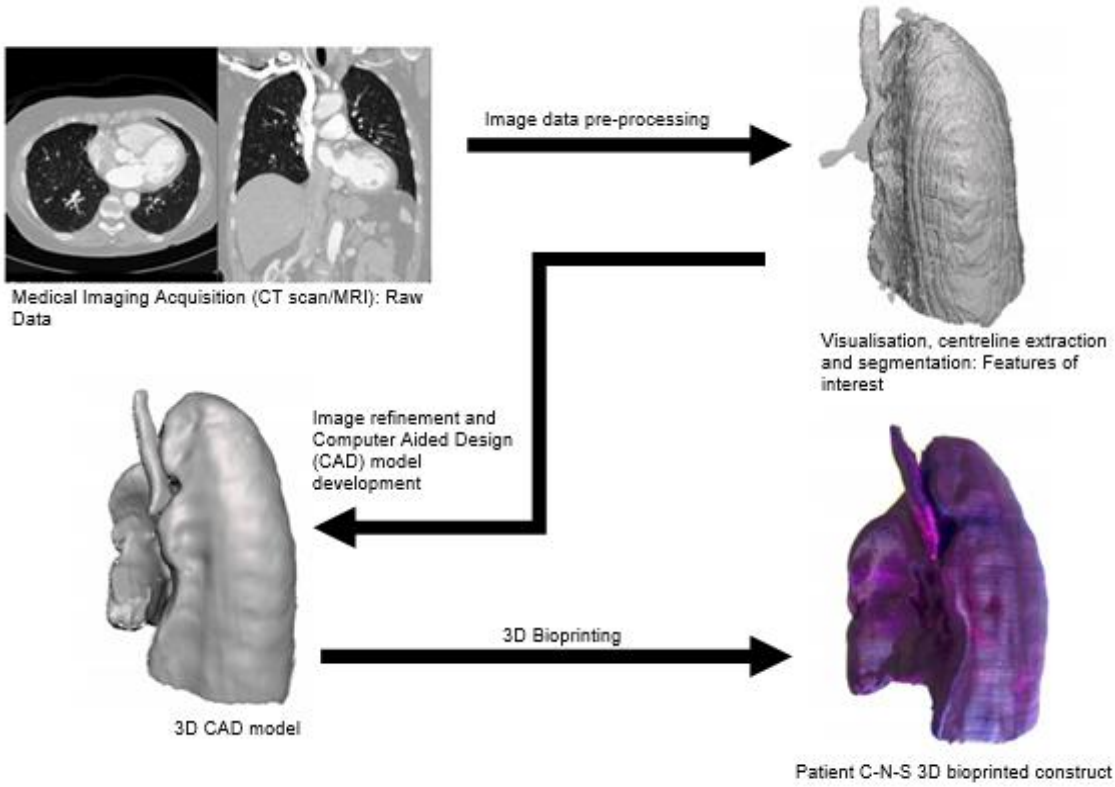


Figure 5.2: Schematic providing an overview of the proposed procedure. The steps are as follows: The area of interest is captured, the image is processed and refined, a CAD model is developed and lastly, the patient Customized-Neural-Scaffold is bioprinted. This image is adapted from Bücking *et al.,* 2017 under the Creative Commons Legal Code Attribution 4.0 International Licence.

5.6.1 Data Pre-Processing

Due to the fact that GPU memory is limited, the computing of entire medical image datasets may not be possible (Smistad *et al.,* 2014, Smistad *et al.,* 2015). Additionally, medical data contains large amounts of data volume that are computer intensive, time consuming and unnecessary to compute if surgeons and medical staff are only interested in a defined region of the image (Bücking *et al.,* 2017; Lesage *et al.,* 2009; Reynisson *et al.,* 2015; Smistad *et al.,* 2014). According to Smistad *et al.,* 2014, anatomical areas considered to be outside of the region of interest are generally found at the borders of the captured image (Smistad *et al.,* 2014). With this in mind, to ensure optimal GPU performance, with the employment of a cropping algorithm (Reynisson *et al.,* 2015; Smistad *et al.,* 2014) or generic down sampling and quantization techniques (Lesage *et al.,* 2009), the volume of medical data required to be processed is beneficially minimised and in turn execution time is advantageously reduced (Reynisson *et al.,* 2015; Smistad *et al.,* 2014). This is in turn, helps to ensure that the first stage in efficient data computation can occur timelessly before surgery. Due to the fact that cropping of datasets has been successfully achieved for airways (Lo *et al.,* 2012; Reynisson

et al., 2015; Smistad *et al.,* 2014), blood vessels (Lesage *et al.,* 2009; Narayanaswamy *et al.,* 2010; Yang *et al.,* 2018) and coronary arteries (Yang *et al.,* 2012) as well as for the brain (Smistad *et al.,* 2014), liver (Okada *et al.,* 2012; Smistad *et al.,* 2014; Yang *et al.,* 2018), kidneys, spleen, aorta, gallbladder, pancreas and vena cava (inferior) (Okada *et al.,* 2012), we propose the need for a cropping algorithm to reduce the data size for medical images relating to newly acquired nerve damage.

In addition to data cropping, a smoothing data algorithm or a regulating algorithm needs to be utilised to reduce the dataset's sensitivity to noise, contrast and size (**Figure 5.2**) (Reynisson *et al.,* 2015; Smistad *et al.,* 2014). Furthermore, smoothing will limit the chance of data leakage (data falling outside the area of interest) (Reynisson *et al.,* 2015). This is especially required for CT scan image data (Reynisson *et al.,* 2015; Smistad *et al.,* 2014). Due to the fact that cropping of datasets has been successfully achieved for the airways (Reynisson *et al.,* 2015; Smistad *et al.,* 2014) and vessels (Smistad *et al.,* 2014), we propose the usage of a smoothing algorithm to limit data leakage for nerve damage imaging.

Due to the fact that progressive loss of neural tissue occurs shortly after the primary injury, especially in spinal cord trauma (Oudega *et al.,* 2005), we propose the implementation of the above-mentioned type of algorithms for nervous tissue image pre-processing. With time efficient data pre-processing, we propose that decreasing the time required for the pre-processing image step will beneficially decrease the time required for the whole workflow and therefore, can aid in quicker medical responses.

5.6.2 Centerline Extraction and Segmentation

Following image pre-processing, image centerline extraction and image segmentation need to be performed on the cropped and smoothed dataset. In brief, centreline extraction represents the area of interest at a structural level as a line is positioned to run through the centre of the intended structure in the image (Smistad, 2012; Smistad *et al.,* 2015). Moreover, centerline extraction aids in describing 3D shapes exhibiting circular symmetry and is required for the analysis of shape and the processing of the given geometries (Liu *et al.,* 2014). In addition, by performing a centerline extraction, an accurate length of the structure can be obtained, which assists in the virtual planning and navigation of surgeries associated with tubular structures, for example the aorta and coronary arteries (Liu *et al.,* 2014). Since the implementation of a GPU to perform parallel centerline algorithmic calculations, the previous limitations of poor accuracy and extensive computation times (CPU implementation) have been resolved (Munera *et al.,* 2012). Due to the fact that centerline extraction has been successful in tubular structures, we envisage a similar algorithm implementation (after

cropping and smoothing) working for nerve tissue medical image data, despite its compact nature (Sunderland, 1990).

Following centerline extraction, the modified dataset will then be optimized using an image segmentation algorithm. Since this proposal is for a decrease in GPU processing time, we propose the use of a semi-automated segmentation algorithm so that time efficiency and accuracy can be merged (automatic segmentation sacrifices accuracy (Yang *et al.,* 2018) and manual segmentation is time consuming (Yang *et al.,* 2018) and in the development of the proposed C-N-S neither are not be feasible). Principally, image segmentation is employed to relate individual elements with a common property (i.e. relating to a common organ) (Smistad *et al.,* 2015). Furthermore, image segmentation permits the visualisation of the structure of interest, whilst removing additional information deemed unnecessary. Additionally, image segmentation allows for the analysis of further features found within the structure of interest, for example tumour volume calculations (Smistad *et al.,* 2015). More importantly, segmentation allows for patient- and injury-specific considerations to be made (Bücking *et al*., 2017; Smistad *et al.,* 2015). In a paper by Bücking *et al*., 2017, they provide an overview of freely available segmentation software that are applicable to any anatomical region of the body (Bücking *et al*., 2017) and because of this, these software's need to be considered in the production of patient C-N-S. Lastly, the resulting image of the computation is a 3D rendering of the structure of interest (Figure 2) (Bücking *et al*., 2017). Due to the fact that anatomical anomalies such as aneurisms, stenoses, stents and calcifications can also benefit from such modelling (Lesage *et al.,* 2009), we see potential for image segmentation to aid in the detection of traumatic nerve damage as such modelling may assist in the detection of foreign matter in and around the injured nerve fibre.

5.6.3 3D Bioprinting

The final stage in the formation of patient C-N-S is post processing and entails the conversion of the segmented image into a 3D bioprintable format. To achieve this, the segmented image needs to be converted into a 3D mesh (**Figure 5.2**), using a CAD tool, so that it is in a form that is able to be bioprinted (Gcode). Post-processing is required to repair any segmentation and staircasing errors as well as removing additional structures that are unnecessary (Bücking *et al*., 2017). Furthermore, this implementation has seen the successful bioprinting of the lungs, ribs and liver (Bücking *et al*., 2017). Due to the repair aspect of the post-processing stage, we propose this method to be used for neural tissue medical imaging as due to the nature of nerve injuries any checking mechanisms will ensure the C-N-S will be as patient specific as it can be.

5.7 Patient Implications, Considerations and Limitations of C-N-S

Due to the fact that the patient is the main priority in any clinical setting, health care professionals need to harness any opportunities to decrease time spent on unnecessary tasks such as medical image processing. Since there is a limited time period in which doctors can attempt to assist patients brought into casualty with newly sustained nerve damage, a decrease in medical image processing will be extremely beneficial to the patient and the medical staff. Since GPU implementation will shorten the time required to perform computationally intensive calculations (Castaño-Díez *et al.,* 2008, Eklund *et al.,* 2013; Pratx and Xing, 2011), cropping the data sets to the region of interest will further shorten the time required for processing (**Figure 5.3**) (Smistad *et al.,* 2015). From the schematic it is evident that despite the extra steps involved, the implementation of GPU systems will beneficially reduce the time required to process the data and diagnose the condition before patients undergo nerve replacement surgeries. In addition, 3D printing of the patient specific C-N-S has the potential to provide the successful nerve damage clinical therapeutic due to the fact that the C-N-S will be derived from high resolution patient images.

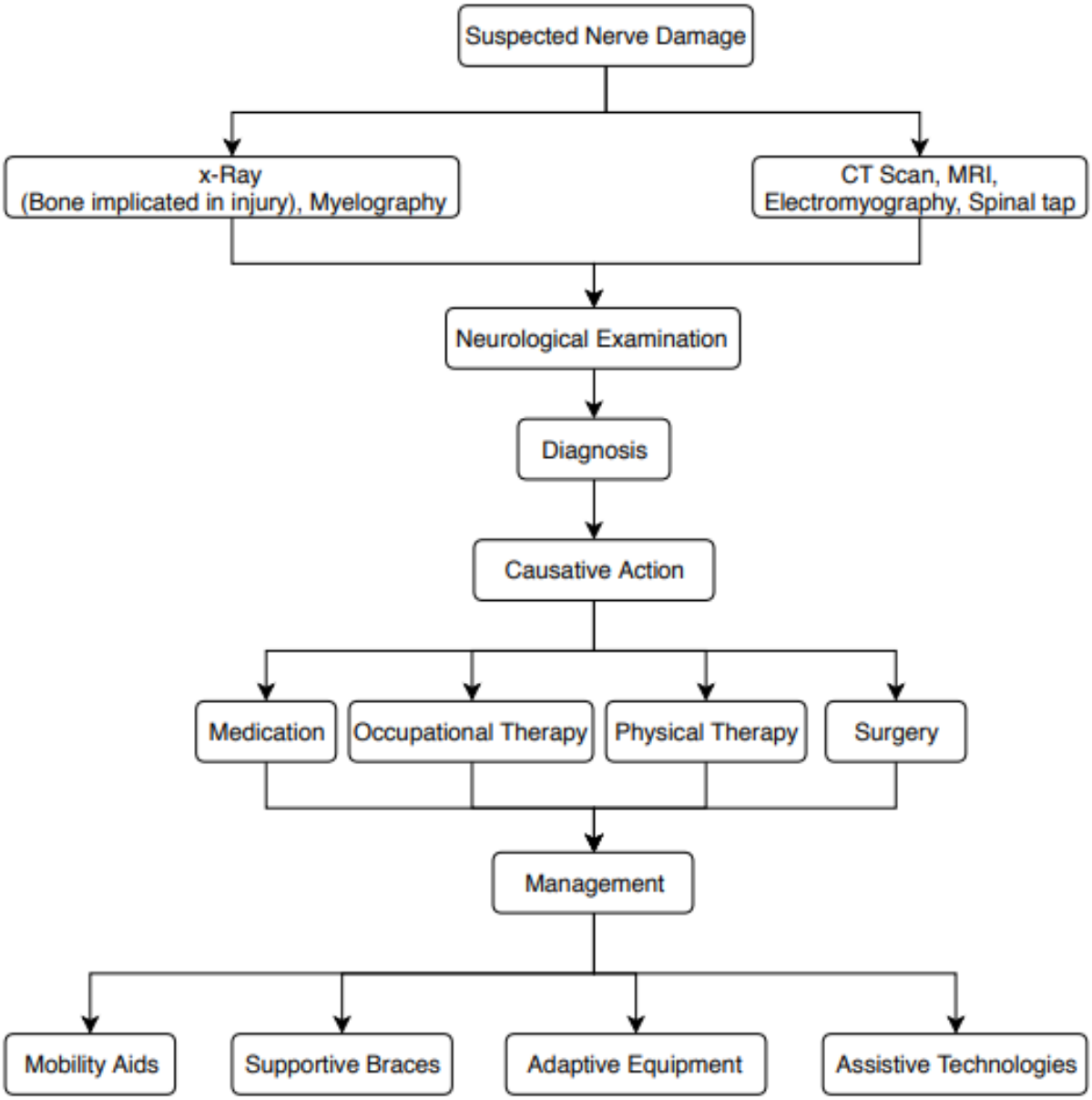


Figure 5.3: Schematic displaying the proposed workflow that should be implemented in health care settings to diagnose potential nerve damage. This proposal provides a time efficient solution to preparing patients for surgery, which can potentially aid in patient regaining the functioning of the nerve using the fabricated C-N-S.

Despite the foreseeable benefits of C-N-S implementation, there are several considerations that have to be highlighted. Since this proposal is for the usage of common medical imaging equipment, 3D medical scanners should be considered as they are able to acquire free-form information from complex and hard-to-scan anatomical structures without the need to hold a defined pose. In addition, 3D scanners are also compatible with 3D printers and therefore need to be considered for nerve damage applications (Haleem and Javaid, 2018; Straub and Kerlin, 2014). Due to the fact that that GPUs will accelerate 3D printer file slicing, it is possible that it may aid in lowering material loss and assist in overall 3D printing optimization. Since extrusion-based 3D bioprinters are known to have low resolution when compared to other

printing methods (Ozbolat and Hospodiuk, 2016), technological advancements in 3D extrusion bioprinters is required to produce constructs with resolution at a similar quality to that of the medical images. In addition to this, wide spread implementation of powerful GPU systems in desktop computers controlling the software for the chosen 3D bioprinter is required to implement this proposal. Although these may be costly considerations, the patients receiving the 3D bioprinted C-N-S will benefit from it with the possibility of improving their quality of life and wellbeing. Due to the inherent limited memory of GPUs systems (Smistad *et al.,* 2014), we propose the consideration and usage of computer-based servers, which could assist in supplying additional processing power, to beneficially decrease the time required for computation even more than GPU systems alone. Lastly, although not covered in this technical note, we envisage the development of algorithms to provide a means of data checking to ensure that the printed structure is as close to "perfect" as possible. To achieve this, algorithms need to be developed to check the data file before the data is sliced in a 3D printing program. Subsequently, once the STL file has been generated, a second algorithm should be developed to verify whether each layer of the patient C-N-S corresponds in dimensions to the layers above and below it. If a discrepancy is found in either of the checks, the algorithm should send out a notification and automatically re-perform the problematic step as well as any steps that follow it. In this way, despite requiring more seconds to re-perform the mistake, the time required for each step is minute and the data will still be processed in real-time. Therefore, even with the mistake, the time required for image processing will still be rescued, whilst proving a more accurate scaffold to be printed.

The limitations to this proposal are that the proposed method is largely for hollow tube structures (tubular structures) whereas nerves are a solid cylindrical structure (Sunderland, 1990). In spite of this, the 2D geometry as well as the volume of the tubular structure cylinder and the nerve cylinder will be similar. Due to the fact that the 2D structure is used to fabricate the 3D structure, the similarities in the 2D structure will allow for the translation from tubular image data processing to nerve damage image processing. Despite this, this limitation has to be kept in mind during data image processing. We propose the merger of algorithms for solid organ structures and tubular structures to overcome the hollow nature of lumen-based anatomical structures. Lastly, the current regulatory challenges facing customized 3D printed constructs cannot be ignored (Hourd *et al.,* 2015). However, this challenge should not limit the progression towards implementing this proposal.

5.8 Conclusion

The proposal of the merging of medical image cropping and 3D printing techniques provides a novel approach for providing patient specific Customized-Neural-Scaffolds (C-N-S) for

patients suffering with newly acquired nerve damage. Since nerve damage is particularly patient specific and nerve damage treatments remain unsuccessful, this proposal provides a possible opportunity to make a difference in patient care. Since medical imagining is the first tear in any nerve damage case, medical imaging processing time remains to be the limiting factor when it comes to patient care. The amalgamation of these concepts will see a beneficial decrease in the processing time of medical images whilst providing patients with C-N-S for their individual injury specifications. Despite the foreseeable benefits, shortfalls in the current infrastructure will affect the implementation of this proposal. In spite of this, we encourage researchers to attempt and implement the proposed structure to hopefully provide the much-needed solution to nerve damage.

5.9 References

Aljohani, W., Ullah, M. W., Zhang, X. and Yang, G. (2018). Bioprinting and Its Applications in Tissue Engineering and Regenerative Medicine. International Journal of Biological Macromolecules, **107** (Part A), 261–275.

Benfey, M. and Aguayo, A. J. (1982). Extensive Elongation of Axons from Rat Brain into Peripheral Nerve Grafts. Nature, **296**, 150–152.

Bishop, E. S., Mostafa, S., Pakvasa, M., Luu, H. H., Lee, M. J., Wolf, J. M., Ameer, G. A., He, T. C. and Reid, R. R. (2017). 3-D Bioprinting Technologies in Tissue Engineering and Regenerative Medicine: Current and Future Trends. Genes & Diseases. **4** (4), 185–195.

Bücking, T. M., Hill, E. R., Robertson, J. L., Maneas, E., Plumb, A. A. and Nikitichev, D. I. (2017). From Medical Imaging Data to 3D Printed Anatomical Models. PLoS One. **12** (5), e0178540.

Castaño-Díez, D., Moser, D., Schoenegger, A., Pruggnaller, S. and Frangakis, A. S. (2008). Performance Evaluation of Image Processing Algorithms on the GPU. Journal of Structural Biology. **164**, 153–160.

Chin, L. S., Mesfin, F. B. and Dawodu, S. T. (2018). Spinal Cord Injuries. Medscape. https://emedicine.medscape.com/article/793582-overview#a1 (Accessed Nov 9, 2018).

Cleveland Clinic. (2017). Paralysis: Diagnosis and Tests. Cleveland Clinic. https://my.clevelandclinic.org/health/diseases/15345-paralysis/diagnosis-and-tests (Accessed Nov 9, 2018).

Dalca, A., Danagoulian, G., Kikinis, R., Schmidt, E. and Golland, P. (2011). Segmentation of Nerve Bundles and Ganglia in Spine MRI Using Particle Filters. Medical Image Computing and Computer-Assisted Intervention. **14** (Part 3), 537–545.

David, S. and Aguayo, A. J. (1981). Axonal Elongation into Peripheral Nervous System “Bridges” after Central Nervous System Injury in Adult Rats. Science. **214** (4523), 931–933.

Derakhshanfar, S., Mbeleck, R., Xu, K., Zhang, X., Zhong, W. and Xing, M. (2018). 3D Bioprinting for Biomedical Devices and Tissue Engineering: A Review of Recent Trends and Advances. Bioactive Materials. **3** (2), 144–156.

Donderwinkel, I., van Hest, J. C. M. and Cameron, N. R. (2017). Bio-Inks for 3D Bioprinting: Recent Advances and Future Prospects. Polymer Chemistry. **8** (31), 4451–4471.

Eklund, A., Dufort, P., Forsberg, D. and LaConte, S. M. (2013). Medical Image Processing on the GPU – Past, Present and Future. Medical Image Analysis. **17** (8), 1073–1094.

Fenrich, K. and Gordon, T. (2004). Canadian Association of Neuroscience Review: Axonal Regeneration in the Peripheral and Central Nervous Systems – Current Issues and Advances. Canadian Journal of Neurological Sciences. **31** (2), 142–156.

Giannitelli, S. M., Accoto, D., Trombetta, M. and Rainer, A. (2014). Current Trends in the Design of Scaffolds for Computer-Aided Tissue Engineering. Acta Biomaterialia. **10** (2), 580–594.

Gibson, E., Giganti, F., Hu, Y., Bonmati, E., Bandula, S., Gurusamy, K., Davidson, B., Pereira, S. P., Clarkson, M. J. and Barratt, D. C. (2018). Automatic Multi-Organ Segmentation on Abdominal CT With Dense V-Networks. IEEE Transactions on Medical Imaging. **37** (8), 1822–1834.

Gordon, T. (2016). Nerve Regeneration in the Peripheral and Central Nervous Systems. The Journal of Physiology. **594** (13), 3517–3520.

Guarnieri, G., Izzo, R. and Muto, M. (2016). The Role of Emergency Radiology in Spinal Trauma. The British Journal of Radiology. **89** (1061), 20150833.

Guo, J., Su, H., Zeng, Y., Liang, Y.-X., Wong, W. M., Ellis-Behnke, R. G., So, K.-F. and Wu, W. (2007). Reknitting the Injured Spinal Cord by Self-Assembling Peptide Nanofiber Scaffold. Nanomedicine: Nanotechnology, Biology and Medicine. **3** (4), 311–321.

Guvendiren, M., Molde, J., Soares, R. M. D. and Kohn, J. (2016). Designing Biomaterials for 3D Printing. ACS Biomaterials Science & Engineering. **2** (10), 1679–1693.

Haleem, A. and Javaid, M. (2018). 3D Scanning Applications in Medical Field: A Literature-Based Review. Clinical Epidemiology and Global Health. **7** (2), 199-210.

Hourd, P., Medcalf, N., Segal, J. and Williams, D. J. (2015). A 3D Bioprinting Exemplar of the Consequences of the Regulatory Requirements on Customized Processes. Regenerative Medicine. **10** (7), 863–883.

Houschyar, K. S., Momeni, A., Pyles, M. N., Cha, J. Y., Maan, Z. N., Duscher, D., Jew, O. S., Siemers, F. and van Schoonhoven, J. (2016). The Role of Current Techniques and Concepts in Peripheral Nerve Repair. Plastic surgery international. **2016**, 1–8.

Hsieh, F.-Y. and Hsu, S. (2015). 3D Bioprinting: A New Insight into the Therapeutic Strategy of Neural Tissue Regeneration. Organogenesis. **11** (4), 153–158.

Huang, Y.-C. and Huang, Y.-Y. (2006). Biomaterials and Strategies for Nerve Regeneration. Artificial Organs. **30** (7), 514–522.

Huebner, E. A. and Strittmatter, S. M. (2009). Axon regeneration in the peripheral and central nervous systems. Results and problems in cell differentiation. **48**, 339–351.

Jessop, Z. M., Al-Sabah, A., Gardiner, M. D., Combellack, E., Hawkins, K. and Whitaker, I. S. (2017). 3D Bioprinting for Reconstructive Surgery: Principles, Applications and Challenges.

Journal of Plastic, Reconstructive & Aesthetic Surgery. **70** (9), 1155–1170.

Kačarević, Ž., Rider, P., Alkildani, S., Retnasingh, S., Smeets, R., Jung, O., Ivanišević, Z. and Barbeck, M. (2018). An Introduction to 3D Bioprinting: Possibilities, Challenges and Future Aspects. Materials. **11** (11), 2199.

Kaur, D. and Kaur, Y. (2014). International Journal of Computer Science and Mobile Computing Various Image Segmentation Techniques: A Review. International Journal of Computer Science and Mobile Computing. **3** (5), 809–814.

Knowlton, S., Anand, S., Shah, T. and Tasoglu, S. (2018). Bioprinting for Neural Tissue Engineering. Trends in Neurosciences. ***41*** (1), 31–46.

Lee, S.-J., Esworthy, T., Stake, S., Miao, S., Zuo, Y. Y., Harris, B. T. and Zhang, L. G. (2018). Advances in 3D Bioprinting for Neural Tissue Engineering. Advanced Biosystems. **2** (4), 1700213.

Lesage, D., Angelini, E. D., Bloch, I. and Funka-Lea, G. (2009). A Review of 3D Vessel Lumen Segmentation Techniques: Models, Features and Extraction Schemes. Medical Image Analysis. **13** (6), 819–845.

Levin, H. S., Amparo, E., Eisenberg, H. M., Williams, D. H., High, W. M., McArdle, C. B. and Weiner, R. L. (1987). Magnetic Resonance Imaging and Computerized Tomography in Relation to the Neurobehavioral Sequelae of Mild and Moderate Head Injuries. Journal of Neurosurgery. **66** (5), 706–713.

Levine, P. A., Paling, M. R., Back, W. C. and Cantrell, R. W. (1987). MRI vs. High-Resolution CT Scanning: Evaluation of the Anterior Skull Base. Otolaryngology–Head and Neck Surgery. 1987. **96** (3), 260–267.

Ligon, S. C., Liska, R., Stampfl, J., Gurr, M. and Mülhaupt, R. (2017). Polymers for 3D Printing and Customized Additive Manufacturing. Chemical Reviews. **117** (15), 10212–10290.

Liu, B., Telea, A. C., Roerdink, J. B. T. M., Clapworthy, G. J., Williams, D., Yang, P., Dong, F., Codreanu, V. and Chiarini, A. (2014). Parallel Centerline Extraction on the GPU. Computers & Graphics. 41 (1), 72–83.

Lo, P., van Ginneken, B., Reinhardt, J. M., Yavarna, T., de Jong, P. A., Irving, B., Fetita, C., Ortner, M., Pinho, R., Sijbers, J., Feuerstein, M., Fabijanska, A., Bauer, C., Beichel, R., Mendoza, C. S., Wiemker, R., Lee, J., Reeves, A. P., Born, S., Weinheimer, O., van Rikxoort, E. M., Tschirren, J., Mori, K., Odry, B., Naidich, D. P., Hartmann, I., Hoffman, E. A., Prokop, M., Pedersen, J. H. and de Bruijne, M. (2012). Extraction of Airways From CT (EXACT'09). IEEE Transactions on Medical Imaging. **31** (11), 2093–2107.

Mandrycky, C., Wang, Z., Kim, K. and Kim, D.-H. (2016). 3D Bioprinting for Engineering Complex Tissues. Biotechnology Advances. **34** (4), 422–434.

Mayo Clinic. (2018). Spinal cord injury. Mayo Clinic. https://www.mayoclinic.org/diseases-conditions/spinal-cord-injury/diagnosis-treatment/drc-20377895 (Accessed Nov 9, 2018).

Moattari, M., Moattari, F., Kaka, G., Kouchesfahani, H. M., Sadraie, S. H. and Naghdi, M. (2018). Comparison of Neuroregeneration in Central Nervous System and Peripheral Nervous System. Otorhinolaryngology Head and Neck Surgery. **3** (4), 1–3.

Mobini, S., Spearman, B. S., Lacko, C. S. and Schmidt, C. E. (2017). Recent Advances in

Strategies for Peripheral Nerve Tissue Engineering. Current Opinion in Biomedical Engineering. **4**, 134–142.

Munera, F., Rivas, L. A., Nunez, D. B. and Quencer, R. M. (2012). Imaging Evaluation of Adult Spinal Injuries: Emphasis on Multidetector CT in Cervical Spine Trauma. Radiology. **263** (3), 645–660.

Murphy, S. V. and Atala, A. (2014). 3D Bioprinting of Tissues and Organs. Nature Biotechnology. **32** (8), 773–785.

Narayanaswamy, A., Dwarakapuram, S., Bjornsson, C. S., Cutler, B. M., Shain, W. and Roysam, B. (2010). Robust Adaptive 3-D Segmentation of Vessel Laminae from Fluorescence Confocal Microscope Images and Parallel GPU Implementation. IEEE Transactions on Medical Imaging 2010. **29** (3), 583–597.

Ohana, M., Moser, T., Moussaouï, A., Kremer, S., Carlier, R. Y., Liverneaux, P. and Dietemann, J.-L. (2014). Current and Future Imaging of the Peripheral Nervous System. Diagnostic and Interventional Imaging. **95** (1), 17–26.

Okada, T., Linguraru, M. G., Hori, M., Suzuki, Y., Summers, R. M., Tomiyama, N. and Sato, Y. (2012). Multi-Organ Segmentation in Abdominal CT Images. In *2012 Annual International Conference of the IEEE Engineering in Medicine and Biology Society*; IEEE, **100**, 3986–3989.

Oudega, M., Moon, L. D. F. and de Almeida Leme, R. J. (2005). Schwann Cells for Spinal Cord Repair. Brazilian Journal of Medical and Biological Research. **38** (6), 825–835.

Ozbolat, I. T. and Hospodiuk, M. (2016). Biomaterials Current Advances and Future Perspectives in Extrusion-Based Bioprinting. Biomaterials. **76**, 321–343.

Petcu, E. B., Midha, R., McColl, E., Popa-Wagner, A., Chirila, T. V and Dalton, P. D. (2018). 3D Printing Strategies for Peripheral Nerve Regeneration. Biofabrication. **10** (3), 032001.

Pinho, A. C., Fonseca, A. C., Serra, A. C., Santos, J. D. and Coelho, J. F. J. (2016). Peripheral Nerve Regeneration: Current Status and New Strategies Using Polymeric Materials. Advanced Healthcare Materials. **5** (21), 2732–2744.

Pratx, G. and Xing, L. (2011). GPU Computing in Medical Physics: A Review. Medical Physics. **38** (5), 2685–2697.

Rengier, F., Mehndiratta, A., von Tengg-Kobligk, H., Zechmann, C. M., Unterhinninghofen, R., Kauczor, H.-U. and Giesel, F. L. (2010). 3D Printing Based on Imaging Data: Review of Medical Applications. International Journal of Computer Assisted Radiology and Surgery. **5** (4), 335–341.

Reynisson, P. J., Scali, M., Smistad, E., Hofstad, E. F., Leira, H. O., Lindseth, F., Nagelhus Hernes, T. A., Amundsen, T., Sorger, H. and Langø, T. (2015). Airway Segmentation and Centerline Extraction from Thoracic CT – Comparison of a New Method to State of the Art Commercialized Methods. PLoS One. **10** (12), e0144282.

Richardson, P. M., McGuinness, U. M. and Aguayo, A. J. (1980). Axons from CNS Neurones Regenerate into PNS Grafts. Nature. **284**, 264–265.

Saito, S., Ozawa, H., Fujioka, M., Hikishima, K., Hata, J., Kurihara, S., Okano, H. J. and Ogawa, K. (2018). Visualization of Nerve Fibers around the Carotid Bifurcation with Use of a 9.4 Tesla Microscopic Magnetic Resonance Diffusion Tensor Imaging with Tractography.

Head Neck. **40** (10), 2228–2234.

Seol, Y.-J., Kang, T.-Y. and Cho, D.-W. (2012). Solid Freeform Fabrication Technology Applied to Tissue Engineering with Various Biomaterials. Soft Matter. **8** (6), 1730–1735.

Shah, L. M. and Ross, J. S. (2016). Imaging of Spine Trauma. Neurosurgery. **79** (5), 626–642.

Smistad, E. (2012). GPU-Based Airway Tree Segmentation and Centerline Extraction, PhD. Institutt for datateknologi og informatikk, Norway.

Smistad, E., Elster, A. C. and Lindseth, F. (2014). GPU Accelerated Segmentation and Centerline Extraction of Tubular Structures from Medical Images. International Journal of Computer Assisted Radiology and Surgery. **9** (4), 561–575.

Smistad, E., Falch, T. L., Bozorgi, M., Elster, A. C. and Lindseth, F. (2015). Medical Image Segmentation on GPUs – A Comprehensive Review. Medical Image Analysis. **20** (1), 1–18.

Steward, M. M., Sridhar, A. and Meyer, J. S. (2013). Neural Regeneration. In *New Perspectives in Regeneration. Current Topics in Microbiology and Immunology*; Heber-Katz, E., Stocum, D. L., Eds.; Springer, Berlin, Heidelberg, **367**,163–191.

Stoll, G., Wilder-Smith, E. and Bendszus, M. (2013). Imaging of the Peripheral Nervous System. In *Handbook of Clinical Neurology*; Elsevier B.V. **115**, 137–153.

Straub, J. and Kerlin, S. (2014). Development of a Large, Low-Cost, Instant 3D Scanner. Technologies. **2** (2), 76–95.

Sunderland, S. S. (1990). The Anatomy and Physiology of Nerve Injury. Muscle and Nerve. **13** (9), 771–784.

Thakkar, R. S., Malloy, J. P., Thakkar, S. C., Carrino, J. A. and Khanna, A. J. (2012). Imaging the Postoperative Spine. Radiologic Clinics of North America. **50** (4), 731–747.

Tins, B. J. (2017). Imaging Investigations in Spine Trauma: The Value of Commonly Used Imaging Modalities and Emerging Imaging Modalities. Journal of Clinical Orthopaedics and Trauma.**8** (2), 107–115.

Wang, Z., Abdulla, R., Parker, B., Samanipour, R., Ghosh, S. and Kim, K. (2015). A Simple and High-Resolution Stereolithography-Based 3D Bioprinting System Using Visible Light Crosslinkable Bioinks. Biofabrication. **7** (4), 045009.

Williams, A. (2014). Central Nervous System Regeneration--Where Are We?. QJM. **107** (5), 335–339.

Yang, G., Kitslaar, P., Frenay, M., Broersen, A., Boogers, M. J., Bax, J. J., Reiber, J. H. C. and Dijkstra, J. (2012). Automatic Centerline Extraction of Coronary Arteries in Coronary Computed Tomographic Angiography. The International Journal of Cardiovascular Imaging. **28** (4), 921–933.

Yang, X., Yang, J. D., Hwang, H. P., Yu, H. C., Ahn, S., Kim, B.-W. and You, H. (2018). Segmentation of Liver and Vessels from CT Images and Classification of Liver Segments for Preoperative Liver Surgical Planning in Living Donor Liver Transplantation. Computer Methods and Programs in Biomedicine. **158**, 41–52.

Yue, Z., Liu, X., Coates, P. T. and Wallace, G. G. (2016). Advances in Printing Biomaterials

and Living Cells. Current Opinion in Organ Transplantation. **21** (5), 467–475.

Zhang, B., Gao, L., Gu, L., Yang, H., Luo, Y. and Ma, L. (2017). High-Resolution 3D Bioprinting System for Fabricating Cell-Laden Hydrogel Scaffolds with High Cellular Activities. Procedia CIRP. **65**, 219–224.

CHAPTER 6
CONCLUSIONS AND RECOMMENDATIONS

6.1 Conclusion

The increased frequency of TBI globally, continues to highlight the lack of successful treatments for patients with TBI. It is estimated that annually 64-74 million people globally will suffer a new TBI. Compounding this issue is the vast scale of TBI severities which can lead to lifelong disability and in some cases death. This alone emphasizes the need for a successful treatment that can be applied shortly after injury to improve the patient's quality of life.

Unfortunately, no real improvements in TBI treatment has occurred due to a few core reasons. Firstly, the CNS is inherently poor in regeneration after injury and the formation of the glial scar, from the primary injury, further inhibits the regeneration process. Secondly, the propagation of brain damage through secondary injury mechanisms further limits the success of prospective treatments. Lastly, and possibly most importantly, the unsuccessful TBI treatments have attempted to treat TBI in a unilateral approach, despite TBI being a multifactorial injury.

The research presented in this dissertation is a merger between biomaterial science, tissue engineering, polymer synthesis, peptide modulation and 3D printing for the design of an aECM scaffold that was 3D printable, biodegradable, cytocompatible and of the adequate brain stiffness. This study provided an *in vitro* evaluation of two 3D printed, optimized, peptide-based hydrogel biomaterials for applications in TBI.

The literature review provided a comprehensive evaluation of the current natural materials utilised in the formation of aECM scaffolds for several tissue engineering applications. Using the information as a guide, the various biomaterials were selected for the design and formulation of the 3D printable aECM scaffold. During the optimization phase, two IPN biomaterials, namely a semi and full IPN, were designed as potential applications in TBI.

The core aim of this work was to develop a 3D printed, self-assembled biomaterial artificial extracellular matrix (aECM) for potential nerve regeneration in TBI applications. The potential TBI application of the biomaterials was substantiated by the significant similarities in structural morphology to the native rat cortex. Cell studies utilising the PC12 neuronal cell line model, demonstrated that despite the IPN biomaterial being biocompatible, the IPNs are capable of supporting cell growth and potentially migration and proliferation. Furthermore, nuclear

eccentricity and nuclear area studies further confirmed the neuro-compatibility of the novel biomaterials as well as providing further evidence of potential augmentation of proliferation. These results suggest that both of the IPN scaffolds would be safe for *in vivo* implantation in a TBI rat model. Lastly, since there is an ongoing need for patient customisable treatments, a proposed method for the design of Custom-Neural-Scaffolds in an attempt to make patient customisable treatments a reality is presented.

6.2 Recommendations

Apart from the benefits presented in this research, a limitation to the present study was that no tensile and compressive mechanical testing could be conducted since both the IPN scaffold systems were soft in nature. Furthermore, the nerve regenerative abilities as well as the effects of delayed nerve repair of the two IPN scaffolds were not investigated in an *in vivo* model. Additionally, a foreseeable limitation of this research is the procurement of 3D printers is very costly and hence the ability of patients accessing this treatment may be limited. As a result, this may further limit the success of the IPN systems as time efficiency is critical to a successful treatment outcome.

In terms of the PEGDA aECM hydrogel attempted in this work, the solidification of the hydrogel could be improved if future researchers utilize different crosslinking strategies. Furthermore, altering the design of the 3D printing needles may assist in preventing needle leakage and more controlled extrusion. In addition, future research should be directed towards different 3D printing techniques that do not require the material to be too viscous.

The current dissertation provided a comprehensive evaluation of the design, fabrication and characterization of two 3D printed GelMA-based aECM scaffolds for potential applications in TBI. It is recommended that studies be conducted to improve and decrease the rate of degradation of both IPN systems. Since the accuracy of 3D printing was not conducted in this work, a shape/volume analysis could be considered as future work discussion. In addition, it is recommended that proliferation studies are conducted to ensure the host tissue remains healthy (no cancer induction). Additionally, it is recommended that further antimicrobial studies are performed on a greater number of pathogens associated with brain infections in order to augment the usage of Genipin in TBI formulations. Due to the cytocompatibility of the IPN biomaterials further research should be conducted to determine the *in vivo* response and performance of the IPN biomaterials. Furthermore, a correlation between the *in vitro* and *in vivo* data can be investigated. Lastly, histological examinations and the degree of functional recovery can be evaluated through the assessment of functional deficits.

APPENDICES

Appendix A1

Received: 9 October 2019 | Revised: 24 March 2020 | Accepted: 28 March 2020
DOI: 10.1002/jbm.a.36981

Check for updates

REVIEW ARTICLE

Society For Biomaterials WILEY

Three-dimensional printing of extracellular matrix (ECM)-mimicking scaffolds: A critical review of the current ECM materials

Kate Da Silva | Pradeep Kumar | Yahya E. Choonara | Lisa C. du Toit | Viness Pillay

Wits Advanced Drug Delivery Platform Research Unit, Department of Pharmacy and Pharmacology, School of Therapeutic Sciences, Faculty of Health Sciences, University of the Witwatersrand, Johannesburg, 7 York Road, Parktown, 2193, South Africa

Correspondence
Viness Pillay, Wits Advanced Drug Delivery Platform Research Unit, Department of Pharmacy and Pharmacology, School of Therapeutic Sciences, Faculty of Health Sciences, University of the Witwatersrand, Johannesburg, 7 York Road, Parktown, 2193, South Africa.
Email: viness.pillay@wits.ac.za

Funding information
National Research Foundation of South Africa; University of the Witwatersrand, Johannesburg; National Research Foundation

Abstract

The loss of tissues and organs through injury and disease has stimulated the development of therapeutics that have the potential to regenerate and replace the affected tissue. Such therapeutics have the benefit of reducing the reliance and demand for life-saving organ transplants. Of the several regenerative strategies, 3D printing has emerged as the forerunner in regenerative attempts due to the fact that biologically and anatomically correct 3D structures can be fabricated according to the specified need. Despite the progress in this field, improvement is still limited by the difficulty in fabricating scaffolds that adequately mimic the native cellular microenvironment. In response, despite the complexities of the native extracellular matrix (ECM), the inclusion of ECM components into bioinks has emerged as a cutting-edge research area in terms of providing possible ECM-mimicking abilities of the 3D printed constructs. Furthermore, the development of ECM-mimicking scaffolds can potentially assist in improving personalized patient treatments. This review provides a critical analysis of selected naturally occurring ECM components as well as synthetic self-assembling peptides in their ability to provide the required ECM microenvironment for tissue regeneration. The success and possible short comings of each material, as well as the specific characteristics of each bioink, are evaluated.

KEYWORDS
3D printing, ECM-mimicking scaffolds/materials, extracellular matrix, regenerative medicine, tissue engineering

1 | INTRODUCTION

Globally, a shortage of patient-compatible tissues and organs results in significant waiting times for patients to undergo organ transplant surgeries (Donderwinkel, van Hest, & Cameron, 2017). As of October 2018, the United States of America Department of Health and Human Services have reported that 115,000 patients are requiring life-saving organ transplants while only 14,500 donors are available (https://optn.transplant.hrsa.gov/). While the number of donors has increased from 5,200 since June 2017 and the number of patients requiring organ transplants has dropped slightly from 120,000 during the same time frame (Derakhshanfar et al., 2018), the supply–demand ratio remains severely disproportionate. In an attempt to provide patients with solutions, 3D printing has emerged as the forerunner in regenerative medical attempts and is potentially the future of organ transplants.

Three-dimensional (3D) bioprinting allows for the creation of complex and anatomically correct structures through the integration of cells and biomaterials (Gopinathan & Noh, 2018). Due to the fact that the goal of the fabricated structure is to ultimately replace the

 © 2020 Wiley Periodicals LLC

Appendix A2

TISSUE ENGINEERING: Part C
Volume 25, Number 7, 2019
© Mary Ann Liebert, Inc.
DOI: 10.1089/ten.tec.2019.0052

termis
Tissue Engineering
& Regenerative Medicine
International Society

METHODS ARTICLE

Preprocessing of Medical Image Data for Three-Dimensional Bioprinted Customized-Neural-Scaffolds

Kate Da Silva, BSc, BMedScHons, Pradeep Kumar, BPharm, MPharm, PhD, Yahya E. Choonara, BPharm, MPharm, PhD, Lisa C. du Toit, BPharm, MPharm, PhD, and Viness Pillay, BPharm, MPharm, PhD

Despite the promising nerve regeneration research, the lack of a therapeutic scaffold to completely restore neurological function is still ongoing and the demand in providing patients with a successful therapeutic outcome is ever increasing. With the advancements in three-dimensional (3D) bioprinting, custom scaffolds with a predetermined size and shape have been successfully fabricated, which can be utilized in nerve damage regenerative attempts to potentially aid in the regaining of nerve function. With the documented success of graphical processing unit (GPU) implementation utilized for image-guided surgeries of tubular and organ structures, we propose the implementation of known processing methods as a means to drastically decrease the time required to process medical images related to nerve damage. In addition, we further propose that the merging of medical image cropping and 3D printing techniques provides a novel approach for providing patient-specific customized-neural-scaffolds for patients suffering with newly acquired nerve damage. Finally, we provide a proposed schematic that incorporates the implementation of GPUs and 3D printing, which we propose will beneficially decrease the waiting times for medical staff to provide patients with customized neural treatments.

Keywords: time-efficient data preprocessing, customized-neural-scaffolds (C-N-S), graphical processing units (GPUs), 3D bioprinting, nerve regeneration, algorithms

Impact Statement

Nerve damage, which can be devastating, triggers several biological cascades, which result in the insufficiencies of the human nervous system to provide complete nerve repair and regain of function. Since no therapeutic strategy exists to provide immediate attention and intervention to patients with newly acquired nerve damage, we propose a strategy in which accelerated medical image processing through graphical processing unit implementation and three-dimensional printing are combined to produce a time-efficient, patient-specific (custom-neural-scaffold) solution to nerve damage. This work aims to beneficially shorten the time required for medical decision-making so that improved patient outcomes are achieved.

Introduction

THE NERVOUS SYSTEM plays an undeniable role in the functioning of several bodily systems, including, but not limited to, the coordination of locomotion, sensory perception, various aspects of homeostasis, and the propagation of information around the body.[1] Nerve system damage can be caused by physical trauma to the nerve fiber or through neurodegenerative disease mechanisms and affects both the peripheral nervous system (PNS) and the central nervous system (CNS).[1] In higher organisms with limited and variable nerve regeneration capabilities (largely attributed to the surrounding nerve environment), regeneration can be achieved (injury dependent) in the PNS, whereas regeneration in the CNS is limited due to a slower clearance of injury matter, the formation of an astroglial scar, and the impedance of neural impulses.[1–6] To restore neurological function, effective axonal communication must be established before,

Wits Advanced Drug Delivery Platform Research Unit, Department of Pharmacy and Pharmacology, School of Therapeutic Sciences, Faculty of Health Sciences, University of the Witwatersrand, Johannesburg, Parktown, South Africa.

Appendix B1

K. Da Silva[1], P. Kumar[1], Y.E. Choonara[1] and V. Pillay[1]

[1]Wits Advanced Drug Delivery Platform, Department of Pharmacy and Pharmacology, Faculty of Health Sciences, University of the Witwatersrand, 7 York Road, Parktown 2193, South Africa.

Introduction: Nerve damage is caused through various injuries that range in severity. Despite 3D bioprinting emerging as an important technique in regenerative attempts, progress is limited by the inability of mimicking the native microenvironment. The shortfall in successful nerve regeneration therapeutics provides a venture into the development of an artificial extracellular matrix (aECM) scaffold to overcome the current issues. This study aims to develop a 3D printed, self-assembled biomaterial aECM for potential neuroregeneration.

Methods: Gelatin Methacryloyl (GelMA) was synthesized using the method established by Van Den Bulcke *et al.,* 2000 and was characterized physicochemically. Bioink gels were prepared by adding native peptides (elastin and collagen) to GelMA and then crosslinked by different mechanisms. Bioinks were physicochemically characterized using Fourier-Transform Infrared Spectroscopy (FTIR) and then the viscoelastic properties were established.

Results: Peptide combination bioinks showed higher shear storage modulus (G') values than aECM gels containing the individual peptides in the GelMA alone. Full and partial interpenetrating network (IPN) bioinks demonstrated degradability by day 8 and 14, respectively. Furthermore, bioinks were insoluble in water at 37 °C. Bioinks were successfully 3D printed into 1x1x4 cm porous scaffolds. Preliminary deconvolution of the Amide I peak with a Gaussian model, indicated that the protein secondary structure of the bioinks were predominately random coils.

Discussion: This study provides an alternative novel bioink for 3D printing neuro applications. Results demonstrated that crosslinking affects G' values and solubility which beneficially influences degradation. Mechanical strength testing is required to establish whether bioink scaffold strength mimics native neural tissues. Scaffolds have the potential to form native bodily protein networks that could assist in neuroregeneration.

Presented at: School of Therapeutic Sciences (STS) Biennial Research Day 2019, University of the Witwatersrand

Appendix B2

3D Printed, Artificial Extracellular Matrix for Potential Neuroregeneration

Kate Da Silva[1], Pradeep Kumar[1], Yahya E. Choonara[1] and Viness Pillay[1*]
[1]Wits Advanced Drug Delivery Platform, Department of Pharmacy and Pharmacology, Faculty of Health Sciences, University of the Witwatersrand, 7 York Road, Parktown 2193, South Africa.
Email: kate.dasilva@students.wits.ac.za, vines.pillay@wits.ac.za

Purpose: Current therapeutic approaches for Traumatic Brain Injury (TBI) are mainly focused on preventing further brain damage rather than facilitating tissue regeneration. Due to the importance of the native extracellular matrix (ECM) in the formation of new tissues and networks, the development of an artificial matrix system that can promote tissue regeneration after injury could beneficially influence the native tissue reparative process as well as potentially decreasing fibrotic scar formation. The aim of this study is to develop a 3D printed, self-assembled biomaterial artificial extracellular matrix (aECM) to potentially facilitate nerve regeneration.

Methods: 3D printing interpenetrating polymer network (IPNs) biomaterial gels were formulated through the blending of Gelatin Methacrylamide (GelMA), synthesized through the modification of gelatin with methacrylic anhydride, and native brain peptides (elastin and collagen). To achieve good printing resolution through a 0.2 mm internal diameter needle for a 10x10 mm scaffold (1 mm line spacing), extrusion pressure ranged from 3.8 - 4.3 bar with a print speed of 10 mm/s. The printing cartridge temperature was kept at 18 °C whilst the platform temperature was set to 13 °C. Lastly, IPN biomaterial gels were subjected to physicochemical, physicomechanical and viscoelastic analysis.

Results: ^{1}H NMR results confirmed the composition of the GelMA polymer through the increase of the methacrylate vinyl signal at δ=5.9 ppm and δ=6.3 ppm. At low temperatures, peptide combination biomaterials indicated the formation of an elastic gel network evident by a considerably higher shear storage modulus (G') than shear loss modulus (G'') in comparison to aECM gels containing the individual peptides in the GelMA alone. Peptide inclusion was shown to have no effect on the ability of GelMA to form several covalent interactions after crosslinking. This was evident by IPN biomaterials being insoluble in water above 37 °C due to the covalent crosslinks impeding helix formation between the gelatin chains. Furthermore, the protein Amide backbone was shown to be intact after two minutes of UV exposure at 365 nm. The partial IPN biomaterial exhibited a slightly stronger network stability in comparison to the full IPN biomaterial as degradation was evident at day 14 and day 8, respectively. Lastly, 3D printing was shown to decrease the melting point of the system in comparison to the GelMA polymer alone.

Conclusion: Novel 3D printable biomaterials were developed through the blending of a semisynthetic polymer and native peptides. Peptide inclusion to the GelMA polymer was shown to beneficially increase the elasticity of the fabricated network which alludes to the formation of native body protein networks. The novel fabricated IPN 3D printable biomaterials may provide the crucial solution to overcoming the current TBI therapeutic shortfalls by potentially assisting in neuroregeneration.

Presented at: Annual Conference on Pharmaceutical Sciences of the Academy of Pharmaceutical Sciences (Young Scientist of the Year) 2019.

Appendix B3

3D PRINTED, ARTIFICIAL EXTRACELLULAR MATRIX FOR POTENTIAL NEUROREGENERATION

Da Silva, K.[1], Kumar, P.[1], Choonara, Y. E. [1] and Pillay, V.[1]

[1]Department of Pharmacy and Pharmacology (Wits Advanced Drug Delivery Platform), School of Therapeutic Sciences, Faculty of Health Sciences, University of the Witwatersrand.

Current therapeutic approaches for Traumatic Brain Injury (TBI) focus on preventing further damage rather than facilitating tissue regeneration. Due to the importance of the extracellular matrix (ECM) in tissue formation, an artificial matrix that can promote tissue regeneration after injury could beneficially influence the native tissue reparative process and potentially decrease fibrotic scar formation. The aim is to develop a 3D-printed, artificial extracellular matrix (aECM) for potential neuroregeneration. 3D-printed interpenetrating polymer network (IPNs) biomaterial gels were formulated through the blending of Gelatin Methacrylamide (GelMA) and brain peptides. Achieving high printing resolution through a 0.2 mm internal diameter needle, extrusion pressure ranged from 3.8-4.3 bar with a print speed of 10 mm/s. IPN gels were subjected to physicochemical/physicomechanical and viscoelastic analysis. At low temperatures, peptide IPNs formed elastic gel networks with a considerably higher storage modulus than loss modulus in comparison to individual peptides with GelMA alone. Peptide inclusion had no effect on GelMA forming covalent interactions after crosslinking as IPN biomaterials were insoluble in 37 °C water (covalent crosslinks impede gelatin chain helix formation). Furthermore, the protein backbone was intact after two minutes of UV exposure. The partial IPN exhibited a stronger network stability over the full IPN as degradation was evident at day 14 and 8, respectively. Novel 3D-printable biomaterials were developed through blending a semisynthetic polymer with native peptides. Peptide inclusion increases the network elasticity which alludes to native protein network formation. The IPNs may provide the solution to overcoming TBI therapeutic shortfalls by potentially assisting in neuroregeneration.

Word count: 250 words

Acknowledgements: This research has been funded by the National Research Foundation (NRF) of South Africa.

Presented at: Annual Molecular Biosciences Research Trust (MBRT) Postgraduate Research Day 2019, University of the Witwatersrand

Appendix B4

11th Wits Cross Faculty Postgraduate Symposium: Abstract

NAME: KATE DA SILVA
DEGREE AND YEAR OD STUDY: MSc Medicine (Pharmacy), 3rd Year
FACULTY: Health Science
SCHOOL: Therapeutic Sciences
STUDENT NUMBER: 790180
STUDENT EMAIL: kate.dasilva@students.wits.ac.za
INDICATE YOUR CHOICE: Oral
TITLE of RESEARCH TOPIC: A Peptide-based 3D-Printed Artificial Extracellular Matrix for Potential Neuroregeneration in Traumatic Brain Injury
SUPERVISOR NAME: Prof. Viness Pillay, Prof. Yahya Choonara, Assoc. Prof. Pradeep Kumar

Keywords: Traumatic Brain Injury, Artificial Extracellular Matrix, neuro-regenerative 3D printing

---

Often described as the “silent epidemic”, Traumatic Brain Injury (TBI) is not recognized as a public health crisis and yet is a major contributor to death and disability globally. TBI is defined as any disruption to normal brain functioning caused by an external force (1). In South Africa (SA), the yearly incidence of TBI has been estimated at 316 per 100 000 people (2), however, the overall incidences are likely to be higher due to a lack of a South African TBI databank and insufficient studies focussing on the incidence and prevalence of TBI in SA (3). Due to the wide variations in the clinical manifestation of TBI, TBI treatment strategies are based on a “one-size-fits-all” approach and poorly address individual patient needs. This work focuses on the design of a novel peptide-based 3D-printed, interpenetrating polymer network systems as artificial Extracellular Matrix (aECM) hydrogels for potential neuroregeneration in TBI. IPN hydrogels were formulated by blending gelatin methacryloyl (GelMA) with collagen and elastin and crosslinked through different mechanisms. Achieving high printing resolution through a 0.2 mm bore needle, extrusion pressure ranged from 3.8-4.3 bar with a print speed of 10 mm/s for a 10x10x10 mm scaffold. Protein backbone functionality remained unaffected after 2 minutes of UV curing (365 nm) to induce polymeric crosslinking. Gaussian deconvolution of the Amide I band, indicated that the proteins of IPN hydrogels assembled into confomations potentially mimicking the ECM microenvironment. During rehydration a “shape-memory” feature was discovered, facilitating brain tissue mimicry. IPN hydrogels also promoted high cell viability and migration through the hydrogels, indicating the development of a suitable suitable aECM microenviroment. In conclusion, the 3D-printed IPN hydrogels may provide a promising solution to overcome current limitations in the therapeutic modalities for TBI by facilitating neuroregeneration as an aECM with brain tissue mimicry.

REFERENCES: (please use the format shown below)

1. Faul, M.; Xu, L.; Walk, M. M.; Coronado, V. G. In Traumatic Brain Injury in the United States: Emergency Department Visits, Hospitalizations and Deaths 2002-2006. Atlanta (GA): Centres for Disease Control and Prevention, National Center for Injury Prevention and Control, **2010**.
2. Nell, V.; Brown, D. S. O. *Soc. Sci. Med.* **1991**, *33*, 289-296.
3. Naidoo, N. *S Afr Med J.***2013**, *103*, 613-614.

Presented at: 11th Wits Cross Faculty Postgraduate Symposium 2020, University of the Witwatersrand

Appendix B5

Regeneration and Repair: Designing a 3D-Printed Artificial Extracellular Matrix for Potential Neuroregeneration in Traumatic Brain Injury

Kate Da Silva[1], Pradeep Kumar[1], Yahya E. Choonara[1] and Viness Pillay[1]

[1]Wits Advanced Drug Delivery Platform, Department of Pharmacy and Pharmacology, Faculty of Health Sciences, University of the Witwatersrand, 7 York Road, Parktown 2193, South Africa.

Annually, it is estimated that 50 million people globally will suffer a Traumatic Brain injury (TBI) with TBI considered to be one of the leading causes of disability, morbidity and mortality in all age groups. TBI treatment strategies are based on a “one-size-fits-all” approach and are insufficient in addressing individual patient needs. The current study presents novel 3D-printed peptide-based interpenetrating polymer networks (IPN) as artificial extracellular matrix (aECM) hydrogels for potential neuroregeneration. IPN hydrogels were formulated by blending gelatin methacrylamide (GelMA) with collagen and elastin and crosslinked through different mechanisms. Achieving high printing resolution through a 0.2 mm bore needle, extrusion pressure ranged from 3.8-4.3 bar with a print speed of 10 mm/s for a 10x10 mm scaffold. Differential Scanning Calorimetry (DSC) confirmed the formation of two IPN systems as denaturation of the gelatin helix of the GelMA polymer required more energy for the Full-IPN (168.18 °C), indicating a greater protein stability, than the Semi-IPN (140.59 °C). The full-IPN demonstrated anti-microbial activity and possibly indicates a self-sterilizing feature that can potentially lower infection rates post-transplant. Scanning Electron Microscopy imaging (SEM) indicated the IPN systems have an ordered, porus microstructure with independent, smooth “pockets” seperated by thin walls. IPN hydrogels also promoted high *in vitro* cell viability, attachment and migration throughout the hydrogels, indicating a suitable aECM microenviroment. In conclusion, the 3D-printed IPNs may provide a promising solution to overcome current limitations in the therapeutic modalities for TBI by facilitating neuroregeneration as an aECM with brain tissue mimicry.

Presented at: Faculty of Health Sciences Biennial Research Day 2020, University of the Witwatersrand